

PLANETESIMAL FORMATION BY DUST COAGULATION

FREDRIK WINDMARK

Breaking through the barriers with sweep-up growth

Referees:

Prof. Dr. Cornelis P. Dullemond

Prof. Dr. Mario Trieloff

August 2013

Fredrik Windmark: *Planetesimal formation by dust coagulation*, Breaking through the barriers with sweep-up growth, © August 2013

Dissertation

submitted to the
Combined Faculties of the Natural Sciences and Mathematics
of the Ruperto-Carola-University of Heidelberg, Germany
for the degree of

Doctor of Natural Sciences

Put forward by

Fredrik Windmark

Born in: Motala, Sweden

Oral Examination: 5.11.2013

ABSTRACT

When the protostellar nebula collapses to form a star, some of the gas and dust is left in the form of a protoplanetary disk. Exactly how the subsequent formation of planetesimals proceeds is still not fully understood, but the coagulation of the dust is believed to play a vital role. One of the main problems with this picture is that a number of barriers have been identified, at which bouncing, fragmentation and radial drift prevent the formation of large bodies.

We have investigated via theoretical models how large dust grains can grow in the presence of these barriers. This was done by examining some of the many assumptions that are generally used in the dust evolution modeling. We implemented a realistic model for the outcome of dust collisions, and we also studied the effect of velocity distributions and particle clumping, as well as the fate of large dust grains that drift inwards towards the star. In this process, we identified a new channel for planetesimal formation, and describe the initial steps towards an inside-out formation model where we give a prediction of the size and spatial distribution of the first generation of planetesimals.

ZUSAMMENFASSUNG

Beim Kollaps eines protostellaren Nebels zu einem Stern verbleibt ein Teil des Gases und Staubs in Form einer protoplanetaren Scheibe. Wie die anschließende Entstehung von Planetesimalen genau verläuft ist noch nicht vollständig verstanden, aber es wird angenommen, dass Koagulation von Staubteilchen eine wichtige Rolle spielt. Eines der Hauptprobleme hierbei ist jedoch, dass viele Wachstumsbarrieren identifiziert worden sind, weil radialer Drift, Fragmentierung und das voneinander Abprallen der Staubkörner die Bildung von großen Körpern verhindern.

Wir haben mit Hilfe theoretischer Modelle untersucht, zu welcher Größe Staubkörner in der Anwesenheit dieser Barrieren heranwachsen können. Dies wurde durch Untersuchung einiger der vielen Annahmen durchgeführt, die standardmäßig in der Modellierung der Staubentwicklung verwendet werden. Wir implementierten ein realistisches Modell für den Ausgang von Staubkollisionen, und studierten die Wirkung der Geschwindigkeitsverteilung und Partikelverklumpung, sowie, was mit den in Richtung des Sterns driftenden großen Staubkörnern geschieht. Dabei haben wir einen neuen Weg für Entstehung der Planetesimale entwickelt und beschreiben die ersten Schritte eines Modells in dem Planetesimale in den inneren Scheibenregionen zuerst gebildet werden. Wir geben eine erste Vorhersage zur Größe und räumlichen Verteilung der ersten Planetesimalgeneration an.

PUBLICATIONS AND AUTHORSHIP

The ideas and results presented in this thesis have previously appeared or will appear in the following publications:

Windmark, Birnstiel, Güttler, Blum, Dullemond, Henning, A&A (2012), vol 540, A73

Windmark, Birnstiel, Ormel, Dullemond, A&A (2012), vol 544, L16

Drążkowska, Windmark, Dullemond, A&A (2013), vol 556, A37

Windmark, Ormel, Birnstiel, Dullemond, in prep.

Windmark, Okuzumi, Drążkowska, in prep.

The details of authorship are listed individually for each thesis chapter:

Chapter 1: Everything was written by me. I made all the figures except for Figures 1.1, 1.4 and 1.6, which were reproduced with permission from the original authors.

Chapter 2: Everything was written by me, and I made all the figures. The scientific development, including the collision model creation and implementation, and the running and interpretation of the simulations was done by me. Parts of the collision model were created in close collaboration with Carsten Güttler and Jürgen Blum.

Chapter 3: Everything was written by me, and I made all the figures. The idea of velocity distributions was initially conceptualized together with Chris Ormel, and the numerical implementation was done in collaboration with Til Birnstiel. The subsequent testing of the code, as well as the running and interpretation of the simulations, was done by me.

Chapter 4: Everything was written by me, and I made all the figures. The scientific development, including the clustering formalism and modeling and the running and interpretation of the simulations, was done by me.

Chapter 5: Everything was written by me, and I wrote the original Sect. 5 of the paper. The original work was lead by Joanna Drążkowska with significant input from me. The collision model was adapted from my work, and I was involved in its implementation. The results and conclusions were a direct product of our collaboration.

Chapter 6: Everything was written by me, and I made all the figures. The scientific development, including the making of the toy model and the running and interpretation of the simulations was done by me. The idea of the planetesimal pileup was a result of a collaboration with Satoshi Okuzumi, and Joanna Drążkowska contributed significantly to the discussion.

CONTENTS

1	INTRODUCTION	1
1.1	A brief overview of planet formation	2
1.2	Observations of planetary systems	9
1.2.1	The Solar System	9
1.2.2	Meteorites	11
1.2.3	Exoplanets	13
1.3	The protoplanetary disk	15
1.3.1	Observational constraints	15
1.3.2	Theoretical disk structure	17
1.4	Dust evolution	19
1.4.1	The dust spatial distribution	19
1.4.2	Relative velocities	23
1.4.3	Dust collision physics	26
1.4.4	Dust coagulation	28
1.4.5	Barriers to growth	30
1.4.6	Alternative planetesimal formation scenarios	33
1.5	The aim of this thesis	34
2	PLANETESIMAL FORMATION BY SWEEP-UP COAGULATION	37
2.1	Introduction	38
2.2	Motivation behind the development of a new collision model	40
2.2.1	Overview of recent experiments and simulations	41
2.2.2	Individual treatment of collisions	44
2.3	Implementation of the model	45
2.3.1	Sticking and bouncing thresholds	46
2.3.2	An energy division scheme for fragmentation	47
2.3.3	A new mass transfer and cratering model	49
2.3.4	Fragmentation distribution	52
2.3.5	Implementation of the model	53
2.4	The dust-size evolution model	55
2.5	Results	55
2.5.1	The collision outcome space	56
2.5.2	The dust-size evolution	60
2.5.3	A growth toy-model	66
2.5.4	Forming the first seeds	69
2.6	Discussion and conclusions	70
3	VELOCITY DISTRIBUTION EFFECTS ON THE GROWTH BARRIERS	73
3.1	Introduction	73
3.2	Method	74
3.2.1	Collision models	75
3.2.2	The velocity distribution	76
3.3	Results	77
3.3.1	The fragmentation barrier	78

3.3.2	The bouncing barrier	79
3.3.3	Breaking through the barriers	80
3.4	Discussion and conclusions	81
3.A	Stochastic and deterministic relative velocity sources	82
3.B	A resolution study	84
4	PARTICLE GROWTH IN CLUSTERING: HOW FAR CAN DUST COAGULATION PROCEED?	87
4.1	Introduction	87
4.2	Particle clustering in turbulence	89
4.3	Coagulation in clumps explained	91
4.3.1	Intuitive way of looking at clumping	92
4.3.2	The pair correlation function	92
4.3.3	Full implementation of the radial distribution function	95
4.4	Numerical implementation and cluster modeling	96
4.4.1	Collision models	97
4.4.2	Velocity distributions	98
4.4.3	Modeling the clustering factor	99
4.4.4	A simplified clustering model	102
4.5	Dust evolution models with clustering	103
4.5.1	The effect of a velocity PDF on the steady state	104
4.5.2	The effect of clustering on the steady state	108
4.5.3	Growth timescale	111
4.6	Discussion and Conclusions	113
5	GROWTH BREAKTHROUGH AT THE INNER EDGE OF DEAD ZONES	115
5.1	Introduction	115
5.2	A brief overview of Monte Carlo dust evolution	117
5.3	Dead zone and pressure bump formation at the snow line	119
5.4	The disk and collision models	120
5.5	Sweep-up growth at the inner edge of dead zones	121
5.6	Discussion and conclusions	125
6	PILE-UP OF PLANETESIMALS IN THE INNER PROTOPLANETARY DISK	127
6.1	Introduction	127
6.2	Drift and growth timescales	129
6.2.1	Radial drift	129
6.2.2	Particle growth	132
6.2.3	A drift and growth toy model	133
6.3	Numerical model	134
6.4	Results	136
6.4.1	Pure coagulation	136
6.4.2	Sweep-up growth	138
6.5	Discussion and conclusions	140
7	SUMMARY AND OUTLOOK	143
	BIBLIOGRAPHY	147

INTRODUCTION

It is today clear that our Solar System is not the only one to harbor planets. In fact, the exoplanet observations of the last years have even shown planets to be ubiquitous in our Galaxy, and their properties display a remarkable diversity. There are now planets discovered that are smaller than Mercury and many times larger than Jupiter, and the distances between them and their host stars range from only a few times the radius of the star and up to thousands of AU (1 AU = the mean distance between the Sun and the Earth), and some are even free-floating. Planets can be rocky or gaseous, and systems can be either neatly ordered like the Solar System, or made up of planets with highly eccentric or inclined orbits. It seems like the planet formation process is capable of occurring anywhere in connection to star formation. This is an amazing discovery, but also surprising, as theoretical studies on the contrary seem to identify more and more barriers against planet formation. At the moment, it is still uncertain how planets can form at all given these barriers.

The basis of the planet formation theories is the protoplanetary disk, which is the gaseous, circumstellar disk around a young star. Tiny dust grains made out of silicates, metals, organics or ices, make up a small fraction of such a disk, and it is these grains that are the building blocks of planet formation. As the grains interact with the surrounding gas, they start to collide with each other and stick together to form successively larger aggregates in what is called incremental growth or dust coagulation. However, as the grains get more and more decoupled from the gas, they collide at increasing collision velocities, and at some point, they start to bounce or fragment during collisions. Grains that anyway manage to grow instead drift rapidly inwards towards the star and are lost. These effects give rise to barriers that efficiently prevent any further growth, and because this in the first models occurred for meter-sizes at 1 AU, they are often collectively referred to as the meter-size barrier¹. The later stages, where the gravity kicks in, are generally better understood than the coagulation stage. However, the outcome is highly dependent on the initial planetesimal size-distribution, which due to the growth barriers is still largely unknown.

In this thesis, I have investigated the planetesimal formation stage, and probed how large dust aggregates can grow through coagulation by investigating the robustness of the growth barriers. This stage is uncertain for numerical reasons, but there are also microscopic uncertainties; e. g. what

¹ This is a popular historical term which is inaccurate, both because the barrier can occur anywhere between sizes of millimeters to several meters depending on the local disk conditions, and because the barriers have different physical origins. We will from now on instead refer to the collective term as "growth barriers".

happens when two grains collide, or how does the turbulence affect the velocities of individual grains; and macroscopic uncertainties, e. g. what is the real structure of the protoplanetary disk and how does its features affect the dust motion. An important part of my work has been to answer parts of these questions and bring the microscopic and macroscopic dust evolution closer together.

Through this thesis, we will follow the story of the dust evolution from micrometer-sized grains to kilometer-sized planetesimals, but we will first need to know more about the background. For the remainder of this introduction, I will therefore describe the important concepts of planet formation, and give an overview centered around the aspects of dust growth and planetesimal formation.

1.1 A BRIEF OVERVIEW OF PLANET FORMATION

It is first necessary to give a rough overview of the star formation process. The first step is taken in the environment of a giant molecular cloud. Compared to the interstellar medium (ISM) average, these clouds are cool and relatively dense, which allows for star formation to initiate. The stability of the cloud substructure can in an idealized form be described by the balance between the outward gas pressure and the inward gravitational force. The critical Jean's mass is the mass required for the gas pressure to be overcome for a subset of the cloud in the form of a sphere of radius equal to the Jean's length, R_J , and is roughly equal to

$$M_J \simeq 2M_\odot \left(\frac{c_s}{0.2 \text{ km s}^{-1}} \right)^3 \left(\frac{n}{10^3 \text{ cm}^{-3}} \right)^{-1/2}, \quad (1.1)$$

where $c_s \sim 0.2 - 0.5 \text{ km s}^{-1}$ is the sound speed and $n \sim 10^4 - 10^6 \text{ cm}^{-3}$ is the gas number density. If the Jean's mass is exceeded, the substructure starts to collapse into a protostellar core. From the Jean's mass approximation, we find that the typical mass of such a collapsing core is on the order of a few M_\odot , which can be compared to the total giant molecular cloud mass that can be as high as $10^7 M_\odot$ spread over $\lesssim 100 \text{ pc}$. This means that stars rarely form alone, but that the environment instead is rather crowded, and full of interactions even during the subsequent planet formation stage. Most such clusters only disperse after $0.1 - 1 \text{ Gyrs}$ due to gravitational interactions and tidal forces. Except for a few studies (Adams 2010), the effects of intra-cluster interactions are however largely ignored in the context of planet formation, and we will from now on focus on the isolated evolution of a stellar core.

It is very difficult to spatially resolve even the nearest cloud cores or circumstellar disks in the Solar neighborhood. It can therefore be useful to characterize the young stellar objects (YSOs) by their spectral energy distribution (SED), which describes the flux distribution from an object as a function of frequency or wavelength. Lada (1987) and Andre et al. (1993)

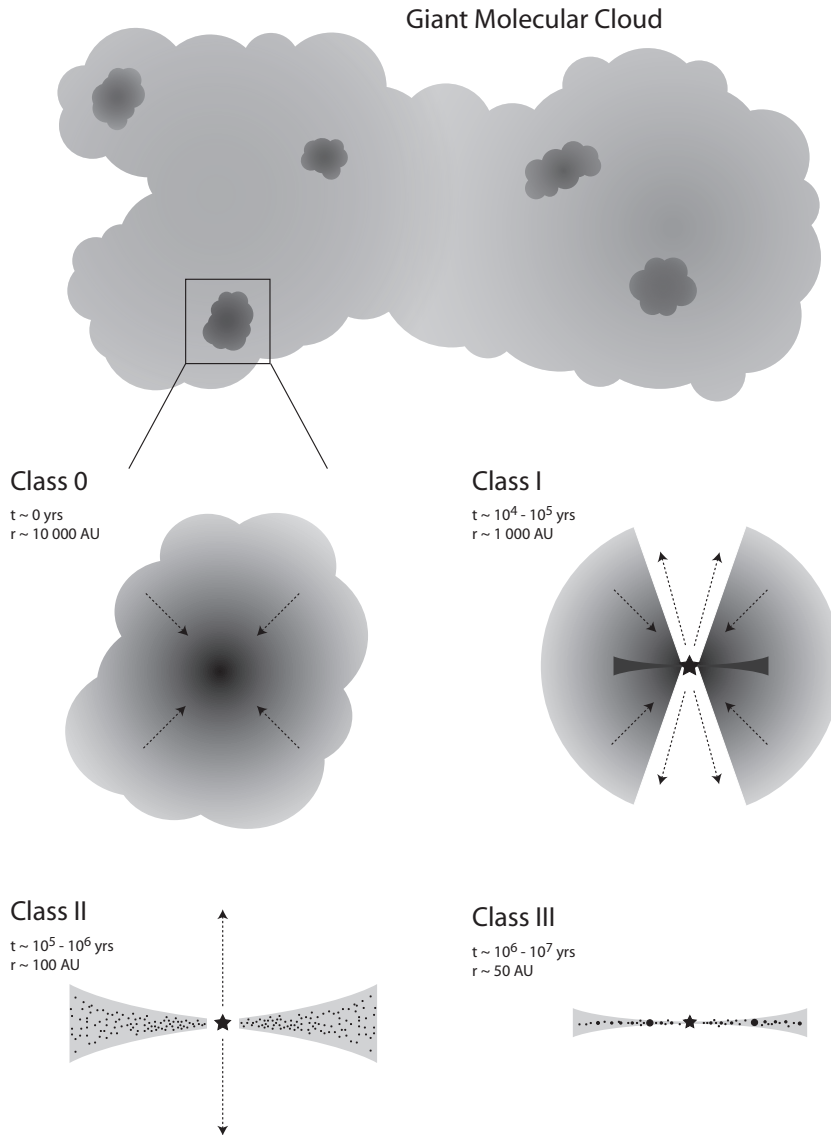


Figure 1.1: Illustration of the star formation process and the evolution of the pre-main sequence star and its disk. The observational classes are defined by the degree of IR excess, but correspond well to the physical processes of gravitational collapse, the accretion of the stellar envelope and formation and dissipation of the circumstellar disk.

developed a classification system based on the slope in the near- to mid-IR (corresponding to wavelengths between 2-20 μm):

$$\alpha_{\text{IR}} = \frac{\Delta \log(\lambda F_{\lambda})}{\Delta \log(\lambda)}. \quad (1.2)$$

This is an especially interesting spectral region for the YSOs, because they all show an IR excess above the stellar blackbody radiation. This is caused by the opacity of the hot dust in the stellar envelope or disk, which causes the stellar radiation to get re-emitted at longer wavelengths. In the case of a blackbody or star, $\alpha_{\text{IR}} < -1.6$, but when the emission is dominated by the non-central source, the slope changes. Below, we briefly discuss the

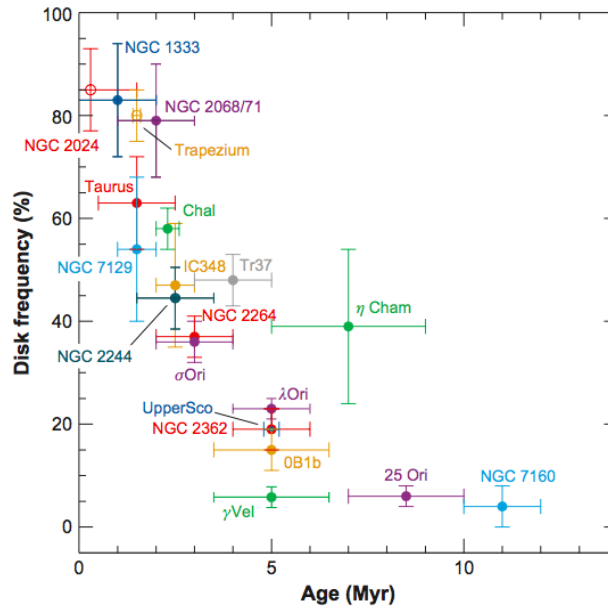


Figure 1.2: By measuring the IR-excess of the stars in different young stellar clusters, it is possible to determine the fraction of sun-like stars with disks as a function of the cluster age, and from that, the mean disk lifetime. Figure reproduced from Wyatt (2008).

general properties of the YSO classes and the evolution of their inferred physical properties, which are also shown in the sketch of Fig. 1.1.

Class 0 (no measurable excess below $20 \mu\text{m}$): During the gravitational collapse phase, the emission originates from an embedded central luminosity source that until the advent of the Spitzer telescope could only be indirectly observed through the properties of the envelope. All of the radiation is re-emitted at long wavelengths, and the SED peaks in the far-IR or at mm wavelengths, indicating warm (but not hot) envelope temperatures of $T < 70 \text{ K}$.

Class I ($a_{\text{IR}} > 0.3$): Because the infalling material possesses angular momentum that must be conserved, most of the mass will not fall directly into the stellar core, but will instead form a circumstellar accretion disk. During the collapse, lasting $\sim 10^4 - 10^5$ years, the density and temperature of the core increases, which raises the outward pressure. At temperatures of $T \sim 2000 \text{ K}$, the pressure finally balances the inward gravitational force, and the protostar is formed. During the contraction, the envelope becomes hot enough ($>70 \text{ K}$) to become visible in the mid-IR. As the disk matter is accreted onto the protostar, viscosity and gravitational torques causes angular momentum transport to the outer regions. The result is the moving inward of the majority of the disk matter, while some mass moves outwards to conserve angular momentum, creating a disk with a size up to 1000 AU (Hartmann et al. 1998).

Class II ($-0.3 < a_{\text{IR}} < 0.3$): As matter is accreted and dust grains grow, the strength of the IR excess decreases, and the object can be identified through its emission as a composite from both the star and disk. The low-

mass ($< 2 M_{\odot}$) sources are also called T Tauri sources, after the archetypical T Tauri star. Because the properties of these stars are similar to those of the Sun, and because they are the most numerous, the T Tauri stars are the main objects of the planet formation studies. More massive YSOs are referred to as Herbig Ae/Be stars.

Class III ($\alpha_{\text{IR}} < -1.6$): The IR excess disappears after 1-10 Myrs, which indicates that the disk has finally dispersed. As pioneered by Haisch et al. (2001), the characteristic disk dispersal time can be obtained by observing individual stellar clusters and determining the fraction of stars with IR excess. If the cluster age can be determined by e. g. main sequence fitting, it is then possible to make a plot as shown in Fig. 1.2, which indicates a mean disk lifetime of ~ 3 Myrs. Exactly how the disk disappears is still a matter of debate, but likely candidates are due to photoevaporation as the star initiates its hydrogen-burning at the main sequence, or due to the formation of massive planets that sweep or stir up the gas, or a combination thereof (Alexander et al. 2006; Rosotti et al. 2013). The disk lifetime sets a time constraint on the process of planet formation, as the gaseous Jupiter-like planets must be formed before the gas has dissipated. The wealth of observed massive planets therefore indicates that the giant planet formation must occur on timescales faster than ~ 1 Myr.

We now turn the focus to the planet formation aspect, which is summarized schematically in Fig. 1.3. The first steps of planet formation is the dust coagulation, which is vital for almost all formation scenarios. Most of what we know about the initial dust properties come from interstellar extinction studies. One of the fundamental properties of dust is its capability of attenuating light (shorter wavelengths more efficiently than longer), which is the main cause of interstellar extinction and reddening. By comparing a reddened star to a similar, unreddened star, it is therefore possible to examine the dust content along the line of sight. Using wavelength-dependent dust opacities, Mathis et al. (1977) modeled the effects of various dust size-distributions and compositions and compared to the observed extinction curves. Their findings are known as the MRN distribution, which has a shape $n(a) \propto a^{-3.5}$, where the largest particles are $\sim 1 \mu\text{m}$ in size. From these fittings, and also utilizing absorption lines, we also know the dust grains to be composed of silicates, hydrocarbons and mixtures of frozen-out H_2O and CO .

Because of the interaction between the solids and the surrounding gas, relative velocities Δv are induced between the grains, and because the dust density in the disk ($\rho_{\text{d}} \gtrsim 10^{-15} \text{ g cm}^{-3}$) is significantly increased compared to the ISM ($\rho_{\text{d}} \lesssim 10^{-20} \text{ g cm}^{-3}$), collisions between the grains are frequent. If we consider the collisions between two particle species with number densities $n_{\text{d},i}$ and $n_{\text{d},j}$, and a collisional cross section $\sigma = \pi(a_i + a_j)^2$, the collision rate becomes

$$f_{\text{coll}} = n_{\text{d}} \sigma \Delta v . \quad (1.3)$$

Due to intermolecular forces, primarily van der Waals forces for silicates and dipole forces for ices, small grains tend to stick together as they collide.

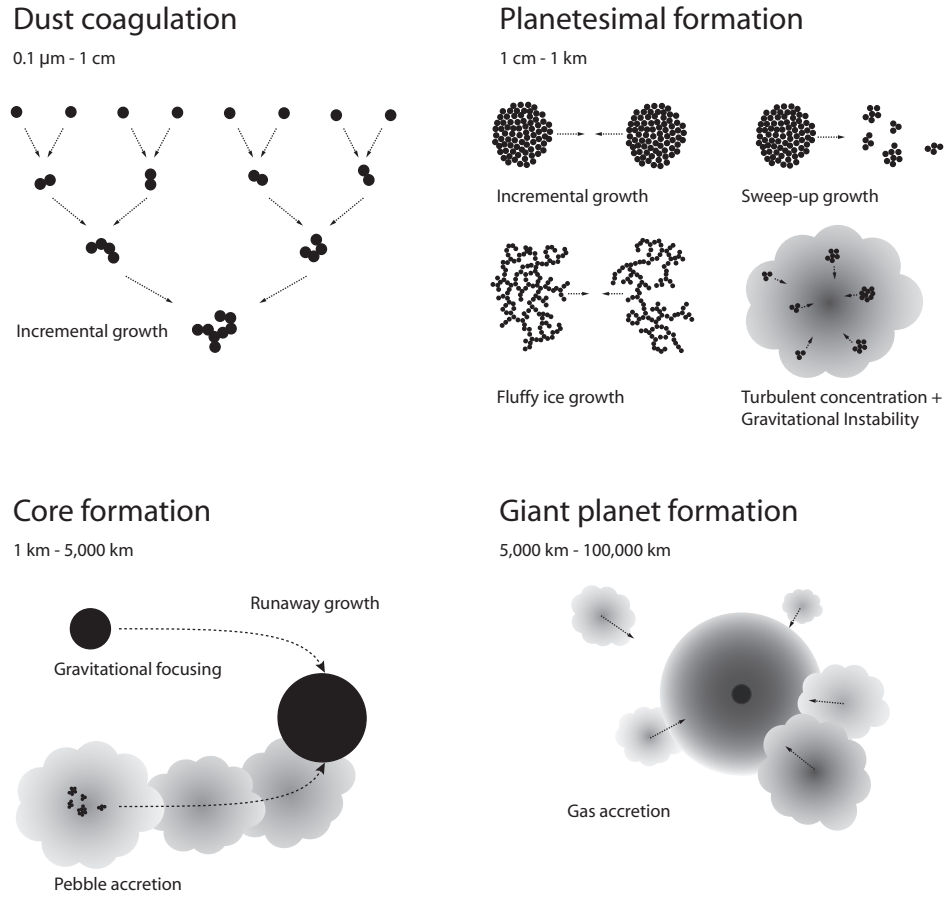


Figure 1.3: Illustration of the primary mechanisms involved in the canonical planet formation process. The initial building blocks are the $0.1 - 1 \mu\text{m}$ monomers that stick together via intermolecular forces, and $1 - 100$ Myrs later, the results are gas giants and rocky planets. The planetesimal formation stage occurring in between is still poorly understood, although a number of possible formation channels exist. Once at km-sizes, gravity helps the planetesimals to both survive the high-velocity collisions and to enhance the accretion efficiency of the other planetesimals and surrounding dust pebbles.

If we assume a monodisperse growth scenario where the particle population can be described by a delta-function of mass m and size a , the growth rate becomes

$$\frac{dm}{dt} = mf_{\text{coll}} = \rho_d \sigma \Delta v, \quad (1.4)$$

where $\rho_d = m \cdot n_d$ denotes the dust mass density. To translate this to size, we take $dm = 4\pi a^2 \zeta da$ and $\sigma = 4\pi a^2$ to obtain

$$\frac{da}{dt} = \frac{\rho_d}{\zeta} \Delta v, \quad (1.5)$$

which gives a growth timescale

$$t_{\text{growth}} = a \left(\frac{da}{dt} \right)^{-1} = \frac{a \zeta}{\rho_d \Delta v}. \quad (1.6)$$

We now consider a typical disk at 1 AU, which would have a midplane mass density of $\rho_d \sim 10^{-11} \text{ g cm}^{-3}$ or larger. Assuming dust grains of solid density $\zeta = 1 \text{ g cm}^{-3}$, grains of size $a = 10^{-4} \text{ cm}$ have relative velocities of $\Delta v \sim 1 \text{ mm s}^{-1}$, which gives a growth timescale of $t_{\text{growth}} \sim 3 \text{ yrs}$, which is significantly shorter than the disk lifetime. When the grains grow larger, they start to decouple from the gas and increase their relative velocities further. 1 cm grains have relative velocities of $\Delta v \sim 1 \text{ m s}^{-1}$, which gives $t_{\text{growth}} \sim 30 \text{ yrs}$. It is from this little experiment clear that grain growth will be significant in the protoplanetary disk, and that kilometer-sized bodies have the capability of forming on very short timescales.

As noted above, as the grains grow, their relative velocities increase rapidly in the presence of turbulence and drift. At meter-sizes at 1 AU, the boulders are predicted to collide at the highest velocities of 10 – 100 m s^{-1} (Brauer et al. 2008). At these high collision velocities, the particles tend to bounce or fragment rather than stick together. Simultaneously, because the grains do not experience the pressure support that the gas does, they naturally try to orbit at slightly faster velocities. The result is a constant headwind which causes a loss of angular momentum and inward drift on short timescales. Meter-sized boulders at 1 AU are predicted to drift into the star on timescales of 100 yrs. All of these effects have turned out to efficiently prevent any growth to larger sizes (Weidenschilling 1977a, 1980; Nakagawa et al. 1986). A number of scenarios have been suggested for how these growth barriers might be overcome (some of which are discussed in Sect. 1.4.6), but a fully self-consistent scenario has yet to be produced.

Ignoring for now the problem of how the planetesimals are formed, the next step in the formation process is when the kilometer-sized planetesimals continue their growth aided by self-gravity in what is called embryo formation. Gravity aids the growth in two major ways. Firstly, it makes the bodies more resilient towards fragmentation, as mass loss now requires both disrupting the body and ejecting the fragments out of the gravitational potential well. Such collisions can be modeled numerically by e. g. the SPH method (Benz & Asphaug 1999; Leinhardt & Stewart 2009). A likely outcome of high-velocity collisions is that planetesimals would survive in the form of rubble piles, held together primarily by their self-gravity.

Collisions between similar-sized planetesimals might however still be problematic if the impact velocities are too high. It is believed that turbulent stirring, the random pull that the turbulent gas exerts on the bodies, will lead to velocity excitation to relative velocities of several 100 m s^{-1} . This would be enough for destructive collisions (Nelson 2005; Nelson & Gressel 2010), and is known as the kilometer-size barrier. One way to circumvent this problem could be to very quickly form planetesimals that are massive enough to be resilient enough to the destructive collisions. Another possibility is for the primary mode of planetesimal growth to be due to accretion of smaller dust grains (Ormel & Okuzumi 2013).

It can however be noted that all planetesimal collision models assume the bodies to be rocky, which is far away from the aggregate structures of

the initial dust grains. The primary effect believed to cause the thermal processing required for the rocky bodies to form is by the decay of short-lived radioactive nuclides (primarily ^{26}Al and ^{60}Fe). This process is effective, but works on timescales of several Myrs (Henke et al. 2012). However, as we noted earlier, planetesimals might form on timescales much faster than that, and so what happens to the first generation of much weaker dusty planetesimals still remains to be explored.

The second effect of gravity is the increase of the collisional cross section beyond the geometrical. The gravitational focusing leads to an augmented cross-section which for two equal-sized bodies can be given by

$$\sigma_{\text{gf}} = \pi a^2 \left(1 + \frac{v_{\text{esc}}^2}{v_{\infty}^2} \right) \sim m^{4/3} \quad \text{for } v_{\text{esc}}^2 > v_{\infty}^2 \quad (1.7)$$

where $v_{\text{esc}}^2 = 4Gm/a$ is the escape velocity and v_{∞} is the relative velocity between the bodies at infinite distance to each other. This means that for a massive body in a quiescent disk, the enhanced cross-section can lead to a many-fold increase in accretion rate. The gravitational focusing gives rise to an interesting effect known as runaway growth, which occurs because the augmented cross-section starts to scale with the mass to a power of 4/3 compared to 2/3 for the geometrical cross section. We showed in Eq. 1.4 that assuming a constant ρ_{d} and Δv , the mass growth rate is proportional to σ . The result is that the most massive body in a group will grow to double its mass at a faster rate than the second most massive body in the group. This runaway growth process proceeds for as long as $v_{\text{esc}}^2 > v_{\infty}^2$.

When the body has reached a certain mass, called the isolation mass, typically $0.01\text{-}1 M_{\oplus}$, it will assert its gravitational forces on the remaining population which is stirred up enough for the gravitational focusing to lose in efficiency. The smaller bodies then have time to catch up, and an oligarchic growth regime proceeds where a number of large oligarchs grow in tandem in separate feeding zones (Ida & Makino 1993; Kokubo & Ida 2000). Oligarchic growth ends when the oligarch mass is comparable to the total mass of the small bodies, in which mutual resonances between the oligarchs excite the motions of the smaller bodies. This leads to a brief period of chaos, where the oligarchic feeding zones are emptied of the last material. The result is planetary cores with masses of $\sim 1 M_{\oplus}$ in the inner disk, and $\sim 10 M_{\oplus}$ in the outer, with little possibility of growing further.

The existence of gas giants in the outer disk means that we have a constraint on the timescale on which these planets must form. Because the majority of the mass of these giants is made up of their gaseous envelopes, it means that the cores must form on timescales shorter than the disk dissipation timescale. The timescales on which core accretion (Mizuno 1980; Pollack et al. 1996) occurs is relatively fast in the inner part of the disk, but at larger stellar distances, growth by planetesimal accretion alone becomes problematic. A way around this might be by pebble accretion, where the gas flow around a growing core enhances the accretion rate of cm-sized dust grains (Lambrechts & Johansen 2012; Ormel 2013).

This core accretion phase is simultaneously affected by the gravitational interaction between the core and the surrounding disk, which is the cause for rapid radial migration. If the planet has a mass of $\sim 1 M_{\oplus}$, the interaction drives spiral density waves, exerting so-called Lindblad torques which generally results in inward migration. At the same time, however, the interaction between the planet and the gas on the same orbit gives rise to a co-orbital torque which can result in migration in either direction. These processes combine into Type I migration, with a final effect that is still largely unknown (Kley & Nelson 2012). As the planets grow to $\sim 10 M_{\oplus}$, they become massive enough to open a gap, and the planet starts to migrate inward by Type II migration, which occurs on the disk accretion timescale.

From this brief summary of planetary formation and migration, we can conclude that there are a number of effects that are very strong, but still poorly understood. Although tempting, it is therefore very challenging to infer anything about the primordial disk conditions based upon the present-day locations of planets.

1.2 OBSERVATIONS OF PLANETARY SYSTEMS

We will now discuss some of the constraints on the planet formation process that can be obtained from the observations of planetary systems. We divide this into three parts; what can be learned from the planets and asteroids in our Solar System, from the meteorites impacting on Earth and from the exoplanetary systems.

1.2.1 *The Solar System*

In the Solar System, we distinguish between two distinct populations of planets: the four inner rocky terrestrial planets, and the four outer gas giants. This points towards a significant change in the primordial disk environment somewhere between the orbits of Mars and Jupiter. One such important change is called the snow-line, which describes the critical point where H_2O transitions from only being able to exist in the form of gas, to outside, where it can freeze out into solids. The existence of ices in the outer regions is interesting for planet formation for several reasons: it leads to an increase in the total solid mass by a factor of about four, and ices are believed to have widely different collisional properties from silicates.

It is also possible to use the mass distribution of the Solar System bodies to derive a minimum primordial disk mass that is required for the planets to have formed. The concept is called the minimum mass Solar Nebula (MMSN), and was introduced and developed by Weidenschilling (1977b) and Hayashi (1981). The initial dust and gas mass of the protoplanetary disk is a vital property that remains difficult to measure by direct means in other systems, and the MMSN is therefore an important first step towards understanding the initial conditions. To obtain the MMSN, we 1) take the masses of the metals of each body (including the asteroid belt)

and enhance it with a combination of hydrogen and helium to obtain Solar composition, 2) divide the Solar System into annuli centered on each body, and 3) spread the enhanced mass of each body over its annulus. The result is a radial gas surface density profile that can be described by

$$\Sigma_{g,\text{MMSN}}(r) = 1700 \cdot \left(\frac{r}{1 \text{ AU}}\right)^{-3/2} \text{ g cm}^{-2}. \quad (1.8)$$

It is important to note that the MMSN only describes the distribution of the current-day Solar System. Because both the gas and the disk evolves with time, and migration and scattering is believed to strongly influence the dust, planetesimals, cores and planets, the MMSN marks only the absolute minimum of mass that the Solar nebula must have contained. The derived present-day distribution might therefore be very different from the initial conditions of planet formation. To date, however, it remains a commonly used benchmark for comparison between different dust evolution models. [Desch \(2007\)](#) took the later evolutionary stages into account by considering the migration and redistribution from the core formation stage and found

$$\Sigma_{g,\text{Desch}}(r) = 51000 \cdot \left(\frac{r}{1 \text{ AU}}\right)^{-2.2} \text{ g cm}^{-2}. \quad (1.9)$$

The result is an enhancement by more than order of magnitude in the inner disk compared to the MMSN, but with a steeper profile, and this model does still not take the mass loss from the planetesimal formation stage into account. The conclusion we can draw from this is that the initial disk conditions remain highly uncertain, and a disk parameter study is vital to fully gauge the capability of any planetesimal formation scenario.

The asteroid belt located between Mars and Jupiter is generally considered a region of failed planet formation, and the present day asteroid belt is thought to be a steady-state population of fragments produced by collisional and dynamical evolution, mostly kept safe from the gravitational perturbations of the planets. The smaller bodies are produced by either collisions or fragmentation from spin-up by solar radiation via the Yarkovsky-O'Keefe-Radzievskii-Paddack (YORP) effect, and bodies are lost through collisions and drift due to interaction with the solar radiation via the Yarkovsky effect (as summarized by [Bottke et al. 2006](#)).

Under the assumption that the planetesimal formation proceeded in the same way in the asteroid belt as for the planets, it is an ideal population to study for constraining the size distribution of the initial planetesimals in the Solar System. By considering the collisional evolution from its initial formation to the present day asteroid belt, [Morbidelli et al. \(2009\)](#) claimed that the planetesimals were born big, but [Weidenschilling \(2011\)](#) found that the same result could be obtained with initially small planetesimals. The focus of both of these studies was to reproduce the bump in asteroid size distribution at ~ 100 km, as shown in Fig. 1.4. Recently, the analytical study of [Lithwick \(2013\)](#) found that the 100 km bump could be reproduced using small planetesimals by considering the transition from runaway growth to so-called trans-hill growth.

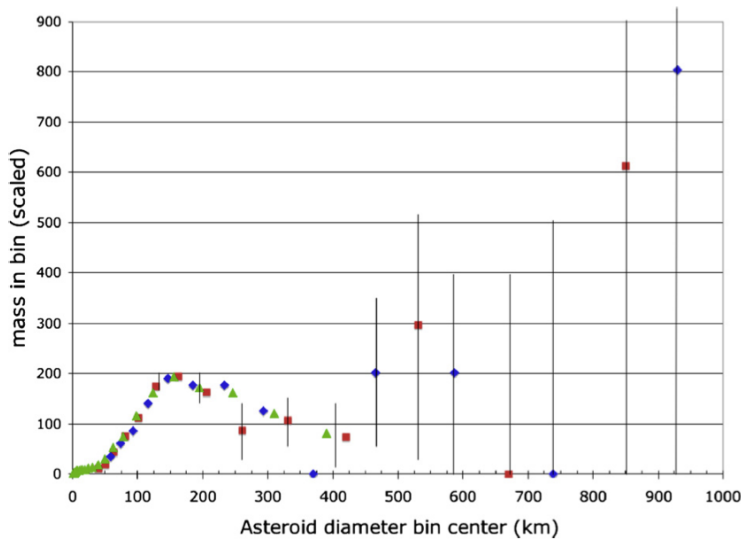


Figure 1.4: The observed size distribution of the present-day asteroid belt. Figure from [Cuzzi et al. \(2010\)](#).

Some asteroids, like Vesta, also show some properties that makes it possible to character the size-distribution of the smallest bodies in the asteroid belt. Although Vesta is believed to belong to the first generation of planetesimals, as inferred from its widespread differentiation, parts of its surface are still unsaturated. This means that close to all impact craters can be distinguished, and because Vesta is also massive enough to not experience global seismic shaking due to large impacts, it is possible to constrain the sizes of the impactor population that formed the craters ([Marchi et al. 2013](#)). This is however challenging, as it relies on assumptions of impact probabilities and the physics behind the actual crater formation to connect a given impact to a certain impactor size.

1.2.2 Meteorites

Another great source of information comes from the structure and composition of meteorites, which are fragments from asteroid disruptions that have been ejected or drifted from the asteroid belt into the Earth's orbit. The low level of detail that dust coagulation and planetesimal formation studies are limited to has however prevented any direct comparisons to the wealth of information that the meteorites can provide. In this section, we aim to discuss some of the meteoritic constraints that are starting to become relevant for further constraining the dust coagulation studies.

Most of the meteorites fall into one of the two major classes; chondrites and achondrites. The chondrites are primitive meteorites that were never differentiated, and as such appear relatively unaltered since their formation. The chondrites are the most common class of meteorites by far, and they are classified as such because they contain chondrules, which are mm-sized molten or partially molten droplets that in some cases make up as

much as 80% of the volume. They are surrounded by a matrix of fine dust, and mm-cm-sized calcium-aluminium-rich inclusions (CAIs) are also common. The achondrites, on the other hand, have been differentiated and do not contain any chondrules. They likely originated from the either first generation of planetesimals that formed simultaneously with the CAIs, or from the surfaces of the planets or largest asteroids (Markowski et al. 2007).

The main application for meteorites is arguably the ability to perform radioactive dating to determine their time of formation. Any method to determine the ages of observed stars or exoplanetary systems remains highly uncertain, but radioactive dating is capable of putting extremely accurate time constraints on the formation of our Solar System. The dating is performed by considering the abundance ratio of a radioactive element and its decay product. By accurately knowing the decay channels and the decay half-times, and by making assumptions regarding the abundance of the initial decay product, it is possible to determine the time at which the initial radioactive material was first solidified from gaseous or liquid form. The most accurate substances can be found in the CAIs (primarily Pb-Pb and Al-Mg). This dating puts the CAIs as the first known solids to have formed in the Solar System, and their time of formation is put to 4567.30 ± 0.16 Myrs ago, roughly 1 – 3 Myrs before the formation of chondrules found in the same meteorites (Russell et al. 2006). There are also indications that chondrules within the same body formed ~ 0.5 Myrs apart (Kita et al. 2000, 2005; Villeneuve et al. 2009).

Chondrules also have many interesting properties themselves, and the question of how they were formed has spawned an entire field by itself. They show evidence of being molten once or multiple times before they were included in their parent body, and they contain volatile elements like S and Na that would have rapidly disappeared if the melting and resolidification had taken place over an extended period of time. This means that the chondrule formation must occur from a process capable of heating the material to its melting temperatures at 1900 K (from an ambient temperature of ~ 200 K), and then rapidly cool it down again to temperatures below 650 K (above which S volatilizes) on timescales of hours. Exactly how this occurs is still a topic of discussion, but there are formation scenarios with heating near the Sun followed by outwards transpiration, in shock waves, or by impact melting, disk lightning or magnetic flares (Connolly et al. 2006). All of these scenarios have their own problems in either producing the required rapid cooling, occurring in the first place, or being able to reproduce the vast amount of chondrules that are observed.

All these things can tell us a lot about the initial stages of dust coagulation. The presence of CAIs from the very first stages of star formation means that coagulation must at some point have been able to reach cm-sizes. The extended chondrule formation time also puts an interesting constraint on their formation, as some chondrules must have formed together with the CAIs, yet some others several Myrs later. This means that the coagulation phase must have been fast, but also inefficient. The growth

timescales that we calculated with Eq. 1.5 speaks for much faster growth than 1 Myr, which means that there must have been a mechanism that kept most or all of the dust grains small. It is also interesting to note that there exists no structure in the chondrites larger than 1 cm, but they rather seem to be mostly composed of building blocks of 1 mm and smaller. This might be due to aerodynamic or thermodynamic effects related to their formation, but it can also mean that coagulation was unable to proceed to larger sizes.

A major caveat is that the exact significance of chondrites and chondrules for the planet formation is still unclear. Because the meteorites that reach the Earth are produced by fragmentation from asteroid collisions, it is possible that the meteorites only originate from the asteroid surfaces, and thus say little about the asteroid cores or their global densities in the Solar nebula. This makes it possible that meteorites are only a small population of bodies that had little to do with the actual planetesimal formation, and were accreted by them only afterwards with little real impact on the global evolution. However, in order for this to be cleared up, deep samples would need to be obtained in-situ from the asteroids, which has so far not been possible.

1.2.3 *Exoplanets*

We now leave the Solar System, and look for constraints in other planetary systems. This has been possible only for the last two decades, and was initiated by the first definite exoplanet discovery, 51 Peg b, by [Mayor & Queloz \(1995\)](#). This discovery was however merely the end of a long hunt for the exoplanets that had started with the construction of a new generation of accurate radial velocity spectrographs in the 1970's. The radial velocity technique was the first successful, and until recently the by far most productive method for discovering exoplanets. It relies on the fact that a planetary companion causes a small but non-negligible shift in the center-of-mass of its host system, which creates a periodic variation in the stellar radial velocity on the order of $1\text{-}30\text{ m s}^{-1}$ depending on the planetary mass and distance to the host star.

With a mass of half of Jupiter's but with a semi-major axis of only a few percent of Mercury's orbit, 51 Peg b turned out to be a very odd type of planet, and in the following years, many more like it has been observed. This was a highly surprising discovery, as the consensus before their time of discovery was that all planetary systems were formed and ordered in the same way as the Solar System. These Hot Jupiters are also much too massive to have been formed in situ, simply because the inner disk cannot contain so much mass. This put the spotlight on a previously ignored effect, namely the migration of planets, caused by gravitational torques being exerted by the gaseous disk on the planet (as summarized by [Kley & Nelson 2012](#)).

Thanks to recent years large-scale surveys like the Kepler mission ([Borucki et al. 2010](#)), we today know of over 900 exoplanets, and over 3 000

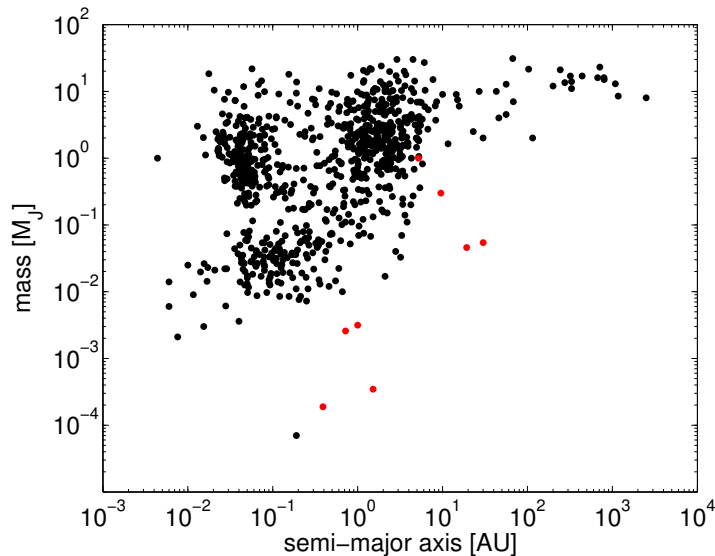


Figure 1.5: Distribution of exoplanet masses and stellar distances (black) and the Solar System planets (red). Data taken from exoplanet.eu.

candidates. Besides the radial velocity method, there are today a number of successful methods for exoplanet observations. The transit method uses the change in the stellar light curve as the planets eclipses their host star; direct imaging requires the light from the star to be filtered away; astrometry uses the change in center-of-mass in the apparent position on the sky; and microlensing, which uses the brief gravitational lensing effect by a star and planetary system passing the line of sight.

If the Solar System predicts ordered planetary growth, the wealth of exoplanetary systems indicates the opposite. In Fig. 1.5, we show the distribution of planetary masses versus semi-major axes, which shows the substantial fraction of Hot Jupiters, and also another class of Hot Neptunes, but a significant (and real) lack of intermediate-sized planets. We also note massive planets at extremely large stellar distances, at which the growth timescale through coagulation would well exceed the disk lifetime. These planets indicate either another type of formation by gravitational instabilities, or significant planet-planet scattering events in the inner disk. Exoplanetary systems also tend to be rather eccentric compared to the almost circular orbits of the Solar System. As any orbits would be rapidly circularized inside a gaseous disk, this indicates the importance of late time planetary dynamics. The cause for the lack of Solar System-like bodies is likely due to observational bias, as all the counted methods most sensitive to massive planets at either small or large distances from their host stars. Given time and increased sensitivity, it will be possible to determine how common our own Solar System is.

An important connection between the planet formation processes and the observed exoplanets can be made by the use of planet population synthesis models (Ida & Lin 2004; Mordasini et al. 2009). These models rely on simplified prescriptions for all the growth processes from plan-

planetesimals to the finished terrestrial and giant planets, and can be used to compare the current theoretical understanding of the planet formation process to the observed properties of the currently known exoplanetary systems. Because so many uncertainties remain in the planet formation process, and they by design sacrifice accuracy for computational speed, their results remain highly speculative but still very interesting. A strong limitation to the current generation of synthesis models lies in the huge uncertainties involved in the planetesimal formation processes. Currently, the initial size and spatial distribution of planetesimals remain largely unconstrained, which makes the initial conditions for the synthesis models more or less a free parameter. If we could better understand the planetesimal formation process, these models could then make direct predictions for the rest of the planet formation process.

1.3 THE PROTOPLANETARY DISK

We finally focus on the protoplanetary disk, and consider the structure and evolution of the gas and the dust components. First, we discuss the observational constraints, and then continue with an overview of the theoretical understanding.

1.3.1 *Observational constraints*

We have previously discussed the major properties of the YSOs and how the IR-excess behaves as they evolve, but observations can tell us a lot more about the disk structure, temperature and composition. Although the gas completely dominates the total disk mass, this component is the one that is most difficult to observe, as the gas is highly transparent to the stellar radiation. The most important gas feature is the $H\alpha$ excess, caused by the accretion flow onto the star. During the gravitational collapse, the accretion rate in the disk is on the order of $10^{-7} - 10^{-8} M_{\odot} \text{ yr}^{-1}$, but it drops rapidly to $10^{-7} - 10^{-9} M_{\odot} \text{ yr}^{-1}$ during the T Tauri phase (Nakamoto & Nakagawa 1994). In the later stages, the accretion rate stops completely. This transition from accreting to non-accreting appears to be very abrupt, in contradiction to what would happen for a purely viscously accreting disk, where the rate would instead decrease slowly when more mass is gradually accreted.

The dust is easier to detect than the gas, as it is highly opaque in the IR, and its re-radiation of the stellar radiation results in an IR excess compared to the blackbody emission of the star alone, with the majority of the energy re-emitted at wavelengths between 1-100 μm . As excess in different wavelengths corresponds to different emission temperatures, it is possible to use the SED to map the structure of the protoplanetary disk, as shown in Fig. 1.6. The most energetic disk emission comes from the inner rim, with emission temperatures of ~ 1500 K, and its significant contribution of up to half the total IR flux means that it is likely that this region is puffed up to a larger surface (Dullemond et al. 2001). Because the near-IR bump always

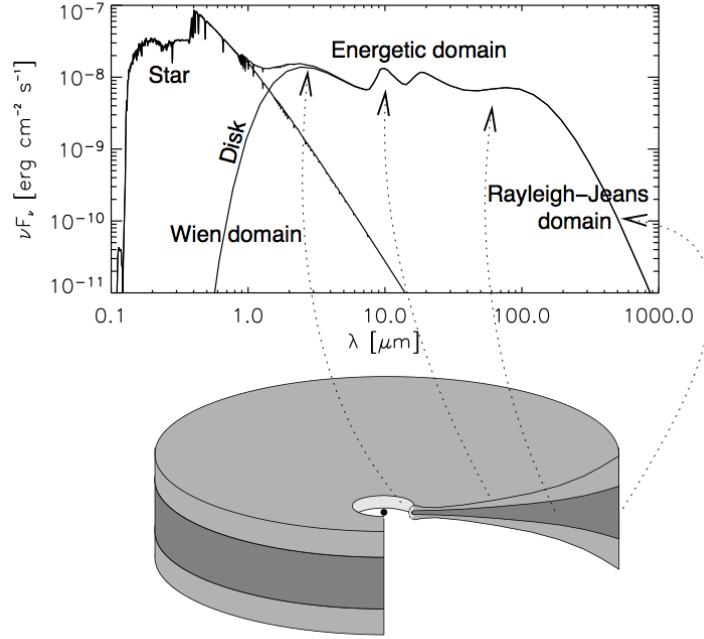


Figure 1.6: A schematic view of the SED, showing the blackbody of the star and the infrared excess from the circumstellar disk. Because the emission strength depends on the temperature, it is possible to use the SED to map the different component of the disk. Figure from [Dullemond et al. \(2007\)](#).

occurs at these temperatures, it is believed that the inner rim is formed due to an evaporation front of the silicate grains. The mid-IR excess likely originates from the disk surface, which would need to exhibit some flaring (i.e. the ratio of the disk height to stellar distance increases with the stellar distance) to be heated enough by the star. Finally, the far-IR likely corresponds to the cooler disk midplane, which is shielded from the direct stellar radiation by the surface layers, and is instead heated indirectly by the re-emission from dust grains in the upper layers.

The observations at millimeter wavelengths probe the cold outer regions. In this region, assuming an optically thin disk and that the emission comes from an isothermal region, the flux can be described by the Rayleigh-Jeans law

$$\nu F_\nu \approx \nu \kappa_\nu B_\nu(T) M_d / d^2, \quad (1.10)$$

where ν denotes the frequency, κ_ν is the opacity per dust mass, $B_\nu(T)$ is the Planck function at a temperature T , M_d is the total dust mass and d is the source distance. This is useful, because it gives a relation between the millimeter-observations and the total dust mass, assuming that the dust opacity can be approximated. Using this technique, [Andrews et al. \(2009\)](#) estimated the disk masses to lie in the range of $0.005 - 0.14 M_\odot$.

Another important emission feature occurs at $10 \mu\text{m}$, which is also visible in Fig. 1.6, arises from resonance features of the crystalline structure,

and specifically by the stretching of the Si-O bonds. There is also a similar, slightly less strong 18 μm feature due to the bending of the O-Si-O bonds. These features disappear with grain growth, and are therefore excellent tools for mapping the presence of small dust in the upper layers of the disks (van Boekel et al. 2003).

By understanding the dust absorption properties from the laboratory, it is also possible to construct models for comparison to the dust size distribution. If we take an opacity law like

$$\kappa_\nu \propto \nu^\beta, \quad (1.11)$$

where β depends on the dust size distribution, the dust flux becomes $F_\nu \propto \nu^{\beta+2}$. This means that Eq. 1.10 can be used at mm-wavelengths to calculate the spectral index of the opacity law, which makes it possible to do direct predictions of the dust size distribution. This type of modeling has been performed by e.g. Testi et al. (2003) and Ricci et al. (2010b), and indicate the presence of mm- to cm-sized grains in the observed disks.

Because of their low opacities, it is however difficult to detect grains that are larger than this, which means that a potentially significant dust mass fraction are invisible to the observations. In debris disks, it is however possible to infer the presence of large bodies by the detection of warm dust. If warm dust is detected, it must be continuously re-supplied by larger bodies, as the small dust undergoes rapid migration due to Poynting-Robertson drag (Martin & Livio 2013).

1.3.2 Theoretical disk structure

To further understand the structure of the protoplanetary disk, we consider an axisymmetric disk in hydrostatic vertical equilibrium. This arises from a balance between the vertical gravitational force component and the gas pressure. A simplification can here be made as the disk mass is only a small fraction of the stellar mass, at $M_d \sim 0.01M_*$, which means that we can disregard the self-gravitational component from the disk. We also assume the disk to be vertically isothermal ($T(z) = \text{const}$) and geometrically thin ($H_g/r \ll 1$). The vertical gravitational acceleration is then given by

$$\frac{\partial\Phi}{\partial z} = \frac{GM_*}{r^2} \frac{z}{r} = \Omega_k^2 z, \quad (1.12)$$

where G is the gravitational constant, r is the stellar distance, z the vertical distance and $\Omega_k = \sqrt{GM_*/r^3}$ is the Keplerian frequency. This is balanced by the vertical pressure gradient

$$\frac{\partial P}{\partial z} \frac{1}{\rho_g} = \frac{\partial \rho}{\partial z} \frac{c_s^2}{\rho_g}, \quad (1.13)$$

where the pressure is given by $P = \rho_g c_s^2$ and where ρ_g is the gas density. The sound speed can be calculated from

$$c_s = \sqrt{\frac{k_B T}{\mu m_p}}, \quad (1.14)$$

where k_B is the Boltzmann constant, T is the temperature, $\mu = 2.34$ is the mean molecular weight (assuming 75% molecular hydrogen and 25% helium) and m_p is the proton mass. Solving for the hydrostatic equilibrium gives

$$\rho_g(r, z) = \rho_{g,0}(r) \exp\left(-\left(\frac{z}{2H_g}\right)^2\right), \quad (1.15)$$

where the midplane density is given by

$$\rho_{g,0}(r) = \frac{\Sigma_g(r)}{\sqrt{2\pi}H_g}, \quad (1.16)$$

and where we have taken $H_g = c_s/\Omega_k$ to be the pressure scale-height and $\Sigma_g(r) = \int_{-\infty}^{\infty} \rho_g(r, z) dz$ to be the gas surface density.

We can now continue to the disk density in the radial direction. Assuming a viscosity ν acting in the disk, the gas will experience a continuous friction due to the differential rotation. If we consider the gas to consist of thin sheets, the interaction between two adjacent sheets will cause the outer to get accelerated and the inner to be decelerated. The result is an outwards angular momentum transport, and an inwards flow of matter. From this, it is possible to calculate the radial velocity of the gas, as first derived by [Lynden-Bell & Pringle \(1974\)](#):

$$v_g(r) = -\frac{3}{\Sigma_g\sqrt{r}} \frac{\partial}{\partial r} (\Sigma_g\nu\sqrt{r}). \quad (1.17)$$

The surface density evolution can then be found from the vertically integrated mass conservation equation:

$$\frac{\partial \Sigma_g}{\partial t} = \frac{3}{r} \frac{\partial}{\partial r} \left(\sqrt{r} \frac{\partial}{\partial r} (\Sigma_g\nu\sqrt{r}) \right). \quad (1.18)$$

It is clear that viscosity is an important parameter for the disk evolution. The molecular viscosity is however much too low to alone drive the observed accretion rates, and a second source is necessary. What that source is is still not certain, but a common solution is to use the parametrized α -viscosity by [Shakura & Sunyaev \(1973\)](#):

$$\nu = \alpha c_s H_g, \quad (1.19)$$

where the dimensionless α -parameter specifies the degree of turbulence, and for protoplanetary disks usually takes values between 10^{-5} to 10^{-2} .

One of the best candidates for the source of turbulence is the magneto-rotational instability (MRI; [Balbus & Hawley 1998](#)). This is caused by the coupling between the gas and the magnetic field, where the differential rotation between the dust layers in the radial direction causes a shear which induces turbulence. In the Kolmogorov turbulence model, the energy is then assumed to be put into unstable large-scale eddies (with lifetimes $\tau_L \sim \Omega_k^{-1}$), that quickly decay into smaller eddies in a cascade that proceeds down to the dissipation scale, where the remaining kinetic energy

is converted into heat. Recent work by e. g. [Okuzumi & Hirose \(2011\)](#) and [Dzyurkevich et al. \(2013\)](#) have also begun to explore the vertical structure of the MRI, and the concept of dead zones, where the gas ionization is low enough for the MRI to get attenuated. This, along with non-ideal effects like ohmic dissipation and ambipolar diffusion will be critical to understand the extent and transport efficiency of the MRI active regions.

1.4 DUST EVOLUTION

As we have discussed before, the dust evolution is highly important factor for planet formation, and it also affects the disk structure through its opacity to the stellar radiation. As we briefly showed in Eq. 1.5, the dust growth naturally depends on the density of the dust grains along with their relative velocity, and also what happens when two dust grains collide. To model the evolution of the dust, it is therefore important to determine the spatial distribution of the dust and how it reacts to the gas around it.

1.4.1 *The dust spatial distribution*

Dust particles in protoplanetary disks are subject to gravity and centrifugal forces, but they are also affected by the aerodynamic drag from the disk gas. A fundamental concept for the aerodynamics is the concept of stopping time, which describes on what timescale a change in the gas flow is reflected on the inertial particles suspended in the flow ([Whipple 1972b](#)). More precisely, it can be defined as the time it takes for the gas drag to cause an order of unity change in the particle momentum

$$t_s = \frac{mv}{|F_D|}. \quad (1.20)$$

m is here the particle mass and v its velocity and F_D is the drag force. The drag force for a spherical particle of radius a moving in a gas of density ρ_g is

$$F_D = \frac{1}{2} C_D \pi a^2 \rho_g v^2, \quad (1.21)$$

where C_D is the drag coefficient, which depends on the interaction between the gas and the particle. If the particle size is smaller than the mean free path of the gas λ (or exactly $9/4 \cdot \lambda$), the drag can be considered as the collective result of individual collisions with gas molecules. This is called Epstein drag, and has a drag coefficient

$$C_D = \frac{8}{3} \frac{v_{\text{th}}}{v}. \quad (1.22)$$

$v_{\text{th}} = (8/\pi)^{1/2} c_s$ is the mean thermal velocity of the gas molecules. If the particles are larger, the particle is in the Stokes regime, and the gas instead needs to be treated as a fluid. The strength of the drag force in this regime

depends on the particle Reynolds number, which is defined as the ratio between the inertial force and the viscous force

$$\text{Re} = \frac{2av}{\nu_{\text{mol}}} . \quad (1.23)$$

Where $\nu_{\text{mol}} = 1/2 \cdot v_{\text{th}} \lambda_{\text{mfp}}$ is the gas molecular viscosity. The drag force in the Stokes regime behaves in a non-linear fashion and can only be analytically calculated in the limit of small and large Re, and have to be empirically determined in the intermediate case. The drag coefficients introduced by Whipple (1972a) are still most commonly used, and are given by

$$C_D = \begin{cases} 24 \text{Re}^{-1}, & \text{Re} > 1 \\ 24 \text{Re}^{-0.6}, & 1 < \text{Re} < 800 \\ 0.44, & \text{Re} > 800 . \end{cases} \quad (1.24)$$

The stopping times then become

$$t_s = \begin{cases} t_s^{(\text{Ep})} = \frac{a\zeta}{\rho_g v_{\text{th}}}, & a < \frac{9}{4} \lambda_{\text{mfp}} \\ t_s^{(\text{St}_1)} = \frac{4a}{9\lambda_{\text{mfp}}} \cdot t_s^{(\text{Ep})} = \frac{2}{9} \frac{\zeta a^2}{\nu_{\text{mol}}}, & \text{Re} < 1 \\ t_s^{(\text{St}_2)} = \frac{2^{0.6}}{9} \frac{\zeta}{\rho_g^{1.4}} \frac{a^{1.6}}{\nu_{\text{mol}}^{0.6} v_{\text{th}}^{0.4}}, & 1 < \text{Re} < 800 \\ t_s^{(\text{St}_3)} = \frac{6\zeta a}{\zeta v_{\text{th}}}, & \text{Re} > 800 . \end{cases} \quad (1.25)$$

In protoplanetary disks, most of the dust grains are sufficiently small to always have $\text{Re} < 1$, so that they only experience the first Stokes regimes. Because of the uncertainty in the larger Stokes regime, for the rest of this work, we will ignore the latter regimes, and approximate even the largest dust grains to be in Stokes regime 1. At these sizes, because the particles are anyway so decoupled from the gas, the exact drag regime is much less important than in the case of small particles that are strongly affected by the turbulence and drift.

The gas mean free path can be calculated from

$$\lambda_{\text{mfp}} = \frac{1}{n\sigma_{\text{H}_2}} , \quad (1.26)$$

where $n = \rho_g / \mu m_p$ is the gas midplane number density and $\sigma_{\text{H}_2} = 2 \cdot 10^{-15} \text{cm}^2$ is the molecular cross section.

As we shall see later, when calculating the dust aerodynamics, it is often instructive to use the dimensionless Stokes number (unrelated to the drag regimes discussed above), which we define as the ratio of the stopping time and the turnover time of the largest eddies. This gives

$$\text{St} = \frac{t_s}{\tau_L} = t_s \Omega_k . \quad (1.27)$$

For the Epstein and Stokes 1 drag regimes, we then get

$$\text{St} = \begin{cases} \text{St}^{(\text{Ep})} = \frac{\pi}{2} \cdot \frac{a\zeta}{\Sigma_g}, & a < \frac{9}{4} \lambda_{\text{mfp}} \\ \text{St}^{(\text{St}_1)} = \frac{2\pi}{9} \cdot \frac{a^2 \zeta}{\lambda_{\text{mfp}} \Sigma_g}, & a > \frac{9}{4} \lambda_{\text{mfp}} . \end{cases} \quad (1.28)$$

We now have sufficient understanding of how the dust couples to the gas to turn to its spatial distribution, and first focus on the vertical structure. A particle suspended in gas at a height z above the midplane is going to feel the vertical component of the stellar gravity, $F_{\text{grav}} = -mz\Omega_{\text{k}}^2$. As it starts to fall towards the midplane, it feels the frictional force described in Eq. 1.21, and the equilibrium settling velocity can thus be obtained by equating the two forces (Dullemond & Dominik 2005). Following Birnstiel et al. (2010a), we solve for z and limit the settling speed to velocities lower than half the vertically projected Kepler velocity, which yields

$$v_{\text{d}}^z = -z\Omega_{\text{k}} \min(0.5, \text{St}) , \quad (1.29)$$

with the settling timescale

$$\tau_{\text{sett}} = \frac{z}{v_{\text{d}}^z} = \frac{1}{\Omega_{\text{k}} \min(0.5, \text{St})} . \quad (1.30)$$

Combined with coagulation but in the absence of any other physics, all dust grains would grow and settle towards the disk midplane to form a razor thin disk on a timescale of a few hundred years. As observations can detect dust grains also suspended at high altitudes above the midplane, it is clear that there must be some other effect in action. It turns out that this effect is turbulence. One of the effects of turbulence besides adding viscosity is to smear out any density distribution, as particles are being thrown around by the transient turbulent eddies. This leads to turbulent diffusion, and if we consider a point distribution in 1D, it would after a time t be smeared out and assume a Gaussian distribution of half-width

$$L(t) = \sqrt{2D_{\text{d}}t} , \quad (1.31)$$

where D_{d} is the dust turbulent diffusion coefficient

$$D_{\text{d}} = \frac{D_{\text{g}}}{\text{Sc}} = \frac{D_{\text{g}}}{1 + \text{St}^2} . \quad (1.32)$$

Sc is here the Schmidt number, defined as the ratio between the gas and particle diffusivity, as estimated by Youdin & Johansen (2007). The gas diffusion coefficient due to turbulent viscosity can be obtained from the α -parametrization as

$$D_{\text{g}} = \alpha c_{\text{s}} H_{\text{g}} , \quad (1.33)$$

and the turbulent diffusion timescale can then be given by

$$\tau_{\text{diff}} = \frac{L^2}{D_{\text{d}}} . \quad (1.34)$$

We can now calculate the dust scale-height by equating Eqs. 1.30 and 1.34 and taking $L = h_{\text{d}}$. Limiting the dust scale-height to never be larger than the gas scale-height, we get

$$h_{\text{d}} = H_{\text{g}} \min \left(1, \sqrt{\frac{\alpha}{\min(0.5, \text{St})(1 + \text{St}^2)}} \right) . \quad (1.35)$$

This means that small particles that are well coupled to the gas will take the same scale-height as the gas, but the more decoupled they get, or the weaker the turbulence, the more they settle towards the midplane.

When we now have a feeling for how particles move and behave in the vertical direction, we can turn to their radial velocities. The important thing to note is that although the gaseous disk is pressure supported in the radial direction, the solid particles do not feel this pressure. This causes a differential motion between the dust and the gas, causing a gas drag even on relatively small bodies. The equation of motion for the gas in a thin disk is

$$\frac{v_{\phi,g}}{r} = \frac{GM_*}{r^2} + \frac{1}{\rho_g} \frac{dP}{dr}, \quad (1.36)$$

where $v_{\phi,g}$ is the azimuthal gas velocity and P is the gas pressure. If we disregard the pressure, the gas would orbit at the Keplerian speed $v_k = (GM_*/r)^{1/2}$. However, as both the gas density and sound speed tend to increase with decreasing R , this gives rise to a non-negligible outward pressure force that causes the gas to move at slightly sub-Keplerian velocities. If we assume the gas density and temperature profiles to be given by $\Sigma_g \sim r^{-p}$ and $T \sim r^{-q}$, the gas pressure would become

$$P = \rho_g c_s^2 \sim r^{-k}, \quad (1.37)$$

where $k = -3/2 - p - q/2$. The pressure gradient can then be written

$$\frac{1}{\rho_g} \frac{dP}{dr} = -k \frac{c_s^2}{r}, \quad (1.38)$$

and Eq. 1.36 then becomes

$$v_{\phi,g}^2 = v_k^2 (1 - 2\eta), \quad (1.39)$$

where

$$2\eta = -\frac{r}{v_k^2} \frac{1}{\rho_g} \frac{dP}{dr} = k \frac{c_s^2}{v_k^2} \quad (1.40)$$

describes the degree of sub-Keplerianity. If we assume an MMSN disk with $p = 3/2$ and $q = 1/2$, we get $k = 13/4$. Assuming a typical $c_s/v_k = H_g/r = 0.03$, we get $v_{\phi}/v_k = (1 - 2\eta)^{1/2} = 0.9985$, a deviation from the Keplerian velocity by only a fraction of a percent. Although a small number, with a Keplerian velocity of 30 km s^{-1} at 1 AU, the gas would still be sub-Keplerian by 40 m s^{-1} . Because a solid particle does not feel the pressure, this is the kind of headwind velocity that it faces if it is sufficiently decoupled from the gas.

We will skip ahead a couple of steps, but the radial velocity of a particle in the end depends on two terms (see [Adachi et al. 1976](#) and [Weidenschilling 1977a](#) for a detailed description):

$$v_r = \frac{v_g}{1 + \text{St}^2} - \frac{2\eta v_k}{\text{St} + \text{St}^{-1}}. \quad (1.41)$$

The first term comes from the fact that the gas is being slowly accreted, and drags the particle along with it, with $v_g \sim 1 \text{ cm s}^{-1}$ calculated in Eq. 1.17. This effect is strongest for the very smallest particles, but decreases rapidly as the particles start to decouple from the gas flow. The second term comes from the differential motion between the particle and the gas described above. For small particles in the limiting case of $St \ll 1$, the differential rotation gives rise to a continuous drag force that decelerates the particle, and for large particles with $St \gg 1$, the particle is sufficiently decoupled to never adjust itself to the gas velocity, but instead experiences a headwind that continuously removes angular momentum from the particle. The intermediate case, where $St = 1$ experiences the combination of these two effects, gives rise to the maximum drift velocity.

By calculating the drift timescale $v_{\text{drift}} = r/v_r$, it is easy to realize that particle drift is problematic. Continuing with the example above, a maximum drift velocity of $v_r = 2\eta v_k \sim 40 \text{ m s}^{-1}$ would at 1 AU mean that a particle would drift inwards and get lost in the star in $t_{\text{drift}} = r(dr/dt)^{-1} \sim 100 \text{ yrs}$. This is highly problematic, and even if the particles are small enough to only experience a fraction of the maximum drift velocity, t_{drift} is still $\ll t_{\text{disk}}$, which means that the disk should get emptied of most of its dust on timescales much less than what is observed. The drift barrier and possible solutions to it is discussed in more detail in Sect. 1.4.5.

1.4.2 Relative velocities

To calculate the dust collision rates and collision outcomes, it is vital to know the relative velocities between the particles. Relative velocities can be caused by the drift and settling velocities described above, but the interaction between the dust and the gas also induces other velocity effects, causing the dust to collide at velocities ranging from less than mm s^{-1} and up to 100 m s^{-1} . The velocity sources are described below.

Brownian motion

Brownian motion arises from particle's thermal movement, i. e. the interaction between the particle and individual gas particle. Because this is a basic question of momentum transfer, it is an effect which is strongest for the smallest particles:

$$\Delta v_{\text{bm}} = \sqrt{\frac{8k_b T(m_t + m_p)}{\pi \cdot m_t m_p}}, \quad (1.42)$$

where k_b is Boltzmann's constant, and T is the temperature. Between two μm -particles, this yields relative velocities of $\sim 1 \text{ mm s}^{-1}$, but already for 10 μm -particles, the relative velocities has dropped by an order of magnitude. Even so, because of the strong gas coupling for the smallest particles efficiently attenuates the other velocity sources, Brownian motion is the dominating source in the very first coagulation regime.

Turbulence

Turbulent motion arises from the MRI described earlier, and its effect on the dust motion can roughly be divided into three different regimes, depending on how well coupled the particle is to the gas compared to the eddy lifetime. The smallest particles are so well coupled to the gas that they will stay in the same eddy throughout its lifetime. This means that their relative velocities are small, as they very quickly adjust to the same local gas flow. For intermediate-sized particles, the stopping times start to become so long that they can be ejected from the smallest, Kolmogorov-scale eddies. At this point, they become ballistically flung between eddies, which causes a rapid boost in relative velocities. As the particles grow, they start to couple to larger and more energetic eddies, and therefore receive larger kicks and higher relative velocities. When the particles have grown too large, however, their stopping times become larger than the lifetime of the largest eddies, and their coupling to the turbulence start to weaken, lowering the relative velocities.

Because the sizes between the largest and the smallest eddies in a protoplanetary disk is very large, from ~ 0.1 AU to ~ 1 km at a 1 AU distance to the star, numerically simulating the exact effect of turbulence on the dust motion is very challenging. One parametrization of the effect of turbulence was derived analytically by [Ormel & Cuzzi \(2007\)](#), drawing upon the work by [Voelk et al. \(1980\)](#) by using a set of limiting cases for particles of different stopping times compared to the eddy lifetimes. For equal-sized particles, this yields

$$\Delta v_t = \begin{cases} c_s \sqrt{2\alpha \cdot St}, & St \ll 1 \\ c_s \sqrt{2\alpha/St}, & St \gg 1 \end{cases} . \quad (1.43)$$

where the maximum velocity is achieved for $St = 1$, corresponding to when the particle couple of the largest eddies. As we can see, the relative velocity depends strongly on the turbulent strength. For $\alpha = 10^{-2}$, the highest relative velocities can reach almost 100 m s^{-1} at 1 AU, whereas $\alpha = 10^{-4}$ leads to relative velocities of 10 m s^{-1} . Even for low turbulence, these velocities are still likely to be destructive for the dust grains.

Radial drift

The radial drift causes relative velocities between particles if they couple differently to the surrounding gas ([Whipple 1972a](#); [Weidenschilling 1977a](#)). The relative velocity is then simply the difference between the deterministic drift velocities of the two particles:

$$\Delta v_r = |v_{r,1} - v_{r,2}| , \quad (1.44)$$

where v_r is obtained from Eq. 1.41.

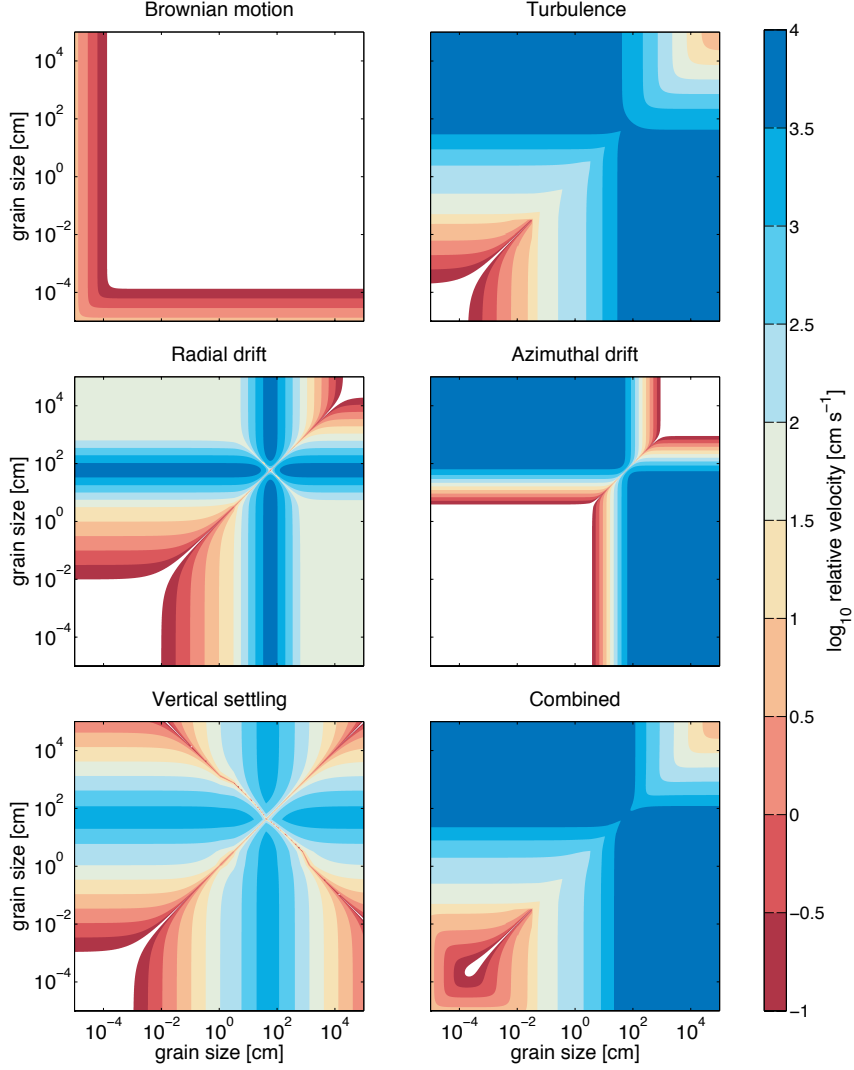


Figure 1.7: The relative velocity for each particle pair calculated separately for the five velocity sources and combined in the last panel. We take an $\alpha = 10^{-3}$ and a distance of 1 AU from the central star. The particle size that corresponds to Stokes number unity is equal to $a = 70$ cm, which is where many of the velocity sources peak.

Azimuthal drift

The azimuthal relative velocities occur for the same reasons as the radial drift, and arise from the azimuthal gas drag. The relative velocity between two particles is determined by the difference in drift velocity:

$$\Delta v_\phi = |v_{\phi,1} - v_{\phi,2}|. \quad (1.45)$$

where the azimuthal drift of a particle is calculated from

$$v_\phi = \frac{\eta v_k}{1 + \text{St}^2} \quad (1.46)$$

Vertical settling

As particles settle towards the midplane at different velocities, this gives rise to relative velocities between different-sized particles. In this thesis, we utilize a dust code which does not resolve the vertical structure, but instead uses a vertically integrated approach to track the dust settling. We therefore calculate the average settling velocity at one scale-height, resulting in

$$\Delta v_{\text{sett}} = \Omega_k \cdot |h_{d,1} \cdot \min(\text{St}_1, 0.5) - h_{d,2} \cdot \min(\text{St}_2, 0.5)| \quad (1.47)$$

where h_d is the dust scale-height as described in Eq. 1.35.

In Fig. 1.7, we finally give the resulting relative velocity field for the five relative velocity sources individually, and also the total relative velocity, calculated from

$$\Delta v = \sqrt{\Delta v_{\text{bm}}^2 + \Delta v_{\text{t}}^2 + \Delta v_{\text{r}}^2 + \Delta v_{\text{p}}^2 + \Delta v_{\text{sett}}^2}. \quad (1.48)$$

From the figure, we note the importance of Brownian motion for the smallest of the particles, and it is also clear that all particles below $\text{St} < 1$, even moderate turbulence dominates over the drift sources. This is particularly true for particles of similar sizes. It is also interesting to note that as the particles grow to $\text{St} \gg 1$ but still sub-kilometer sizes, the relative velocities drop below 1 m s^{-1} . Even the turbulent stirring introduced by Nelson (2005) is believed to be low for these particles, so that this region becomes a temporary calm zone for the smaller planetesimals. This is however not true if we consider the relative velocities between a large particle and a smaller, which would lead to an increased importance of the type of sweep-up growth that is the main focus of this thesis.

1.4.3 *Dust collision physics*

Though the collisional outcome may initially seem like a simple problem, it depends on a huge number of parameters, such as the grain size, mass, porosity, structure and composition, and the impact velocity, impact parameter and angle (Blum & Wurm 2008). Only in the problem of planetesimal formation, the grain masses span over 30 orders of magnitude, and the impact velocities over 6 orders of magnitude. Analytically calculating the outcome for anything more than two compact spheres is very difficult, and studying the outcome experimentally or numerically is also extremely challenging.

The first type of collision outcome that the smallest grains will experience is so-called hit-and-stick growth, at which the two dust grains stick together by virtue of the weak van der Waals force for silicates. This is a short-range force between two adjacent surfaces, which arises due to induced electrical dipoles in the adjacent layers of contact. In the case of ices, the particles instead stick due to the stronger dipole force. The definition of hit-and-stick-growth is that there is little restructuring of the body, which

requires the collision energy to be small, less than approximately 5 times the rolling energy (Güttler et al. 2010). This is the energy dissipated when a monomer, the smallest dust building block, rolls over another monomer with an angle of $\pi/2$, and is given by

$$E_{\text{roll}} = \frac{\pi}{2} a_0 F_{\text{roll}} , \quad (1.49)$$

where $a_0 \sim 10^{-4} - 10^{-5}$ cm is the monomer radius and $F_{\text{roll}} \sim 10^{-4}$ dyn is the rolling force for silicates, which can be measured experimentally (Heim et al. 1999). The criterium for a hit-and-stick collision is then:

$$\frac{1}{2} m_{\mu} \Delta v^2 \leq 5 E_{\text{roll}} , \quad (1.50)$$

where m_{μ} is the reduced mass. In terms of velocity, this becomes

$$\Delta v \leq \sqrt{\frac{5\pi a_0 F_{\text{roll}}}{m_{\mu}}} . \quad (1.51)$$

During this type of growth, fractal aggregates form that become successively larger and more porous with each collision. For silicates, this growth can continue to roughly ~ 100 μm sizes before restructuring becomes important.

At higher collision energies, the collision becomes an argument of energy dissipation. During a collision, energy can be dissipated by monomer-monomer rolling, sliding, twisting and breaking (Dominik & Tielens 1997). In order for a sticking event to occur, enough energy has to be dissipated for the weak van der Waals forces to become sufficiently adhesive. If an aggregate is porous, restructuring is easy, and sticking can occur at relatively high velocities. However, with restructuring follows compaction, which limits the capability for restructuring in the following collision (Weidling et al. 2009). If all of the energy can not be dissipated, but is also not strong enough to break (many) monomer bonds, bouncing may occur, where both particles rebound off each other with very little mass gain or mass loss. This is highly dependent on the grain and collision properties, but the transition from sticking to bouncing occurs at velocities in the $\Delta v = 1 - 10$ cm s $^{-1}$ range for silicates Kothe et al. (2013a), though it is uncertain whether it happens at all for ices (Wada et al. 2011).

At yet higher collision energies, monomer bonds start to break. If the mass ratio is large between the two aggregates, the collision energy will only be deposited locally, leading to erosion in the form of cratering around the region of impact. The more similar the aggregates are in size, however, the more globally can the energy be distributed, and the more global the fragmentation becomes as a result. If the fragmentation occurs over the whole aggregates, it is often called catastrophic fragmentation. Benz & Asphaug (1999) showed that for rocky bodies, the critical energy needed to cause fragmentation decreases with size, because the larger a particle is, the higher likelihood it has to suffer from cracks and faults. Similar results have also been found in the laboratory for silicate aggregates, where the

fragmentation threshold velocity has been found to be $v_f = 100 \text{ cm s}^{-1}$ for mm-sized particles (Blum & Münch 1993) and $v_f = 40 \text{ cm s}^{-1}$ for 5 cm-particles Schräpler et al. (2012). No laboratory experiments have so far been possible for ices, but numerical simulations using molecular dynamics (where the interactions between all adjacent monomers are evolved during a collision) find the fragmentation velocity for $\sim 100 \mu\text{m}$ -sized aggregates to be as high as $v_f = 1000 - 5000 \text{ cm s}^{-1}$ (Wada et al. 2009).

Numerical simulations are useful, because they allow for the probing of collision properties for the grain growth from monomer sizes and up to aggregates containing up to $\sim 10^5$ monomers, a region which the laboratory has difficulties investigating. At too large monomer numbers, however, the computational time becomes too long for the simulations to be feasible. The laboratory, on the other hand, is mostly restricted to collisions between $\sim 0.5 \text{ mm}$ and upwards. This is a problem, because there is at the moment a big discrepancy between the numerical and laboratory work with no current possibilities for direct comparison.

The problem is that the molecular dynamics (Wada et al. 2011; Seizinger & Kley 2013a) has issues reproducing the bouncing collisions that are frequently observed in the laboratory Weidling et al. (2012); Kothe et al. (2013a). Cases can be made for both methods. The molecular dynamics simulations are highly reliant on the microphysics of the interactions between monomers, which have to be measured in the laboratory or determined theoretically. This is problematic, because the collisional outcome does not only depend on the absolute values for the interactive forces, but also on the ratios between each other. If sliding would turn out to be incorrect, this will also change the amount of rolling, twisting and breaking in a collision. The laboratory is on the other hand not capable of self-consistently forming their first aggregates, but need to construct them artificially. This means that the initial properties of the dust grains that are being investigated might not coincide with what we would have as a result of the first stages of coagulation.

There is also a second type of numerical simulations using the SPH method, which considers the macroscopic energy dissipation via expressions for the compressive strength and the bulk modulus (Geretshauser et al. 2010, 2011; Meru et al. 2013), where the macroscopic properties are determined from laboratory experiments. This method is in principle very useful for determining the collision properties of dust grains with sizes of dm and above, a region which both molecular dynamics and the laboratory experiments have difficulties exploring. It does however still have some issues with reproducing the outcome from the laboratory experiments, and is going to need further calibrations.

1.4.4 *Dust coagulation*

The simple monodisperse growth scenario described in Eq. 1.5 is a useful method to understand the general behavior of the dust, but is not sufficient if we want to accurately determine how the dust evolves with time. How-

ever, as the dust growth from monomers to planetesimals spans over such an extreme range in mass and size, and the dust population initially consists of $\sim 10^{40}$ bodies, simulating the evolution of a full size-distribution is non-trivial. In this thesis, we have primarily used the dust evolution code developed by [Brauer et al. \(2008\)](#) and [Birnstiel et al. \(2010a\)](#), and we will here give a brief overview of how it works.

To solve the the dust evolution problem for so many particles, some sort of statistical approach is necessary. One method is to use a Monte Carlo approach, in which a small number of particles are chosen to represent larger swarms of particles with identical properties ([Ormel & Spaans 2008](#); [Zsom & Dullemond 2008](#)). Another, more common method is to solve the Smoluchowski equation. This is a very general continuum approach that has had numerous applications outside of astronomy since its development by [Smoluchowski \(1916\)](#). In a planet formation context, it also has a long history ([Weidenschilling 1980](#); [Wetherill & Stewart 1989](#); [Lee 2001](#); [Dullemond & Dominik 2005](#); [Tanaka et al. 2005](#)). In this statistical approach, we let the dust-grain number density $n(m, r, z)$ be a function of the grain mass m , the distance to the star r , and the height above the mid-plane z , and we give it in number of particles per unit volume per unit mass. The total dust density can therefore at a point (r, z) be written as

$$\rho(r, z) = \int_0^\infty m \cdot n(m, r, z) dm, \quad (1.52)$$

and the change in number density with respect to time can then be given by the Smoluchowski equation as

$$\begin{aligned} \frac{\partial}{\partial t} n(m, r, z) &= \frac{1}{2} \int_0^m n(m - m') n(m') K(m - m', m') dm' \\ &\quad - n(m) \int_0^\infty n(m') K(m, m') dm' \\ &\quad + \frac{1}{2} \int_0^\infty \int_0^\infty n(m') n(m'') L(m', m'') S(m, m', m'') dm' dm'' \\ &\quad - n(m) \int_0^\infty n(m') L(m, m') dm', \end{aligned} \quad (1.53)$$

where we for ease of reading have dropped the dependency of r and z . The coagulation and fragmentation kernels are given by

$$K(m, m', r, z) = \sigma \Delta v p_c, \quad (1.54)$$

$$L(m, m', r, z) = \sigma \Delta v p_f, \quad (1.55)$$

where σ is the collisional cross section, Δv is the relative velocity, and p_c and p_f are the coagulation and fragmentation probabilities.

The first two terms are due to coagulation. The first term describes how particles enter the mass range $m + dm$ due to coagulation between two particles whose total mass sum up to m . The 1/2 is to avoid double counting the particle pairs. The second term describes how particles leave the mass range by having a particle of mass m coagulate with any other particle.

The last two terms are due to fragmentation. The third term describes how particles enter the mass range as fragments due to a collision between any two particles. $S(m, m', m'')$ is here the fragmentation matrix, and describes the fragment distribution as a result of the fragmenting collision between m' and m'' . The fourth term describes how particles leave the mass range due to a fragmenting collision between a particle of mass m and any other particle.

Determining the collision kernels and particularly the coagulation and fragmentation probabilities, as well as the fragmentation matrix, is non-trivial, and relies on both dust dynamics and collisional physics. This is a major part of this thesis, and will be discussed at length in following chapters.

Unless the problem is very simplified (i.e. the idealized analytical kernels discussed by [Ohtsuki et al. 1990](#); [Wetherill 1990](#); [Lee 2000](#)), the Smoluchowski equation has to be solved numerically, and it is necessary to discretize Eq. 1.53. This however leads to a problem, as having a finite number of bins means that particle collisions do not give a resulting particle mass m_p that corresponds to one of the existing logarithmically spaced mass bins. To solve this, the code uses the Podolak algorithm, where the mass of the resulting particle is distributed into the two adjacent mass bins $m_j < m_p < m_{j+1}$ according to

$$\epsilon = \frac{m_p - m_j}{m_{j+1} - m_j}, \quad (1.56)$$

where $\epsilon \cdot m_p$ is put into mass bin m_{j+1} , and $(1 - \epsilon) \cdot m_p$ is put into mass bin m_j . This approach is however susceptible to numerical diffusion, which always occurs, as $m_{j+1} > m_p$ means that mass is put into a bin that is more massive than the physical particle created in the collision. If the spacing between the mass bins is too coarse, this can lead to a significant, artificially sped up growth rate. To avoid this, a sufficiently high mass resolution of 7-40 bins per mass decade is required ([Lee 2001](#); [Okuzumi et al. 2009](#)).

The code that we use is capable of tracking the dust evolution either locally, or in the radial direction. It is in principle possible to use a code which can track both the radial and vertical direction, but this is very costly in terms of computational time. An important innovation introduced by [Brauer et al. \(2008\)](#) was therefore the vertically integrated dust evolution. Because of settling, particles of different stopping times tend to be distributed with different scale-heights, but because the coagulation process is local, two grains at different heights would not be able to collide with each other. By vertical integration of the dust distribution, it is possible to modify the collision kernel to take this into account, a trick that saves us from having to calculate the dust in the vertical direction.

1.4.5 *Barriers to growth*

Throughout the introduction, it has been clear that the dust growth is subject to a number of barriers that are problematic for the growth to plan-

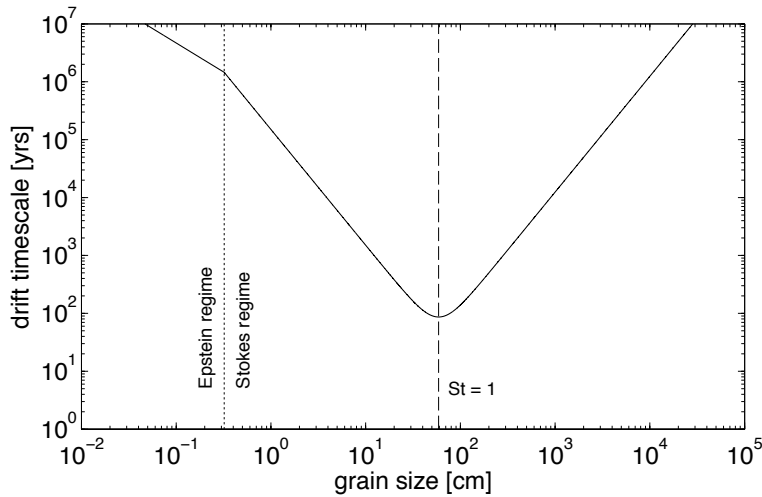


Figure 1.8: The drift timescale in an MMSN disk at 1 AU for different grain sizes. Also included is the transition grain size from the Epstein to the Stokes drag regime, and the size corresponding to $St = 1$.

etesimal sizes. In this section, we aim to summarize and further describe these different growth barriers.

The radial drift barrier has been known for a long time (Whipple 1972b; Weidenschilling 1977a). Due to gas drag, the particles constantly lose angular momentum and drift inward. The drift timescale can be very fast, as shown in Fig. 1.8 and calculated from Eq. 1.41. However, if the particles are sufficiently large ($>10^4$ cm), the drift becomes slow enough to keep the particles in the disk for the entire disk lifetime. This is a difficulty for the planetesimal formation, because there either needs to exist a mechanism to keep the dust in place for longer periods of time, or the formation mechanism needs to be able to grow the particles from cm- to several meters in size on timescales shorter than 100 years.

The drift barrier in the inner part of the disk is the focus of Chapter 6, where we will show that the particle growth might indeed be fast enough to avoid the drift. The radial drift is also a big problem for explaining the presence of dust in the observed protoplanetary disks. A solution to this could be pressure bumps, which was suggested by Barge & Sommeria (1995) and Klahr & Henning (1997). Pinilla et al. (2012b) studied this with a coagulation code, where artificial pressure bumps were distributed periodically over the disk. In the pressure bumps, the pressure gradient changes sign, which causes particles to gather at the bump. The bumps however need to be sufficiently long-lived and also strong enough to counter the turbulent diffusion. Exactly how such pressure bumps would form is however up to debate, and most suggestions so far can only create transient bumps that would decay within a few 100 orbits (Uribe et al. 2011; Dittrich et al. 2013). In Chapter 5, we instead discuss the effects of the pressure bump formed at the snowline.

The bouncing and fragmentation barriers are both related to how the collision energy in a body is dissipated. If the collision energy is too high

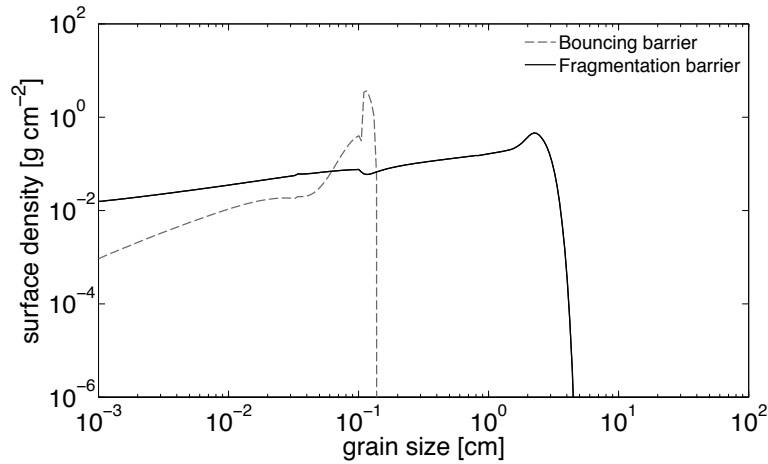


Figure 1.9: The resulting steady state size distribution due to the collisional growth barriers. The simulations were run at 1 AU for an MMSN disk with $\alpha = 10^{-4}$, with the bouncing threshold at $v_b = 5 \text{ cm s}^{-1}$, and the fragmentation threshold at $v_f = 100 \text{ cm s}^{-1}$.

for sticking but too low for fragmentation, they will simply bounce as a result, compacting each other in the process. When the dust grains can neither gain nor lose mass, their growth halts (Güttler et al. 2010; Zsom et al. 2010). If the grains are even larger, they start to experience fragmentation or erosion, which has been known for a long time (Weidenschilling 1980; Blum & Münch 1993; Brauer et al. 2008). Because either outcome is negative for growth, the absolute strength of the fragmentation does not directly matter, as grow either way is impossible.

In Fig. 1.9, we show the resulting distributions for both of the collision barriers using the local code of Birnstiel et al. (2010a). In the case of the fragmentation barrier, whenever a particle becomes too large, it fragments, and the individual fragments can again grow up towards the fragmentation barrier, creating a growth/fragmentation cycle and a final steady state. In the case of the bouncing barrier, the largest particles are incapable of both growth and erosion, and will instead result in a pile-up right at the barrier. The smallest sizes will slowly get depleted, but the timescale for this increases with the decreasing number densities. Although the bouncing collisions still needs to be understood and investigated further, the fragmentation between similar sizes seems unavoidable. In Chapter 2, we instead explore the possibility of growth between grains of very different sizes.

The charge barrier was introduced by Okuzumi (2009) and further developed by Okuzumi et al. (2011a,b). Because the disk gas is heated and partly ionized, a fraction of it exists in the form of free ions and electrons. Because the electrons have lower masses than the ions, they move around at higher velocities, and therefore interact more often with the dust. As a result, this causes the dust grains to be negatively charged on average. For two dust grains to collide, they therefore first have to overcome the Coulomb barrier. If the dust grains are small, they move with low relative

velocities and might therefore have too low kinetic energies to overcome the static repulsion. This could cause a total growth halt already at sizes of a few μm . On the other hand, if only a few particles manage to grow large in a region where the grain charging is lower and then introduced by radial mixing or settling, they would be able to easily overcome the electrostatic forces. This problem remains to be investigated in more detail, however.

1.4.6 *Alternative planetesimal formation scenarios*

As we discussed in the previous section, the scenario with incremental growth (between similar-sized particles) is frustrated by the existence of a number of barriers. Because of this, some alternative planetesimal formation scenarios have been suggested in recent years that have gained a lot of ground. To put our work on dust coagulation into context, we here summarize the principle ideas of some of them.

The very first suggestion for the planetesimal formation involves gravitational instability by the dust as it settles towards the disk midplane (Safronov & Zvjagina 1969; Goldreich & Ward 1973). If the disk is non-turbulent, the dust would settle into a progressively thinner layer until gravitational instability kicks in, resulting in the collapse and formation of planetesimals. This picture is however problematic, as first realized by Weidenschilling (1980). As a result of the dust settling, turbulence is generated due to the Kelvin-Helmholtz instability, which efficiently prevents the dust from ever forming the densities required for the gravitational instability to occur.

One scenario that has gained a lot of popularity in recent years is planetesimal formation by streaming instabilities with subsequent gravitational collapse, first introduced by (Johansen et al. 2007). So far, we have only discussed the impact that the gas has on the dust, but if the relative densities between the two are similar, there will also be a significant feedback from the dust to the gas (Youdin & Goodman 2005). The resulting streaming instability has been shown to lead to very strong concentrations of the solids, with concentration factors of up to 1000. As a result of the clumping, the Roche density can be exceeded, leading to gravitational collapse by clumps of hundreds of kilometers in size, although the final planetesimal size has yet to be determined due to resolution issues and uncertainties in secondary physical effects. A limitation to this scenario is that it requires very high densities of particles that are sufficiently decoupled from the gas with $St \sim 0.1 - 1$ (Bai & Stone 2010). Although this is a promising scenario which is capable of forming planetesimals even far out in the disk, creating the necessary conditions is not necessarily trivial. Dust evolution models have shown that the collisional barriers are likely to limit the dust population to sizes much smaller than this, and for streaming instabilities to occur in the first place, the dust-to-gas ratio also needs to be above the canonical value.

A scenario related to the above was suggested by [Cuzzi et al. \(2008\)](#) and further discussed by [Cuzzi et al. \(2010\)](#). This also relies on the interplay between the dust and the gas. If cm-sized particles (in their models corresponding to chondrules) are suspended in a turbulent gas flow, they will become ejected from the turbulent eddies and gather in the high-strain regions. This effect is called turbulent concentration, and can cause transient dust concentration factors that mostly amount to 10 – 100, but every now and then, by pure chance, these enhancement factors can reach as high as 10^4 . When this happens, the grains might become self-gravitating, and slowly sink into a rubble pile which becomes a planetesimal. For such strong clumping to occur, however, the particles need to have very similar aerodynamic properties, which requires them to be confined within a very limited size-range, and also for the particle stopping times to correspond roughly to the lifetimes of the smallest-scale eddies ([Pan et al. 2011](#)). One could argue that the bouncing barrier might create exactly these conditions, but this has yet to be studied. In Chapter 4, we discuss the coagulation in such clumps, which is highly relevant for this scenario.

A recent study by [Okuzumi et al. \(2012\)](#) suggests that icy planetesimals can form with such extremely high porosities that both the fragmentation and the drift barrier can be avoided. Based on molecular dynamics simulations by [Suyama et al. \(2012\)](#), they argue that the compaction caused by collisions is so inefficient that the coagulation will lead to internal dust densities as low as $10^{-5} \text{ g cm}^{-3}$. They argue that such aggregates are highly resilient against fragmentation, and also find that it will even lead to growth timescales significantly shorter than the drift. According to this suggestion, compaction would only occur once the planetesimals have formed, due to self-gravity or ram pressure ([Kataoka et al. 2013](#)). It should however be noted that the molecular dynamics simulations that the collision model in the study is based on are limited to aggregate sizes of $\sim 100 \mu\text{m}$, which might not necessarily be accurate for km-sized bodies.

1.5 THE AIM OF THIS THESIS

This thesis focuses on the first stages of planet formation, and aims to probe how far dust coagulation can reach in the presence of the dust growth barriers. The core result of the thesis is the discovery and development of a new planetesimal formation scenario by sweep-up, and a majority of the work is dedicated to discussing various aspects of this mode of growth. Apart from the sweep-up, we discuss various aspects that are also relevant for the general dust evolution and for some of the other planetesimal formation scenarios discussed in the previous section.

Chapter 2 focuses on the creation and implementation of a realistic collision model. By taking into account the latest results from the laboratory and numerical simulations, we implement a model that includes sticking, bouncing, fragmentation, erosion, mass transfer and smooth transitions between them. In line with previous work on dust evolution with complex

collision physics, we find that such a collision model indeed matters, and courtesy of the capabilities of the Smoluchowski dust evolution approach, we also identify a new growth channel for planetesimal formation.

Chapter 3 studies the effect of velocity distributions on the dust collision rates and impact outcomes. We find that the existence of a velocity distribution smears out the collisional barriers, by allowing a few low-velocity sticking collisions to occur between particles that on average only fragment. This can allow for a few lucky particles to break through the barriers and initiate sweep-up growth towards planetesimal sizes.

Chapter 4 extends the work of the previous section to also take into account clustering between the particles. We consider a few of the clustering effects, and find that they are ideal for the creation of larger grains, as the clusters lead to higher collision rates between the sticking, low-velocity collisions. We also speculate the clustering might lead to collision rates that are high enough to overcome the radial drift barrier in the outer disk.

Chapter 5 explores the outcome of coagulation at the pressure bump created at the snowline. We find that by allowing the larger "privileged" particles that can form in dead zones to radially mix with smaller particles in the active regions, growth breakthrough can occur and sweep-up be initiated at the location of the pressure bump.

Chapter 6 investigates the formation and drift of planetesimals in the inner region of the disk. Due to a switch between the gas drag regimes and the increased solid densities, we find that proto-planetesimals formed by the sweep-up mechanism can grow fast enough to avoid the radial drift barrier in the inner few AU of the disk. In this way, planetesimals can form on timescales of only a few thousand years. We speculate that this might explain the mass distribution of the terrestrial planets in the Solar System and the recently discovered compact exoplanetary systems.

PLANETESIMAL FORMATION BY SWEEP-UP COAGULATION

Adapted from Windmark, Birnstiel, Güttler, Blum, Dullemond, Henning, A&A (2012), vol 540, A73¹

ABSTRACT

The formation of planetesimals is often accredited to the collisional sticking of dust grains. The exact process is unknown, as collisions between larger aggregates tend to lead to fragmentation or bouncing rather than sticking. Recent laboratory experiments have however made great progress in the understanding and mapping of the complex physics involved in dust collisions. In this chapter, we study the possibility of planetesimal formation using the results of the latest laboratory experiments, particularly by including the *fragmentation with mass transfer* effect, which can lead to growth even at high impact velocities. We present a new experimentally and physically motivated dust collision model capable of predicting the outcome of a collision between two particles of arbitrary mass and velocity. The new model includes a natural description of cratering and mass transfer, and provides a smooth transition from equal- to different-sized collisions. It is used together with a continuum dust-size evolution code, which is both fast in terms of execution time and able to resolve the dust at all sizes, allowing for all types of interactions to be studied without biases. For the general dust population, we find that bouncing collisions prevent any growth above millimeter-sizes. However, if a small number of cm-sized particles are introduced, for example by either radial mixing or created by velocity distributions, they can act as a catalyst and start to sweep up the smaller particles. In an MMSN disk at a distance of 3 AU, 100-meter-sized bodies are formed on a timescale of 1 Myr, but in a denser disk environment, we find that 10-km-sized planetesimals can form within 0.1 Myrs. Direct growth of planetesimals is a possibility thanks to a combination of the bouncing barrier and the fragmentation with mass transfer effect. The bouncing barrier is here even beneficial, as it prevents the growth of too many large particles that would otherwise only fragment among each other, and it creates a reservoir of small particles that can be swept up by larger bodies. However, for this process to work, a few seeds of cm-size or larger have to be introduced artificially.

¹ See page ix for details on authorship.

2.1 INTRODUCTION

One of the oldest and most popular planetesimal formation scenarios is based on incremental growth, in which the formation of planets starts in the protoplanetary disk with micron-sized dust particles that collide and stick together by surface forces, forming successively larger aggregates (Weidenschilling 1980). The next stage in the formation process is the gravity-aided regime where planetesimals have formed that are so massive that the gravity starts to affect the accretion and the strength of the body.

However, to reach this regime, kilometer-sized bodies are required, something that has proven difficult to produce owing to a number of effects such as fragmentation and bouncing (Blum & Münch 1993), rapid inward migration (Whipple 1972a), and electrostatic repulsion (Okuzumi et al. 2011a,b). A new planetesimal formation channel was introduced by Johansen et al. (2007, 2011), in which mutual gravity plays a role between meter-sized boulders in turbulent and locally overdense regions, resulting in the rapid formation of kilometer-sized bodies. However, even the meter regime is difficult to reach only by the coagulation of dust aggregates.

The micron-sized dust particles are coupled tightly to the surrounding gas, and their relative velocities are driven primarily by Brownian motion. Since the resulting relative velocities are small, on the order of mm s^{-1} , the particles stick together by means of van der Waals forces. However, as the particles increase in size, they become less coupled to the gas, and a number of effects increase the relative velocities between them. For cm-sized particles, the predicted relative velocity is already 1 m s^{-1} , and m-sized boulders collide at velocities of $\sim 10 \text{ m s}^{-1}$. At these high collision energies, the particles tend to fragment rather than stick (Blum & Wurm 2008), which effectively prevents further growth (Brauer et al. 2008; Birnstiel et al. 2010a).

In the protoplanetary disk, gas pressure supports the gas against the radial component of the stellar gravity, causing it to move at slightly sub-Keplerian velocities. Solid bodies do not however experience the supporting gas pressure, and instead drift inward. As the particles grow larger, their relative velocities with respect to the gas increase, causing a significant headwind and a steady loss of angular momentum. At a distance of 1 AU , radial drift can cause meter-sized bodies to spiral inwards and get lost in the star on a timescale of a few hundred orbits (Weidenschilling 1977a; Nakagawa et al. 1986). The fragmentation and drift barriers have been shown to efficiently prevent growth above 1-100 cm, but to reach the gravitational regime, bodies that are roughly nine orders of magnitude more massive are needed.

The study of the dust evolution has until recently primarily been done using simplified dust collision models in which colliding dust grains either stick together or fragment (Brauer et al. 2008; Birnstiel et al. 2010a). The simplicity of the models has been a necessity because of large uncertainties

and the small parameter space covered in terms of mass, porosity, and collision velocity in the laboratory experiments and numerical simulations.

Recent years have however seen good progress in the laboratory experiments, as summarized by [Blum & Wurm \(2008\)](#). To provide a more complete and realistic collision model, [Güttler et al. \(2010\)](#) reviewed a total of 19 different experiments with aggregates of varying masses, porosities, and collision velocities. In these experiments, the complex outcome was classified into nine different types. [Zsom et al. \(2010\)](#) implemented this collision model in a Monte Carlo dust-size evolution code. The results showed clear differences from the previous collision models, and allowed for the identification of the most important of the different collision types. They also found the important effect of dust grain bouncing at millimeter sizes that halts the grain growth even before it reaches the fragmentation barrier. With the inclusion of a vertical structure, [Zsom et al. \(2011\)](#) still found bouncing to be prominent, but the vertical settling also allowed for a number of other collision effects to occur.

Progress has also been made with numerical simulations of dust (silica and ice) aggregate collisions using molecular dynamics codes with up to 10,000 monomers corresponding to aggregate sizes of around 100 μm ([Wada et al. 2009, 2011](#)). On the basis of these simulations, [Okuzumi et al. \(2012\)](#) argued that growth was possible for ices up to velocities of 70 m s^{-1} , and silicates up to 7 m s^{-1} . With this model, they were able to form extremely porous icy planetesimals. [Geretschauser et al. \(2010, 2011\)](#) also developed a dust collision code using SPH for particle sizes of cm and upwards. There is currently a discrepancy between the simulations and the laboratory experiments, where the simulations have difficulties reproducing the bouncing events and generally observe much higher fragmentation threshold velocities. In this chapter, we analyze primarily the (more pessimistic) laboratory data, but there is a great need to get the two fields to agree.

One possible way to grow past the fragmentation barrier is so-called fragmentation with mass transfer, which was observed by [Wurm et al. \(2005\)](#) and can happen in a collision between a small projectile and a large target. The projectile is fragmented during the collision and a part of it is added as a dust cone to the surface of the larger particle, provided that the mass ratio of the two particles is large enough to avoid fragmentation of the larger body. The mass transfer efficiency was studied by [Kothe et al. \(2010\)](#), who also showed that multiple impacts over the same area still lead to growth. [Teiser & Wurm \(2009a,b\)](#) showed that growth of the target is possible even for collision velocities higher than 50 m s^{-1} , and [Teiser et al. \(2011\)](#) proved that the target could still gain mass even at large impact angles. These experiments have all shown that dust growth may proceed for large bodies at high velocities, and indicate that this effect might even be able to produce planetesimals via collisional accretion.

For the study of the dust-size evolution, the Monte Carlo approach of [Ormel & Spaans \(2008\)](#) and [Zsom & Dullemond \(2008\)](#) has the distinct advantage that it permits the simulation of a large number of particle

properties and collision outcomes. A representative particle approach is used where a few particles correspond to larger swarms of particles with the same properties. Each particle is given a set of properties, and each individual collision of the representative particles is followed. This approach uses very little computer memory, and adding extra properties costs very little in terms of execution time. If we wish to study the effect of mass transfer, however, the Zsom et al. approach has some problems, as it only tracks the grain sizes where the most mass can be found in the system. It therefore has difficulties in resolving wide size distributions, which is required for the type of bimodal growth that the fragmentation with mass transfer effect would produce.

Another method is the continuum approach, in which the dust population is described by a size distribution (Weidenschilling 1980; Nakagawa et al. 1981). The conventional continuum approach is the Smoluchowski method, where the interactions between particles of all sizes are considered and updated simultaneously. This leads to very fast codes for a one-dimensional parameter-space (i.e. mass) compared to the Monte Carlo approach. Adding additional properties such as porosity and charge is however very computationally expensive in terms of memory usage and execution time if one does not include steps such as the average-porosity scheme of Okuzumi et al. (2009). With the continuum approach, however, the dust is resolved at all sizes, allowing for all types of dust interactions without any biases. This approach is also fast enough to follow the global dust evolution in the whole disk.

The aim of this chapter is to describe the creation of a new collision model describing the outcome of collisions between dust aggregates of various sizes and velocities, that is fast enough to be used with continuum codes. In this new model, we take into account recent progress in laboratory experiments, especially the mass transfer effect described above, and take a physical approach to transition regions from growth to erosion where the experiments are sparse. We then use this model in size evolution simulations using the local version of the code developed by Birnstiel et al. (2010a) to study its implications for the formation of the first generation of planetesimals.

The background of the new model and all the experimental work that it is based on is discussed in Sect. 2.2, and its implementation is described in Sect. 2.3. In Sect. 2.4, we discuss the properties of the disk in our local dust evolution simulations, as well as the implicit Smoluchowski solver that we have used. Finally, in Sects. 2.5 and 2.6, we discuss the results of the new model and show how the existence of a bouncing barrier may even be beneficial to the growth of planetesimals.

2.2 MOTIVATION BEHIND THE DEVELOPMENT OF A NEW COLLISION MODEL

Models to describe the growth of dust aggregates can generally be divided into two parts: A *collision model* describes the result of a collision between

two dust particles of arbitrary properties (i.e. mass, porosity) and velocities. A *dust evolution model* uses the collision model to describe the evolution of the particle properties of an entire population of dust particles as they collide and interact with each other. In this section, we describe the latest laboratory experiments and our effort to produce a collision model that can take these results into account while still streamlining it to work well with continuum dust evolution codes. This means that the collision model cannot be as complex as the one developed by Güttler et al. (2010), but needs to focus on the most important collision types and aggregate properties. Nevertheless, we were able to include results that were not well-established or even known when the model of Güttler et al. was developed.

2.2.1 Overview of recent experiments and simulations

Numerous laboratory experiments have been performed to probe the collision parameter space of silicate dust grains, as summarized by Blum & Wurm (2008). This is a daunting task, as planet formation spans more than 40 orders of magnitude in mass and 6 orders of magnitude in collisional velocity and collisional outcomes are affected by for example porosity, composition, structure and impact angle. The classical growth mechanism of dust grains is the hit-and-stick mechanism, which has been well-studied in both laboratory experiments (Blum & Wurm 2000, BW00) and numerical simulations (Dominik & Tielens 1997; Wada et al. 2009). Sticking collisions are also possible via plastic deformation at the contact zone (Weidling et al. 2012, WGB12) and geometrically by penetration (Langkowski et al. 2008, LTB08).

Owing to limited data, previous collision models have with few exceptions only included sticking, cratering, and fragmentation with simplistic thresholds (Nakagawa et al. 1986; Weidenschilling 1997; Dullemond & Dominik 2005; Tanaka et al. 2005; Brauer et al. 2008). To study the effect of the progress in laboratory experiments, Güttler et al. (2010) and Zsom et al. (2010) presented a collision model containing nine different collisional outcomes and used this in the Monte Carlo dust evolution code developed by Zsom & Dullemond (2008). Their model contained three types of sticking collisions in addition to the normal hit-and-stick, and they identified two growth-neutral bouncing effects and three different fragmentation effects in which the largest particle is eroded. They found that several of the new collision types played a role in the dust-size evolution, which proved the necessity for a more complex dust collision approach than previously used. Before even reaching the fragmentation barrier, at which fragmentation events between similar-sized particles prevent further growth, they identified the so-called bouncing barrier. Bouncing collisions between smaller particles of intermediate velocities proved to be an efficient barrier for growth even for grains as small as a millimeter. It should be clarified that bouncing is, in principle, not bad for growth. The bouncing barrier is a

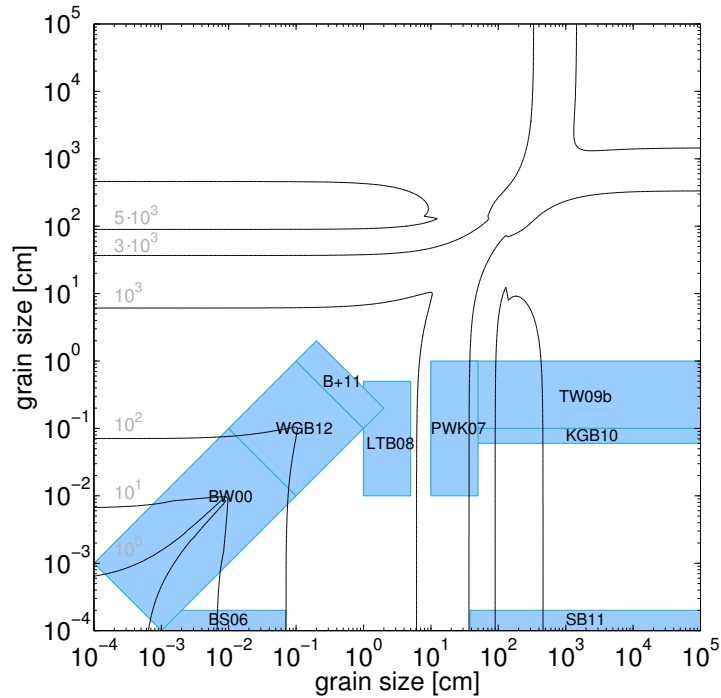


Figure 2.1: The size-size parameter space of the dust collision experiments (blue boxes) providing the basis for the new collision model. All marked experiments are discussed in more detail in Sect. 2.2.1. The contours and gray labels mark the collision velocities in cm s^{-1} expected from the disk model described in Sect. 2.4, and do not always coincide exactly with the velocities studied in the experiments.

problem because of the lack of sticking over such a large range of masses and velocities, which prevents the particles from growing any further.

Bouncing between dust aggregates remains a hotly discussed topic. It has been reported from a large number of laboratory experiments with different setups and material properties (Blum & Münch 1993; Heißelmann et al. 2007; Langkowski et al. 2008; Kelling & Wurm 2009; Güttler et al. 2010; Weidling et al. 2012), but molecular dynamics simulations contain significantly less or no bouncing (Wada et al. 2007, 2008, 2009, 2011; Paszun & Dominik 2009; Seizinger & Kley 2013a). These rebounding events happen in collisions where the impact energy is so high that not all can be dissipated by the restructuring of the aggregates. Wada et al. (2011) argue that this would happen only for very compact aggregates where the coordination number is high, which contradicts what is seen in the laboratory. In the present study, we base our model on laboratory experiments, but bouncing is clearly a very important matter for the dust growth and will need to be investigated in future studies.

In our new model, we implement the most important collision types identified by Zsom et al. (2010), and also take into account the results of a number of recent experimental studies. Many new experiments have been performed that have increased our understanding of the collision physics of dust aggregates. In Fig. 2.1, we plot the parameter space of a selection

of important laboratory experiments that provide the basis for the new collision model.

Provided that the mass ratio is large enough between the two particles (from now on called the projectile and the target for the smallest and largest particle), the projectile can fragment and parts of it stick by van der Waal forces to the surface of the target. This was studied by [Wurm et al. \(2005\)](#) and [Teiser & Wurm \(2009b, TW09b\)](#) for mm- to cm-sized projectiles shot onto a mounted dm-sized dust target at velocities of up to 56.5 m s^{-1} . It was found that the accretion efficiency even increased with velocity, and could be as high as 50% of the mass of the fragmented projectile, where [Güttler et al. \(2010\)](#) only assumed a constant 2%. This effect was also observed by [Paraskov et al. \(2007, PWK07\)](#) in drop tower experiments where the target also was free-floating without a supported back. The mass transfer efficiency at slightly smaller velocities ($1.5 - 6 \text{ m s}^{-1}$) and for millimeter-sized projectiles was studied in more detail by [Kothe et al. \(2010, KGB10\)](#), who confirmed the velocity-positive trend. [Teiser & Wurm \(2009a\)](#) and [Kothe et al.](#) also studied multiple impacts over the same area, and could conclude that growth was possible even then, without the newly accreted material being eroded. It was also found that growth was possible even at very steep impact angles. [Beitz et al. \(2011, B+11\)](#) performed experiments between cm-sized particles at even smaller velocities (8 mm s^{-1} to 2 m s^{-1}) and detected mass transfer even at velocities as small as 20 cm s^{-1} , right at the onset of fragmentation.

This mode of growth, where small projectiles impact large targets, is related to the work of [Sekiya & Takeda \(2003, 2005\)](#), who performed numerical studies to determine whether small fragments formed in an erosive collision could be reaccreted back onto the target by gas drag. The conclusion was that if the fragments were μm -sized, and the target is sufficiently large, the gas flow would actually compel the fragments to move around the target, thereby preventing reaccretion. For the mass transfer effect, it is important to verify whether this effect could prevent $100\text{-}1000 \mu\text{m}$ -sized projectiles from impacting on the target in the first place. The importance of this effect can be estimated with a simple comparison of timescales using reasonable parameters for the disk model (discussed in more detail in Sect. 2.4). The stopping time of a small particle is given by

$$\tau_s = \frac{\xi a_p}{\rho_g \cdot \bar{u}} \sim 2500 \text{ s}, \quad (2.1)$$

where $\xi \sim 1 \text{ g cm}^{-3}$ is the solid density of the projectile, $a_p \sim 100 \mu\text{m}$ is its radius, $\rho_g \sim 10^{-10} \text{ g cm}^{-3}$ is the expected midplane gas density at 3 AU, and $\bar{u} \sim 4 \cdot 10^4 \text{ cm s}^{-1}$ is the mean thermal velocity of the gas. The time it would take for the projectile to pass the target is given by

$$\tau_{\text{pass}} = \frac{a_t}{\Delta v} \sim 0.2 \text{ s}, \quad (2.2)$$

where $a_t \sim 100 \text{ cm}$ is a typical target size and $\Delta v \sim 5000 \text{ cm s}^{-1}$ the relative velocity between the particles. Since $\tau_s \gg \tau_{\text{pass}}$, it would take too

long for the projectile to adjust to the gas flow around the target, and the two particles would collide. If the projectiles were instead only $1 \mu\text{m}$ in size, the timescales would not differ so much, and the gas flow might play a role.

Another recent experimental result is the refinement of the threshold velocity for destructive fragmentation, where the target is completely disrupted. [Beitz et al. \(2011\)](#) performed experiments to determine the onset of global fragmentation of the particles, and found that cm-sized particles fragmented at 20 cm s^{-1} , much below the 1 m s^{-1} threshold found for mm-sized particles by [Blum & Münch \(1993\)](#). This points towards a material strength that decreases with mass, as predicted for rocky materials by [Benz & Asphaug \(1999\)](#) among others. This result can be explained by a probability of faults and cracks in the material that increases with particle size, and that it is along these cracks that both global breaking and fragmentation takes place. No experiments have as of yet been performed to study the fragmentation threshold of differently sized dust aggregates, but one can generally assume that the velocities needed increase with the size ratio, as seen in both experiments and simulations of collisions between rocky materials ([Stewart & Leinhardt 2011](#); [Leinhardt & Stewart 2012](#)).

To provide more data in the transition region between sticking and bouncing, [Weidling et al. \(2012\)](#) studied collisions between particles $0.5 - 2 \text{ mm}$ in size and at velocities of $0.1 - 100 \text{ cm s}^{-1}$. In these experiments, sticking collisions were found (in coexistence with bouncing events) for higher velocities than previously expected ([Blum & Wurm 2000](#); [Güttler et al. 2010](#)), and enough data now exists to define a transition regime between only sticking and bouncing. Similar experiments with smaller particles roughly $100 \mu\text{m}$ in size were performed by Kothe et al. (unpublished), and are consistent with the threshold of Weidling et al.

[Schräpler & Blum \(2011, SB11\)](#) also performed erosion experiments between μm -sized monomer projectiles and mounted high-porosity aggregates for velocities of up to 60 m s^{-1} , to determine the erosion efficiency as a function of the collision velocity and the surface structure. They discovered that the initial stages of the monomer bombardment are very efficient even at small velocities, but after the most loosely bound monomer chains had been knocked off and the surface had been compacted, the erosion was found to have greatly decreased.

2.2.2 *Individual treatment of collisions*

In the collision model of [Güttler et al. \(2010\)](#), a binary approach was used for the particle mass ratios and porosities. Below a certain set critical mass ratio, $r_c = m_t/m_p = 10, 100, 1000$, the collision was treated as being between equal-sized particles, leading for example to global fragmentation if two large particles collided at high velocities. If the mass ratio was above the critical ratio, the particles were assumed to have different sizes, and a high-velocity collision would instead lead only to cratering. The same approach was taken for the porosity. Below a critical porosity $\phi_c = 0.4$, a

particle was considered to be porous for the purpose of determining the collision outcome, and above it, the particle was assumed compact. Combining these two binary properties gave eight different collision scenarios, where the collision outcome was determined by the particle masses, porosities, and relative velocities.

In the new model, we instead used the current laboratory data to interpolate between the two extreme mass-ratios. This provides a continuous transition from equal-sized to differently sized collisions, and allows us to distinguish between the collisions of particles of different sizes at intermediate mass-ratios, and provides a natural and smooth transition between the two extremes. We can therefore determine the velocity needed to cause global fragmentation for a specific mass-ratio, which gives us a more precise tool to assess when global fragmentation becomes local cratering.

It is however necessary for us to make a simplification regarding the porosity of the dust grains. Adding additional properties to the dust grains is very computationally expensive for continuum codes such as the Smoluchowski solver that we use for the dust-size evolution, compared to Monte Carlo codes. In the Monte Carlo approach, each timestep consists only of one collision between a representative particle and a swarm of identical particles. After the collision, the properties (i.e. mass, porosity, charge) of the representative particle is updated, and a new timestep is initiated. This means that for a simulation with n representative particles, each new property adds only an additional time $O(n)$ to the execution time.

In the Smoluchowski method, one has to numerically solve a number of differential equations to update the number density of all mass bins. For each grain size, n^2 interaction terms need to be considered, where n is the number of mass bins. This is because a mass bin can collide with all bins including itself, but fragmentation can also cause mass to be put into it by a collision between two other bins. If an additional property such as porosity were included, $m = n$ porosity bins would need to be included, and for each $n \cdot m$ bin, $(n \cdot m)^2$ interactions need to be considered, and the code would be slower by a factor of $O(m^3)$. To include porosity in the Smoluchowski solver, we would therefore require some analytical trick such as an average porosity for each mass bin described in [Okuzumi et al. \(2009\)](#). This is however outside the scope of this chapter, and we instead assume that all particles are compact at all times. This is likely a good approximation for larger particles outside the hit-and-stick region, as bouncing collisions quickly lead to compaction of the particles. This finally gives us one single collision scenario, where we can for a collision between any two given particles determine the outcome based on their masses and relative velocities.

2.3 IMPLEMENTATION OF THE MODEL

We now describe how the new collision model was created and implemented into the code. We choose to include only the collision types that proved to be the most important in the simulations of [Zsom et al. \(2010\)](#).

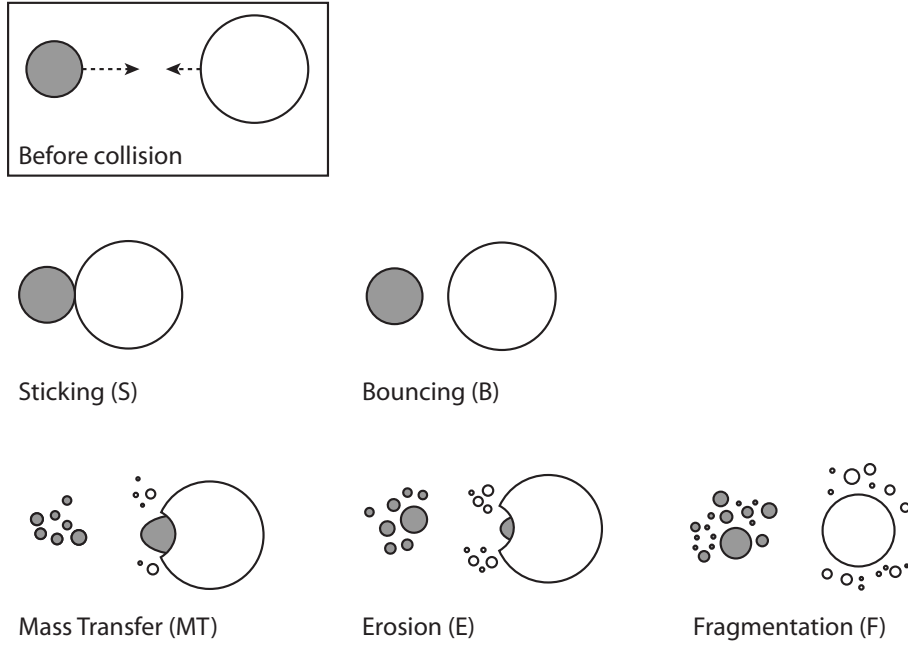


Figure 2.2: Sketch of the five possible outcomes described in Sect. 2.3 sorted in rough order of collision velocity. Mass transfer and erosion act simultaneously in a collision, and we define a mass transfer collision as leading to net growth for the target, and an erosive collision leading to net mass loss.

The collision types considered here are sticking and bouncing as well as the transition between them, mass transfer combined with erosion, and destructive fragmentation. These types are shown schematically in Fig. 2.2, and discussed in detail in Sects. 2.3.1-2.3.3. In Table 2.1, we provide a summary of all the symbols used in this section.

2.3.1 Sticking and bouncing thresholds

We consider two dust grains colliding with a relative velocity Δv . The projectile has a mass m_p and the target a mass $m_t \geq m_p$. Weidling et al. (2012) found that the mass-dependent sticking and bouncing threshold velocities can be written as

$$\Delta v_{\text{stick}} = \left(\frac{m_p}{m_s} \right)^{-5/18} \quad [\text{cm s}^{-1}] \quad (2.3)$$

and

$$\Delta v_{\text{bounce}} = \left(\frac{m_p}{m_b} \right)^{-5/18} \quad [\text{cm s}^{-1}], \quad (2.4)$$

where $m_s = 3.0 \cdot 10^{-12}$ g and $m_b = 3.3 \cdot 10^{-3}$ g are two normalizing constants calibrated by laboratory experiments, and the $\Delta v \propto m^{-5/18}$ proportionality is consistent with the theoretical models of Thornton & Ning (1998). The above two thresholds mean that collisions with $\Delta v < \Delta v_{\text{stick}}$

result in 100% sticking, and $\Delta v > \Delta v_{\text{bounce}}$ result in 100% bouncing (provided that neither of the particles involved are fragmented). Inbetween these two thresholds, we have a region where both outcomes are possible, as described in more detail in Sect. 2.3.5.

2.3.2 An energy division scheme for fragmentation

From the fragmentation with mass transfer experiments described in the previous section, we assume that mass transfer with a range of efficiencies occurs in all cases where the projectile fragments. If the target also fragments, the mass transfer is negligible compared to the huge mass loss, and we can safely ignore it. We therefore need to determine for each collision whether one, both, or neither of the particles fragment.

The majority of the dust collision experiments have however been performed between either equal-sized or very different-sized particles. To interpolate between these two extremes, we need to consider the collision energy of the event, and determine how this energy is distributed between the two particles. Not only the collision energy of an event matters when determining the degree of fragmentation, but also the mass-ratio between

Table 2.1: Symbols used in the collision model

Symbol	Meaning
$a_{\text{p/t}}$	radius of the projectile/target
$m_{\text{p/t}}$	mass of the projectile/target
Δv	relative velocity between the particles
Δv_{stick}	sticking threshold velocity
m_s	sticking threshold normalizing constant
Δv_{bounce}	bouncing threshold velocity
m_b	bouncing threshold normalizing constant
$v_{\text{p/t}}$	center-of-mass velocity of the projectile/target
μ	relative mass of the largest remnant
m_{rem}	mass of the largest remnant
m_{mt}	mass transferred from the projectile to the target
ϵ_{ac}	accretion efficiency during mass transfer
m_{er}	mass eroded from the target due to cratering
Δm_t	net mass change from mass transfer and erosion
ϵ_{net}	net accretion efficiency from mass transfer and erosion
v_μ	velocity needed to fragment with largest remnant μ
m_μ	fragmentation threshold normalizing constant
m_0	mass of a monomer ($= 3.5 \cdot 10^{-12}$ g)
m_{frag}	total mass of the fragments

the two particles. In two collisions with equal collision energy but different mass-ratios, we expect the higher mass-ratio collision to be less efficient in completely disrupting the target, as the energy will be more locally distributed around the contact point. To take this into account, we choose to look at the particles in the center-of-mass frame. In this frame, the massive particle moves more slowly than the small one, and during the moment of collision, the kinetic energy of the particles is reduced to zero. Physically, this corresponds to a fully plastic collision where all the energy is consumed by deformation and fragmentation.

In this approach, we assume that the kinetic energy of each particle in the center-of-mass frame will be used to try to fragment itself. The velocities of the two particles in the center-of-mass frame are given by

$$v_p = \frac{\Delta v}{1 + m_p/m_t}, \quad (2.5)$$

$$v_t = \frac{\Delta v}{1 + m_t/m_p}. \quad (2.6)$$

All velocities in the center-of-mass frame will from now on be denoted as v and then mean either v_p or v_t . The above equations imply that the largest particle has the lowest velocity in the center-of-mass frame. In the case of an extreme mass ratio, $m_p/m_t \rightarrow 0$, the center-of-mass velocity of the projectile and target is given by $v_p = \Delta v$ and $v_t = 0$, respectively.

During a fragmenting collision, the relative size of the largest remnant can be described by

$$\mu_{p/t} = \frac{m_{\text{rem}}}{m_{p/t}}, \quad (2.7)$$

where m_{rem} is the mass of the largest remnant and $m_{p/t}$ the original particle mass. Depending on their sizes and material strengths, the two original particles can be fragmented to different degrees. In this model, each collision partner is treated individually with a μ_t and μ_p for the remnant of the target and the projectile, respectively. We define the center-of-mass velocity required for the largest remnant to have a relative mass μ as v_μ .

Blum & Münch (1993) and Lammel (2008) studied the threshold velocities needed for two mm-sized particles to fragment with largest remnants of relative masses $\mu = 1.0$ and $\mu = 0.5$, where the former corresponds to the onset of fragmentation and the latter to a largest remnant equal to half of the original particle. Beitz et al. (2011) studied the threshold velocities for cm-sized particles. Interpolating between the results for the two sizes, the center-of-mass frame threshold velocity can be written as

$$v_\mu = (m/m_\mu)^{-\gamma} \quad [\text{cm s}^{-1}], \quad (2.8)$$

where m_μ is a normalizing constant calibrated by the laboratory experiments and $\gamma = 0.16$. The fragmentation threshold velocity is given by $v_{1.0}$, where $m_{1.0} = 3.67 \cdot 10^7$ g. The velocity required for the largest fragment to have half the size of the original particle is $v_{0.5}$, where $m_{0.5} = 9.49 \cdot 10^{11}$

g. The relative mass of the largest fragment is fitted by a power law that depends on velocity and mass

$$\mu(m, v) = C \cdot \left(\frac{m}{1 \text{ g}} \right)^\alpha \cdot \left(\frac{v}{1 \text{ cm s}^{-1}} \right)^\beta . \quad (2.9)$$

The above equation is valid for all velocities $v > v_{1.0}$. By fitting the $\mu(m, v)$ plane to the two parallel threshold velocities given by Eq. (2.8), we get

$$\alpha = \log(2) / \log(m_{1.0} / m_{0.5}) = -0.068 , \quad (2.10)$$

$$\beta = \alpha / \gamma = -0.43 , \quad (2.11)$$

$$C = m_{1.0}^{-\alpha} = 3.27 \text{ [g}^{-\alpha}] . \quad (2.12)$$

This means that at a larger collision velocity, the particle will fragment more considerably and the size of the largest fragment will decrease. More mass is therefore put into the lower part of the mass spectrum.

We can from Eq. 2.9 determine the largest fragment for each of the particles in the collision, and also use it to identify fragmenting collisions. If $\mu_p < 1$ and $\mu_t \geq 1$, only the projectile fragments and mass transfer occurs. If both $\mu_p < 1$ and $\mu_t < 1$, both particles fragment globally. Since the center-of-mass velocity v is inversely proportional to the mass of the particle, we never have a case where only the target fragments and the projectile is left intact, even if v_μ decreases with mass.

2.3.3 A new mass transfer and cratering model

We use a new realistic approach to distinguishing between collisions where the target experiences either net mass gain due to mass transfer, or a net mass loss due to cratering. During each collision, we assume that there is simultaneously:

- mass added to the target from the projectile via mass transfer;
- mass eroded from the target due to cratering.

We also assume that these two effects act independently of each other. This is illustrated in Fig. 2.3, and can also be seen in the high-velocity experiments of [Teiser & Wurm \(2009b\)](#). The mass change of the largest particle can be described by

$$\Delta m_t = m_{\text{mt}} - m_{\text{er}} , \quad (2.13)$$

where $m_{\text{mt}} = \epsilon_{\text{ac}} \cdot m_p$ is the mass added by mass transfer with the accretion efficiency $0 \leq \epsilon_{\text{ac}} \leq 1$ and $m_{\text{er}} = \epsilon_{\text{er}} \cdot m_p$ is the mass lost due to cratering with the efficiency $\epsilon_{\text{er}} \geq 0$. An increase in the velocity not only leads to increased mass transfer, but also increased cratering. This makes it possible to naturally determine when growth becomes erosion.

The mass transfer efficiency is obtained from [Beitz et al. \(2011\)](#) and [Kothe et al. \(2010\)](#), and depends on both the particle porosity and velocity. Since we are unable to track the porosity of the particles, we assume a

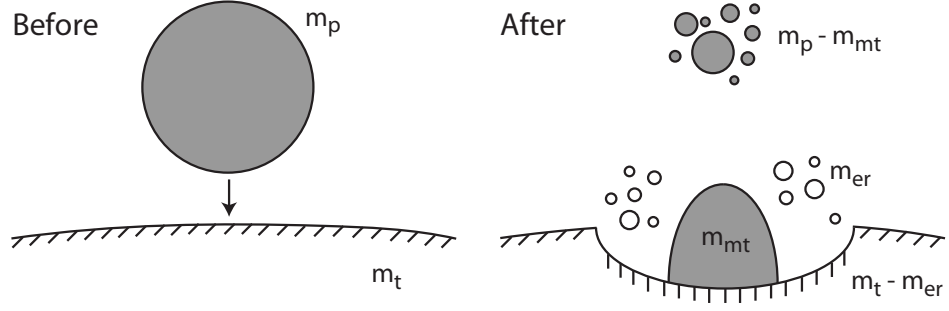


Figure 2.3: Sketch of the combined cratering and mass transfer process that occurs during a high-enough velocity collision between a projectile with mass m_p and a target with mass m_t . During the collision, an amount m_{mt} is added from the projectile to the target, and the rest of the projectile is converted into small fragments with a total mass $m_{p,frag}$. An amount m_{er} is simultaneously eroded from the target, and the final mass of the target is given by $m'_t = m_t + m_{mt} - m_{er}$.

constant porosity difference of $\Delta\phi = 0.1$ between the two dust aggregates, where the target is always the more compact one. This is likely a reasonable approximation for larger particles that have left the hit-and-stick phase and have had time to compact during bouncing collisions, which is the region where mass transfer can be expected. In our prescription, we also include a fragmentation threshold velocity dependence, so that the efficiency is always the same for the same degree of projectile fragmentation. This results in

$$\epsilon_{ac} = -6.8 \cdot 10^{-3} + 2.8 \cdot 10^{-4} \cdot \frac{v_{1.0,beitz}}{v_{1.0}} \cdot \frac{\Delta v}{1 \text{ cm s}^{-1}}, \quad (2.14)$$

where $v_{1.0,beitz} = 13 \text{ cm s}^{-1}$ is the onset of the fragmentation for the 4.1 g particles used by [Beitz et al. \(2011\)](#), and $v_{1.0}$ is the fragmentation threshold calculated for the mass of the projectile, both calculated using Eq. 2.8. We also enforce a minimum efficiency of 0, and a maximum efficiency of 0.5, as indicated by [Wurm et al. \(2005\)](#). Owing to the process of fragmentation and mass transfer considered here, a higher value would not be reasonable as it would be indicative of complete sticking, which has never been observed at these velocities.

If the collision energy is not high enough to fragment the particles globally, some of the energy is still used to break up local bonds between monomers around the contact point, resulting in cratering. The cratering efficiency has however only been studied in a couple of laboratory experiments. For monomer projectiles, [Schr apler & Blum \(2011\)](#) found an erosion efficiency given by

$$\epsilon_{er} = \frac{m_{er}}{m_p} = 1.55 \cdot 10^{-4} \cdot \frac{\Delta v}{1 \text{ cm s}^{-1}} - 0.4, \quad (2.15)$$

where m_{er} is the amount of eroded mass and $m_p = m_0$ is the projectile mass, and $m_0 = 3.5 \cdot 10^{-12} \text{ g}$ is the monomer mass. [Paraskov et al. \(2007\)](#)

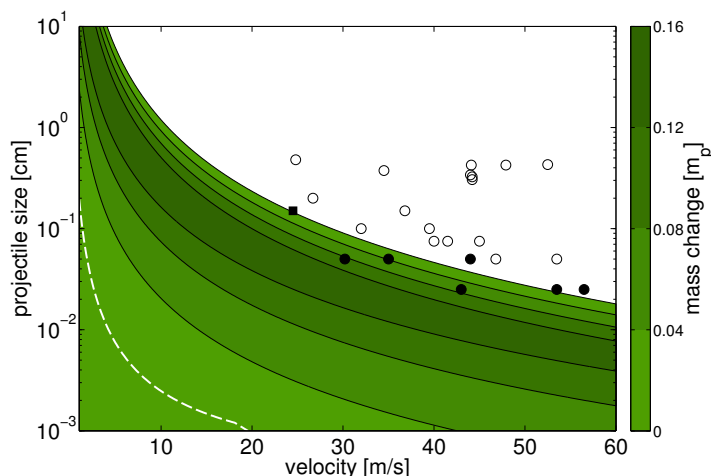


Figure 2.4: The threshold between growth and erosion from the model compared to the mass-transfer experiments performed by [Teiser & Wurm \(2009b\)](#). Filled circles show experiments where the target gained mass, and open circles where it lost mass. The white dotted line shows the threshold for the highly uncertain erosion prescription from cratering experiments (collisions above the line result in erosion, and collisions below result in growth). The contours are in intervals of 4% net accretion efficiency and mark the region with net growth in the final prescription calibrated using the Teiser & Wurm data.

studied the erosion of porous targets with both solid and porous projectiles, and found widely results depending on the porosities of the projectile and target. Their results are therefore highly uncertain, but roughly agree with an erosion efficiency of

$$\epsilon_{\text{er}} = \frac{3}{400} \cdot \frac{\Delta v}{1 \text{ cm s}^{-1}}, \quad (2.16)$$

We however note that for the more compact dust aggregates expected after the compression by the bouncing phase, the erosion efficiency should be far lower, as generally seen by [Teiser & Wurm \(2009b\)](#). To interpolate between the two experiments where the degree of erosion has been measured, we assume a mass power-law dependence of

$$\epsilon_{\text{er}} = a \cdot \left(\frac{m_{\text{p}}}{m_0} \right)^k \cdot \frac{\Delta v}{1 \text{ cm s}^{-1}} + b, \quad (2.17)$$

where a , b , and k are fitting parameters. The above two erosion experiments indicate the efficiency of the two different physical effects. In monomer impacts, the projectile hits single surface monomers and sometimes manages to break the bonds between a couple of them in a process resembling the collisions between billiard balls. For larger projectiles, restructuring of the target absorbs a lot of the collision energy, and a crater is formed both because of surface compaction and the breaking of monomer bonds. Direct comparisons and interpolations between the efficiencies of the two effects can not be done without huge uncertainties. A direct interpolation between the two effects yields $a = 1.55 \cdot 10^{-4}$, $b = -0.4$, and $k = 0.14$, but

we present below another way of obtaining a reasonable erosion prescription.

As previously discussed, during a collision, erosion and mass transfer usually occur simultaneously, and the net mass change of the target is given by Eq. 2.13. For $\Delta m_t > 0$, the target experiences net growth, and for $\Delta m_t < 0$, the target experiences net erosion. With this prescription, the transition region is extremely sensitive to the efficiency of the erosion.

In Fig. 2.4, we plot the results of the mass transfer experiments performed by Teiser & Wurm (2009b). We compare this to the threshold between growth and erosion ($\Delta m_t = 0$) obtained from the mass transfer prescription of Eq. 2.14 and the erosion prescription of Eq. 2.17. The threshold derived using the experiment erosion interpolation is given by the white dashed line, and is very pessimistic compared to the mass-transfer experiments.

Since the experimental erosion prescription is obtained from a very different parameter space than we are interested in, it is highly uncertain, and much more so than the mass transfer experiments discussed below. We therefore choose to calibrate the three parameters a , b , and k of Eq. 2.17 using the experimentally obtained threshold between growth of erosion of Teiser & Wurm (2009b). This results in

$$\begin{aligned} a &= 9.3 \cdot 10^{-6} , \\ b &= -0.4 , \\ k &= 0.15 . \end{aligned} \tag{2.18}$$

Comparing the net growth efficiency of this fit marked by the contours in Fig. 2.4 to the mass transfer experiments of Kothe et al. (2010) (with 1 mm projectiles at velocities of 1-6 m s⁻¹) and Wurm et al. (2005) (with 1-10 mm projectiles up to 25 m s⁻¹) results in a rough agreement, even though our model is slightly pessimistic compared to their results, with net efficiencies that are roughly half of theirs. Regardless of this discrepancy, we take this conservative estimate of the experiments and use it for our model.

2.3.4 Fragmentation distribution

During cratering, mass transfer, and destructive fragmentation events, the mass of each fragmented particle is divided into two parts: the power-law distribution and the largest fragment. The fragment power-law was determined experimentally by Blum & Münch (1993), used in the model of Güttler et al. (2010), and is written

$$n(m)dm \propto m^{-\kappa} dm , \tag{2.19}$$

where $n(m)dm$ is the number density of fragments in the mass interval $[m, m + dm]$, and $\kappa = 9/8$.

If the mass of the largest remnant is given by $\mu \cdot m$, where μ is the relative size of the largest remnant described by Eq. 2.9, the total mass that is put into the power-law distribution is equal to $(1 - \mu) \cdot m$. We define the upper

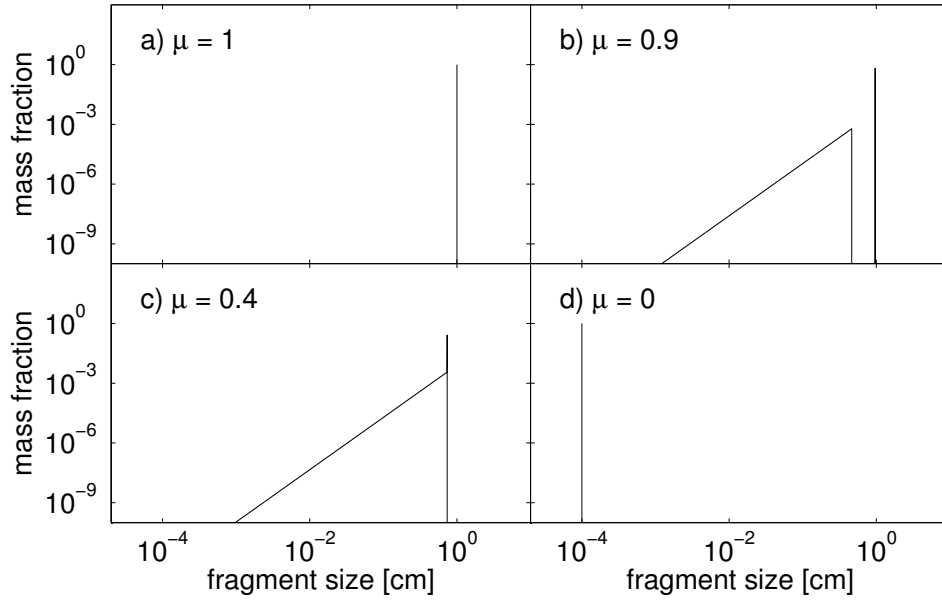


Figure 2.5: The fragment mass distribution for a 1 cm-sized particle after destructive fragmentation events of varying degrees. The largest remnant is equal to in a) $\mu = 1$, b) $\mu = 0.9$, c) $\mu = 0.5$, and d) $\mu = 0$ in units of the original particle mass.

limit to the fragmentation distribution to be $\min[(1 - \mu), \mu] \cdot m$. This means that as long as $\mu < 0.5$, we have a single distribution up to the largest remnant. For $\mu > 0.5$, on the other hand, more than half of the mass is put into the largest remnant, which is then detached from the power-law distribution.

This fragmentation recipe is similar to the four-population model of Geretshauser et al. (2011), with the difference that we treat the fragmentation of both particles individually. It is able to describe all different degrees of fragmentation, and in Fig. 2.5, we present the fragment distribution for four different values of μ . In a), we are at the onset of the fragmentation, and all of the mass is returned to the remnant, leading to no erosion. In b), more than half of the mass is put into the remnant, which is therefore detached from the size distribution, and in c), the erosion is so strong that the remnant becomes part of the power-law distribution. Finally, in d), the particle is completely pulverized, and all of the mass is converted into monomers.

2.3.5 Implementation of the model

We now summarize the conditions and outcome of each individual collision type as they have been implemented into the code. The different types are, in order, sticking, transition from sticking to bouncing, bouncing, mass transfer combined with erosion, and destructive fragmentation, and they are all shown schematically in Fig. 2.2. The conditions for sticking and bouncing are given in Eqs. 2.3 and 2.4, and we use Eq. 2.9 to determine

which, if any, of the particles get fragmented during a collision, resulting in fragmentation with mass transfer or destructive fragmentation.

Sticking: ($\Delta v < \Delta v_{\text{stick}}$)

The two particles stick together and form a bigger particle of size $m_{\text{big}} = m_t + m_p$.

Sticking/bouncing transition: ($\Delta v < \Delta v_{\text{bounce}}$)

Transition from 100% sticking to 100% bouncing. We assume a logarithmic probability distribution between $\Delta v_{\text{stick}} < \Delta v < \Delta v_{\text{bounce}}$ given by

$$p_c = 1 - k_1 \cdot \log_{10}(\Delta v) - k_2 \quad (2.20)$$

where p_c is the coagulation probability. At the sticking threshold (Eq. 2.3), we know that the sticking probability is $p_c = 1$, and at the bouncing threshold (Eq. 2.4), the coagulation probability is $p_c = 0$. The constants are then

$$k_1 = \frac{18/5}{\log_{10}(m_b/m_s)} = 0.40 \quad (2.21)$$

$$k_2 = \frac{\log_{10}(m_p/m_s)}{\log_{10}(m_b/m_s)} \quad (2.22)$$

Bouncing: ($\Delta v > \Delta v_{\text{bounce}}$), ($\mu_p > 1$) and ($\mu_t > 1$), ($\Delta v < v_{\text{er}}$)

If the collision energy is too high to result in a sticking collision but too low to fragment or erode any of the particles, the collision results in a growth-neutral bouncing event. The two masses involved in the collision are left unchanged. This type of collision results in the compaction of both particles, although we ignore any porosity changes in this model.

Mass transfer/erosion: ($\mu_p < 1$) and ($\mu_t > 1$) or ($m_{\text{er}} > 0$)

If the collision velocity is high enough, erosion of the target will occur (Eq. 2.17). Simultaneously, if only the projectile fragments, we have a fragmentation with mass transfer event (Eq. 2.14). The resulting mass change of the target is given by Eq. 2.13.

The fragmented mass from the projectile is divided into two parts, a power-law and the largest remnant, with a total mass of $m = (1 - \epsilon_{\text{ac}})m_p$. The power-law distribution has a total mass of $m_{\text{frag}} = (1 - \epsilon_{\text{ac}})(1 - \mu_p)m_p$ and the largest fragment a mass $m_{\text{rem}} = (1 - \epsilon_{\text{ac}})\mu_p m_p$. The fragments excavated from the target by the cratering are distributed according to a power-law distribution as described in Sect. 2.3.4, with an upper limit equal to m_{er} .

Fragmentation: ($\mu_p < 1$) and ($\mu_t < 1$)

Finally, if the collision velocity is high enough and the mass ratio not too large, we get a destructive fragmentation event where both particles are fragmented. We treat the fragmentation of each particle individually, and get two separate fragment distributions, one for the projectile and one for the target. Each distribution is divided into two parts; the fragmentation power-law distribution with a total mass of $m_{\text{frag}} = (1 - \mu_{p/t})m_{p/t}$ and the largest fragmentation remnant with a mass of $m_{\text{rem}} = \mu_{p/t}m_{p/t}$.

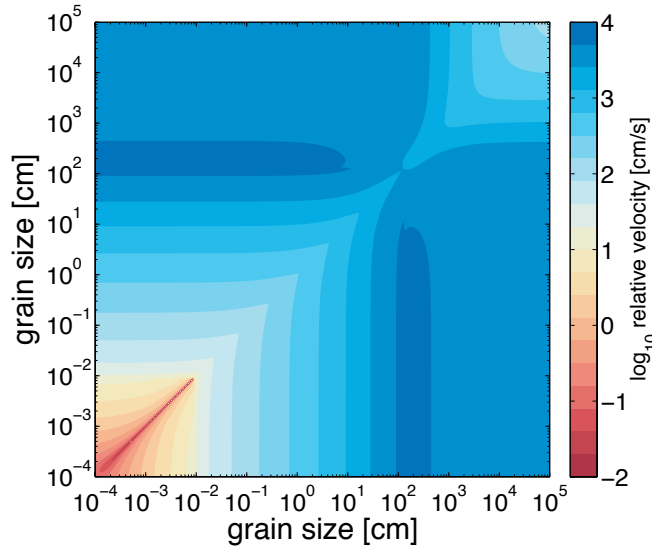


Figure 2.6: The relative velocity field at 3 AU in an MMSN disk, calculated from the velocity sources described in Sect. 1.4.2 and using the parameters given in Table 2.2.

2.4 THE DUST-SIZE EVOLUTION MODEL

With the collision model described in the previous section, it is possible to determine the outcome of the collision between any two particles. In this work, we use the local version of the dust evolution code developed by Birnstiel et al. (2010a), which has been used together with the new collision model to study the dust-size evolution. A summary of the parameters used for the disk model is given in Table 2.2.

We follow the dust-size evolution locally at a distance of 3 AU from the star. To describe the gas distribution over the disk, we use the minimum-mass solar nebula (MMSN) model (Weidenschilling 1977b; Hayashi et al. 1985). This model is based on the current Solar System, where the mass of all the planets is used to predict the minimum total mass that would have been needed to form them. In Eq. 1.8, we gave the expression as

$$\Sigma_g(r) = 1700 \left(\frac{r}{1 \text{ AU}} \right)^{-1.5} [\text{g cm}^{-2}], \quad (2.23)$$

where r is the distance to the central star. At 3 AU, this results in a gas surface density of 330 g cm^{-2} , and if we assume an initial dust-to-gas ratio of 0.01, a dust surface density of 3.3 g cm^{-2} . For the relative velocities, we take into account all the sources described in Sect. 1.4.2, and the total velocity field at 3 AU is shown in Fig. 2.6.

2.5 RESULTS

We performed local simulations of the dust-size evolution using the collision model described in Sect. 2.3 and the evolution code briefly described in Sect. 2.4. In this section, we discuss the outcome of the new collision

Table 2.2: Disk model parameters used in the simulations.

Parameter	Symbol	Value	Unit
distance to star	r	3	AU
gas surface density	Σ_g	330	g cm^{-2}
dust surface density	Σ_d	3.3	g cm^{-2}
gas temperature	T	115	K
turbulence parameter	α	10^{-3}	-
maximum drift velocity	v_n	$3.9 \cdot 10^3$	cm s^{-1}
sound speed	c_s	$6.4 \cdot 10^4$	cm s^{-1}
solid density of dust grains	ζ	1.6	g cm^{-3}

model and compare it to those of previous models. We also show the results of the simulations and compare the growth of the large particles to a simple analytical model.

2.5.1 *The collision outcome space*

With the new collision model, we can determine the outcome of a collision between two particles of arbitrary masses and velocities. In the upper panels of Fig. 2.7, we plot the collision outcome as a function of projectile size and collision velocity for two different mass ratios. This can be compared to the outcome of Güttler et al. (2010) for compact particles shown in the bottom panels. It can here be noted that our model naturally describes the transition between the two extreme cases of equal-sized and differently sized particle collisions, while Güttler et al. defined a critical mass ratio to distinguish between the two regimes. The upper right panel in the figure thus only gives a single snapshot in this transition.

In the left panels, the two particles are of equal size, and the models produce comparable results. In the new model, the sticking region has been enlarged by the inclusion of a transition region where both sticking and bouncing is possible. In the fragmentation region, the mass-dependent fragmentation threshold has decreased the velocity needed to fragment larger particles, and increased the velocity needed for the smallest particles. The net outcome is that the width of the bouncing region has decreased significantly.

In the right panels, the target has a mass that is 1000 times the mass of the projectile. Some important differences can be seen in the fragmentation regime. We can first of all note the new natural transition from growth to erosion that is produced by the balance between growth from fragmentation with mass transfer and erosion from cratering (Eq. 2.13). At this mass ratio, erosion quickly becomes complete fragmentation. When the mass ratio is increased yet further, the fragmentation region decreases and is replaced by erosion.

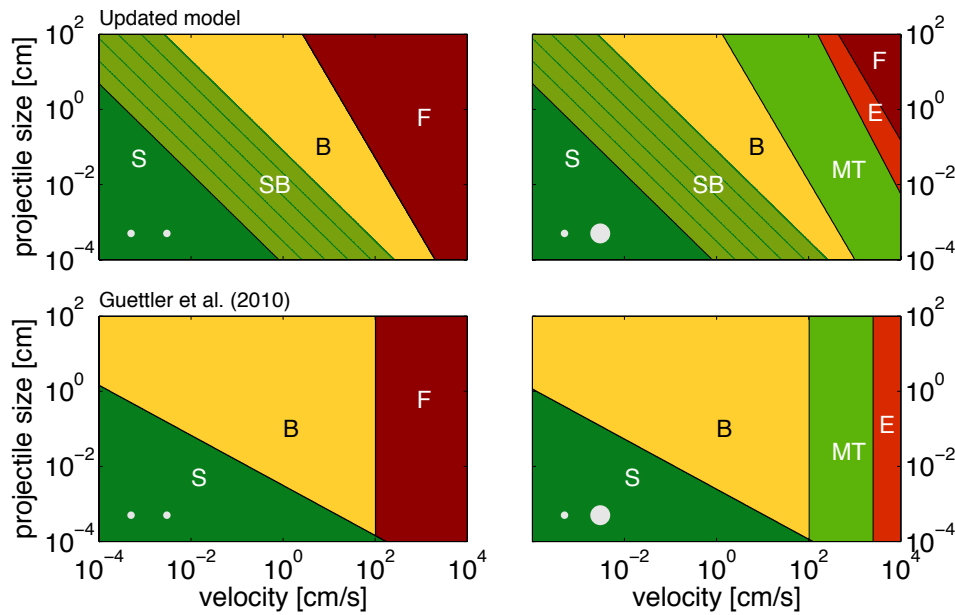


Figure 2.7: Comparison between the new collision model (top) and the model of Güttler et al. (2010) (bottom). The left and right panels show the outcome for equal- and differently sized collisions, respectively. Green regions mark collisions that are growth-positive for the target, yellow marks growth-neutral, and red marks growth-negative. ‘S’ marks sticking, ‘SB’ the sticking to bouncing transition, ‘B’ bouncing, ‘MT’ net mass transfer, ‘E’ net erosion, and ‘F’, fragmentation. In the transition region, the green parallel lines each mark a decrease in sticking probability by 20%.

As long as the projectile is fragmenting, velocities below the erosion threshold always cause to growth, and a cm-sized projectile can initiate mass transfer at velocities as small as about 20 cm s^{-1} (which is exactly the result of Beitz et al. 2011). At $\Delta v = 10 \text{ m s}^{-1}$, projectiles smaller than around 1 cm are required for growth. The maximum projectile size decreases with velocity as the erosion grows stronger, and at $\Delta v = 50 \text{ m s}^{-1}$, growth is only possible for projectiles smaller than $100 \mu\text{m}$.

We predict overall more fragmentation and cratering than in the previous model of Güttler et al. (2010). However, one very important change is that growth via fragmentation with mass transfer is now possible at higher velocities than the 20 m s^{-1} that was the previously predicted threshold, and provided that the projectile is small enough, even a collision at 50 m s^{-1} as predicted in the disk model can lead to growth of the target (which was a direct conclusion of Teiser & Wurm 2009b).

Sticking collisions are also possible at larger sizes, and growth-positive mass transfer works at much lower velocities than the previously assumed 1 m s^{-1} . Even if the bouncing region shrinks in size, we demonstrate below that this is insufficient to remove the bouncing barrier. If we insert a particle above the bouncing barrier, however, the relative velocity required for it to interact beneficially with the particles below the bouncing barrier

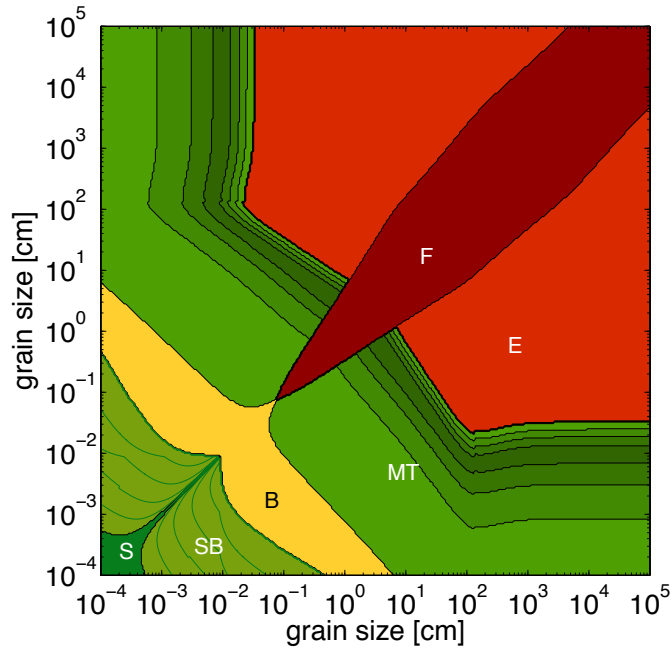


Figure 2.8: The collision outcome for all pairs of particles with the relative velocity field calculated in Fig. 2.6 and with the same labels and color code as in Fig. 2.7. Also included is the net mass transfer efficiency, given in intervals of 4%.

has been decreased. These two results turn out to be quite important, as discussed in more detail in Sect. 2.5.2.

The collision outcome for the new model depends on the mass of both the projectile and the target, and in the current disk model, we use only the average relative velocity between each particle pair. This means that a collision between a given pair in the evolution model always results in the same outcome, and it would therefore be instructive for us to plot the outcome in the particle size-size space. In Fig. 2.8, we have used the relative velocity field calculated in Sect. 2.4 at a distance of 3 AU to determine the outcome for each collision pair.

In this figure, the bouncing barrier is clearly visible. Owing to the too high collision velocities, dust grains of sizes $100 - 800 \mu\text{m}$ that interact with smaller particles will bounce if the particle is not smaller than $10 \mu\text{m}$. In this case, a small number of collisions will lead to sticking, but in order to pass the wide bouncing region, a grain would need to experience 10^9 such sticking collisions. The small particles however themselves coagulate to $100 \mu\text{m}$, making growth through the bouncing barrier very difficult.

Collisions between two equal-sized particles larger than 1 mm will result in destructive fragmentation, but depending on what it collides with, a 1 mm -sized particle can also be involved in sticking, bouncing, mass transfer and erosive collisions. Owing to the fragmentation with mass-transfer effect, a meter-sized boulder can grow in collisions if its collision partner is of the right size, in this case smaller than $200 \mu\text{m}$. As we can see in this plot,

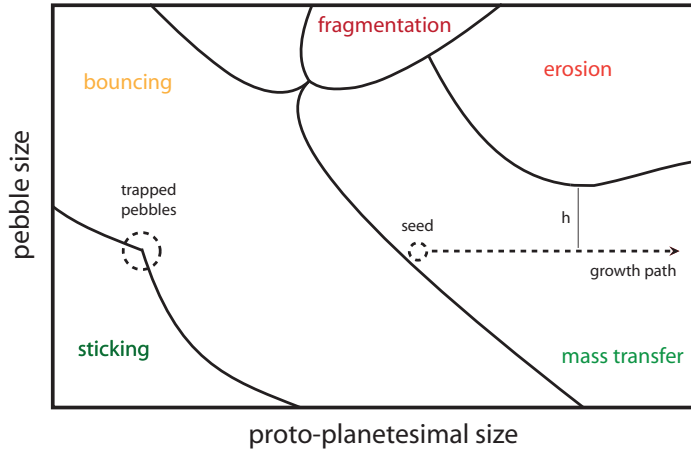


Figure 2.9: A zoomed-in sketch of the collision outcome space shown in Fig. 2.8. The dashed horizontal line shows the interaction path that the seed will experience during its growth. The h parameter illustrates the minimum distance between the interaction path and the erosive region. A positive h means that the boulder/small particle interactions will always be growth-positive, and a negative h means that the growth will at some point be stopped by erosion.

the key to growing large bodies is therefore to sweep up smaller particles faster than they get eroded or fragmented by similar-sized collisions.

From Fig. 2.8, we can already see without performing any simulations that a cm-sized particle would be capable of growing to large sizes if it collides with the right projectiles. The important parameter needed to determine this is illustrated in Fig. 2.9, which contains a sketch of a part of the collision outcome plot. Because of the bouncing region, most of the particles will be found in the region marked in the figure. A boulder needs to interact beneficially with these bouncing particles in order to grow, so the horizontal interaction path needs to at all times be in the growth-positive mass-transfer region. This can be illustrated with the h parameter, which gives the minimum difference between the interaction path and the erosive region. If h is positive, the boulder will always interact beneficially with the bouncing particles, but if h for some reason was to become negative, the growth of the boulder would stop.

We can now highlight the interesting effect that turbulence has on the collision outcome. For particles of sizes between $10 \mu\text{m}$ and 10cm , turbulence is the dominant velocity source. If the relative velocity is higher in this regime, the bouncing barrier will be pushed to smaller sizes. The larger particles are however not as much affected by a stronger turbulence, as these sizes are also affected by both radial and azimuthal drift. This means that the h parameter will remain constant or possibly even increase with stronger turbulence. Strong turbulence might therefore even be beneficial for this mode of growth, as the larger particles will now interact with generally smaller particles, which we from Fig. 2.4 know promotes

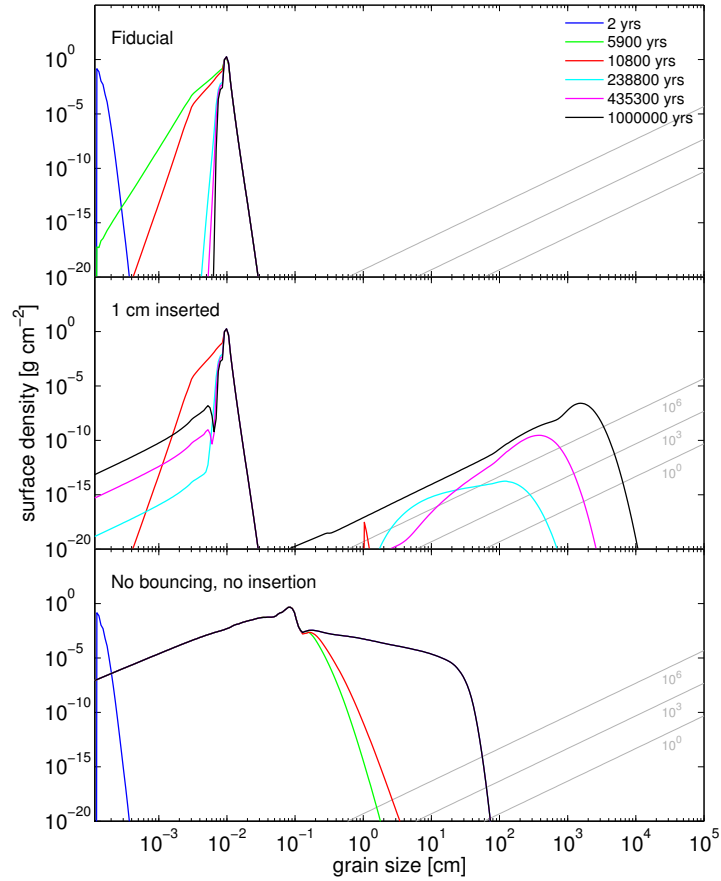


Figure 2.10: The surface density evolution of the dust population for three different simulations at a local simulation at 3 AU. The gray diagonal lines correspond to the required surface densities for a total number of particles of 1, 10^3 and 10^6 in an annulus of thickness 0.1 AU. In the *upper panel*, all particles initially have a size of 10^{-4} cm, and snapshots are taken between 2 and 10^6 years. In the *middle panel*, we have run the same simulation, but after 10,800 years, a small number of 1 cm-particles have artificially been inserted. In the *lower panel*, the bouncing barrier has been replaced with sticking, allowing the particles to freely coagulate to larger sizes.

the mass transfer effect. Because of this, even if the boulders due to strong turbulence have relative velocities of $\sim 100 \text{ m s}^{-1}$, they can grow in interactions with the small particles at the bouncing barrier, as these have correspondingly decreased in size.

2.5.2 The dust-size evolution

We performed simulations using the new collision model together with the local version of the Birnstiel et al. (2010a) continuum dust-size evolution code. In Fig. 2.10, the mass distribution of the particle sizes is given at different timesteps for the three different experiments discussed in detail below.

2.5.2.1 Growth up to the bouncing barrier

In the fiducial case presented in the top panel, the simulations are initiated using all dust made up of μm -sized monomers. At these small sizes, the relative velocity is driven by Brownian motion, and as the particles collide with each other, they stick together and form larger aggregates. This leads to a rapid coagulation phase where the aggregates grow to $100 \mu\text{m}$ in around 1000 years. At this point, the particles have grown large enough to become affected by the turbulence, which quickly increases the relative velocities. As we predicted in Fig. 2.8, the bouncing region is too wide to be surpassed, and the growth halts at the bouncing barrier.

At this stage, the only particles that can grow are the smaller ones, and as time proceeds, more and more particles get trapped at the bouncing barrier. This causes the number of small particles to continue decrease, leading to a continuously narrowing size-distribution. After 10^5 years, virtually all particles can be found to have sizes of $100 \mu\text{m}$, with very steep distribution tails between 60 and $300 \mu\text{m}$. If nothing else is done, this is how the dust evolution ends. The bouncing barrier efficiently prevents any further growth, and all particles remain small.

2.5.2.2 A seeding experiment

To investigate the potential of the mass transfer effect, we performed an experiment where a very small number (i.e. 10^{-18} of the total mass) of 1 cm -particles are artificially inserted as "seeds". As can be seen in Fig. 2.8, the interaction between the 1 cm and $100 \mu\text{m}$ -particles results in mass transfer and growth of the larger particle, and we expect the inserted particles to be able to grow. The seeds are inserted at a single time $t = 10,800$ years, when the particles have reached the semi-stable state at the bouncing barrier, and the result can be seen in the middle panel of Fig. 2.10. Exactly how the seeds are formed will not be discussed in this chapter, but given the small number of seeds required, stochastic effects, small variations in local disk conditions or grain composition and/or properties might suffice to produce them. Some other possibilities are briefly discussed in Sect. 2.5.4.

To better understand the complex interaction between all the particles in this experiment that now follows, we introduce the collision frequency plot given in Fig. 2.11. This shows the collision frequency between each particle pair plotted on top of the collision outcome map of Fig. 2.8, making it possible for any given time to identify the dominating collision type for a given particle size.

The first two snapshots in the collision frequency plot are taken after 2 and 5900 years, and are identical to the fiducial case discussed earlier. At the bouncing barrier, we can see some interaction between the $200 \mu\text{m}$ particles and the smallest particles that do lead to growth, but the frequency is much too small to have any significant effect.

After 10,800 years, the 1 cm seeds are inserted, and they grow to larger boulders by sweeping up the small particles trapped at the bouncing barrier. As the boulders grow, one can after $\sim 200,000$ years see a tail of parti-

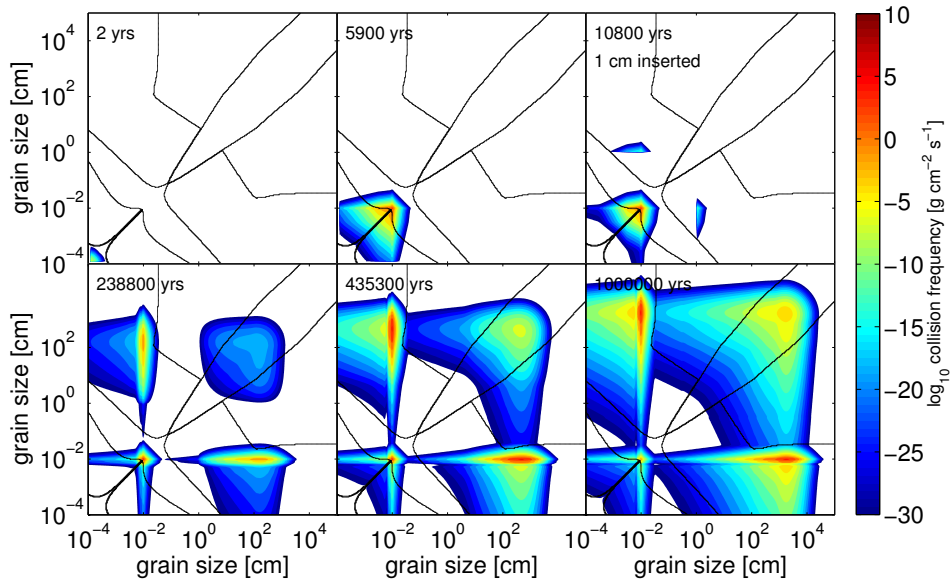


Figure 2.11: The collision frequency map for the scenario where 1 cm-particles are artificially inserted at $t = 10,800$ years. The interaction frequency is plotted for each particle pair at six different timesteps plotted on top of the collision outcome space of Fig. 2.8. This makes it possible to identify the dominating interaction for each particle size. Note the persistently high peak of interactions with particles stuck below the bouncing barrier at 1 mm in size. As the large particles grow, they also sometimes collide among themselves, producing a tail of particles capable of also sweeping up the bouncing particles. This causes an increase in both mass and number for the large particles, and a continuous widening of the size-distribution.

cles with intermediate sizes appear behind them. These are formed by the rare collisions between the large boulders, and from a single event, two large bodies have been multiplied to a myriad of fragments also capable of sweeping up the particles at the bouncing barrier. This effect causes the population of boulders to not only grow in total mass, but also in number, which causes a steady and significant increase in similar-sized fragmentation.

It can also be noted how the vertical distribution of dust around the midplane affects this stage of the evolution. Even if there is a huge amount of particles trapped at the bouncing barrier, they are so small that many of them are pushed out from the midplane due to turbulent mixing. The boulders are however so large that they have decoupled significantly from the gas, and are therefore mostly trapped in the midplane. This causes the sweep-up rate of the mm-sized particles by the boulders to be distinctly lower than without a vertical structure, and also the internal collisions between the boulders to be relatively more common.

The smallest particles that are produced by global fragmentation and erosion mainly experience two different interactions. In the early stages, the smallest fragments are generally being swept up by the 100 μm -sized particles stuck at the bouncing barrier, since these particles dominate com-

pletely both in number and mass. They have therefore never any time to coagulate to larger sizes themselves, but instead aid in the growth of the bouncing particles, which are in turn swept up by the boulders. At later stages, as the boulders become more numerous, it is also possible that the smallest fragments are swept up directly by the boulders. If this growth continues even longer, the two effects become equally efficient, and even later, the boulders will start dominating in the sweep-up. Regardless of what sizes the small fragments interact with, in the end, they are still beneficial for the growth of the boulders.

In the end, a number of 10-70 m boulders have managed to form, and the total amount of mass in the large particles has increased by the huge factor of 10^{12} from what was initially inserted into the system, even though the total boulder mass is still very small compared to the total dust mass. We find that the limiting case for the growth at this point is not so much erosion or fragmentation as it is the growth timescale (see also [Johansen et al. 2008](#)). If the simulation runs for longer than 10^6 years, the boulders can keep on growing and several hundred-meter boulders can form. In other places in the disk with higher dust densities and relative velocities, larger boulders will be able to form on the same timescale.

Growth by sweep-up gives us an explanation of how the collision part of the growth barrier can be circumvented, but we have in these simulations disregarded the effect of the orbital decay from gas drag. The growth timescales in [Fig. 2.10](#) exceed by several orders of magnitude the lifetime of meter-sized bodies subject to radial migration. To survive, the bodies need to either form on a timescale very much shorter than observed in our simulations, which we find unlikely, or some effect needs to exist that prevents the orbital decay over an extended period of time ([Barge & Sommeria 1995](#); [Klahr & Henning 1997](#); [Brauer et al. 2007](#); [Pinilla et al. 2012b](#)).

2.5.2.3 *Removing the bouncing barrier*

To illustrate the importance of the bouncing barrier, we devised an experiment in which all the bouncing collisions are removed and replaced by sticking. There is therefore nothing that prevents the coagulation phase from continuing to larger sizes. The results of this simulation are shown in the lower panel of [Fig. 2.10](#).

The particles can now grow unhindered until they reach about 1 mm in size. At this point, they begin to fragment among themselves, as we can see in [Fig. 2.8](#). Since most of the dust can be found at this size, heavy fragmentation occurs, and a cascade of smaller particles are produced. These small particles again grow up to larger sizes, where most of them again fragment. From the collision outcome plot, we can however see that some particles can be lucky, and instead sweep up only smaller particles via mass transfer. They therefore avoid fragmentation, and keep on growing, and form the distribution tail extending from 1 mm and upwards.

At a size of roughly 1 meter, the only way to grow is by colliding with $100 \mu\text{m}$ or smaller particles. However, in the absence of a bouncing barrier,

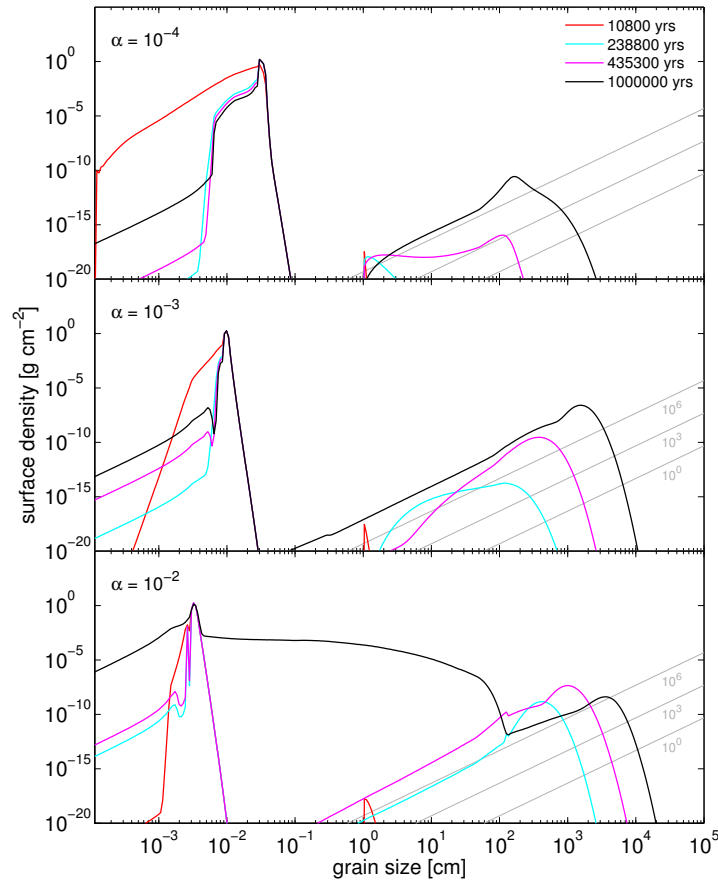


Figure 2.12: The surface density evolution of the dust population for three different turbulence strengths ($\alpha = 10^{-4}, 10^{-3}, 10^{-2}$) at 3 AU, with seeds inserted artificially after $t = 10,800$ years.

most of the mass is found instead in 1 mm particles. This means that almost all of the interactions become erosive, and the growth halts.

In the above example, we saw that increasing the stickiness of particles in the end actually *prevented* the growth of large boulders. From this result, we can draw the conclusion that the bouncing barrier might even be beneficial for the formation of planetesimals. By hindering the growth of most particles, growth might be possible for the lucky few.

2.5.2.4 The effect of turbulence

We have so far studied only one single turbulence parameter of $\alpha = 10^{-3}$. This value is however uncertain for nebular models, and to investigate the dust evolution in different velocity fields, we also study the cases of $\alpha = 10^{-4}$ and $\alpha = 10^{-2}$. The latter represents a strong turbulence that completely dominates over the azimuthal and radial drifts and results in relative velocities up to 100 m s^{-1} . In the former case, the turbulence is weak, and contributes very little to the velocities of the larger particles. In Fig. 2.12, we plot the resulting size evolutions for the three turbulence parameters but otherwise identical initial conditions. The middle panel is here the same as the middle panel of Fig. 2.10 and is included for reference.

It can first of all be noted that growth to larger sizes is possible even in the case of very high turbulence, as we predicted using Fig. 2.9. This is due to the decrease in size of the bouncing particles as the turbulence increases. The smaller impacting projectiles can therefore cause the boulder to grow also at higher velocities, as seen in Fig. 2.4.

The growth timescale is affected by the turbulence in several different ways. Firstly, it increases the relative velocities between the particles, leading to higher collision frequencies and therefore to more rapid growth. Higher impact velocities also lead to a higher net mass transfer efficiency, which in Fig. 2.4 is seen to be particularly low for velocities below 10 m s^{-1} . A higher turbulence also mixes small particles further away from the midplane, which decreases their midplane densities where the largest boulders gather, lowering the growth rate. From Fig. 2.12, it is clear that the growth-positive effects predominate, leading to enhanced growth at higher turbulence. In the low turbulence case, the growth is especially slow for particles of sizes between 1 cm and 100 cm. In this regime, the relative velocities are very low since the contributions from the azimuthal and radial drift are small, causing very low net mass accretion efficiencies during the sweep-up growth.

In the $\alpha = 10^{-2}$ case, we can see in the final snapshot that a separate peak has appeared for the largest boulders. This peak occurs when the boulders have fragmented so much between themselves that the large intermediate-sized fragments are at number densities roughly equal to the boulders, which in this case happens after $\sim 600,000$ years. At this point, the boulders are significantly eroded and fragmented, which creates even more intermediate-sized particles capable of yet more fragmentation. This results in a fragmentation cascade, and a rapid flattening of the size-distribution. This does not however cause all the large particle to be destroyed, and those that survive can continue to grow by sweeping up the small bouncing particles that still dominate both in terms of number and total mass. This effect also occurs for the cases of weaker turbulence if the simulations run long enough, but is never severe enough to cause a complete halt of the growth.

We have demonstrated that growth can also proceed in regions of high turbulence. An MRI turbulent disk might however also create an additional velocity source, where local gas density fluctuations can excite the orbital eccentricities of the planetesimals. [Ida et al. \(2008\)](#) found that this can lead to velocities beyond break-up even for small planetesimals, although they studied only collisions between equal-sized bodies. In our model where only the material strength of the body is included, a collision between two large and similarly sized bodies will be destructive even in regions of very low turbulence, such that in this regime, it has little effect on our conclusions. Excited planetesimal orbits however also increase the impact velocities of the small particles, which could pose a problem. In previous cases, growth had been possible in regions of high turbulence because the sizes of the bouncing particles were simultaneously suppressed by the turbulence, but this is not necessarily the case in the scenario stud-

ied by Ida et al. This might cause greater erosion of the growing planetesimals, but investigating this further is beyond the scope of this chapter.

2.5.3 A growth toy-model

The concept of sweep-up growth has also been studied previously by Xie et al. (2010), in what they called snowball growth. Their approach was to disregard most of the collision physics and first stages of sweep-up, and they developed a more idealized, bidisperse model, in which one population of artificially inserted km-sized planetesimals grows by sweeping up the smaller population. They also identified the potential for these planetesimals to grow to as large as 100 km before the destructive collisions between the planetesimals themselves starts to limit the growth.

To verify our results from the simulations, we here consider a somewhat simplified version of the work of Xie et al. (2010) and Johansen et al. (2008). We assume a bidisperse scenario where a single lucky seed of mass m grows in a sea of smaller particles of mass m_s . We are here only interested in the growth rate of the seeds, and assume that the seeds are always few enough so that the collisions between themselves can be neglected. The growth of the large body can then be described by

$$\frac{dm}{dt} = \sigma \Delta v \cdot \epsilon_{\text{net}} n_s m_s, \quad (2.24)$$

where $\sigma = \pi (a_s + a)^2 \sim \pi a^2$ is the collisional cross-section, Δv the relative velocity, n_s the number density of the small particles, and ϵ_{net} the average net mass-gain efficiency of a collision. The change in size a with respect to mass can be written as $dm = 4\pi\zeta a^2 da$, where $\zeta = 1.6 \text{ g cm}^{-3}$ is the internal density of the large body. We can now write

$$\frac{da}{dt} = \frac{1}{4} \frac{\rho_s}{\zeta} \epsilon_{\text{net}} \Delta v, \quad (2.25)$$

where $\rho_s = n_s m_s$ is the mass density of the small particles. As a first assumption, we assume that the relative velocity is only caused by turbulence, and for small particles can therefore be estimated by (Weidenschilling & Cuzzi 1993; Cuzzi et al. 2001)

$$\Delta v = \sqrt{3\alpha \text{St}} \cdot c_s, \quad (2.26)$$

where $\alpha = 10^{-3}$ is the turbulence parameter, St is the Stokes number of the seed, and c_s the sound speed in the gas given by

$$c_s = \sqrt{\frac{k_b T}{\mu m_p}}, \quad (2.27)$$

where k_b is Boltzmann's constant, T is the temperature of the gas, $\mu = 2.3$ is the mean molecular weight, and m_p the proton mass. We assume ρ_s to be constant and unaffected by the sweeping-up of the large boulder, and

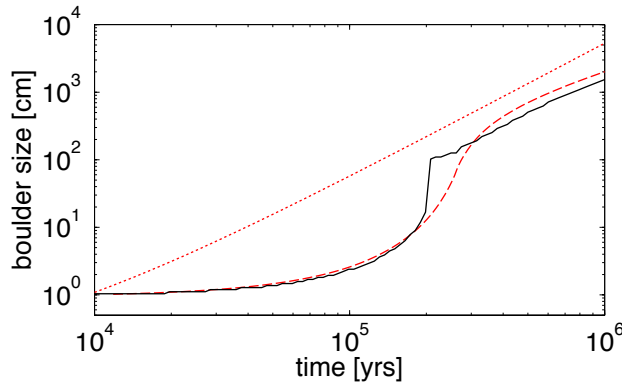


Figure 2.13: The growth of a boulder in the simulations (black) compared to two growth estimates (red). The dotted line corresponds to the simple estimate with a crude turbulent relative velocity expression and a constant mass accretion efficiency, and the dashed line also considers the exact velocity and accretion efficiency terms as those used in the simulations.

that the vast majority of the dust mass is found in the small bodies (which is clearly always the case in Fig. 2.10).

When the seed has grown large, it is very little affected by the vertical mixing due to the turbulence, and is mostly found near the midplane. It is clear that the differential settling between the seed and the small particles is important here, as the seed can only interact with the small subset of all the particles that can be found around the midplane. To calculate the midplane density of the small particles, ρ_s , we can therefore use Eq. 1.35. Under these assumptions, Eq. 2.25 can be solved analytically:

$$a(t) = \left(\frac{1}{8} \epsilon_{\text{net}} \frac{\rho_s}{\xi} \sqrt{\frac{3}{2} \frac{\xi}{\Sigma_g} \pi \alpha \cdot c_s (t - t_0) + \sqrt{a_0}} \right)^2. \quad (2.28)$$

As a first comparison, we solve the seed size evolution above and compare it to the growth rate of the large particle peak in the middle panel of Fig. 2.10. The result is given in Fig. 2.13, assuming a constant $\epsilon_{\text{net}} = 0.1$, and we can note that although the final size corresponds roughly to that of the simulations, it is clear that a lot of physics is missing. This is mainly due to two reasons. Assuming a constant accretion efficiency reflects badly the situation where the real efficiency ranges between 0 – 0.15, and the simple relative velocity prescription of Eq. 2.26 only takes into account the turbulence, and is also not valid for large particles.

We therefore make a slightly more advanced model, in which we take into account both the full accretion efficiency from Eq. 2.13, and all four velocity sources discussed in Sect. 2.4. Eq. 2.25 is then solved numerically, and the resulting solution given in Fig. 2.13 is now clearly able to track the complicated evolution process from the simulations.

We can now use the understanding we gained from the exercise to investigate the capabilities of the sweep-up growth. We will here investigate the effect of three different factors on the seed growth; the density of the

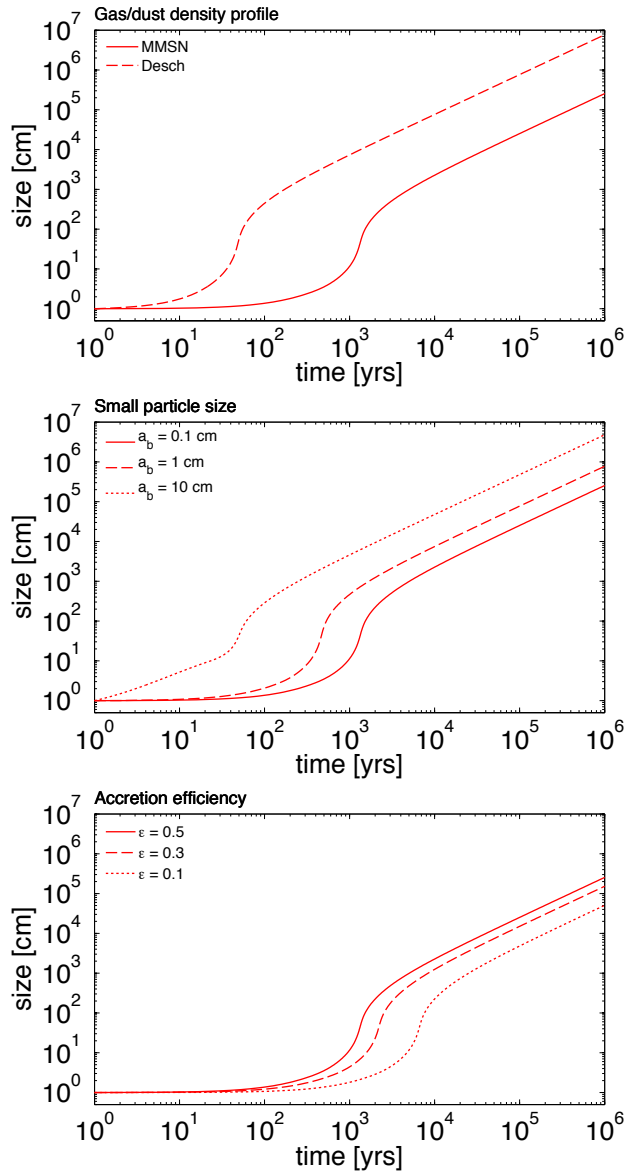


Figure 2.14: The seed size evolution for variations in three different parameters. The solid line marks the default parameters which take an MMSN disk at 1 AU, with $\alpha = 10^{-4}$, an accretion efficiency $\epsilon = 0.5$, and a small particle size = 0.1 cm.

midplane gas and dust, which is determined by both the radial density profiles, as well as the size of the small particle population, and we also study the effect of the accretion efficiency. Because the collision model that we have developed in this work is highly complicated and not very transparent, we instead assume a constant accretion efficiency. The results and parameters used are given in Fig. 2.14, and they are discussed separately below.

In the simulations, we assumed an MMSN disk, which is by its definition the very minimum mass needed to describe the present-day Solar System. As such, it is likely to be a poor description of the initial disk conditions at the onset of the planetesimal formation. [Desch \(2007\)](#) took

some of the late-stage evolution processes into account by considering the planet formation from an initial planetesimal distribution and including planet migration, and found a radial distribution that we described in Eq. 1.9. Even though the predicted densities are significantly higher, it still neglects the mass loss and redistribution in the planetesimal formation stage, and the initial densities are likely to have been even higher. The increase in solid density leads to significantly higher collision rates and faster growth.

Also related to the solid density is the size of the small particle population. As we alluded to in Sect. 2.5.2.4, the settling of the small particle population also plays a vital role. The larger and more decoupled these particles are, the more they settle towards the midplane, which increases the collision rates with the seeds. As we can see, this can have a big effect. However, if the particles (in this case) are smaller than 0.1 cm, their size does not matter, as they will all follow the gas scale-height.

Finally, we also investigate the effect of the accretion efficiency, which will obviously also affect the growth rate. We can however note that even though the accretion efficiency is poorly constrained from the laboratory, it will at most change less than an order of magnitude, which has less impact than a change in for example the radial density profile.

Finally, we note that this growth toy model is obviously a simplification that does not take into account the destructive similar-sized impacts, but it does show the potential for sweep-up to form planetesimals at relevant timescales. In the innermost disk, we find that 10-km-sized planetesimals are capable of forming in 10^5 years or less.

2.5.4 *Forming the first seeds*

As previously discussed, the existence of a bouncing barrier might be beneficial for the planetesimal formation, as it prevents too many large bodies from forming, keeping the lucky ones that do form from fragmenting and eroding among themselves. It is however necessary for at least some cm-sized seeds to form and initiate the sweep-up process. In this chapter, we have not investigated in detail how this might happen, but there are many possibilities, of which a few will be investigated in detail in later chapters.

Firstly, it is possible for some lucky particles to grow through the bouncing barrier simply by interacting with a sufficient number of smaller particles, as can be seen in the collision outcome plot in Fig. 2.8. For this to happen, however, it is necessary to have a wide enough size-distribution for there to be enough small particles for the lucky particles to interact with. This, it turns out, is difficult, as we have in these simulations found that the particle size-distribution will quickly narrow as all the small dust coagulate up to the bouncing barrier. If extra mass is continuously introduced into the system during the first 10,000 years or so, for example by the nebular infall of the collapsing protostellar cloud, the particle size-distribution could be wide enough for some seeds to be formed.

A possibility which is related to the above is the introduction of a velocity distribution for each particle-size, which was first introduced by [Okuzumi \(2009\)](#) as a mechanism to break through the charge barrier. Most studies of the dust-size evolution have however considered only the average relative velocity between two particles, but in reality, some particles will also collide at both much higher and lower velocities. If some particles are lucky enough to only collide with others at low velocities, they might stick together when they would otherwise only bounce, and then grow large enough to initiate sweep-up. This is the main focus of [Chapter 3](#), and the method is further developed in [Chapter 4](#).

[Beitz et al. \(2012\)](#) also found in laboratory experiments that chondrules and dust aggregates tend to stick at higher velocities than collisions between two dust aggregates, so that early chondrules could grow where dust could not. Similarly, calcium- and aluminium-rich inclusions (CAIs) are cm-sized particles that are believed to have been formed early near the Sun and transported outwards within the disk ([Ciesla 2009](#)), proving that at least some particles managed to grow this large. These could constitute the first generation of seeds.

Finally, larger particles may form outside the snow-line mixed with ices, or inside a quiescent dead zone, and drift inwards to a region where sweep-up becomes possible. This is the fundamental idea that we investigate in [Chapter 5](#).

2.6 DISCUSSION AND CONCLUSIONS

To explore the possibility of growth of dust particles into planetesimal sizes by collisions, we have implemented a new collision model that is motivated both physically and experimentally. It has been streamlined to work with continuum codes, while still being able to take into account all important collision types identified in previous work. In combination with continuum dust evolution codes, all dust grains can be resolved independently of their numbers, something that we have found essential for the study of growth of dust grains to greater than cm-sizes.

Even though collisions between large similarly sized dust grains generally lead to fragmentation, this is not necessarily true for larger mass ratios if the projectile is small enough. As shown in laboratory experiments, if the projectile is smaller than 0.1-1 mm in size, fragmentation with mass transfer can cause growth of the target for impact velocities as high as 60 m s^{-1} . For dust grains to grow larger than cm-sizes via collisions, the number of large particles has therefore to be very small to avoid destructive fragmentation among themselves, and most of the dust mass remains at small sizes.

In our simulations, we have found that direct growth of planetesimals via dust collisions is a strong possibility. In addition, the bouncing barrier introduced by [Zsom et al. \(2010\)](#) might be beneficial or even vital for the planetesimal formation, as it provides a natural way of ensuring that most of the dust population remains small. These small dust particles are ideal

for the sweep-up process if larger bodies manage to form. By artificially inserting a few 1 cm-sized seeds into our simulations, we have discovered that they can sweep up the small dust via fragmentation with mass transfer and grow to ~ 100 meters in size on a timescale of 1 Myr. This leads to exciting new possibilities that need to be taken into account when studying dust growth in protoplanetary disks.

An interesting aspect of the sweep-up scenario is its capability to produce planetesimals while simultaneously retaining a significant amount of sub-mm dust grains in the disk. These small grains are necessary to explain the high dust opacities at mm-wavelengths observed around T Tauri stars even after several Myrs (Birnstiel et al. 2010b; Ricci et al. 2010a; Pérez et al. 2012). Without any growth barriers, or if the planetesimals form too fast, the population of small grains are likely to get depleted quickly. In this scenario, however, the planetesimal growth could proceed unseen for at least 0.1 – 1 Myrs before they are numerous enough to affect the the small dust. Sweep-up growth could also be an explanation to the structure of the chondrites (Cuzzi et al. 2010). As most of the chondrules are mm-sized or smaller, they would correspond well to the population of small grains that are being accreted by the growing planetesimals in the sweep-up scenario. Because of the uncertainties involved in the formation of chondrules, however, this remains speculative (Connolly et al. 2006).

The growth rate observed in the simulations is relatively slow, mainly due to a low mass transfer-efficiency, the high turbulence that kicks the small particles away from the midplane where the boulders are concentrated, and the low dust densities even at radii as small as 3 AU. This means that it might be necessary to form planetesimals in regions with enhanced densities such as in pressure bumps, or sufficiently close to the star, where it can be accelerated, and also that there is a need for the radial drift to be prevented over long timescales. We have however found that this growth mechanism has the potential to be a lot faster, and that 10-km-sized bodies can form in 10^5 years. This is in rough agreement with the results of Xie et al. (2010), who on the other hand started with initial planetesimal sizes of 1 km.

A benefit of this mode of growth is its capability to function in regions of high turbulence with relative velocities reaching 100 m s^{-1} . This is because the turbulence affects not only the size at which projectiles start to erode larger particles, but also simultaneously the size of the particles at the bouncing barrier. Another important effect we have found is that a very small number of seeds are necessary to initiate sweep-up. As the large particles collide with each other, they will create a number of intermediate-sized particles that are also able to sweep-up the small particles, causing the population of large particles to increase not only in total mass, but also number.

Exactly how these seeds would be introduced into the system is something that is discussed in great detail throughout Chapters 3-5. We have shown that thanks to a combination of more efficient sticking found in recent laboratory experiments and our ability to numerically resolve very

small numbers of particles, the bouncing barrier can be either overcome or circumvented. If the dust size-distribution is wide enough, a small number of lucky particles might grow over the barrier via hit-and-stick collisions with much smaller particles. This shows that the initial conditions of planet formation might be very important to how the dust growth proceeds.

Our present study has helped to illustrate where the focus of future laboratory experiments should lie. It is clear that for collisional growth of larger particles to be possible, it has to occur between particles of very different sizes. However, very few experiments have been performed to quantify the amount of erosion or mass transfer that occurs for various projectile sizes, porosities, velocities, and impact angles, and the understanding of the physical process remains unclear. The maximum size a projectile can reach while aiding the growth of the target by mass transfer determines whether the small bouncing particles cause erosion or growth of the large boulders. It is also necessary in the lab to determine the smallest projectile size that still leads to growth. Laboratory experiments show that monomer impacts lead to erosion, but whether erosion still occurs at 10 or 100 μm is unknown. To determine in which parameter space fragmentation with mass transfer occurs, more experiments need to be performed.

With an implicit scheme, this code runs fast in terms of execution time, and should be suitable for global disk simulations. This is something that we explore further in Chapter 6, where we consider both the growth and drift in the inner few AU of the protoplanetary disk, and find that sweep-up growth is capable of breaking through not only fragmentation barrier, but also the drift barrier. Generally, it will also be possible to investigate how this more sophisticated collision model affects the dust sizes further out in the disk at 50-100 AU where comparison with observations is possible.

VELOCITY DISTRIBUTION EFFECTS ON THE GROWTH BARRIERS

Adapted from Windmark, Birnstiel, Ormel, A&A (2012), vol 544, L16¹

ABSTRACT

It is unknown how far dust growth can proceed by coagulation. Bouncing and fragmenting collisions make up a collective collisional barrier that prevents further growth. However, in almost all previous dust-size evolution studies, only the mean collision velocity has been considered, neglecting that a significant fraction of the collisions will occur at both much lower and higher velocities. In this chapter, we study the effect of the probability distribution of impact velocities on the collisional dust growth barriers. We assume a Maxwellian velocity distribution for colliding particles to determine the fraction of sticking, bouncing, and fragmentation, and implement this into a dust-size evolution code. We also calculate the probability of growing through the barriers and the growth timescale in these regimes. The result is that the collisional growth barriers are not as sharp as previously thought. With the existence of low-velocity collisions, a small but important fraction of the particles manage to grow to masses orders of magnitudes above the main population. A particle velocity distribution softens the fragmentation barrier and removes the bouncing barrier. It broadens the size distribution in a natural way, allowing the largest particles to become the first seeds that initiate sweep-up growth towards planetesimal sizes.

3.1 INTRODUCTION

As particles in protoplanetary disks grow by coagulation, they decouple more and more from the surrounding gas, which increases their relative velocities. At the fragmentation barrier, collision energies are high enough to cause particle destruction, halting the dust growth at centimeter to meter sizes (Brauer et al. 2008). Zsom et al. (2010) also introduced the bouncing barrier, which stops the growth at even smaller sizes. In this case, the collision energies are too low to cause any particle destruction, but also too high for sticking, with growth-neutral bouncing events as the result.

In the previous chapter, we suggested a sweep-up scenario where the fragmentation barrier can be circumvented. We found that even though collisions between equal-sized particles generally lead to fragmentation, if the mass-ratio is large enough, growth of the larger particle can occur even

¹ See page ix for details on authorship.

at very high velocities. In this scenario, the growth initially stalls at the bouncing barrier, but if a small number of slightly larger "seed" particles are introduced, they rapidly sweep up the smaller particles and grow to very large sizes. The growth barriers in this case limit the number of large particles and therefore reduce the number of destructive collisions among them. Exactly how the first seeds are formed is however still not clear.

All prior dust coagulation models have until now relied on the mean value to describe the velocity at which a collision occurs. In reality, the relative velocities between the particles that arises because of Brownian motion and turbulence does not take a single value, but is better represented by a probability distribution, owing to geometrical and stochastic effects. Here, we focus on turbulence since it is the dominating source of relative velocity between the small grains below the fragmentation barrier. There are relative velocity sources that can be described as deterministic, e.g. radial and azimuthal drift, but these are of little importance at the point of the collisional barriers (see Sect. 3.A for more details).

A general formula for the probability distribution function (PDF) of particle relative velocities is however unavailable, despite the efforts of many numerical and experimental works. There is tentative evidence that the PDF for particles with large Stokes numbers ($St \sim 1$, those that couple to the driving scales of the turbulence) is Maxwellian or close to it (Carballido et al. 2010; Dittrich et al. 2013). However, at smaller sizes (where particles couple to the Kolmogorov scale) the PDF may be better characterized by wide, exponential tails (Wang et al. 2000; Pan & Padoan 2010; Hubbard 2012). Future numerical and analytical modeling is desired to refine and interpret these data. In this work, as a first step, we assume that turbulent velocities are Maxwellian distributed.

A velocity distribution allows some collisions to result in sticking where the average outcome would produce a bouncing or fragmentation event. This causes the barriers to blur out, and might allow for some lucky particles to just by sheer chance repeatedly experience only low-velocity collisions and grow to larger sizes than the main population.

In this chapter, we show the effect of such a velocity distribution in a local dust-size evolution code, not only as a method for creating lucky larger particles, but also to see how it affects the general dust population. In Sect. 3.2, we describe the collision model and velocity distribution implementation, and in Sects 3.3 and 3.4, we discuss the simulation results.

3.2 METHOD

We implement a Maxwellian velocity distribution together with three simple collisions models into a local version of the dust-size evolution code of Birnstiel et al. (2010a). We consider relative velocities arising only from Brownian motion and turbulence, which are the dominant sources for small or similar-sized particles, and for the disk properties, we take the minimum mass solar nebula (Weidenschilling 1977b). We refer to Table 3.1 for all the parameters used in this work.

Table 3.1: Disk model parameters used in the local simulations.

Parameter	Symbol	Value	Unit
Distance to star	r	1	AU
Gas surface density	Σ_g	1700	g cm^{-2}
Dust surface density	Σ_d	17	g cm^{-2}
Gas temperature	T	280	K
Sound speed	c_s	$1.0 \cdot 10^5$	cm s^{-1}
Turbulence parameter	α	10^{-4}	-
Solid density of dust grains	ζ	1	g cm^{-3}

3.2.1 Collision models

In this work, we take simplified versions of the collision model developed in the previous chapter. We present three different models, where the possible outcome of a collision is one of the three collision types of sticking, fragmentation, and bouncing, so that $p_s + p_f + p_b = 1$, where p is the probability of each collision outcome. In the first model, SF (sticking + fragmentation), we study the effect on the fragmentation barrier, in the second, SBF (sticking + bouncing + fragmentation), we study the bouncing barrier, and in the third, SBF+MT (sticking + bouncing + fragmentation + mass transfer), we show a scenario where growth breakthrough occurs.

For the fragmentation, we assume that destruction of both particles always occurs above a given collision velocity

$$p_f = \begin{cases} 0 & \text{if } \Delta v < v_f \\ 1 & \text{if } \Delta v > v_f, \end{cases} \quad (3.1)$$

where we take $v_f = 100$ cm/s as the fragmentation threshold velocity as found by [Blum & Münch \(1993\)](#). The fragments are put in a size-distribution described by $n(m)dm \propto m^{-1.83} dm$.

With bouncing included (where both particles involved are kept unchanged), the sticking efficiency is written as

$$p_s = \begin{cases} 1 & \text{if } \Delta v < v_b \\ 0 & \text{if } \Delta v > v_b, \end{cases} \quad (3.2)$$

where we take a bouncing threshold velocity $v_b = 5$ cm/s, which is the upper limit to the bouncing threshold velocity found by [Weidling et al. \(2012\)](#).

In the collision model SF, we only include sticking and fragmentation, and take $p_s = 1 - p_f$. In the collision model SBF, we account for all three effects, and write the bouncing probability as $p_b = 1 - p_s - p_f$.

Finally, in the collision model SBF+MT, we include a simple prescription for the mass transfer events discussed in detail in Chapter 2. These occur when the particle mass ratio is so high that the largest particle can avoid

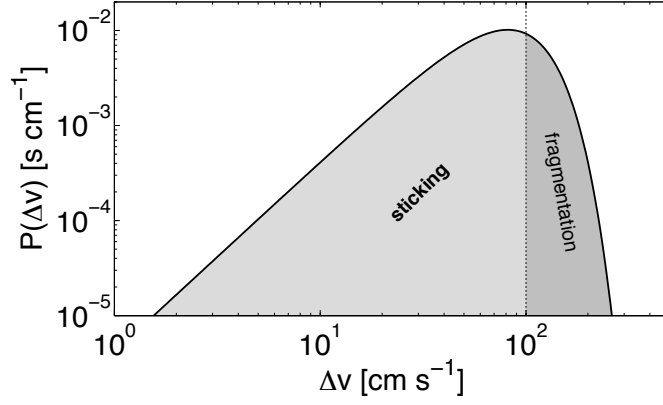


Figure 3.1: Example of the Maxwellian velocity probability distribution for $\Delta v_{\text{rms}} = 100 \text{ cm s}^{-1}$. The differently shaded areas show the resulting outcome for collision model SF.

destruction, and only the smaller particle is fragmented with a fraction of its mass being added to the surface of the larger. To mimic this effect, we assume that all fragmenting collisions above a critical mass ratio $m_1/m_2 > 30$ result instead in sticking where 10% of the mass of the smaller particle is deposited onto the larger one. This is an arbitrary threshold which is poorly constrained by laboratory experiments, and it might be lower or much higher.

3.2.2 The velocity distribution

The collision rate between two particle species i and j for a certain collision outcome is classically calculated from

$$f_{ij} = n_i n_j K_{ij}, \quad (3.3)$$

where n is the number density and K_{ij} is called the kernel, given by

$$K_{ij}(\Delta v_{\text{rms}}) = \sigma_{ij} \Delta v_{\text{rms}} P_{s/b/f}(\Delta v_{\text{rms}}), \quad (3.4)$$

However, if a velocity probability distribution, $P(\Delta v | \Delta v_{\text{rms}})$, is included, the low-velocity collisions are going to collide at different rates than the high-velocity collisions, and the kernel needs to be calculated by integrating over the whole Δv -space:

$$\hat{K}_{ij}(\Delta v_{\text{rms}}) = \sigma_{ij} \int_0^\infty \Delta v P_v(\Delta v | \Delta v_{\text{rms}}) P_{s/b/f}(\Delta v) d\Delta v. \quad (3.5)$$

In this work, we assume that the particles follow a Maxwellian velocity distribution, which when characterized by the root-mean-square velocity Δv_{rms} has the form

$$P(\Delta v | \Delta v_{\text{rms}}) = \sqrt{\frac{54}{\pi}} \frac{\Delta v^2}{\Delta v_{\text{rms}}^3} \exp\left(-\frac{3}{2} \frac{\Delta v^2}{\Delta v_{\text{rms}}^2}\right). \quad (3.6)$$

An example of the velocity PDF is given in Fig. 3.1. We can note that even though the rms-velocity leads to fragmentation, a significant number of collisions will still lead to sticking.

For the turbulent relative velocity, we use the full closed-form expressions derived by Ormel & Cuzzi (2007), which for small particles ($St < 1$, here corresponding to $m \lesssim 10^6$ g) can be approximately written as $\Delta v_{\text{rms}} = \sqrt{2\alpha \cdot St} c_s$, where St is the Stokes number and the rest of the parameters are given in Table. 3.1.

In the simulations, the kernel is calculated using Eq. 3.5, but in the analysis section of this work, we make one approximation. In the full picture, it is clear that the low-velocity sticking collisions will be weighted less than the high-velocity fragmenting collisions when determining the total collision rate for sticking and fragmentation (see Chapter 4 for a more detailed analysis along this line). However, because the Maxwellian velocity PDF is relatively narrow in velocity space, we can approximate the collision rate between the (dominating) sticking collisions and the fragmenting collisions to be equal. As we can see in Fig. 3.1, this is roughly true, as the PDF drops roughly an order of magnitude even a factor 2 away from the mean velocity. Because of this, we can for any collision approximate the total sticking and fragmentation probabilities as

$$\langle p_s \rangle(\Delta v_{\text{rms}}) \approx \int_0^{v_b} P(v) d\Delta v \quad (3.7)$$

$$\langle p_f \rangle(\Delta v_{\text{rms}}) \approx \int_{v_f}^{\infty} P(v) d\Delta v. \quad (3.8)$$

In Fig. 3.2, we plot for the three collision models the integrated sticking, bouncing, and fragmentation probabilities as a function of particle mass, calculated from the underlying rms-velocity from Brownian motion and turbulence. In the SF model, fragmentation occurs much earlier if a velocity distribution is included, but sticking is also a possibility at much higher masses. In the SBF model, sticking is a possible outcome even orders of magnitude above the bouncing threshold, but decreases to very low probabilities. At a mass of $m = 1$ g, the sticking probability is 10^{-3} , but fragmentation is also rare, so that the relative ratio of the two is of the same order of magnitude. This means that growth can still proceed, albeit on longer timescales. Finally, in the SBF+MT model, the situation is identical to the SBF panel, except that the added effect of mass transfer means that collisions above the fragmentation threshold can still lead to growth, provided that the mass ratio between the particles is large enough.

3.3 RESULTS

In Fig. 3.3, the dust size distributions of the simulations with a resolution of 17 bins per mass decade (see Sect. 3.B for a resolution study) are given at $t = 5 \cdot 10^4$ years for the three collision models, with and without a velocity distribution. The different cases are discussed individually below.

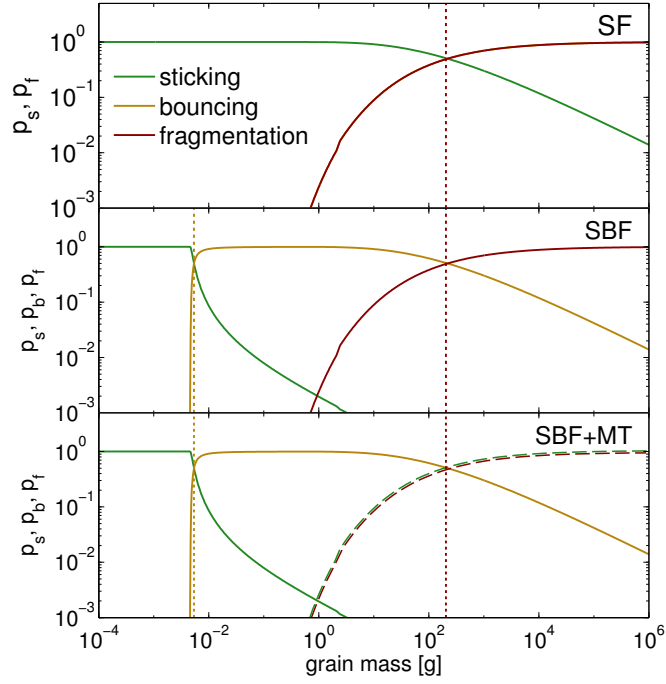


Figure 3.2: The probabilities of sticking (green), bouncing (yellow), and fragmentation (red) for the three collision models as a function of mass. The red-green dashed line in the SBF+MT panel represents mass transfer, where fragmentation can turn into mass gain for large mass ratios. The dotted lines represent the threshold masses without a velocity distribution included.

3.3.1 The fragmentation barrier

In the SF model, dust growth stops in both cases. When there is no velocity distribution, this point occurs abruptly, with no way of growing larger particles, after they have reached a size corresponding to $v_{\text{rms}} = v_f$.

If a probability distribution is considered, growth is both positively and negatively affected. The main peak of the distribution shifts to lower sizes (see Fig. 3.3 inset), because collisions from the high-speed tail of the distribution already start the fragmentation even before the particles reach the nominal barrier. However, there are also lucky particles that successively experience low-velocity collisions, even beyond the barrier. This leads to the tail in the size distribution beyond the barrier seen in Fig. 3.3.

The probability of a particle reaching a mass m before being destroyed can be approximated by assuming that the particles with masses around the peak mass, m_{peak} , dominate the interactions with the larger particles. A particle therefore has to undergo k consecutive sticking collisions in order to grow to a mass of $m = k \cdot m_{\text{peak}}$. The survival chance for particles growing from m_{peak} to $k \cdot m_{\text{peak}}$ can be written as a product of the sequence

$$p_{\text{survival}} = \prod_{i=1}^k p_s(m_i) . \quad (3.9)$$

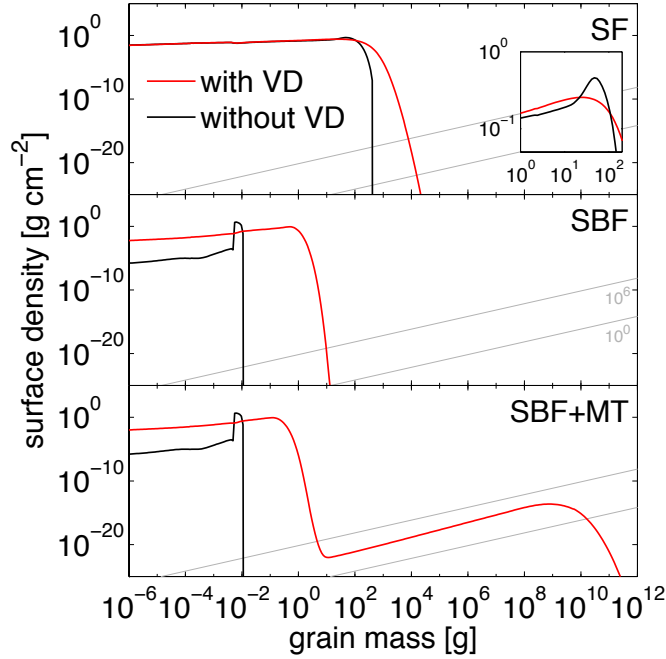


Figure 3.3: Snapshot of the size-distributions for SF (upper), SBF (middle), and SBF+MT (lower) collision models taken after $t = 5 \cdot 10^4$ years, with (red) and without (black) a velocity distribution. The gray diagonal lines correspond to a total of 1 and 10^6 particles within a 0.1 AU annulus.

In Fig. 3.4, we plot the cumulative survival probability under different assumptions. The dashed and solid lines were calculated assuming constant sticking probabilities, and the solid line assumed a velocity/mass-dependent p_s . At a mass of $m = 50m_{\text{peak}}$, the relative velocity had increased by a factor of 2, and the sticking probability had decreased from 0.5 to 0.1 compared to the peak population.

These numbers compare well to the large-particle tail in Fig. 3.3. The largest particles of masses $m = 60m_{\text{peak}}$ have a density decrease of roughly 25 orders of magnitude relative to the peak mass, which is roughly the survival probability that we calculated in the toy-model. Growing to these masses is extremely unlikely, but the sheer number of particles ensures that some lucky particles make it.

3.3.2 The bouncing barrier

In the SBF model, we note two differences between the two cases. One is the discrepancy in the number of small particles. Without a velocity distribution, the small particles are depleted as there is no mechanism that can create them once the main population has grown to the bouncing barrier. This depletion is rapid at first, but gets less effective when the number of small particles drops and the frequency of sticking collisions decreases. If a velocity distribution is included, collisions in the high-velocity tail cause fragmentation and replenish the population of small particles.

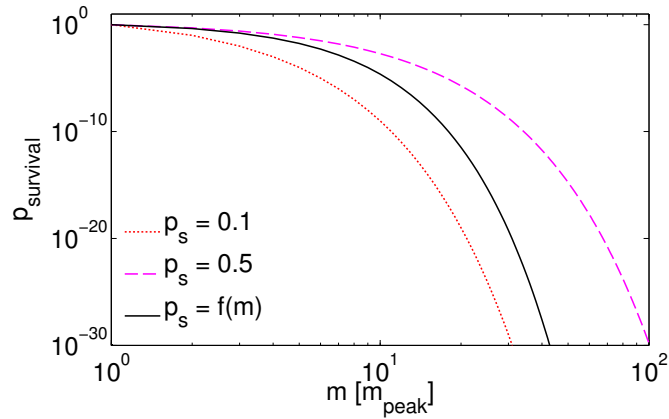


Figure 3.4: The cumulative survival probability of a particle crossing through the fragmentation barrier. The dotted and dashed lines are calculated by constant p_s regardless of particle mass, the solid line by a mass-dependent p_s from Eq. 3.7.

The peak of the distribution shifts significantly towards larger sizes. The reason for this can be seen in Fig. 3.2, where the low-velocity collisions lead to sticking, but even the highest collision velocities are too low to cause any fragmentation. At around $m = 1$ g, the growth halts when the fragmentation probability increases rapidly, while the sticking collisions are rare. This causes a steeper tail of large particles compared to the case of the pure fragmentation barrier.

We find that bouncing collisions never completely halt the dust growth, as there will always be a small chance of sticking. However, the growth timescale may become so large that the growth is effectively halted. If we follow an individual dust grain, we can write its growth timescale as

$$\tau_{\text{growth}} = \frac{m}{dm/dt} = \frac{m}{\sigma v_{\text{rms}} \rho_p p_s} \quad (3.10)$$

where $\sigma = \pi(a + a_p)^2$ is the collisional cross-section and $\rho_p = 1.4 \cdot 10^{-11}$ g cm^{-3} is the midplane mass density of particles that it can collide with. The growth will therefore slow down by a factor proportional to the decrease in p_s relative to unhindered coagulation. In the bouncing barrier, this will cause an increase in the growth timescale by a factor of 10^3 . Taking p_s from Eq. 3.7 and the relative velocity prescription of the previous section, we find that it takes $\sim 10,000$ years for particles to grow to $m = 1$ g. If p_s was to decrease further, for example owing to a lower bouncing-velocity threshold, this timescale would increase correspondingly.

3.3.3 Breaking through the barriers

In the SBF+MT model, we finally implemented the physics that makes it possible for growth also at high velocities. This relies on a mass difference between the particles in the disk, but without a velocity distribution, such a mass difference never occurs.

With the velocity distribution included, the bouncing barrier can be overcome (see model SBF), and the fragmentation barrier is smoothed out (see model SF), which means that a very small (10^6 particles in an 0.1 AU annulus) but important fraction of particles manage to grow large enough purely by chance. This triggers the growth of these few lucky particles by sweeping up the smaller grains trapped below the fragmentation barrier.

Even a single fragmenting collision between two lucky particles will create a myriad of fragments that will also be able to sweep up the particles trapped below the barrier. This means that the rare fragmenting collisions will effectively multiply the number of large particles, and with time, even a handful of lucky particles can by themselves create a significant population of planetesimals.

For sweep-up to occur in the simulations, a very high dynamical range is required. Though the break-through occurs for such a tiny fraction of the population, the sweep-up growth causes a rapid increase in both the number and total mass of the larger grains.

3.4 DISCUSSION AND CONCLUSIONS

We have found that the collisional growth barriers for dust grains are smoothed out and can even be overcome by virtue of a probability distribution of relative velocities among dust grains. Although improbable, sticky, low-velocity collisions can occur at sizes where the mean collisional velocity would lead to only bouncing or fragmentation.

To grow through the fragmentation barrier, a particle needs to be lucky and experience low-velocity collisions many times in a row, which causes a tail of larger particles to extend from the peak of the mass distribution. The exact shape of the large particle tail depends on the velocity distribution and collision model, but in our case, the luckiest particles can grow to around 30-100 times more massive than the average particle trapped below the barrier.

The bouncing barrier is even more affected by the existence of a velocity distribution, and particles can grow to more than three orders of magnitude higher in mass, with the peak being shifted by two orders of magnitude. This occurs because low-velocity collisions lead to sticking, but even the higher velocities are low enough to only cause bouncing. This means that the growth can continue unimpededly until the average relative velocities have increased enough for the fragmentation barrier to start to become important. The bouncing barrier is therefore not a solid barrier at all, unless the growth timescale becomes too long because of the low sticking probability.

We can from this conclude that the low-velocity tail allows some lucky particles to grow beyond the bouncing and fragmentation barriers. This is a promising mechanism to produce the first seeds in the sweep-up scenario introduced in Chapter 2. When the effect of mass transfer is included, these seeds can sweep up the smaller particles trapped by the growth barriers, and start their growth towards planetesimal sizes. The exact shape of

the steady-state size distribution is however highly dependent on the collision model and velocity distribution parameters. In the following chapter, we study the effect of different models and distributions, and also study the effect of particle clumping on the particles' ability to break through the barriers.

3.A STOCHASTIC AND DETERMINISTIC RELATIVE VELOCITY SOURCES

Velocity distributions arise due to the stochastic effects such as Brownian motion and turbulence, as opposed to the deterministic relative velocity sources such as vertical settling and radial and azimuthal drift that instead lead to clearly defined relative velocities. In this work, we assume the stochastic particle motion to dominate over the deterministic sources, which is strictly speaking not valid everywhere, but it is true at the particle sizes of the collisional growth barriers. For a more complete approach that takes both effects into account during the calculation of the PDF, see [Garaud et al. \(2013\)](#).

Describing the turbulent velocity field is complicated and is based on dividing the particle pairs into different regimes based on their coupling to the gas compared to the turnover time of the turbulent eddies ([Voelk et al. 1980](#); [Markiewicz et al. 1991](#); [Ormel & Cuzzi 2007](#)). The relative velocities of intermediate-sized particles (that couple to eddies somewhere in the turbulent cascade) which are the sizes where the collisional growth barriers occur are described by [Ormel & Cuzzi \(2007\)](#) as

$$\Delta v_t \approx c_s \sqrt{K\alpha St}, \quad (3.11)$$

where $2 < K < 3$ is a numerical prefactor that depends on the size-ratio of the particles, α is the turbulent strength, c_s is the sound speed and St is the Stokes number of the largest particle.

In this section, we will focus on the radial drift, which is stronger for the intermediate-sized particles than the azimuthal drift. Radial drift occurs because the dust particles face a constant headwind from the surrounding gas, as the gas is supported by a radial pressure gradient therefore orbits at slightly sub-keplerian velocities (see Sect. 1.4.2 for more details). The equilibrium radial drift velocity for intermediate-sized particles is given by [Weidenschilling \(1977a\)](#) as

$$v_r = -\frac{2\eta v_k}{St + St^{-1}}, \quad (3.12)$$

and the relative velocity between two particles is $\Delta v_r = |v_{r,1} - v_{r,2}|$. The maximum particle drift velocity is given by $2\eta v_k$, but the relative drift velocity quickly decreases for particles that are far away from $St=1$, or for similar-sized particles.

We also need to know at roughly what particle sizes the collisional growth barriers occur. By equating the approximate turbulent velocity to

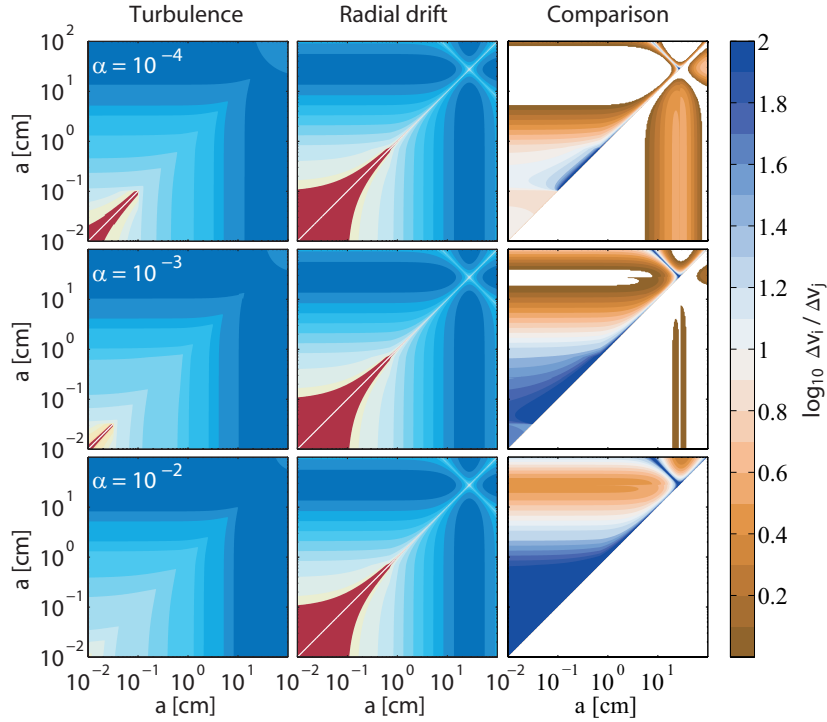


Figure 3.5: Comparison between the relative velocity contribution from turbulence (*left* panel) and the radial drift (*middle*) between particles at 1 AU in an MMSN disk. The *right* panels compare the two sources, and the upper and lower triangles shows where the turbulent and radial relative velocities dominates, respectively. The comparison is given as a ratio between the dominating source and the weaker source. The approximate bouncing barrier locations are $a_{\text{coll}} \approx 1, 0.1, \text{ and } 0.01$ cm for turbulent strengths of $\alpha = 10^{-4}, 10^{-3}, \text{ and } 10^{-2}$.

the bouncing/fragmentation velocity, [Birnstiel et al. \(2009\)](#) gave the fragmentation size as

$$a_{\text{coll}} \simeq \frac{2\Sigma_g}{\pi\alpha\zeta} \cdot \frac{v_f^2}{c_s^2}, \quad (3.13)$$

where Σ_g is the gas surface density, α is the turbulent strength, ζ is the dust solid density, $v_{b/f}$ is the bouncing or fragmentation velocity and c_s is the sound speed.

In Fig. 3.5, we have plotted the relative velocity contribution from the turbulent relative velocities from the full closed-form expressions given by [Ormel & Cuzzi \(2007\)](#) for three different turbulent strengths, and compared it to the relative velocities from the radial drift, with everything calculated for an MMSN disk at 1 AU. In the third panel, we have calculated the ratio of the two sources and the size-size space where each effect dominates. In the figures, we also give the approximate size of the collisional barriers obtained from Eq. 3.13, which are equal to $a_{\text{coll}} \approx 1, 0.1, \text{ and } 0.01$ cm for turbulent strengths of $\alpha = 10^{-4}, 10^{-3}, \text{ and } 10^{-2}$, respectively.

As the radial drift depends on the difference of the aerodynamical properties of the two particles, turbulence will always dominate for similar-

sized particles. This is also true for small particles where the drift is very low, and as the turbulent strength increases, the radial drift contribution becomes less and less important. We can conclude that in the size regime of the collisional growth barriers, the stochastic sources will dominate even for the case of weak turbulence.

It has also been shown that pressure inhomogeneities or bumps, arising from e.g. MHD effects or planets, is an effective way to keep disks dust-rich over millions of years as observed in the outer regions, where the radial drift would normally deplete the disk from dust on timescales of 1 Myr or less (Pinilla et al. 2012b; Ricci et al. 2010b). In these regions, turbulence will always be the dominating velocity source regardless of the turbulent strength.

3.B A RESOLUTION STUDY

In the dust evolution code by Birnstiel et al. (2010a) that we have utilized in this chapter, the Smoluchowski equation has been discretized into a set of logarithmically spaced mass bins. When a sticking or fragmenting event occurs, the mass of the resulting particle(s) will never fit exactly into the existing mass bins. To solve this, the code follows Brauer et al. (2008) and uses the Podolak algorithm, where the resulting mass is distributed between the two nearest mass bins. For normal coagulation studies, the numerical diffusion caused by the Podolak algorithm results in a significantly sped up growth rate unless a sufficiently high mass resolution of 10-40 bins per mass decade is used. This is discussed in more detail in Sect. 1.4.4.

In this study, the Podolak algorithm also gives rise to a second artificial effect that needs to be considered. Because particles that are more massive than the grain at the peak must be lucky and has to grow by only interacting with other particles in low-velocity collisions, it becomes necessary to accurately resolve the high-mass tail of the distribution. Otherwise, if not all sticking events are resolved, the slope of the tail will be incorrect, causing artificially large mass ratios between the luckiest grains and those in the peak. As an example of this, we can consider the extreme case where the lucky particles are represented by a single mass bin m_i . If two grains in the peak undergo a single sticking event, forming a particle of mass $m \ll m_i$, some mass will still be put into mass bin i , even though in reality, the particles would need to undergo several consecutive sticking events to reach a mass m_i . Such a badly resolved large-particle tail could cause an artificial growth breakthrough if we are not careful.

To find a resolution that is sufficiently high for this work, we have performed a resolution study using the SF and SBF collision models and a Maxwellian velocity distribution, and varied the resolution between 5 and 50 bins per decade of mass. The result is shown in Fig. 3.6, and we plot a huge density range of 30 orders of magnitude which roughly corresponds to 1 real particle in an 0.1 AU annulus at 1 AU. As can be seen, the SF case is extremely sensitive to the mass resolution. For the case of the lowest res-

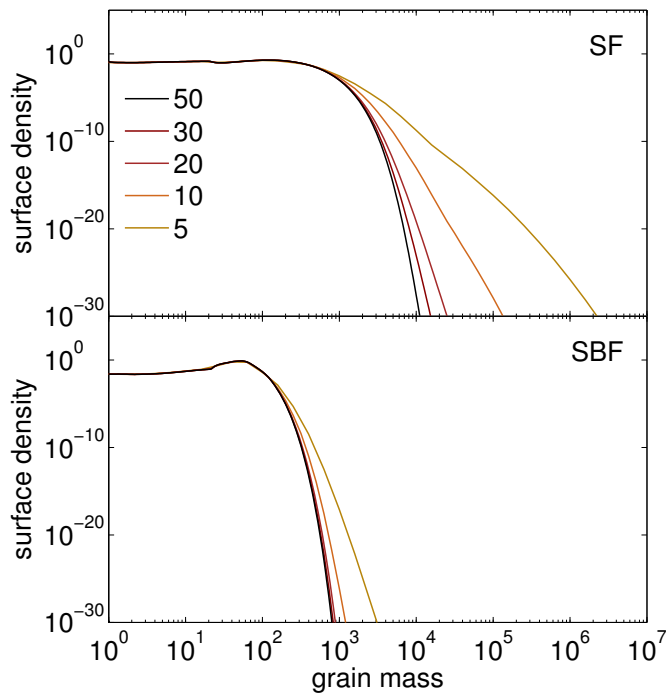


Figure 3.6: The effect of mass resolution on the steady state for the two fiducial collision models with a Maxwellian velocity distribution. The resolutions included are 5, 10, 20, 30 and 50 mass bins per decade.

olution, the largest particles have managed to grow more than two orders of magnitude more massive than in the case where the convergence has been reached, at roughly 30 bins per decade. When including bouncing, however, the results converge much faster and converge already at a mass resolution of 10 bins per decade.

The resolution sensitivity depends on the natural slope of the high-mass tail, which is the result of how quickly the ratio between the sticking and fragmentation probabilities changes with increasing mass or velocity (see Fig. 3.2). If the slope is naturally steep, you need fewer mass bins to accurately represent it, leading to a lower resolution dependency.

From this resolution study, we find that a mass resolution of 30 bins per decade should suffice, although this also depends on the parameters of the collision model. However, because we here only study the growth breakthrough for model SBFMT, where the less resolution-dependent bouncing is included, we settle for an intermediate resolution of 17 bins per decade.

PARTICLE GROWTH IN CLUSTERING: HOW FAR CAN DUST COAGULATION PROCEED?

Adapted from Windmark, Birnstiel, Ormel, A&A (in prep.)¹

ABSTRACT

The collisional growth barriers have long been problematic for the understanding of how large dust particles can form in the protoplanetary disk. However, recent studies have shown that the mean-velocity representation and homogeneous particle distribution commonly used in coagulation models do not always accurately represent the actual disk conditions. In this chapter, we therefore study the robustness of the dust growth barriers in the context of velocity distributions and particle clustering. We give an introduction to coagulation in particle clumps, and implement models for different velocity probability distributions and particle clustering models to a local coagulation code. We then apply and interpret both the conditions as expected from numerical turbulent flow simulations as well as from a more general parameter study meant to represent the potential also of other clustering effects. We find that the peak of the particle size is rather insensitive to the shape of the velocity distribution. However, the tail of large particles is more easily affected, leading to the possibility of particle breakthrough. We also find that clustering is a powerful effect that has the potential to majorly change the dust evolution by preferentially increasing the rate of the low-velocity sticking collisions or by increasing the growth rate to make it comparable or faster than the radial drift. On the other hand, even though the turbulent concentration is capable of increasing growth rates by as much as 10^4 , it is limited by the fact that it clusters at sizes that do not necessarily correspond to where the growth barriers are. This study supports the theory that the fragmentation barrier is solid enough to keep most particles in the disk small. However, our parameter study shows that a common outcome is that a few lucky particles can grow large enough to initiate sweep-up coagulation, leading to a bimodal growth scenario. The expected strengths obtained from the turbulent clustering effects are however still uncertain, and future studies will be needed to more accurately model the particle clustering.

4.1 INTRODUCTION

A longstanding problem in understanding the early stages of planet formation is how the initially micrometer-sized dust grains in the protoplan-

¹ See page ix for details on authorship.

etary disk can grow to kilometer-sized planetesimals. In the classical incremental growth scenario, sticking events result in successively larger dust agglomerates. However, as the particles grow, they decouple from the surrounding gas and collide at increasing collision velocities. At some point, the collision energies are so high that the particles instead start to bounce (Zsom et al. 2010) or fragment (Weidenschilling 1980). This is problematic, as the bouncing and fragmentation barriers occur for sizes smaller than decimeters, while modeling of the later stages require bodies of at least 100 meters in size to successfully form planets (Fortier et al. 2013; Okuzumi & Ormel 2013).

The collisional growth barriers have however also been found to be the best explanation to the presence of sub-mm dust in the protoplanetary disk. As dust grains are the main cause of opacity of disks at mm-wavelengths, coagulation studies are necessary to explain observational findings in protoplanetary disks (Birnstiel et al. 2010b; Ricci et al. 2010a; Pérez et al. 2012), where the maximum grain size and size-distribution are key components. Without any growth barriers, the dust would simply keep on growing, and the small sizes would be depleted (Dullemond & Dominik 2005; Tanaka et al. 2005). A major question is therefore: How can planetesimals be formed while the growth barriers are still there?

A number of alternative formation scenarios have therefore been put forward to explain the formation of planetesimals. These include highly sticky chondrules (Beitz et al. 2012), extremely porous ice agglomerates (Okuzumi et al. 2012), and variants of gravitational instabilities (Goldreich & Ward 1973) with clumping and gravitational collapse via streaming instabilities (Johansen et al. 2007) or turbulent clumping of chondrules (Cuzzi et al. 2008). In all of these cases, the dust size-distribution is still a highly important quantity. In the case of streaming instabilities, particles need to be sufficiently decoupled from the gas and numerous enough to cause feedback to the gas, and the chondrule clumping requires a very narrow dust size-distribution. However, because of the nature of collisional growth barriers, current numerical coagulation models predict that these requirements are not always fulfilled.

In Chapter 2, we introduced the concept of sweep-up coagulation. In this scenario, most of the dust population is kept small by collisional growth barriers, while a few larger "seed" particles can grow by interacting with the surrounding small grains in high-velocity mass transfer collisions. In Chapter 3, and also in Garaud et al. (2013), it was found that these large particles might be created by including impact velocity distributions in the coagulation codes. Two particle populations are then formed, where most of the dust is kept below the barriers, but some grains are lucky enough to grow larger by subsequent low-velocity sticking collisions. These lucky particles become the first seeds in the sweep-up coagulation phase.

But there are still many questions remaining for this scenario. One conclusion was that even though the formation of lucky seeds is possible, it is very improbable, and only a very small number, if any, are going to break through the growth barriers. This is highly dependent on the col-

lision model and shape of the velocity distribution, as well as other disk properties such as gas density and turbulent strength. It is expected that turbulence will be the dominant velocity source in most parts of the disk for the small dust grains, and numerical work on dust particles suspended in turbulent gaseous environment have shown that, depending on the particle properties, the distribution can range between Maxwellian and exponential (Carballido et al. 2010; Wang et al. 2010; Pan & Padoan 2010; Hubbard 2012; Pan & Padoan 2013).

It has also been found both numerically and experimentally that particles of similar aerodynamic properties have a tendency to concentrate into dense, local clusters, which has been studied both outside astronomy (Sundaram & Collins 1997; Shaw 2003; Gustavsson & Mehlig 2011; Gustavsson et al. 2012) and for protoplanetary disk environments (Cuzzi et al. 2008; Pan et al. 2011). Depending on the primary clumping effect, these clusters can reach local solid density enhancement factors up to 10^4 (Bai & Stone 2010; Pan et al. 2011; Hubbard 2012). As clumping occurs primarily for particles of low relative velocity, this could have a potentially large effect on dust coagulation, as local regions with enhanced sticking collisions will affect the equilibrium between sticking and fragmenting collisions.

In this work, we discuss and model coagulation with particle velocity distributions and clustering, primarily in the context of growth breakthrough towards larger sizes and the general effect on the final steady-state distribution, but also its effect on growth timescales. We use both clustering models based on numerical turbulent clustering results, as well as perform a more general parameter study. In Sects. 4.2 and 4.3, we discuss previous results on clumping and give a tutorial on clumping and its implementation into coagulation codes. In Sect. 4.4, we discuss the collision models and velocity distributions used, and the results are described and discussed in Sects. 4.5 and 4.6.

4.2 PARTICLE CLUSTERING IN TURBULENCE

The existence of turbulence in protoplanetary disks is by now evident, as it is required both to explain the observed gas accretion rates (Papaloizou & Lin 1995) and the observed abundances of small particles at high altitudes above the disk midplane (Dullemond & Dominik 2005; Tanaka et al. 2005). The widely accepted theory behind the driver of turbulence is magnetorotational instability (Stone et al. 2000), and the turbulent strength is often described by the nondimensional parameter introduced by Shakura & Sunyaev (1973), which for protoplanetary disks is assumed to be $\alpha \sim 10^{-5} - 10^{-2}$. In turbulent gas, energy is assumed to be put into large-scale eddies of size-scales $L \sim H_g \alpha^{1/2} \sim 10^{-3}$ AU (in the inner disk), where H_g is the gas scale-height. These eddies are unstable, and a cascade follows down to the dissipation (Kolmogorov) scale eddies, with sizes $L_K = L \text{Re}^{-3/4} \sim 1$ km, where $\text{Re} = \alpha c_s H / v_m \sim 10^7$ is the gas Reynolds number. The small scale eddy lifetime is given by $t_K = \text{Re}^{-1/2} t_L$, where $t_L \sim \Omega_k$ is the lifetime of the largest eddies (Ormel & Cuzzi 2007).

In coagulation studies, turbulence is important for several reasons, but is mainly considered for its diffusive properties and as a main cause of the high relative velocities that cause the destructive collisions between dust grains. Another interesting aspect of turbulence that has yet to be looked at in a context of dust coagulation is its clustering capability. Because the dust grains are not perfectly coupled to the gas, dissipative trajectories caused by centrifugal forces in turbulent eddies can cause the ejection of the particles from the eddies, and the formation of transient but dense clusters of particles in regions of low vorticity (Cuzzi et al. 2008; Pan et al. 2011).

This turbulent clustering is optimal for particles with stopping times τ equal to the turn-over time of the smallest eddies, t_K . Clustering of larger particles occurs on larger size scales corresponding to the eddy size that they are most well coupled to (Pan et al. 2011), and smaller particles are too well coupled to the gas to cluster considerably. This size scale for maximal clustering is also where the turbulent velocity starts to cause fragmentation. From the method of Birnstiel et al. (2009), we can put the turbulent velocity for equal-sized particles equal to the fragmentation velocity, and get

$$a_{\text{frag}} \simeq \frac{\Sigma_g}{\pi\alpha\zeta} \cdot \frac{v_f^2}{c_s^2}, \quad (4.1)$$

where Σ_g is the gas surface density, ζ is the solid density, v_f is the fragmentation velocity and c_s is the sound speed. Assuming the particles to be in the Epstein drag regime, the particle size coupled to the Kolmogorov scale can be written as

$$a_K = \sqrt{8/\pi} \cdot c_s t_K \frac{\rho_g}{\zeta}. \quad (4.2)$$

Comparing these two sizes, we get

$$\frac{a_K}{a_{\text{frag}}} = 2\alpha \text{Re}^{-1/2} \cdot \frac{c_s^2}{v_f^2}, \quad (4.3)$$

which is $\sim 0.01 - 0.3$ in the inner disk depending on disk conditions and fragmentation strength. If we also include the bouncing barrier that occurs at smaller relative velocities, we find that clustering might indeed be an important factor in the collisional barrier regime. At larger radii where ices cause the fragmentation velocity to increase, this ratio will decrease.

To quantify the degree of clustering, one can define a concentration factor $C = \rho/\bar{\rho}$ (discussed in detail in Sect. 4.3). Numerical simulations by Cuzzi et al. (2008) find that on larger scales, concentrations of the order of 10 – 100 are to be expected, but Pan et al. (2011) show that on the smallest size-scales relevant for coagulation, the concentrations can reach as high as $C \sim 10^4$. Directly studying such small scale concentrations is however impossible due to wide spatial range of the turbulent cascade and the large difference between dust particle sizes and the Kolmogorov scale, and all studies therefore require significant extrapolation.

Hubbard (2012, 2013) studied the collision frequency of particles of both equal and different τ using artificial turbulent cascade models (shell models) to better resolve the Kolmogorov scale. In this way, both the distribution of relative velocities and the degree of clustering could be studied. Clustering also means that the particles are trapped in the same gas streams, which tends to suppress their relative velocities. It was found that although particles of equal sizes tend to cluster together to $C > 100$, and that the relative velocities of the clustered particles had $\lesssim 1 \text{ m s}^{-1}$, already particles with stopping time ratios of 1.5 have the maximum clumping reduced to $C \sim 2$. This occurs because particles of different stopping times tend to cluster at different locations in the flow (Pan et al. 2011).

Due to other effects, clustering also occurs for larger particle sizes than for the turbulent clustering discussed above. Zonal flows are the products of large-scale variations in the magnetic field, which cause a differential momentum transport to occur, creating regions of slightly faster and slightly slower orbiting gas. This causes transient pressure bumps to form with lifetimes of 10-50 orbits, causing dust particles to get trapped and forming overdensities Johansen et al. (2009). The strength of these overdensities varies. Dittrich et al. (2013) found $C \sim 10^3$ for equal-sized $St = 1$ particles decreasing to ~ 100 for $St = 20$, and < 10 for $St < 0.01$.

Another type of turbulent clustering can occur if the dust to gas ratio is sufficiently high, and the dust is sufficiently decoupled from the gas ($St \gtrsim 10^{-2}$). This will cause a significant momentum feedback from the dust to the gas, and result in streaming instabilities (Youdin & Goodman 2005). This, in turn, lead to even higher concentrations that could be enough to surpass the Roche density ($\rho_p \gtrsim 10^3 \rho_{\text{gas}}$), above which the particles in the clump would be gravitationally bound, and lead to subsequent gravitational instabilities (Johansen et al. 2007; Bai & Stone 2010). However, if the amount of available dust is too small, streaming instabilities might well occur without the subsequent gravitational instabilities, which would be optimal conditions for efficient coagulation.

Particle concentrations will in general act to speed up the overall growth, but if all particle collisions were boosted equally, this would do little for changing the particle size at the fragmentation barrier, which is (somewhat simplified) given by the ratio between the rates of sticking and fragmentation. A key concept in this study will therefore be to take into account that clustering preferentially boosts the low-velocity sticking collisions, which has the potential to majorly affect the maximum particle size.

4.3 COAGULATION IN CLUMPS EXPLAINED

In this section, we intend to give a basic overview of clustered particle distributions, and how this can be modeled in the context of coagulation. This has been discussed in fields outside of planet formation (for a summary from the atmospheric science field, see e.g. Kostinski & Jameson (2000); Shaw et al. (2002); Shaw (2003), which this review is based on). We will discuss both the quantification of clustering, and how it relates to the colli-

sion rate between particles. In Sect. 4.3.1, we will describe an intuitive but limited approach, and in Sects. 4.3.2 and 4.3.3, we will discuss the more general pair correlation function and its result on the collision rate.

First of all, let us give the collision rate for a given collision type between two particle species i and j , assuming only a mean-velocity without any particle clumping:

$$f_{ij} = \bar{n}_i \bar{n}_j K_{ij}, \quad (4.4)$$

where \bar{n} is the mean number density and K_{ij} is called the kernel, given by

$$K_{ij}(\Delta v_{\text{rms}}) = \sigma_{ij} \Delta v_{\text{rms}}, \quad (4.5)$$

where Δv_{rms} is the mean relative velocity and $\sigma_{ij} = \pi(a_i + a_j)^2$ is the geometrical collisional cross section. In a clumpy medium, the mean number density is not sufficient to describe the particle distribution, and we need another formulation to determine the collision rate.

4.3.1 Intuitive way of looking at clumping

We will begin with an intuitive approach to particle clumping, by assuming a box of volume V_b filled with N particles of a single species. The particles are clumped together so that they can be described with a uniform probability distribution over a smaller volume V_c , so that $V_c < V_b$.

The number density of the particles within the clump is $n = N/V_c$, and averaged over the entire box, the number density is $\bar{n} = N/V_b$. We can relate these two densities by $n = V_b/V_c \cdot \bar{n} = C \cdot \bar{n}$, where C is the clumping factor.

In this way, the average collision rate (per velocity per cross-section) over the whole box is

$$\begin{aligned} \frac{f}{\sigma \Delta v} &= \frac{1}{V_b} \int_0^{V_b} n^2 dV = \frac{1}{V_b} \int_0^{V_c} n^2 dV + \frac{1}{V_b} \int_{V_c}^{V_b} n^2 dV = \\ &= \frac{V_c}{V_b} n^2 = \frac{V_c}{V_b} \left(\frac{V_b}{V_c} \right)^2 \bar{n}^2 = C \cdot \bar{n}^2. \end{aligned} \quad (4.6)$$

We can from this conclude that the collision rate scales linearly with the clumping factor of particles. This approach is however not so well suited for dealing with clumping of particles of different particle properties and masses, and describes a more realistic clustering case rather poorly. In order to get further, we will have to employ the pair correlation function.

4.3.2 The pair correlation function

Let us now take a step back, and define what we really mean with a clustered distribution. We first assume that the position in a certain region of the disk is given by a random variable. This randomness comes from the interaction with the stochastic Brownian motion and turbulent flow, making it impossible to use initial conditions (with any realistic accuracy)

to predict the spatial evolution of a particle. An important assumption of most dust coagulation studies is to assume that the spatial properties of particles are homogeneous and Poisson-distributed over each sub-domain. With homogeneous, we here mean that the statistical spatial properties of the particles do not change with their position. Poisson-distributed particles must have their spatial statistics characterized by the Poisson process on all scales, i.e. the number of particles N in any volume V have their probability distribution given by

$$p(N) = \frac{\bar{N}^N \exp(-\bar{N})}{N!}, \quad (4.7)$$

where \bar{N} is the mean particle number in V . It is important to note that the Poisson distribution must be valid on all scales, as positive and negative deviations on smaller scales can cancel each other out and result in Poisson statistics on larger scales.

Now, we can assume that particles are distributed randomly and homogeneously, but they are not necessarily uncorrelated. In fact, as discussed in the previous section, the properties of a turbulent flow will result in the formation of temporary clusters and voids, which means that the relative position between particles are correlated. This can be understood by considering two particles A and B. We pick the position of particle A completely at random (from a uniform probability distribution over the volume). In a clustered medium, particle B then has a conditional probability for position, described and biased by the pair correlation function with particle A.

If we consider a volume element dV so small that it contains at most a single particle, the probability of finding a particle in that volume is $\bar{n}dV$. If particle positions are uncorrelated, the probability of finding particles in each of two volume elements dV_1 and dV_2 separated by a distance r is $P_{1,2} = \bar{n}dV_1 \cdot \bar{n}dV_2$. However, if a correlation exists between particles, we can write the probability as

$$P_{1,2} = \bar{n}dV_1 \cdot \bar{n}dV_2 \cdot [1 + \eta(r)], \quad (4.8)$$

where $\eta(r)$ is the pair correlation function and can be thought of as an enhanced (for $\eta(r) > 0$) or reduced (for $-1 \leq \eta(r) < 0$) likelihood of encountering a particle at a distance of r away from another particle. The former would correspond to a distribution with some form of clustering, and the latter implies a distribution which is distributed even more uniformly than a perfectly random distribution.

From Eq. 4.8, we can write the pair correlation function as the enhanced likelihood of finding a second particle in a volume element dV given the presence of a first one as:

$$\eta(r) = \frac{P_{1,2}}{(\bar{n}dV)^2} - 1. \quad (4.9)$$

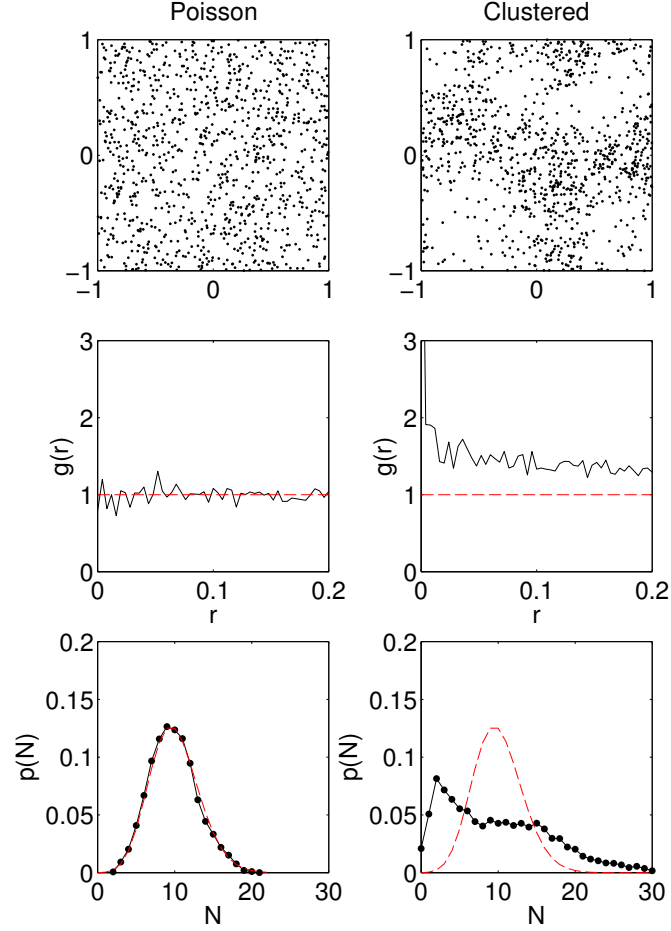


Figure 4.1: Illustration of 1000 particles distributed according to a uniform Poisson distribution (*left column*) and a clustered distribution (*right column*). In the *middle panels*, the radial distribution functions are given for the two cases, and the probability distributions are given in the *lower panels* for a volume with 10 particles on average, where the deviation from the theoretical Poisson distribution (red dashed line) is clear in the case with clustering. Figure adapted from [Kostinski & Jameson \(2000\)](#).

We can also write $P_{1,2} = \langle (n(r)dV)(n(r+dr)dV) \rangle$, where we let $\langle \dots \rangle$ denote the ensemble average. With $\bar{n}dV = \bar{N}$, we get

$$\begin{aligned} \eta(r) &= \frac{1}{\bar{N}^2} \langle N(r)N(r+dr) \rangle - 1 \\ &= \frac{1}{\bar{n}^2} \langle (n(r) - \bar{n})(n(r+dr) - \bar{n}) \rangle, \end{aligned} \quad (4.10)$$

where we assume isotropy, so that the direction dependence can be integrated out by

$$\eta(r) = \frac{1}{4\pi} \oint \eta(\vec{r}) d\Omega. \quad (4.11)$$

In statistical mechanics, another common way of measuring spatial correlations is by the use of the radial distribution function (RDF). This is defined

as the average number of particles at a distance between r and $r + dr$ from a reference particle normalizing by the mean particle density, or

$$g(r) = \frac{dN/N_b}{dV/V_b} = \frac{dN}{dV} \cdot \frac{V_b}{N_b}, \quad (4.12)$$

where N_b and V_b represent the total number of particles and the volume of the entire box, respectively. The expression for the RDF is equivalent to $g(r) = 1 + \eta(r)$, and from now on, we will for convenience use the RDF to describe particle clustering.

In Fig. 4.1, we give an example of a 2D Poisson distribution and a clustered distribution with voids and elongated clumps. In the middle panels, the resulting RDF has been calculated using Eq. 4.12. For the Poisson distribution, $g(r)$ oscillates around unity, corresponding to perfect randomness, but in the clustering case, $g(r)$ is clearly above unity for all investigated radial distances, showing evidence of a spatial correlation between particles. Finally, in the bottom panels, we show the probability distribution for the volume corresponding to a mean of $N = 10$ particles. In the case of clustering, the distribution differs significantly from the Poisson distribution, showing both a peak at lower particle numbers and an extended tail towards larger numbers.

Though the radial distribution function is interesting for describing general clustering, ideally, collisions between particles occur only for $r = 0$ (though realistically, this occurs when r is the sum of the particle radii). This means that in order to calculate the enhanced collision probability, we need to calculate the RDF for the limiting case $r \rightarrow 0$. From Eq. 4.10, we get

$$\lim_{r \rightarrow 0} g(r) = \lim_{r \rightarrow 0} \eta(r) + 1 = \frac{\langle n^2 \rangle}{\bar{n}^2} = \frac{V_b}{V_c} = C, \quad (4.13)$$

where we used the notation from the previous section that $n = \bar{n} \cdot V_b/V_c$, and that the density-squared averaged over the entire volume is equal to $\bar{n}^2 = n^2 V_c/V_b = \bar{n}^2 V_b/V_c$. It should here be noted that directly measuring the clustering for $r \rightarrow 0$ is impossible due to the limited resolution. All clustering values therefore need to be extrapolated over a huge spatial range and are therefore very uncertain, which should be taken into consideration when performing the parameter study.

From this, we find that the collision rate can be given by $f/(\sigma \Delta v) = g(r \rightarrow 0) \cdot \bar{n}^2 = C \cdot \bar{n}^2$, same as in the intuitive picture of the previous section. However, we have still assumed identical particle properties, and no correlation for the relative velocities between particles. We add this in the following section.

4.3.3 Full implementation of the radial distribution function

We now extend the RDF to also contain information about the particle properties, to account for the fact that particles of different aerodynamic

properties cluster differently, and that this clustering also affects their relative velocities and collision rates. To obtain the new RDF, we consider a reference particle of stopping time τ_1 , and calculate its correlation-function with particles of stopping time τ_2 and velocities Δv relative to the reference particle, giving $g(r, \tau_1, \tau_2, \Delta v)$. If we take $\tau_1 = \tau_2 = \tau$, we can recover the original radial distribution function by integrating over all relative velocities:

$$g(r, \tau) = \int g(r, \tau, \Delta v) d\Delta v . \quad (4.14)$$

As we are interested in particle collisions (that occur for $r \rightarrow 0$), we will from now on drop the r dependence in the RDF, and write it as $g(\tau_1, \tau_2, \Delta v)$.

To correctly gauge the impact of the RDF on the coagulation rate, the kernel needs to be modified to take into account that clustering does not boost the collision rate for all relative velocities equally, but only over a limited Δv -range. The modified kernel should therefore be calculated by integrating over the entire Δv -space for each particle pair, so that the collision rate for each collision outcome can be written:

$$\hat{K}_{ij}(\Delta v_{\text{rms}}) = \sigma_{ij} \int_0^\infty g(\tau_i, \tau_j, \Delta v) \Delta v P_v(\Delta v | \Delta v_{\text{rms}}) P_{s/b/f}(\Delta v) d\Delta v , \quad (4.15)$$

where the modeling of $g(\tau_i, \tau_j, \Delta v)$, the velocity distribution $P_v(\Delta v | \Delta v_{\text{rms}})$ and the collision outcome probability $P_{s/b/f}(\Delta v)$ are subject to the following section. With this approach, we can then correctly calculate the collision rate of each individual collision outcome (sticking, bouncing or fragmentation).

A fundamental assumption in this model is that the velocity probability distribution (PDF) and the clustering factor are uncorrelated. In reality, it is difficult to make a distinction between the two, and the clustering will rather directly affect the local velocity PDF. Because the physics is still not fully understood, however, this phenomenological approach makes it easy to quantify the effects of clustering.

4.4 NUMERICAL IMPLEMENTATION AND CLUSTER MODELING

Before we can derive explicit integrations for the RDF, we first set the stage with the coagulation model and the velocity distribution model. We return to the modeling of the clustering in Sect. 4.4.3.

We use the local version of the Smoluchowski dust evolution model developed by Brauer et al. (2008) and Birnstiel et al. (2010a). In the code, we implement velocity distribution and clustering models, and investigate them together with collisions models with variable parameters for the sticking, bouncing and fragmentation, as well as disk parameters such as stellar distance and gas density.

4.4.1 Collision models

There is a lot of physics behind the collision outcome probability $P_{s/b/f}$, which depends on for example the impact velocity and angle as well as particle mass, porosity, structure and composition. There has been a lot of recent progress on the mapping of dust grain collisions, both in the laboratory (Güttler et al. 2010; Schräpler et al. 2012) and numerically (Wada et al. 2007; Seizinger & Kley 2013b; Meru et al. 2013). Even now, the conditions for the different collisional outcomes remain a hotly discussed topic, and the laboratory and numerical work predict very different results in for example the efficiency (or even existence) of bouncing for protoplanetary dust (Wada et al. 2011; Kothe et al. 2013b).

In this work, we take a simple, parametrized collision prescription using sticking, bouncing, fragmentation as the three possible outcomes. For simplicity, we take the outcome to be only velocity dependent, and denote the the probability of a certain outcome as $P_{s/b/f}(\Delta v)$. At any given Δv , we always have $P_s + P_b + P_f = 1$. We describe the probability distribution by a step function:

$$P_s(\Delta v) = \begin{cases} 1 & \text{if } \Delta v < v_b \\ 0 & \text{if } \Delta v > v_b \end{cases}, \quad (4.16)$$

$$P_f(\Delta v) = \begin{cases} 0 & \text{if } \Delta v < v_f \\ 1 & \text{if } \Delta v > v_f \end{cases}, \quad (4.17)$$

where v_b and v_f are the bouncing and fragmentation threshold velocities. From laboratory experiments, we know bouncing to occur at velocities between $1 - 10 \text{ cm s}^{-1}$, and silicate fragmentation to occur at velocities in the wide range between $10 - 700 \text{ cm s}^{-1}$.

For sticking collisions, the resulting particle gets the mass of both the particles involved, and we assume bouncing collisions to be completely neutral, with both colliding bodies totally unaffected. During a fragmenting event, two different outcomes are possible depending on the mass ratio of the particles involved, where we let $m_p \leq m_t$ be the projectile and target mass, respectively. For particles of similar mass, both particles fragment, and the mass is put into a size distribution described by $n(m)dm \propto m^{-1.83}dm$ (Blum & Münch 1993), between the monomer mass $m_0 = 6.7 \cdot 10^{-12}$ and m_t . Fragmenting collisions above a certain mass ratio $M_{\text{er}} = 10 - 1000$ instead only crater, where only the projectile is fragmented and excavates an amount of mass from the target equal to m_p .

Throughout this work, we will refer to two standard collision models that we denote as model SF (sticking + fragmentation, with $v_f = 100 \text{ cm s}^{-1}$), and model SBF (sticking + bouncing + fragmentation, with $v_b = 5 \text{ cm s}^{-1}$ and $v_f = 100 \text{ cm s}^{-1}$).

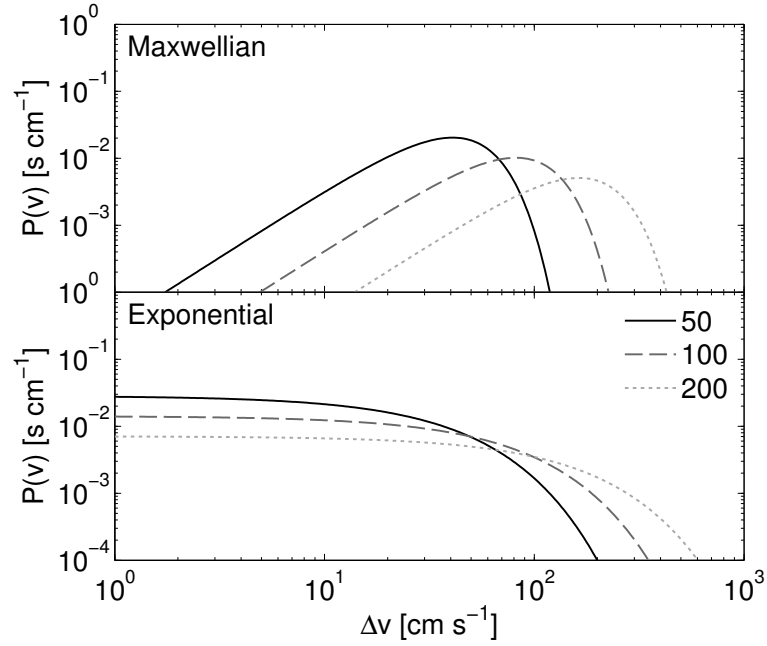


Figure 4.2: Comparison of the two velocity probability distributions for $v_{\text{rms}} = 50, 100$ and 200 cm s^{-1}

4.4.2 Velocity distributions

Due to stochastic and geometrical effects, two particles of some given aerodynamic properties have a wide range of possible velocities at which they can collide. Classically, only the mean relative velocity has been used for determining the collision rate and collision outcome between dust particles, but velocity PDFs were included and studied in Chapter 3 and by [Garaud et al. \(2013\)](#). It was found that this effect has the potential to widely change the resulting dust size distributions by allowing for collisions to lead to sticking at sizes where they would ordinarily only bounce or fragment.

Numerical turbulence studies indicate that the velocity PDF can vary between Maxwellian and an exponential depending on the aerodynamic properties of the particles. In this work, we will therefore extend the previous studies by including both of these distributions. Maxwellian velocity distributions are generally expected for particles of large Stokes numbers ($\text{St} = \tau/\tau_L = \tau\Omega_k \sim 1$, where τ is the particle stopping time, τ_{ed} is the turnover time of the largest eddies and Ω_k is the Keplerian frequency) ([Carballido et al. 2010](#); [Dittrich et al. in prep](#)). In this case, the relative velocities depend on the particles' memory of prior eddies, and will not get correlated in the local environment where they collide. The resulting distribution is given as a function of the root-mean-square velocity, Δv_{rms} , as:

$$P_{\text{max}}(\Delta v | \Delta v_{\text{rms}}) = \sqrt{\frac{54}{\pi}} \frac{\Delta v^2}{\Delta v_{\text{rms}}^3} \exp\left(-\frac{3}{2} \frac{\Delta v^2}{\Delta v_{\text{rms}}^2}\right). \quad (4.18)$$

where we in this work take Δv_{rms} to come from Brownian motion and turbulence Ormel & Cuzzi (2007). For particles of lower Stokes numbers, where particles couple to the Kolmogorov scale turbulence, their velocities have time to get correlated with the local eddy, and the distribution of relative velocities is then better characterized by an exponential distribution (Wang et al. 2000; Pan & Padoan 2010; Hubbard 2012). The distribution is given by

$$P_{\text{exp}}(\Delta v \mid \Delta v_{\text{rms}}) = \frac{\sqrt{2}}{\Delta v_{\text{rms}}} \exp\left(-\sqrt{2} \frac{\Delta v}{\Delta v_{\text{rms}}}\right). \quad (4.19)$$

Examples of these two distributions are given for different mean velocities in Fig. 4.2. Compared to the Maxwellian distribution, the exponential is wider, with a significantly stronger low-velocity population, but also a stronger high-velocity tail. Another important property of the exponential distribution in this context is that the population of low-velocity collisions only decreases slightly with increased mean-velocity, which means that there are always some sticking collisions occurring particle pairs of any mean velocity.

In this study, we have chosen to look at the effects of the two velocity distributions separately, where realistically, we would expect a transition from exponential to Maxwellian to occur in the regime $St \sim 1$.

4.4.3 Modeling the clustering factor

As discussed in Sects. 4.2 and 4.3, the clustering of particles is a highly complex phenomenon and can be caused by many different underlying effects. The primary factors of turbulence are the aerodynamic properties and the relative velocity, and so we want to write the clustering as $g(\Delta v, \tau_i, \tau_j)$, while still keeping the function as simple as possible. We firstly present a model and make fits to previous numerical turbulent studies, and in the next section introduce a simplified and more transparent model suitable for a parameter study.

As discussed by (Pan et al. 2011, PP11), one of the issues of understanding particle clustering on a coagulation aspect is the extrapolation from large scales (their best resolution is $0.09L_K$), down to the coagulation scale at ~ 1 mm. For the large-scale concentrations, PP11 found a Stokes-number dependent clustering factor for equal-sized particles (monodisperse clustering) that we have reproduced from their Fig. 7 into Fig. 4.3, panel a). As a fit, we take an exponential of the form

$$g_{11}(St_K, L_K) = k_A \exp(-k_B \log(St_K/St_{L_K,0})^2), \quad (4.20)$$

where $St_K = \tau/t_K$ is the Kolmogorov Stokes number (this way of normalizing to the smallest instead of the largest eddies is common practice when studying turbulence, and we will for ease of comparison with the simulations of PP11 stick to it for this section). This can reproduce the data fairly well for the parameters $k_A = 18$, $k_B = 0.4$ and $St_{L_K,0} = 0.8$. The aim of the

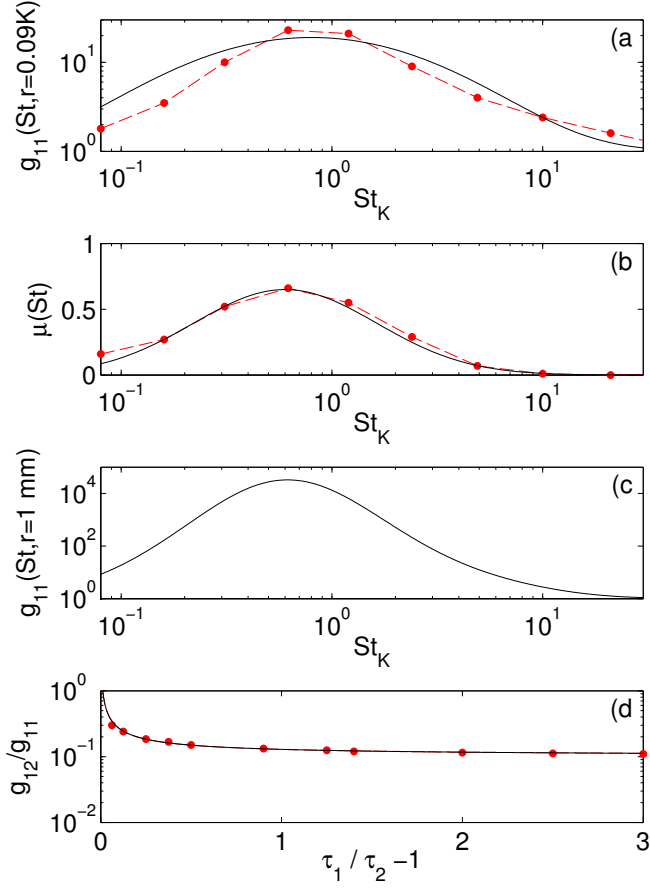


Figure 4.3: Fits for the clustering parameters (black solid lines) to the numerical data (red dashed lines), using [Pan et al. \(2011\)](#) and [Hubbard \(2012, 2013\)](#). Panel a) shows the large-scale RDF and is calculated from Eq. 4.20. Panel b) shows the slope of the extrapolation factor (see Eq. 4.22), and panel c) is the resulting small-scale RDF from Eq. 4.21. Panel d) shows the normalized clumping factor for particles of different sizes, given in Eq. 4.23, and we have in the plot assumed that the [Hubbard \(2013\)](#) data was calculated for $g_{11} = 10$.

fitting was here to reproduce the large-particle tail as well as possible, as this is where we expect the fragmentation barrier to be found.

Secondly, to extrapolate to the smaller scales, PP11 introduced a power-law:

$$g_{11}(St_K, \tilde{r}) = g(St_K, L_K) \cdot \tilde{r}^{-\mu(St_K)}, \quad (4.21)$$

where, $\tilde{r} = r/L_K$ is the particle separation normalized to the Kolmogorov scale, where we take $r = 1$ mm and $L_K = 1$ km in our disk model. To find a description for μ , we take their data (see also their Fig. 6) and fit an exponential of the same form as Eq. 4.20, resulting in

$$\mu(St_K) = k_C \exp(-k_D \log(St_K/St_{K,0})^2), \quad (4.22)$$

where we find that $k_C = 0.65$, $k_D = 0.5$ and $St_{K,0} = 0.6$ provide a good fit, as seen in panel b).

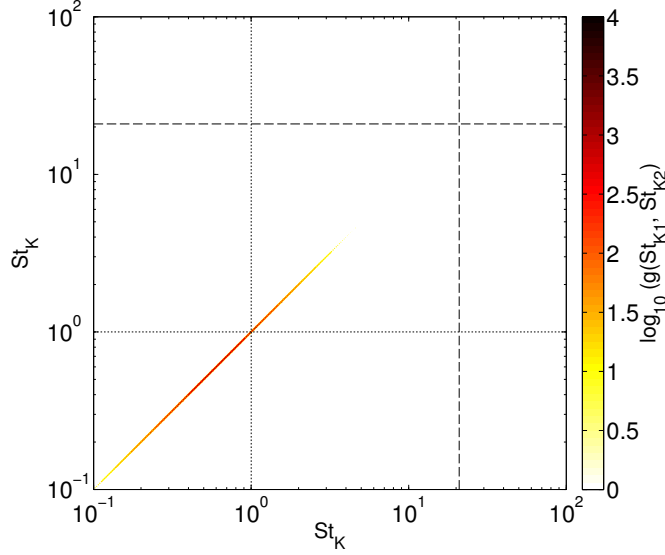


Figure 4.4: The clustering strength for particle pairs of different sizes using the fitted turbulent concentration model summarized in Eq. 4.24. The dashed line shows the mean-velocity fragmentation barrier (see Eq. 4.1) and the dotted line shows $St_k = 1$, roughly the point of maximum clustering (see Eq. 4.2), at which $g \sim 10^4$.

Using Eq. 4.21, it is now possible to construct the small-scale concentration factor, which is given in panel c). We can here note that the concentration at its peak reaches a remarkable 10^4 , but falls off quickly within an order of magnitude in St on both sides.

The clustering between particles of different sizes is very poorly understood, but a first step was taken by Hubbard (2013). They fitted a power-law decrease of the shape $\epsilon^{-0.77}$, where $\epsilon = \tau_1/\tau_2 - 1 \geq 0$. This fit diverges for equal-sized particles, mostly due to modeling reasons because the focus in that study was to investigate the clustering between different-sized particles. This divergence, where the slope is independent on g_{11} might however also have physical reasons. An interpretation of this could be that regardless of how well particles with the same aerodynamic properties cluster, because the clusters of particles of other properties occur at completely different locations, the clustering between different-sized particles would quickly become negligible.

With this interpretation, we take the Hubbard (2013) fit to be the following:

$$\frac{g_{12}}{g_{11}} = \frac{\min(g_{11}, 1 + 0.29\epsilon^{-0.77})}{g_{11}} = \min\left(1, \frac{1 + 0.29\epsilon^{-0.77}}{g_{11}}\right), \quad (4.23)$$

The result is seen in panel d), which we have normalized to an assumed maximum clustering factor of $g_{11} = 10$, which means that g_{12}/g_{11} goes towards $1/g_{11}$ for large ϵ .

Putting these together, we can calculate the clustering strength on the particle size-scale for each particle pair from

$$g(\text{St}_{K1}, \text{St}_{K2}, 1 \text{ mm}) = g_{11}(\text{St}_{K1}, L_K, 1 \text{ mm}) \times \min \left(1, \frac{1 + 0.29\epsilon^{-0.77}}{g_{11}(\text{St}_{K1}, L_K, 1 \text{ mm})} \right), \quad (4.24)$$

where $g_{11}(\text{St}_{K1}, L_K, 1 \text{ mm})$ is the monodisperse clustering for the particle of the strongest clustering, given by Eq. 4.21. To illustrate just what a narrow regime that clustering occurs, we plot the resulting clustering factor for each particle pair in Fig. 4.4. We note that although the maximum clustering strength is extremely high ($g = 10^4$) at its maximum, the clustering is limited both due to that clustering is mostly efficient at $\text{St} = \text{St}_K$, and because different-sized particles tend to cluster at different spatial locations.

Because of the combination of these two effects, it is in Fig. 4.4 clear that the clustering modeled here will have a limited effect on the dust coagulation and fragmentation barrier position (compare the the predicted fragmentation barrier (dashed line) to where the clustering occurs). Any Smoluchowski simulations using this model would therefore result in the exact same end result as without any clustering.

In the following section, we therefore take a slightly simpler clustering model that can be used with the full numerical simulations to study for what parameters clustering would become important.

4.4.4 A simplified clustering model

Using the lessons we learned from the previous fitting, we will now take a slightly simplified and more transparent model for the particle clustering that we can easily integrate and that we can use for our numerical simulations, with parameters that can use to model any type of turbulence. In this way, we can study what degree of clustering that would be needed for the clustering to play an important role, and we can also use it to study other types of clustering.

We choose to describe the clustering behavior by an exponential function of the form:

$$g(\Delta v, \tau_i, \tau_j) = 1 + k_1 \cdot \exp(-k_2 \Delta v - k_3 \epsilon - k_4 \gamma), \quad (4.25)$$

where $\epsilon = \tau_i/\tau_j - 1 \geq 0$ and $\gamma = \log(\tau/\tau_{\max})^2$. k_1 describes the maximum clustering strength, k_2 determines at what relative velocities clustering occurs, k_3 determine how well particles of different stopping times clusters, and k_4 describes how well particles cluster at stopping times different from the point of maximum clustering, τ_{\max} . In the last term, we let τ be the stopping time of the particle farthest away from τ_{\max} . Putting $k_1 = 0$ corresponds to a case without clustering, and $k_2 = 0$, $k_3 = 0$, or $k_4 = 0$ would mean that the clustering is independent of the corresponding property.

We choose to investigate a wide set of parameters where not all are likely results of turbulent concentration, both to account for uncertainties

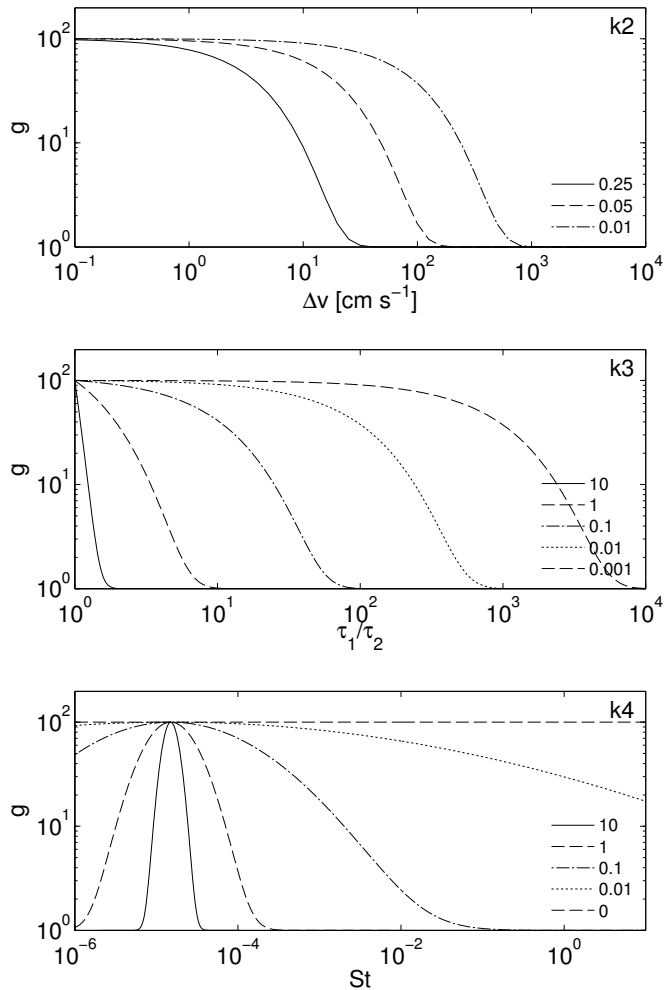


Figure 4.5: Our model for the clustering factor and its dependence on relative velocity, stopping time ratio and absolute Stokes number. Here given for $k_1 = 100$.

in the previous model fit and other accommodate other clustering effects. In Fig. 4.5, we show examples of the different parameters that we have investigated. The outcome is discussed in the next section. To finally calculate the total collision rates and outcome between each particle pair, Eq. 4.15 then needs to be integrated over the full relative velocity space.

4.5 DUST EVOLUTION MODELS WITH CLUSTERING

We have performed a numerical coagulation parameter study using the Maxwellian and exponential velocity PDFs. The results are presented in Sect. 4.5.1, where we discuss and further quantify the effect that the inclusion of a velocity distribution as an extension to what was shown in Chapter 3.

In Sect. 4.5.2, we discuss the results of the cluster parameter study that we have performed with the simplified clustering prescription. For the clustering parameters, we take values that roughly correspond to the de-

Table 4.1: Parameters used in the local simulations.

Parameter	Sym	Value	Unit
Distance to star	r	1, 10, 50	AU
Temperature	T	$280 \cdot r^{-1/2}$	K
Gas density profile	Σ_g	MMSN, Desch	g cm^{-2}
Dust-to-gas ratio	-	0.01	-
Turbulent strength	α	$10^{-4}, 10^{-3}, 10^{-2}$	-
Velocity distribution	-	Mean, Maxw., Exp.,	-
Clustering strength	k_1	$0, 10^1, 10^2, 10^3, 10^4, 10^5$	-
Clustering width	k_2	0.01, 0.05, 0.25	-
Clustering width	k_3	$10^{-3}, 10^{-2}, 10^{-1}, 10^0, 10^1$	-
Clustering width	k_4	$0, 10^{-2}, 10^{-1}, 10^0, 10^1$	-
Dust solid density	ζ	1	g cm^{-3}
Bouncing threshold	v_b	5, 50, 100	cm s^{-1}
Fragmentation threshold	v_f	5, 50, 100	cm s^{-1}
Erosion mass ratio	m_{crit}	$10^1, 10^2, 10^3$	-

tailed turbulent concentration model, but we also consider parameters that can be expected for e. g. zonal flows and streaming instabilities. The clustering effect is studied using the exponential velocity PDF, as this is what we expect for the smaller particles ($\text{St} \ll 1$) where the collisional barriers are expected.

A list of the investigated parameters is given in Table 4.1. We vary the disk parameters, i.e. the stellar distance, radial density profile and turbulent strength; the collision model parameters, i.e. the bouncing and fragmentation threshold velocities, and the critical erosion mass ratio (see Sect. 4.4.1), the velocity distribution type (see Sect. 4.4.2) and clustering parameters (see Sect. 4.4.3).

Finally, in Sect. 4.5.3, we also briefly show how the inclusion of a velocity distribution and clustering can cause shorter growth timescales for small dust grains.

4.5.1 The effect of a velocity PDF on the steady state

The results from the pure velocity PDF parameter study are given in Fig. 4.6. To understand the outcome of the inclusion of a velocity distribution, we can go back to Fig. 4.2. We now consider collision model SF, where all collisions occurring above $v_{\text{frag}} = 100 \text{ cm s}^{-1}$ lead to fragmentation, and all below lead to sticking. If only the mean velocity is considered, particle-pairs colliding at a mean velocity below or above will either result in always sticking or always fragmentation. This transition is clearly visible in the leftmost panels of Fig. 4.6, and is characterized by a very steep density drop at the place of the fragmentation (or bouncing) barrier.

However, if we now consider particle collisions occurring with a velocity PDF, the barriers are not as clearly defined. In Fig. 4.2, it is clear that even if

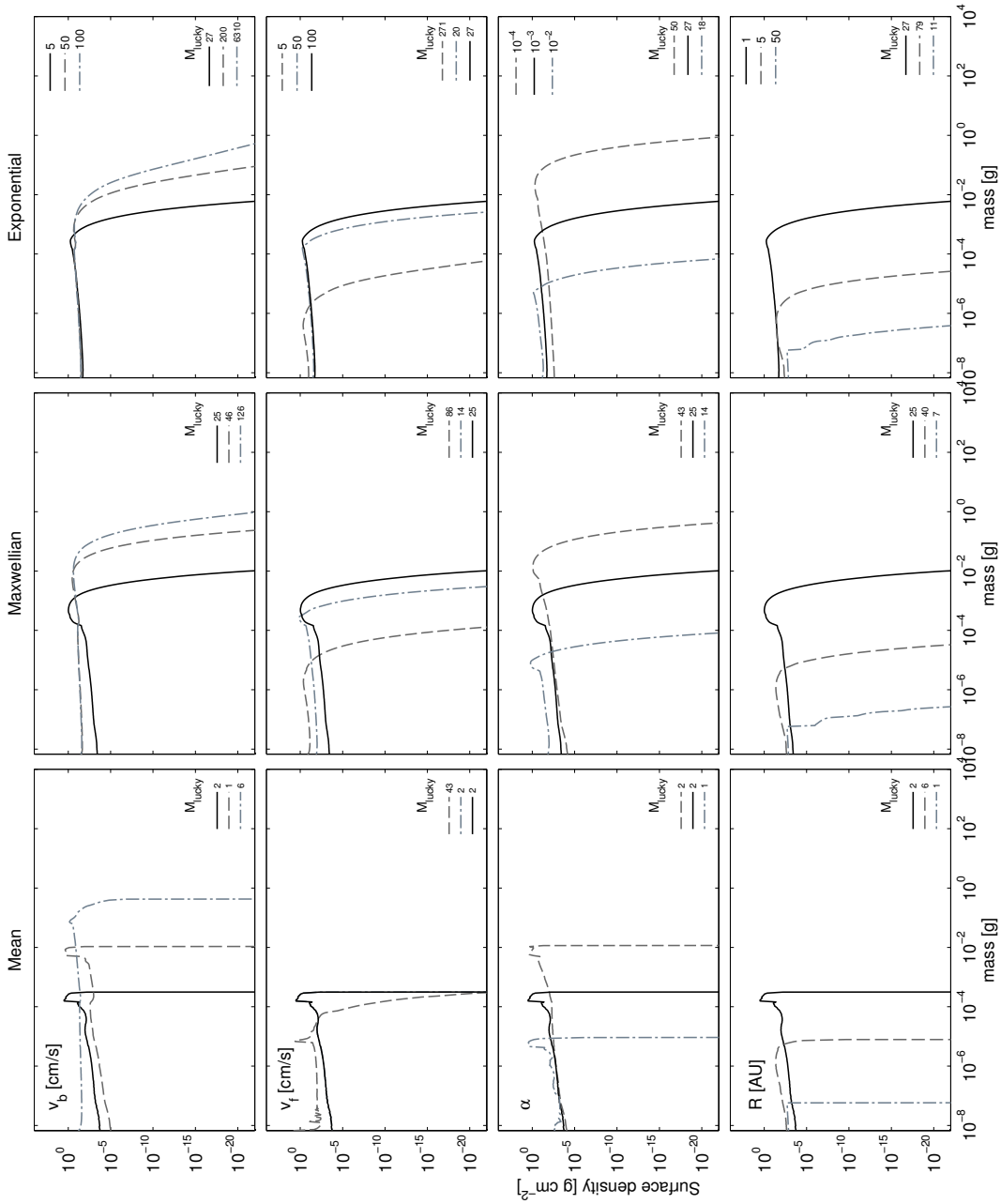


Figure 4.6: Overview of the steady-state distributions for different velocity distributions, with varying parameters α , v_b , v_t , and R . The fiducial model for each PDF is represented by the solid line. For each distribution, we also give the lucky mass fraction (defined in Eq. 4.26).

the mean-velocity is well above the fragmentation threshold, some sticking will occur by the population of low-velocity particles. If we on the other hand consider a low mean-velocity, fragmentation can still occur because of the high-velocity tail. This means that the particles will safely reach a slightly smaller size than before they start to fragment. Summing these two effects up, the fragmentation barrier is smoothed out. Due to the high-velocity population, the peak is generally shifted to slightly smaller sizes, but some particles can also be lucky and only collide in low-velocity sticking collisions, causing them to grow larger than the average size.

A velocity distribution also strongly affects the bouncing barrier. If we consider a particle-pair with a mean-velocity $\Delta v = v_b$ without a velocity PDF, particles are neither going to grow nor fragment, and a bump will form where all particles get stuck. When a PDF is considered, even though the majority of the collisions still lead to growth-neutral bouncing events, a significant number will also collide in the low-velocity sticking regime, and a few will collide in the high-velocity fragmenting regime. This means that the collisions that affect the growth will be predominantly sticking ones, and the growth can continue, albeit at reduced growth rates, until the sticking and fragmentation reach an equilibrium.

The position and shape of the smoothed collision barriers are more difficult to predict than in the case without a PDF. To understand the outcome better, we can calculate the velocity-integrated collision kernel (see Eq. 4.15) over a range of mean-velocities, as plotted in Fig. 4.7 for the case of collision models SF and SBF for both Maxwellian and exponential PDFs. The shapes of the sticking and fragmentation rates depend on two factors: Higher mean-velocities lead to generally higher collision rates, but also that more and more of the collisions result in fragmenting collisions instead of sticking.

This means that the sticking rate first increases with mean-velocity, until the decreasing number of low-velocity events counteract the generally higher collision rates. Comparing the two PDFs, we can note that the differences for low mean-velocities are relatively small. In the exponential case, because the low-velocity collisions contribute very little to the total collision rate, the sticking rate at lower mean-velocities is not significantly enhanced. At higher mean-velocities, however, the Maxwellian PDF results in very few sticking collisions compared to the exponential, leading to discrepancies of several orders of magnitude in the collision rate. The exponential PDF also causes fragmentation to occur earlier, as the high-velocity tail is stronger. The exponential distribution is therefore both beneficial and detrimental for growth, as its width promotes both more sticking and fragmentation.

Generally, the fragmentation barrier occurs roughly when the two collision rates intersect (this is however not entirely true due to the non-zero growth timescale, meaning that replenishing large particles is a slower process than fragmenting them). For collision model SF, this intersection occurs at almost the same mean-velocity for the two PDFs, which is also close to the classical fragmentation threshold.

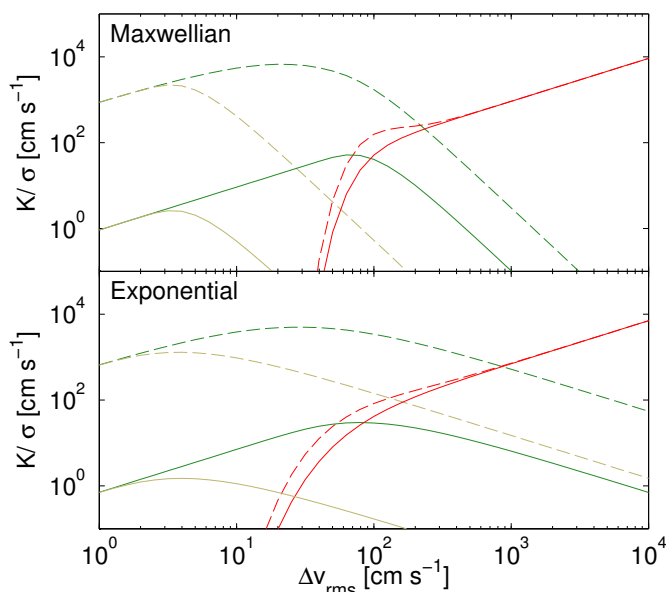


Figure 4.7: The integrated collision kernels for sticking for collision models SF (green) and SBF (brown) and fragmentation (red), which is valid for both models, plotted for the two velocity distributions without (solid) and with (dashed) clustering. The clustering parameters are $k_1 = 10^3$, $k_2 = 0.05$, $k_3 = 0$ and $k_4 = 0$, and we assume collisions between equal-sized particles (see Eq. 4.25).

One important property of a velocity distribution that was identified by [Windmark et al. \(2012b\)](#) and [Garaud et al. \(2013\)](#) was its capability to naturally produce large size ratios between the largest grains and the peak population. This could be important, as larger grains are generally more resilient against collisions with smaller grains than with other similar-sized grains, something which can reduce the fragmentation and even result in growth of the largest grains through mass transfer. Creating very large size ratios is however not trivial, as a single fragmenting collision could be enough to completely pulverize the grain, and it is currently unclear from the laboratory at which critical mass ratio the fragmentation stops (and could be anywhere in the range 10-1000 or even higher). In this work, we ignore the effect of mass transfer, but quantify how much more massive the luckiest particles can get compared to the average grain by introducing the lucky mass fraction

$$M_{\text{lucky}} = \frac{m_{\text{lucky}}}{m_{\text{peak}}}, \quad (4.26)$$

where m_{peak} is the particle mass at the peak of the distribution (in terms of total mass density), and m_{lucky} is the mass of the largest particles in the mass bin with enough mass corresponding to at least 1 physical particle. These values are given in Fig. 4.6 for each simulation. We can here note that for both distribution types, the bouncing barrier is detrimental to the formation of large, lucky particles.

The exponential distribution is more capable of creating large mass ratios than the Maxwellian distribution, and low turbulence is more bene-

ficial than high turbulence. These come from the same effect, which can again be explained by the collision rates shown in Fig. 4.7, and specifically how they depend on Δv_{rms} . Generally, the larger a particle grows, the higher relative velocities it is going to experience. Since the fragmentation rate increases and the sticking rate decreases with mean velocity, it gets successively harder for a particle to be involved in many subsequent low-velocity collisions. If these rates change fast, the sticking probability decreases quickly, and vice versa. If bouncing is introduced, the growth rate starts to decrease at lower Δv_{rms} , and the rates intersect earlier, where the fragmentation rate increases very rapidly, which then affects M_{lucky} . Similarly, if the turbulence is stronger, Δv_{rms} scale more rapidly with m .

To conclude, we find that the inclusion of a velocity distribution is unlikely to change the peak mass noticeably. In the case of bouncing, the velocity distribution will act to overcome the bouncing barrier, but bouncing will still be efficient in preventing large mass ratios from being formed. Work like Birnstiel et al. (2010b) and Pinilla et al. (2012b) should therefore not be much affected by the inclusion of a PDF. We also find that large mass ratios, which are important in a sweep-up scenario, are most likely to form in icy regions where bouncing is less likely, and they also benefit from quiescent regions such as dead zones.

4.5.2 *The effect of clustering on the steady state*

In Fig. 4.8, we show the results of the extensive cluster parameter study using the exponential velocity distribution. We note that parameter k_4 (which describes the strength of the monodisperse clustering away from the maximum stopping time τ_{max}), which we found in Sect. 4.4.3 to be a limiting factor for the effect of turbulent concentration, is here set to 0 by default, as this allows us to better disentangle and analyze the other parameters. This can be imagined as if the clustering was caused by a collection of effects such as turbulent concentration, zonal flows and streaming instabilities that span over a wider size-range than turbulent concentration alone.

The general effect of clustering on the steady state can be understood by considering the collision. Because clustered particles tend to have more correlated velocity vectors, their relative velocities are generally lower. This means that the sticking and fragmentation rates are not enhanced equally by the clustering, but it rather favors the sticking rate, as can be seen in Fig. 4.7. This causes a shift in the intersection between the sticking and fragmentation curves, which means that the clustering causes a shift of the fragmentation barrier towards larger sizes. Because a single fragmentation event can undo a large number of sticking events, and because the particle growth depends on the full size-distribution of particles, the point of intersection does not give the complete picture, but is still reasonable hint of how much the fragmentation barrier gets shifted. Below, we discuss the effect of each of the parameters individually:

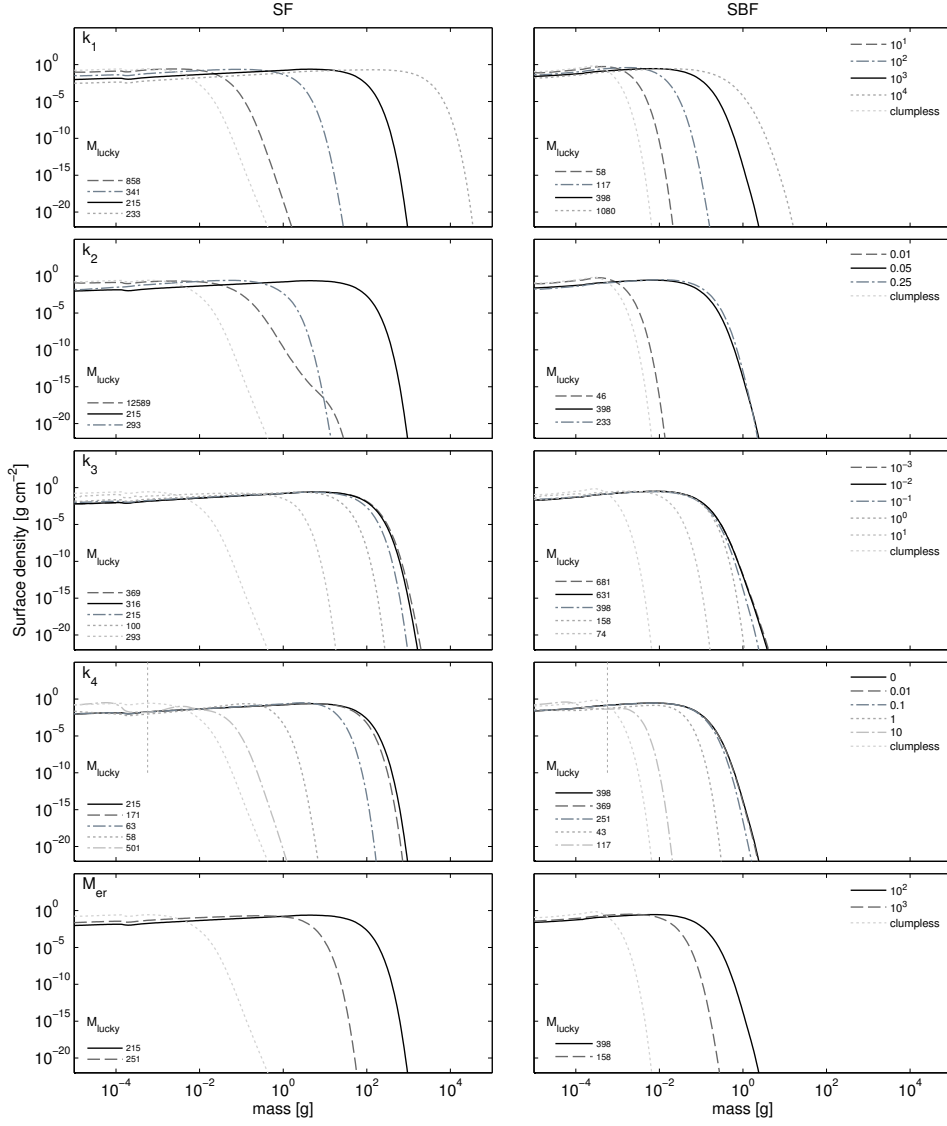


Figure 4.8: Overview of the steady-state distributions for the exponential PDF, with a variation of the parameters k_1 , k_2 , k_3 , k_4 , and M_{er} . The fiducial model for each PDF is represented by the solid line, and the vertical lines in panels k_4 represent the point of maximum clustering. For each distribution, we also give the lucky mass fraction (defined in Eq. 4.26).

- k_1 describes the maximal clustering strength, which directly translates into how much the growth rate is shifted upwards in Fig. 4.7. Clustering values below 10 affect the steady state relatively little, but values above that all give rise to noticeable changes. We can here note that the inclusion of bouncing significantly decreases the effect of clustering. This occurs because growth-neutral bouncing events replace sticking at the intermediate velocities, so that the dominant part of the enhancement from clustering is lost.
- k_2 governs which velocities get boosted by the clustering. In this study, we present three different general cases. For $k_2 = 0.05$, the ben-

eficial effect of the rate enhancement is the strongest, as clustering occurs for essentially all velocities in the sticking regime, with very limited boosting in the fragmentation regime (see Fig. 4.5). When the range of boosted velocities is more narrow, as with the case of $k_2 = 0.25$, only the lowest velocities are affected, which also limits the capability of the clustering. If the clustering is instead wider, as for $k_2 = 0.01$, the fragmentation rate is also enhanced, which works to counteract the sticking rate enhancement. We can note that the kink for the case of SF and $k_2 = 0.01$ occurs due to the shift from complete fragmentation to erosion, which by default is set to $M_{\text{er}} = 100$.

- k_3 determines how much particles of different stopping times will cluster. If the distribution is wide, clustering can enhance the rates of particles of very different stopping times. The beneficial effect of this decreases the more the width grows, as it is the particles around the mass peak that dominate the growth (note that the surface density is given by a very wide log-scale, so the peak is more prominent than it appears in the plots). We can note that even for a very narrow clustering width (in the case of $k_3 = 10$, only particles of mass ratios $\lesssim 5$ are boosted notably), the enhanced growth is significant. This shows how extremely important the collisions between equal-sized particles are for particle growth in general.
- k_4 determines at what particle stopping times that clustering occurs. For large values of k_4 , only particles exactly around τ_{max} will cluster, and small values allows clustering everywhere. We can here see one of the limiting factors of turbulent concentration, as the numerical simulations of [Pan et al. \(2011\)](#) point towards a relatively narrow regime of clustering. In the case of different radial distances or bouncing/fragmentation thresholds, the clustering can take place in a region entirely away from where non-sticking collisions are important, and will then only work to speed up the growth rate.
- We have also investigated the effect of M_{er} , the critical mass ratio above which fragmentation turns into erosion. This is a very important property, as it affects the balance between growth and fragmentation by limiting the detrimental effects of a fragmenting collision. For large values, fragmenting collisions will always be severe, which further works to prohibit the particles from growing large. For small values of M_{er} , the largest particles can escape from being totally destroyed by the particles of the peak population, which allows them to continue their growth at less risk of being completely destroyed.

Finally, we can note that the inclusion of clustering has caused M_{lucky} to shift to much larger values compared to the case without clustering, and it is here possible to reach mass ratios of 100 – 1000 even when bouncing is included, as long as the high-velocity collisions are not too much enhanced. This is because the clustering shifts the point of intersection in Fig. 4.7 to

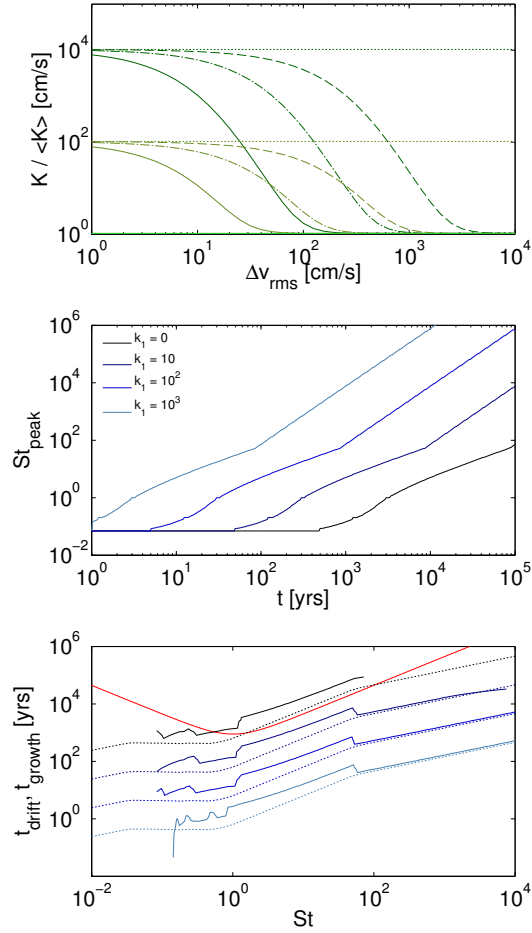


Figure 4.9: The *top panel* shows the integrated collision kernel for a pure sticking scenario with parameters $k_1 = 0, 10^2, 10^4$, $k_2 = 0.01, 0.05, 0.25$, $k_{3,4} = 0$. The *middle panel* gives the peak size for parameters $k_1 = 0, 10^1, 10^2, 10^3$, $k_{2,3,4} = 0$ at $R = 10$ AU. The *bottom panel* gives the drift timescale (red) compared to the numerical (solid) and semi-analytical monodisperse (dashed) growth timescales.

larger relative velocities, where the increase of the fragmentation rate with Δv_{rms} is lowered.

4.5.3 Growth timescale

Besides the effect that clustering has on the collisional barriers, it also affects the growth rate. This is interesting, as the enhanced growth rates could potentially become shorter than the drift timescale, so that the radial drift could be avoided. Clustering would here have the same role as the suggested role of porosity by [Okuzumi et al. \(2012\)](#). As clustering occurs primarily for particles of similar sizes, these enhanced growth rates would be relevant mostly for normal incremental growth between equal-sizes, and not sweep-up, so we here consider a case with pure coagulation to test our theories. This could correspond to growth in the outer regions where ices might push the fragmentation barrier to sufficiently high velocities so

that fragmentation can be avoided completely, as proposed by [Wada et al. \(2009\)](#). As radial drift is the strongest around $St = 1$, and turbulent concentration appears mostly for $St \ll 1$, the clustering of importance here would have to come primarily from zonal flows or streaming instabilities.

Implementing the clustering in a 1D code is beyond the scope of this work, and in this section, we focus on the comparison of the growth and drift timescales. The radial drift velocity of particles is given by

$$\frac{\partial R}{\partial t} = -\frac{2}{St + St^{-1}} \eta_r v_k \quad (4.27)$$

where $v_k = r\Omega$ is the Kepler velocity and

$$2\eta_r = -\frac{1}{r\Omega^2 \rho_g} \frac{\partial P}{\partial r} \quad (4.28)$$

is the ratio of the pressure gradient force to the radial stellar gravity, ρ_g is the gas density and P is the pressure ([Adachi et al. 1976](#); [Weidenschilling 1977a](#); [Nakagawa et al. 1986](#)). The drift timescale can then be calculated from $t_{\text{drift}} = R(\partial R/\partial t)^{-1}$.

The growth timescale can be approximated by considering monodisperse growth, where the particle distribution is represented by a delta-function. The growth rate is then given by

$$\frac{dm}{dt} = g \cdot \rho_d \sigma \Delta v, \quad (4.29)$$

where m is the particle mass, $\rho_d = \Sigma_d/(\sqrt{2\pi}h_d)$ is the dust density, $\sigma = 4\pi a^2$ the collisional cross section and Δv the relative velocity. We here take g to be the clustering factor assuming that all velocities are boosted equally by the clustering, meaning that $g = 1 + k_1$. Taking into account that $dm = 4\pi a^2 \zeta da$, we get

$$\frac{da}{dt} = \frac{\Sigma_d}{\sqrt{2\pi}h_d} \frac{\Delta v}{\zeta}, \quad (4.30)$$

where ζ is the solid density and, following [Birnstiel et al. \(2010a\)](#), we take the dust scale-height to be

$$h_d = H_g \cdot \min \left(1, \sqrt{\frac{\alpha}{\min(St, 0.5)(1 + St^2)}} \right), \quad (4.31)$$

which is valid for the dust near the midplane, which is the region we are interested in. The fact that h_d decreases with St also means that the growth timescale does not increase as much with size, causing even very large particles to grow relatively quickly. The growth timescale can then finally be calculated from $t_{\text{growth}} = a(da/dt)^{-1}$.

In [Fig. 4.9](#), we have investigated the growth and drift of particles at $R = 10$ AU for $\alpha = 10^{-3}$. Like [Okuzumi et al. \(2012\)](#), we consider a pure sticking scenario equivalent to a fragmentation velocity $v_f \gtrsim 50 \text{ m s}^{-1}$

considering that the highest relative velocity mean in this simulation is $\Delta v_{\text{rms}} = 30 \text{ m s}^{-1}$.

In the top panel, we plot the ratio between the integrated collision kernel and the kernel for the mean-velocity without clumping for a number of different models. We can note that contrary to the steady state scenario of the previous sections, in a pure sticking scenario, the growth rate benefits significantly from the enhancement of the higher velocities. At large mean-velocities, the low-velocity population contributes very little to the integrated kernel, and if there is no enhancement of the higher velocities, the kernel enhancement decreases or vanishes completely. In the middle panel, we plot the evolution of the peak position for four models of varying clustering strength during 10^5 yrs, assuming $k_{2,3,4} = 0$ to clearly show the effect of the clumping.

In the bottom panel, we plot the radial drift timescale versus the growth timescales, both measured numerically in the simulations and from the simple monodisperse model presented in this section. For the homogeneous case, the two timescales are very similar, and any type of growth will therefore be accompanied with a significant drift. However, since the timescale changes linearly with the clustering, even a modest clustering of 100 will lead to a greatly enhanced growth timescale that could well be enough to cause growth through the drift barrier. This scenario is however also so highly dependent on the velocities and size-scale that clustering occur, and will need to be studied further.

4.6 DISCUSSION AND CONCLUSIONS

We have performed numerical coagulation simulations to further understand the role of velocity distributions and particle clustering for the evolution of dust in protoplanetary disks. We have studied the role of clustering both for its effects on the collisional growth barriers and how it affects the steady state size distribution, as well as for its effects on the growth timescale, which is important for the understanding of the radial drift barrier. Clustering is caused by a number of effects such as turbulent concentration, zonal flows and streaming instabilities, but we have here focused mostly on the former. Due to numerical limitations, hydrodynamic studies of turbulent concentration have yet to resolve the scales that are relevant for coagulation, and the clustering between particles of different aerodynamic properties are just now starting to get mapped (Hubbard 2013). Because of these uncertainties, we have made both a case study and a more general parameter study.

For the role of velocity distributions, we find results that agree with the previous work of Windmark et al. (2012b) and Garaud et al. (2013). Because the relative velocities between particles are no longer represented by only a mean, a given particle pair now has the possibility to experience all types of collisional outcomes like sticking, bouncing or fragmentation, which tends to smooth out the collisional barriers. Because bouncing collisions lead to neither mass loss or gain, a velocity distribution will allow

the bouncing barrier introduced by [Zsom et al. \(2010\)](#) to be overcome, by making it possible for particles to be involved in many subsequent low-velocity collisions. In this study, we also investigated the effect of both a Maxwellian and an exponential velocity distribution, and found that the broader velocity distribution of the latter allows for even more extended tails in the steady state size distribution.

We have found that in the inner disk, turbulent clustering is the most efficient at just the sizes where the growth-hindering bouncing and fragmentation barriers occur. Clustering is important for the steady state, as it causes the clumped particle to have low relative velocities (in our code modeled as the clumping occurring mainly at these low velocities), which changes the balance between sticking and fragmentation. There are many factors that are important for the clustering effect on coagulation, and we have modeled it as an exponential that decreases with relative velocity, particle size ratio and distance from the point of maximum clustering. If the clumping is significant, above ~ 100 , the fragmentation threshold can be pushed to one or two orders of magnitude of larger sizes. This type of shift could be relevant for the formation of boulders large enough to initiate streaming instabilities. We have also found that clustering leads to generally wider tails of the size distribution towards larger particle sizes. These large size ratios between the largest and the mean particles could result in sweep-up growth and planetesimal formation, as introduced by [Windmark et al. \(2012a\)](#).

Clustering also enhances the particle growth rate. Through a simple argument of timescales, we have found that even a low amount of clustering could work to overcome the radial drift barrier, much in the same way as the role of porosity studied by [Okuzumi et al. \(2012\)](#). We have yet to study the exact effects of this, but it will be the subject of later work.

On its own, velocity distributions would have little effect on previous coagulation studies that have predicted opacities and been the basis for comparison with observations. With clustering, however, we predict that both its effect on the steady state and on the radial drift could have significant effects on the predictions.

GROWTH BREAKTHROUGH AT THE INNER EDGE OF DEAD ZONES

Adapted from Drążkowska, Windmark, Dullemond, A&A (2013), vol 556, A37¹

ABSTRACT

During the dust coagulation phase in the protoplanetary disk, the interaction between the dust and the gas gives rise to both collision barriers and rapid inward drift. Turbulence is a double-edged sword, as it is required to explain the observed gas accretion rates, but it also promotes fragmentation by being the strongest contributor to relative velocities between the dust particles. One solution to this problem might be the concept of dead zones, where the magnetorotational instability (MRI) turbulence is locally suppressed. In this chapter, we use a Monte Carlo code capable of modeling dust growth in both the radial and vertical directions, and study the effect of the dead zone that is thought to form outside of the snow line. Due to the sharp radial variation in the turbulent strength, a pressure bump is also formed, and we find that the combination of the two benefits planetesimal formation in multiple ways. Firstly, the dead zone is a quiescent region where the dust grains grow larger than they normally would before they start to bounce or fragment. Secondly, these "privileged" grains can drift into regions where they are so much more massive than the local grains that they become resilient towards the destructive impacts, and may instead grow large by sweep-up coagulation.

5.1 INTRODUCTION

The collisional growth barriers are caused by the grains colliding with impact energies sufficiently high to cause bouncing or fragmentation (Blum & Münch 1993; Güttler et al. 2010). In Chapter 2, we investigated the collision physics aspect of the barrier, and showed the capability for growth to occur via mass transfer provided that the mass ratio between the grains to occur. Even the updated collision model does little to shift the fragmentation barrier for similar-sized particles, however, but it is still possible for the barrier to be affected by a change in the local disk conditions.

An often quoted possible region for grain growth is the dead zone. MRI is believed to be the main source of turbulence in the disk, but it requires a sufficiently high ionization degree to function. If the ionization degree would be reduced, the coupling between the gas and the magnetic field is also weakened, and the MRI gets suppressed. Because small dust grains

¹ See page ix for details on authorship.

are efficient in capturing ionized gas, the evolution of the dust size distribution is therefore consequently linked to the turbulent strength (Sano et al. 2000; Ilgner & Nelson 2006). The gas ionization degree is also driven primarily by cosmic rays and X-rays, which means that the disk midplane might be shielded from most of the ionization in the first place. This might allow for dead zones to form near the midplane, so that only the upper disk layers are active (Okuzumi & Hirose 2011; Dzyurkevich et al. 2013).

Another possible mechanism for MRI dampening relies on the existence of the snow line, outside of which the solid density is believed to increase drastically due to the freeze-out of water (Hayashi 1981; Kretke & Lin 2007). Because the total available dust surface area increases, the gas ionization degree decreases. In such a dead zone, because the turbulence is not capable of strongly exciting the dust velocities, the dust grains are likely to grow much larger before fragmentation kicks in.

However, even if dead zones allowed for the collisional barriers to be overcome, the radial drift barrier introduced by Whipple (1972b) and Weidenschilling (1977a) would still be problematic. The drift is caused by the fact that the pressure supported gas rotates at slightly sub-Keplerian velocities, which gives rise to a constant gas drag on the dust grains that results in a rapid inward drift. If the grains are sufficiently large and decoupled from the gas ($St \gg 1$), the drift would however be sufficiently slow for the particle to survive. In its essence, the drift barrier is therefore an argument on timescales. In most of the disk, the drift timescale is so much shorter than the growth timescale for $St \sim 1$ that all proto-planetesimals would be lost in the star. If the relative velocities are lower inside a dead zone, the problem of the drift barrier would only worsen.

A possible way around the drift barrier could be for the drift to be halted long enough for the particles to grow to sizes $St \gg 1$. One such promising mechanism is locally positive pressure gradients, or pressure bumps (Whipple 1972a; Barge & Sommeria 1995; Klahr & Henning 1997). If the bumps are strong enough to counteract the turbulent diffusion, they would stop the drift for as long as they existed. By artificially including a large number of static pressure bumps in a dust evolution code, Pinilla et al. (2012b) showed that such bumps are an efficient way of keeping the global dust densities high for prolonged periods of time, provided that they are sufficiently long-lived. It does however seem to be clear that pressure bumps are capable of forming, at least in the azimuthal direction, as shown by van der Marel et al. (2013) in a recent observational study of the transition disk around Oph IRS 48.

It is however still not known exactly how these pressure bumps, radial or azimuthal, would form. One suggestion is as a result of MHD effects (Johansen et al. 2009; Dzyurkevich et al. 2010), but it is uncertain whether these bumps would be sufficiently long-lived. Another possibility could be gap clearing due to one or several giant planets, which could explain the shape of the observed transition disks (Pinilla et al. 2012a), but does little to explain how the planet was formed in the first place. Kretke & Lin (2007) suggested that the dead zone at the snow line could also give rise to

a pressure bump at the inner edge. Because turbulence is the main source of viscosity in the disk, a rapid change due to a dead zone will cause a reduction in the accretion efficiency, and the creation of a pressure bump.

In this chapter, we investigate the effect that the combination of a dead zone and a pressure bump has on the dust growth, particularly with respect to the sweep-up growth and the formation of the first planetesimal seeds. In the two previous chapters, we discussed the mechanism of seed formation where velocity distributions allow for the formation of a few lucky large particles. However, due to the scarcity of laboratory data, there are still no experiments that can directly confirm the structure of lucky grains, or the critical mass ratio for when erosive collisions turn into growth-positive mass transfer events. If the critical mass ratio turned out to be too high ($> 100 - 1000$), the lucky particle scenario would have trouble forming large enough seeds.

We therefore introduce a new possible seed forming mechanism by radial mixing of "privileged" grains from the dead zone and into the active regions. The key to this scenario is considering a non-local coagulation scenario, and in this chapter, we utilize a Monte Carlo code which is capable of following both the radial and vertical dimensions. In Sect. 5.2, we briefly discuss the Monte Carlo code that was used for the simulations. Sect. 5.3 discusses dead zones and pressure bumps in more detail, and Sect. 5.5 shows results from the simulations and explains how the two effects can result in growth breakthrough. Finally, in Sect 5.6, we discuss some caveats and future prospects.

5.2 A BRIEF OVERVIEW OF MONTE CARLO DUST EVOLUTION

We begin with a brief overview of the fundamental concept of dust evolution with the Monte Carlo method, in order to understand the results obtained from code developed by Joanna Drążkowska. For a more complete description, see [Zsom & Dullemond \(2008\)](#) or [Ormel & Spaans \(2008\)](#).

The principle idea of the Monte Carlo approach is to follow the evolution of a small subset of the total dust population, and to use these few particles to understand what happens to the total population. A small number of representative particles are chosen, where each such particle is taken to represent a swarm of particles with identical properties. If the number of representative particles is much smaller than the number of non-representative particles, only the collisions between the representative and the particles in the swarms have to be considered. In this approach, each representative particle i represents a swarm of N_i identical particles. We assume that each swarm has a certain total mass M_{swarm} that remains constant with time, thus allowing the number of physical particles to change.

At each time step, two collision partners are selected by random numbers. For each collision, a representative particle i and a non-representative

particle k are selected as collision partners (allowing also for $i = k$). The probability for a collision in a cell of volume V is given by

$$r_{ik} = \frac{N_k K_{ik}}{V}, \quad (5.1)$$

where K_{ik} is the collision kernel, defined as

$$K_{ik} = \Delta v_{ik} \sigma_{ik}, \quad (5.2)$$

where Δv_{ik} is the relative velocity and σ_{ik} is the collisional cross-section. The collision rate for particle i is then

$$r_i = \sum_k r_{ik}, \quad (5.3)$$

and the total collision rate among all particle pairs is

$$r = \sum_i r_i. \quad (5.4)$$

Firstly, it is decided which representative particle that is involved in the collision. The probability for particle i to be involved in the collision is

$$P_i = \frac{r_i}{r}. \quad (5.5)$$

The probability for particle i to collide with the non-representative particle k then becomes

$$P_{k||i} = \frac{r_{ik}}{r_i}. \quad (5.6)$$

If t_0 is the current time, the collision will occur at a time $t_0 + \tau$, where [Gillespie \(1975\)](#) determined the time step by sampling from an exponential distribution:

$$\tau = -\frac{1}{r} \log(\text{rand}), \quad (5.7)$$

where rand is a random number drawn from a uniform distribution between 0 and 1.

The outcome of the collision is determined by a collision model in a similar fashion to the Smoluchowski case. In the case of e.g. a fragmenting collision, the representative particle is broken up into a power-law of fragments. The new representative particle i is picked randomly from the mass-weighted fragment distribution, and the properties of the swarm corresponding to particle i are also updated. Because the collision always occurs with a non-representative particle k , its new properties are not reflected in the swarm.

To ensure that the resulting dust distribution is not artificially accelerated or slowed down, a sufficient number of representative particles is needed for each box to resolve the size distribution, usually between a few 100-1000. In the code developed by [Drazkowska et al. \(2013\)](#), the vertical and radial dimensions were included by stacking a number of boxes on top of each other in both directions, allowing the particles to move between the boxes. In order to accurately reproduce the analytical kernels in all boxes, an adaptive grid scheme was also included to make sure for each time step that a sufficient number of particles were included in each individual box.

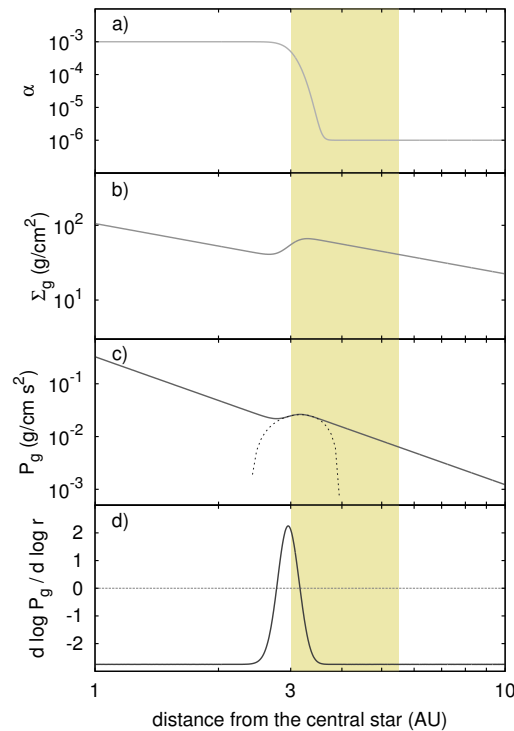


Figure 5.1: The radial variation in a number of different parameters according to the snow line model by Kretke & Lin (2007). The panels show the: a) α -parameter, b) gas surface density, c) gas pressure and the Taylor expansion around the location of the pressure bump, d) the gas pressure gradient. The highlighted region corresponds to the region described and investigated in Sect. 5.5.

5.3 DEAD ZONE AND PRESSURE BUMP FORMATION AT THE SNOW LINE

In this chapter, we utilize an analytical prediction of a single pressure bump occurring at the snow line, based on the work of Kretke & Lin (2007). In this model, the freeze-out of water outside of the snow line causes a damping of the MRI turbulence. Because the gas ionization fraction decreases due to an increased total surface density of solids, the coupling between the gas and the magnetic field is weakened, and consequentially also the strength of the MRI. Because the MRI is the main driver of the viscosity, the accretion rate changes suddenly across the snow line, which causes a pileup of gas. In the model of Kretke & Lin (2007), the change is made directly to the α parameter, which affects the gas surface density steady and pressure gradient as shown in Fig. 5.1.

In this model the degree of ionization is calculated under the assumption that all particles are μm -sized, meaning that the gas ionization rate is simply proportional to the dust-to-gas ratio. However, because of coagulation, the available dust surface area would not be constant, and the ionization rate and MRI strength would increase as the particles grow. Because of bouncing and fragmentation, there will always be a significant

fraction of small particles present in the disk, and we can consider the model to be a good approximation for this study.

In Eq. 1.41, we found that the radial drift of a dust grain depends on the pressure gradient through

$$v_r = -\frac{1}{\text{St} + \text{St}^{-1}} \cdot \frac{r}{v_k^2} \frac{1}{\rho_g} \frac{dP}{dr}, \quad (5.8)$$

where r is the stellar distance, v_k is the Keplerian velocity, ρ_g is the gas density and $P = \rho_g c_s^2$ is the pressure. If a pressure bump forms, it means that there will be a region in the disk where the pressure gradient is positive, so that particles in that region drift outwards until the pressure gradient switches sign again. The result is that the pressure bump region will collect more and more dust as it comes drifting inwards. The only way for the grain to escape the bump is if it is small enough for the turbulence to diffuse it through, or if the pressure bump disappears.

The significant decrease of α in the dead zone also has a significant effect on the local dust evolution. As we saw in Sect. 1.4.2, turbulence is normally the dominant source of high relative velocities between similar-sized particles, and it is significant also for different-sized particles. We have previously seen that $\Delta v \propto c_s \sqrt{\alpha}$, which means that if α decreases by three orders of magnitude, the relative velocity contribution from turbulence would decrease by a factor of 30. In the absence of turbulence, the growth can therefore proceed further (but slower) before fragmentation finally sets in. As we shall see, even if dead zones can not form planetesimals directly due to the still present collisional barriers and the drift barriers, this effect will still turn out to be relevant for the onset of sweep-up growth.

5.4 THE DISK AND COLLISION MODELS

We consider a disk with a steady state surface density profile derived by [Kretke & Lin \(2007\)](#)

$$\Sigma_g = \frac{\dot{M}}{3\pi\alpha_0 c_s h} - \Sigma_A \frac{\alpha_{\text{MRI}}}{\alpha_0} \quad (5.9)$$

where $\dot{M} = 10^{-9} M_\odot \text{ yr}^{-1}$ is the mass accretion rate, $\alpha_0 = 10^{-6}$ is the turbulent strength in the absence of MRI, α_{MRI} is the contribution from the MRI turbulence, and Σ_A is the surface density of the active surface-layer. The total disk mass between 0.1 and 100 AU is then $0.01 M_\odot$. We focus this study on the region around the pressure bump, between $r = 3 - 5.5$ AU, as highlighted in Fig. 5.1. At 3 AU, the disk has a gas surface density $\Sigma_g = 65 \text{ g cm}^{-3}$ and a temperature $T = 140 \text{ K}$. We assume a stationary gas disk, because we due to the computational expense of the simulations are limited to the first 3×10^4 yrs, which is much shorter than the typical disk evolution timescale.

We assume an initial dust to gas ratio of 0.01, and distribute the dust mass into monomers of size $a_0 = 1 \mu\text{m}$. The internal density of the particles is set to $\rho_p = 1.6 \text{ g cm}^{-3}$. For the simulations presented in this

study, we use over a half a million (exactly 2^{19}) representative particles and an adaptive grid resolution of 64 radial and 32 vertical zones. This gives 256 representative particles per cell. Each swarm represents a total mass of $\sim 10^{22}$ g, corresponding to a maximum representative particle size of roughly 10^{10} cm that is obtainable without breaking the requirement of having the the representative particle number much smaller than the number of physical particles in the corresponding swarm.

For the collision model prescription, we use two simplified versions of the collision scheme discussed in Chapter 2. In both models, we determine the sticking probability as a function of relative velocity:

$$p_s(\Delta v) = \begin{cases} 1 & \Delta v < v_s \\ 0 & \text{if } \Delta v > v_b \\ 1 - k & \text{otherwise,} \end{cases} \quad (5.10)$$

where $k = \log(1 + \Delta v - v_s) / \log(1 + v_b - v_s)$ describes the sticking to bouncing transition region described by Weidling et al. (2012). The fragmentation probability is determined by a step function:

$$p_f(\Delta v) = \begin{cases} 0 & \text{if } \Delta v < v_f \\ 1 & \Delta v \geq v_f, \end{cases} \quad (5.11)$$

and we let $v_s = 3 \text{ cm s}^{-1}$, $v_b = 60 \text{ cm s}^{-1}$, and $v_f = 80 \text{ cm s}^{-1}$ be the sticking, bouncing and fragmentation threshold velocities. In model A, during a fragmenting event, the mass of both particles is distributed after the power-law $n(m) \propto m^{-9/8}$ (Blum & Münch 1993).

In model B, we also include the mass transfer effect, which occurs when the particle mass ratio is sufficiently large so that only the smaller of the particles is fragmented. We take $m_{\text{crit}} = 1000$, where $m_{\text{crit}} = m_1/m_2 \geq 1$. We take a mass transfer efficiency of $0.8 \cdot m_2$, meaning that the more massive particle gains 80% of the mass of the smaller particle. It can here be noted that although we in Chapter 2 found the threshold between erosion and mass transfer to be very important for the growth to planetesimal sizes, we are here mostly concerned at the point where sweep-up is initiated. We can therefore safely ignore the erosion, which is more relevant for the later sweep-up stages.

5.5 SWEEP-UP GROWTH AT THE INNER EDGE OF DEAD ZONES

In previous chapters, we have shown that the presence of a collisional growth barrier such as the bouncing or fragmentation barrier can be beneficial for the growth of planetesimals. If only a few seed particles manage to form and break through the barriers, they can initiate sweep-up via mass transfer collisions and continue to grow to kilometer-sizes. We have previously shown that velocity distributions can create size ratios of a few 100 between the luckiest particles and the particles in the peak, but the exact critical mass ratio has yet to be determined in the laboratory. In this

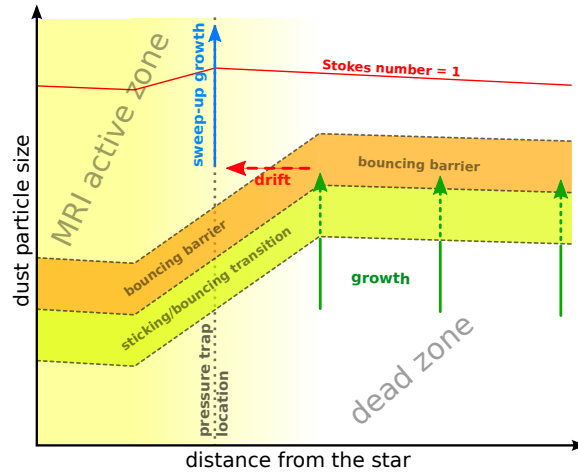


Figure 5.2: Sketch of the proposed growth breakthrough mechanism at the inner edge of a dead zone. The different collision regimes are shifted in size due to the change in α with radius. Large particles can form in the dead zone, and as they drift inwards, they can initiate their sweep-up growth.

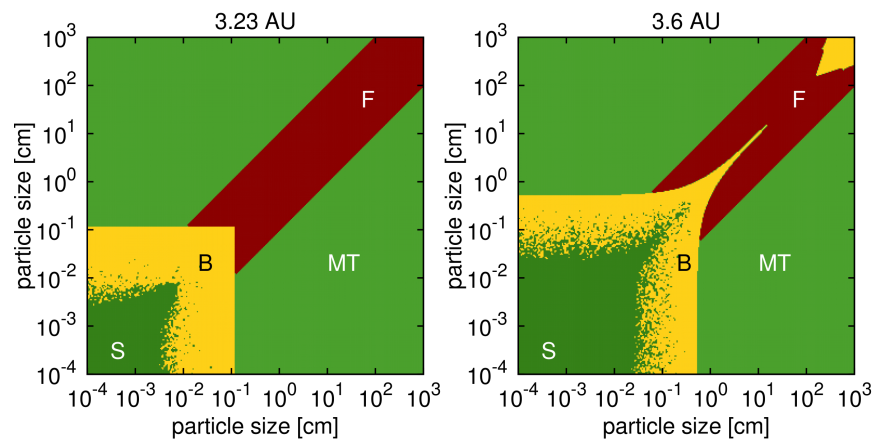


Figure 5.3: The collision outcome field at the location of the pressure bump and inside the dead zone. Green marks where the largest particle will grow in a collision, yellow is where the outcome is neutral, and red marks particle fragmentation, "S" stands for sticking, "B" bouncing, "F" fragmentation, and "MT" mass transfer.

section, we will show that large size ratios of >1000 can also be obtained by considering radial mixing of the "privileged" particles in the dead zones.

Fig. 5.2 shows a sketch of the principle idea of our model. In the MRI active region in the inner disk, the turbulence is stronger than in the dead zone in the outer disk, causing the growth to halt at significantly smaller particle sizes. The radial drift, which increases with particle growth, transports the largest privileged particles to the MRI active region. In doing so, it also transfers them into another collisional regime, where they become seeds that can continue to grow by the sweep-up of the small grains

trapped below the bouncing barrier. At the same time, the pressure bump also prevents the seeds from becoming lost in the star due to drift.

In Fig. 5.3, we give a map of the collision outcomes for collision model B in the midplane at both the location of the pressure bump at 3.23 AU and in the dead zone at 3.6 AU. We can here note the actual differences that we sketched out in the previous figure. The significantly lower turbulence in the dead zone compared to the pressure bump ($\alpha = 10^{-6}$ and $\alpha = 10^{-3}$), means that the particle growth can continue to more than one order of magnitude larger sizes before it is halted by the bouncing barrier. If we ignored radial drift and allowed the growth to proceed locally, the particles would grow to ~ 0.01 cm and ~ 0.5 cm. However, the situation changes drastically when drift is included and particles from different growth regions are allowed to mix.

The result of the dust evolution simulation using collision model B is shown in Fig. 5.4, where we plot the vertically integrated dust density at six snapshots between 500 and 30,000 yrs (the simulation times are more limited compared to the Smoluchowski simulations due to the increased computational expense of the Monte Carlo approach). The dust growth proceeds the fastest in the inner disk, where the relative velocity and the dust density are the highest. After around 1,000 yrs, the particles in the inner disk reach the bouncing barrier and stop growing. As time progresses, particles further out also reach the bouncing barrier, and after roughly 20,000 yrs, the majority of the dust is kept small by the bouncing barrier, and only evolve by slowly drifting inwards.

In Fig. 5.4, we also plot the positions of three selected swarms. All three swarms have identical initial locations and masses, and two of them become seeds for sweep-up, while the third, representing the average particle, does not. As shown in Fig. 5.3, the dead zone allows for the formation of the largest particles, because it is there that the relative velocities are the lowest. Because of the transition regime between sticking and bouncing, however, only a small number of particles manage to grow to the largest sizes before they drift too far inwards. The few particles that do manage, however, find themselves in a region with a higher turbulence, and consequently also higher relative velocities. At this stage, some particles fragment due to similar-sized collisions, but some manage to avoid being disrupted. In the end, the survivors find themselves in a region where most of the particles are significantly smaller, which allows them to grow larger via sweep-up. The selected swarms reach the pressure bump after 27,500 yrs, and their drift halts. After 30,000 years, the two successful seeds have managed to grow to meter-sizes.

A limiting factor of sweep-up growth is when the total number of large particles becomes too high, as this leads to too many fragmenting collisions that counteract the sweep-up. If the number of large particles is limited, however, mass transfer collisions will dominate, and the growth can continue. In our simulations, we find that the inclusion of a smooth sticking/bouncing transition regime is a natural way to create such a limited number of seed particles.

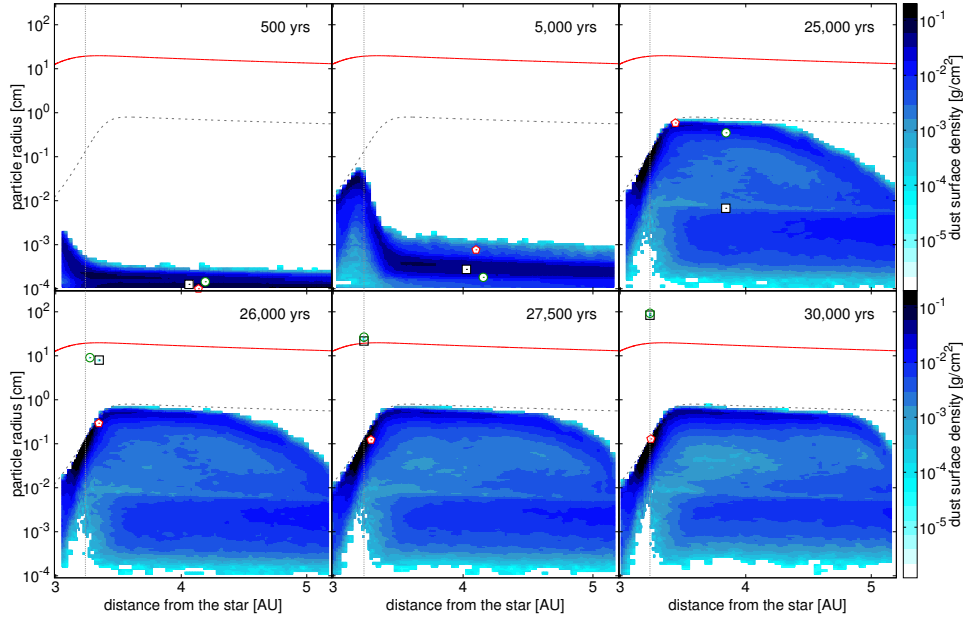


Figure 5.4: The radial variation in the vertically integrated dust density at different time steps using collision model B. The solid line shows the particle size corresponding to $St = 1$, and the dashed line shows the approximate position of the bouncing barrier. The vertical dotted line shows the location of the pressure bump. The symbols mark a few selected representative particles that we include to illustrate the dust evolution.

In Fig. 5.5, we present the evolution of the spatially integrated size-distribution for model B, and Fig. 5.6 shows the evolution of the median and maximum radius of the dust particles for both collision models. Initially, both of the models evolve exactly the same, and the median and maximum particle sizes increase gradually from μm - to mm -sizes. After about 23,000 yrs, the largest particles in model A halt their growth at a size of 0.7 cm when they reach bouncing barrier. The median size continues to grow, because all particles have yet to reach the bouncing regime. In model B, however, the first seeds form and drift inward and initiate the sweep-up, causing a sudden increase in the largest particle sizes up to meter-sizes.

It is also interesting to note the two spikes appearing in the maximum grain size after 23,000 yrs. These represent the formation of the first seed particles that are unlucky enough to fragment with similar-sized particles before they have grown to large-enough sizes to safely continue their sweep-up. It is also clear from Fig. 5.6 that the sweep-up process is so far only local and represent a small fraction of the total dust mass, as the median particle size remains unchanged between models A and B.

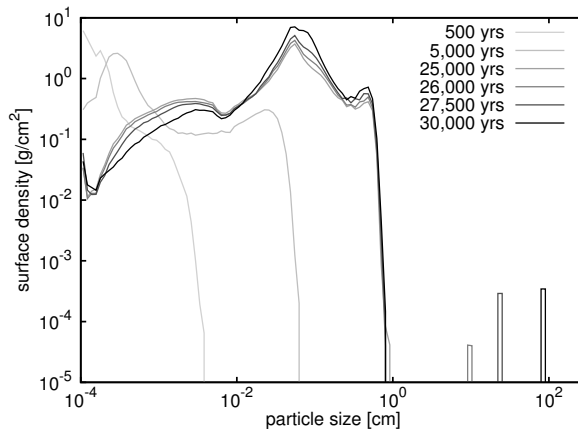


Figure 5.5: The vertically and radially integrated surface density evolution for collision model B.

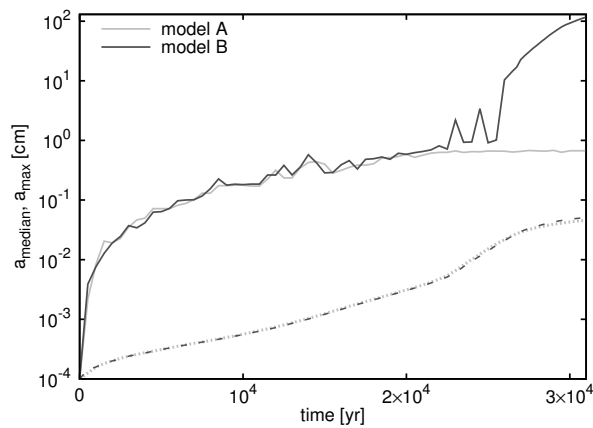


Figure 5.6: The size evolution of the largest (solid) and the median (dashed) sizes for collision models A and B.

5.6 DISCUSSION AND CONCLUSIONS

We have found that a sharp change in the radial structure of a protoplanetary disk can trigger the sweep-up scenario suggested in Chapter 2. We studied the dust growth in the region around the snow line in a low-mass protoplanetary disk, and modeled the disk following the prescription of [Kretke & Lin \(2007\)](#). In this model, the turbulent viscosity changes around the snow line due to a drop in the gas ionization fraction, leading to the formation of a low turbulence region as well as a pressure bump. Due to radial mixing, the privileged particles in the dead zone become seeds that halt their growth at the pressure bump, where they experienced increased growth rates towards planetesimal sizes due to the local enhancement of solids.

Our model includes a number of simplifications. We did not include the gas disk evolution, which is not consistent with the snow line model we implemented, as the gas ionization rate and thus the turbulence strength is dependent on the gas and dust properties. When the dust growth is included, the total dust surface area changes, which would change the

turbulent strength. We focused this study on the disk region around the snow line, where the temperature allows for existence of solid water ice. However, due to the lack of laboratory data both for the ice collision properties and its evaporation, condensation or sintering behavior (Kuroiwa & Sirono 2011; Sirono 2011), we only considered the silicate grain properties. If ices, which are capable of growing larger than silicates, are included, the region could be even more favorable for seed production provided that the ices can survive the sintering and evaporation.

The planetesimal formation model we propose relies on the existence of a growth barrier, such as the bouncing barrier introduced by Zsom et al. (2010). The robustness of the barrier has recently been put into question as the sticking and bouncing efficiency have been shown to exhibit a strong dependence on the internal structure of colliding aggregates as well as the impact parameter (Wada et al. 2011; Kothe et al. 2013a). Even though the results on the bouncing behavior is inconclusive, we argue that fragmentation could also work in a similar fashion for the sweep-up scenario. In a case where fragmentation acts as the main growth barrier, the main dust population would be able to grow a bit further, but might still be swept up by the drifting seeds. As the mass transfer experiments have so far been performed over a limited parameter space only, this possibility would need to be verified experimentally.

The snow line region has been shown to be favorable for planetesimal formation also in previous studies (Schlaufman et al. 2009). Recent work by Martin & Livio (2013) also argue that the snow line region is likely to be the location of asteroid belts also in debris disks, based on the correlation between the snow line location and the observed warm dust belts. It is however worth noting that the planetesimal formation mechanism introduced in this work can take place also at locations other than the snow line. It was also found by Dzyurkevich et al. (2013) that the steep variation in the turbulence strength and pressure bump formation discussed in this work can occur also beyond the metal freeze-out line, meaning the location beyond where gas phase metal atoms thermally adsorb on dust particles. The mechanism discussed in this work also has the potential to result in a narrow planetesimal ring similar to the one suggested by Hansen (2009) to explain the formation and mass distribution of the terrestrial planets in the Solar System.

We find that the thresholds and structure of the protoplanetary disk, such as the snow line and dead zones, could have a great impact on the emergence and evolution of planetary systems. Even outside of a best-case scenario, in a low-mass protoplanetary disk composed of silicates prone to bouncing and fragmentation, some particular locations could allow for their formation even if the global planetesimal formation is difficult.

PILE-UP OF PLANETESIMALS IN THE INNER PROTOPLANETARY DISK

Adapted from Windmark, Okuzumi, Drazkowska, A&A (in prep.)¹

ABSTRACT

In the Solar System, the terrestrial planets have a peculiar mass-distribution that hints towards a primordial ring of planetesimals between 0.7 and 1 AU. There are also indications that many exoplanetary systems with planets at tight orbits, for example the Kepler-11 system, were formed in-situ rather than being a result of planetary migration. In this chapter, we argue that the observed planetary system properties could be a result of the very first stages of formation, when dust coagulates into planetesimals. To investigate this possibility, we implement a collision model that includes the possibility of sweep-up and utilizes impact velocity distributions into a 1D dust-evolution code, and study the dust growth in the first 100,000 years. Because of rapid coagulation and sweep-up in the inner protoplanetary disk, and the increasing decoupling of the planetesimal seeds from the gas as they drift towards the star, we find that planetesimals can form and tend to preferentially pile up in the region between 0.1-3 AU. We find that a sizable population of planetesimals can form in only a few thousand years, and that this population will increase in size and number as more dust drifts inwards from the outer parts of the disk. Outside of the critical pile-up region, however, we find that the strong drift prevents planetesimals from ever forming. It might be that the collisional growth barriers and the radial drift barrier pose such strong limitations on the planetesimal formation that it might have to be considered a local rather than a global feature in the protoplanetary disk.

6.1 INTRODUCTION

Due to the existence of the dust growth barriers, such as the radial drift barrier (Whipple 1972b; Weidenschilling 1977a; Nakagawa et al. 1986), the collisional barriers due to fragmentation and/or bouncing (Blum & Münch 1993; Zsom et al. 2010), and the charge barrier (Okuzumi et al. 2011a,b), it is currently unknown how growth proceeds to the kilometer-sized planetesimals where gravity can start to aid in the accretion. Due to these uncertainties, planet population synthesis models (e.g. Ida & Lin 2004 and Mordasini et al. 2009) usually take the initial planetesimal distribution as a free parameter, only weakly constrained by observations from the Solar

¹ See page ix for details on authorship.

System. One such constraint can be obtained from the size-distribution of the present day asteroid belt and its collision history (Bottke et al. 2005). Another hint can be seen in the mass distribution of the terrestrial planets, where Mercury and Mars are significantly less massive than the Earth and Venus. Because the masses of Mercury and Mars ($\sim 0.1M_E$) are comparable to the theoretically predicted isolation mass, they have been suggested to be surviving protoplanets (Kokubo & Ida 2000; Kokubo et al. 2006), and radioactive dating supports this scenario for Mars (Dauphas & Pourmand 2011).

The protoplanetary growth is believed to come from giant impacts from planetesimals and protoplanets after the dispersal of the gas disk, which is the common explanation for the formation of Earth and Venus. So, assuming that Mercury and Mars are surviving protoplanets, why did they not experience these giant impacts? One plausible explanation is that the planetesimals/protoplanets were initially confined within a narrow ring between 0.7 and 1.0 AU (Hansen 2009). In this scenario, Mercury and Mars were protoplanets initially located at the inner/outer edges of the ring, which were scattered away gravitationally, and hence survived.

The remaining problem is how to make such a narrow planetesimal ring. Walsh et al. (2011) suggested in the so-called Grand Tack model that Jupiter shepherded the planetesimals inwards to 1 AU during its own migration from 3.5 to 1.5 AU, before it again migrated outwards due to a 3:2 mean motion resonance with Saturn. How the inner truncation at 0.7 AU was formed is however unclear.

Another interesting recent discovery are the close-in, tightly packed exoplanetary systems like Kepler-11 (Lissauer et al. 2011; Borucki et al. 2011) and Kepler-33 (Lissauer et al. 2012). They consist of a number of planets with sizes between Earth's and Neptune's, all with orbits within a few times that of Mercury. These systems, and the general existence of hot super-Earths, Neptunes and Jupiters, have previously been explained by migration or planet-planet scattering followed by tidal circularization (Nagasawa & Ida 2011). However, these mechanisms fail to explain the low dispersion of inclinations.

It would perhaps be most natural to think of the planetesimal ring formation or close-in planets as a direct consequence of planetesimal formation rather than as a result of external perturbation. A lot of progress has been made on the simulation and understanding of dust coagulation in recent years. There are now suggested scenarios for overcoming the collisional growth barriers, either by stickier, highly porous ices (Okuzumi et al. 2012; Kataoka et al. 2013) or sweep-up (Windmark et al. 2012a,b; Garaud et al. 2013; Drazkowska et al. 2013). There are also suggestions for how the radial drift barrier can be overcome; either by rapid coagulation (Okuzumi et al. 2012), pressure bumps (Pinilla et al. 2012b) or by pile-up (Youdin & Shu 2002; Laibe et al. 2012).

Because we already know that planetesimal formation is subject to many barriers, it would not be surprising if planetesimals formed and survived in only a limited region of the solar nebula. In this chapter, we investigate

the formation of planetesimals through sweep-up, and find that planetesimals tend to pile up in the inner region as a direct result of the shape of the protoplanetary disk. In Sect. 6.2, we compare the analytical timescales for radial drift and dust growth and implement this in a simple toy-model, and in Sects. 6.3-6.4, we discuss the implementation and results of a collision model capable to handling sweep-up into a 1D coagulation code. Finally, in Sect. 6.5, we discuss the consequences and limitations of these findings.

6.2 DRIFT AND GROWTH TIMESCALES

We first consider the radial drift and dust growth from an analytical perspective. In Sects. 6.2.1 and 6.2.2, we calculate the drift and growth timescales and how they vary with heliocentric distance. A similar derivation and its consequences without growth has previously been discussed by [Laibe et al. \(2012\)](#), but we aim to make the process a bit more transparent. In Sect. 6.2.3, we put the previous results together and follow the growth and drift of particles in a monodisperse toy model.

We assume a protoplanetary disk with surface gas density and temperature profiles given by two power-laws

$$\Sigma_g(r) = \mathcal{F}_{\text{disk}} \Sigma_{g,0} \left(\frac{r}{1 \text{ AU}} \right)^{-p} \text{ g cm}^{-2} \quad (6.1)$$

$$T(r) = T_0 \left(\frac{r}{1 \text{ AU}} \right)^{-q} \text{ K}, \quad (6.2)$$

where r is the radial distance from the star. We will in this work consider two different disks. The minimum mass solar nebula (MMSN) is derived from the present-day Solar System, and has $\Sigma_{0,g} = 1700 \text{ g cm}^{-2}$ with $p = 3/2$ ([Weidenschilling 1977b](#); [Hayashi 1981](#)). The minimum mass extrasolar nebula (MMEN) is derived from the properties of the observed exoplanetary systems, and has $\Sigma_{0,g} = 9900 \text{ g cm}^{-2}$ with $p = 1.6$. Unless otherwise stated, we take a temperature profile with $T_0 = 280 \text{ K}$ and $q = 1/2$. We will in this work assume $\mathcal{F}_{\text{disk}} = 3$ to describe how much more massive the primordial disk was compared to the present-day properties, which in the case of the MMEN corresponds to a disk which is on the verge of gravitational instability.

6.2.1 Radial drift

Solids normally orbit with Keplerian velocities, but the gas is supported by a radial pressure gradient, and thus orbit at slightly sub-Keplerian velocities. As shown in Eq. 1.41, the result is a constant headwind which gives rise to a drag force and inward radial drift with a velocity given by

$$v_r = \frac{\text{St}}{1 + \text{St}^2} \cdot 2\eta v_K, \quad (6.3)$$

where

$$2\eta = -\frac{r}{v_K^2} \frac{1}{\rho_g} \frac{dP}{dr} \sim r^{1-q}, \quad (6.4)$$

is the ratio of the pressure gradient force to the stellar gravity in the radial direction, $v_K = r\Omega = (\frac{GM}{r})^{1/2}$ is the Kepler velocity and c_s is the sound speed (Weidenschilling 1977a). St is the Stokes number, describing how well the particle is coupled to the surrounding gas, and is given by $St = t_s\Omega$, where

$$t_s = \begin{cases} t_s^{(\text{Ep})} = \frac{a\bar{\zeta}}{\rho_g v_{\text{th}}} & \text{if } a < \frac{9}{4}\lambda \\ t_s^{(\text{St})} = \frac{4a}{9\lambda} \cdot t_s^{(\text{Ep})} & \text{if } a > \frac{9}{4}\lambda, \end{cases} \quad (6.5)$$

where $\bar{\zeta}$ is the dust internal density, ρ_g is the gas density, $v_{\text{th}} = (8/\pi)^{1/2}c_s$ is the mean thermal velocity. The mean free path of the gas particles is

$$\lambda = \frac{1}{n_g\sigma_g} = \sqrt{2\pi} \cdot \frac{m_g H_g}{\sigma_g \Sigma_g} \sim \frac{c_s}{\Omega_k \cdot \Sigma} \sim r^{\frac{3}{2}+p-\frac{q}{2}}, \quad (6.6)$$

where $\sigma_g = 2 \cdot 10^{-15} \text{ cm}^2$ is the collisional cross section of the gas molecules, $H_g = c_s/\Omega_k$ is the gas scale-height, and the gas midplane number density is $n_g = \Sigma_g/(\sqrt{2\pi}H_g m_g)$, where m_g is the mass of the gas particles.

The fate of a drifting particle depends on the drag regime it is in, and in the following sections, we look at the drift timescale in the two regimes individually. In both cases, we are interested in how the drift timescale changes as the particle drifts inwards, assuming for now that its size remains constant.

Drift in the Epstein regime

If the particle is small ($a < 9\lambda/4$), the gas drag can be understood as a result of the momentum transfer between the dust particle and the individual gas molecules. The Stokes number is in this regime given by

$$St = \frac{\pi \bar{\zeta} a}{2 \Sigma} \sim r^p, \quad (6.7)$$

and assuming small particles ($St \ll 1$), the drift can be written

$$\frac{\partial r}{\partial t} \sim \eta v_K St \sim r^{1-q} \cdot r^{-\frac{1}{2}} \cdot r^p \sim r^{\frac{1}{2}-q+p}. \quad (6.8)$$

The drift timescale is then

$$t_{\text{drift}} \sim r \left(\frac{\partial r}{\partial t} \right)^{-1} \sim r^{\frac{1}{2}+q-p}. \quad (6.9)$$

This means that as long as $\frac{1}{2} + q - p < 0$ is satisfied, the drift timescale increases as a small particle drift inwards towards the star. This means that particles in the Epstein regime will at some r get a drift timescale that exceeds the disk lifetime, which is the fundamental mechanism of the small particle pile-up with subsequent gravitational instability as suggested by Youdin & Shu (2002).

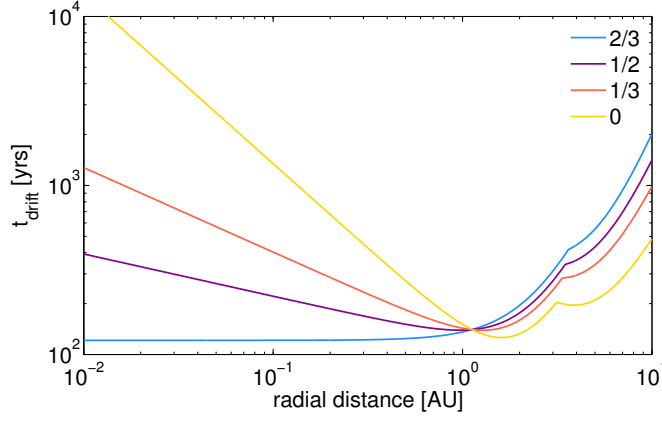


Figure 6.1: The radial-dependent drift timescales for a particle of size $a = 100$ cm in an MMSN disk with four different temperature slopes.

Drift in the Stokes regime

If the dust particle is large ($a > 9\lambda/4$), the gas drag instead arises from an aerodynamic flow around the particle by the gas molecules. This is called the Stokes regime (unrelated to the Stokes number), and assuming a particle Reynolds number < 1 , the Stokes number can be written

$$\text{St} = \frac{\pi \zeta a}{2 \Sigma} \cdot \frac{4a}{9\lambda} \sim r^{-\frac{3}{2} + \frac{q}{2}}. \quad (6.10)$$

For large particles ($\text{St} \gg 1$), the drift velocity is given by

$$\frac{\partial r}{\partial t} \sim \eta v_K \text{St}^{-1} \sim r^{1-q} \cdot r^{-\frac{1}{2}} \cdot r^{-\frac{q}{2} + \frac{3}{2}} \sim r^{2 - \frac{3q}{2}}. \quad (6.11)$$

And the drift timescale is finally

$$t_{\text{drift}} \sim r \left(\frac{\partial r}{\partial t} \right)^{-1} \sim r^{-1 + \frac{3q}{2}}, \quad (6.12)$$

which means that for $q < \frac{2}{3}$, the drift timescale will increase as the large particles drift inwards. In the MMSN disk, this is valid, which means that a drifting planetesimal or protoplanesimal will stop its drift at some finite heliocentric distance. This mechanism was suggested by [Laibe et al. \(2012\)](#) as a means to overcome the drift barrier and cause a particle pile-up in the inner disk. However, if the pile-up occurs too close to the star, the particles would be evaporated due to the high temperatures, which generally occurs between $0.01 - 0.1$ AU.

In Fig. 6.1, we plot the drift timescale for a particle of constant size 100 cm for an MMSN disk with four different temperature slopes between $q = 0$ and $2/3$. At distances larger than 1 AU, the particle is in the Epstein regime and the drift timescale decreases as it moves closer to the star, but as it enters the Stokes regime, the drift timescale suddenly starts to increase.

We can note that for any realistic temperature slope, even though the drift timescale increases the closer in the particle gets, the increase is never

steep enough to completely halt the drift at any reasonable r . In the case of $q = 1/2$, the particle would drift from 1 to 0.01 AU in 1100 yrs, and for $q = 1/3$, the total time increases to 2300 yrs, which is much shorter than the disk lifetime. We can therefore conclude that the increasing drift timescale alone is not sufficient to cause a large particle pile-up. We will however see that when particle growth is included, the picture changes considerably.

6.2.2 Particle growth

For the purpose of the analytical approach, we consider a simplified version of the sweep-up scenario introduced by [Windmark et al. \(2012a\)](#), where one or a few large bodies, or protoplanetesimals, of mass m drift and move around in a sea of small particles of mass m_s , while being few enough to never collide between themselves. The mass growth of the protoplanetesimals can be described by

$$\frac{dm}{dt} = \sigma \Delta v \epsilon \rho_s, \quad (6.13)$$

where $\sigma = \pi(a + a_s)^2 \sim \pi a^2$ is the collisional cross section, Δv is the relative velocity between the large and small particles, ϵ is the sweep-up efficiency, which we for simplicity put to 0.5 ([Wurm et al. 2005](#)). As the protoplanetesimals grow, they settle towards the midplane, and we let $\rho_s = \Sigma_s / (\sqrt{2\pi} h_d)$ be the midplane mass density of small particles.

We assume that the small particles dominate the total dust mass, and that they are small enough to be well coupled to gas, so that the particle scale-height $h_d = H_g$. We also assume the mass of the small particles to be independent on r . For simplicity we consider turbulence as the main relative velocity source. For collisions between a large particle and a smaller, [Ormel & Cuzzi \(2007\)](#) find that $\Delta v = c_s \sqrt{3\alpha / \text{St}}$, where α is the turbulent strength. Taking into account that $dm = 4\pi a^2 \zeta da$, we get

$$\frac{da}{dt} = \frac{\sigma}{4\pi a^2} \frac{\Sigma_s}{\sqrt{2\pi} H_g} \Delta v \epsilon = \frac{\Sigma_s}{\sqrt{32\pi} H_g} \Delta v \epsilon \sim r^{3/4-p-q/4}, \quad (6.14)$$

The growth timescale can finally be written as

$$t_{\text{growth}} = a \left(\frac{da}{dt} \right)^{-1} = a \frac{\sqrt{2\pi} H_g}{\Sigma_s \epsilon \Delta v} \sim r^{-3/4+p+q/4}, \quad (6.15)$$

meaning that as long as $p + q/4 > 3/4$, which is true for all normal disks, the growth timescale of a particle of a given size decreases with decreasing radial distance.

For comparison, we also consider a monodisperse pure coagulation case, where the particles are represented by one single species, and always stick during collisions. This has previously been derived by e.g. [Birnstiel et al. \(2010a\)](#), and the growth rate can be written

$$\frac{da}{dt} = \frac{\Sigma_d}{\sqrt{2\pi} h_d} \frac{\Delta v}{\zeta} \sim r^{-3/4+p+q/4}, \quad (6.16)$$

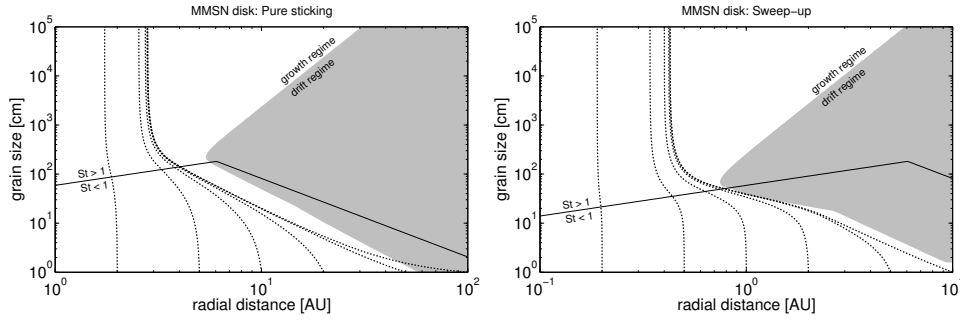


Figure 6.2: The evolution of seed particles in an MMSN disk assuming pure coagulation (*left panel*) and sweep-up (*right panel*). Note the different x-range! The seeds have initial particles sizes $a = 1$ cm, and starting locations between 0.2 – 100 AU. The solid line marks $St = 1$, where the radial drift is the fastest, and the filled gray region marks where $t_{\text{drift}} < t_{\text{growth}}$.

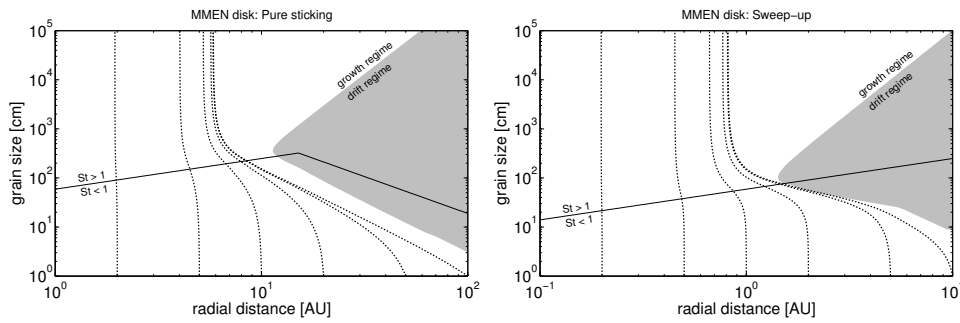


Figure 6.3: The evolution of seed particles in an MMEN disk assuming pure coagulation (*left panel*) and sweep-up (*right panel*). Note the different x-range! See Fig. 6.2 for more details.

with the same radial behavior as the sweep-up scenario, but with a shorter timescale (due to the decreasing scale-height of large particles and a higher sticking efficiency).

6.2.3 A drift and growth toy model

We now combine the results of the previous section, and follow the evolution using a simple toy model, where we numerically integrate the radial drift (Eq. 6.3) and the particle growth (Eqs. 6.14 and 6.16). We consider both coagulation by pure sticking and by sweep-up, and take the MMSN and MMEN disk densities with the same temperature profile, and a dust-to-gas ratio of 200. We assume a turbulent strength $\alpha = 10^{-3}$, a dust solid density $\zeta = 1 \text{ g cm}^{-3}$, and we include the full relative velocity calculations from brownian motion, turbulence using the closed-form expressions of Ormel & Cuzzi (2007), and radial and azimuthal drift (see Birnstiel et al. 2010a for a thorough description of the different sources).

In the sweep-up case, we assume the small particles to have a constant size $a_s = 0.1$ cm, which could be explained by bouncing or fragmentation. As long as the particles are smaller than ~ 0.5 cm, their exact size does not

matter much, as they are all fully coupled to the gas and experience little vertical settling. If the particles are larger than this, however, the vertical settling would lead to increased midplane densities, and therefore faster growth rates. The evolving particles are initiated with a size of 1 cm, and they are inserted at distances between $r = 2 - 100$ AU for the case of pure coagulation, and $r = 0.2 - 10$ AU in the sweep-up case.

In Fig. 6.2, we show the resulting evolution for the MMSN disk, and in Fig. 6.3, we show the results for the MMEN disk. In both cases, we can distinguish between two separate regimes; the grey-marked drift regime where $t_{\text{drift}} \ll t_{\text{growth}}$, where the particles evolve horizontally, and a growth regime where $t_{\text{growth}} \gg t_{\text{drift}}$, and the particles evolve vertically. In the borderline region, both effects are significant, and particle evolution is diagonal.

From the figures, it is clear that regardless of coagulation mode, the drift barrier can be overcome. In the case of pure sticking, the growth rate dominates for all sizes in the inner few AU, and for the slower sweep-up growth, the drift barrier can be overcome inside 1 AU. For drift breakthrough to occur, the particles need to sufficiently fast traverse the region of rapid drift that occurs for $St \sim 1$. Okuzumi et al. (2012) quantified this as the ratio between the growth and drift timescales for $St = 1$, and found that a ratio of ~ 30 was needed for particles to break through without any significant drift. They argued that drift could be overcome for extremely porous ice aggregates as far out as ~ 20 AU. However, because $t_{\text{growth}}(St = 1)$ decreases very rapidly with decreasing r , compared to a more shallow slope for $t_{\text{drift}}(St = 1)$, we find that the same will also occur for compact silicates at distances < 5 AU. In contrast, the growth rate for particles in the Epstein drag regime is a lot slower, and the particle breakthrough might never occur.

As a result, all seeds that are initiated at large radii will halt their drift at the same location, which results in a successive pile-up of solids in a narrowly defined region as time progresses. If the growth mode is by pure sticking, we predict that this pile-up will occur at distances between 3 – 6 AU, and if it is by sweep-up, the pile-up would instead occur between 0.2 – 0.8 AU, depending on the disk properties.

6.3 NUMERICAL MODEL

To accurately determine the evolution of the dust, we need to take the full size distribution into account. For this, we use the 1D Smoluchowski code developed by Birnstiel et al. (2010a).

A major difference from similar previous studies is the implementation of a collision model capable of mass transfer collisions (as the mechanism responsible for sweep-up growth), and the inclusion of impact velocity distributions. The simple collision model presented here is similar to the one presented in Chapter 3, and we will describe it only briefly.

The collision rate between two particle species i and j is given by $f_j = n_i n_j K$, where K is commonly called the collision kernel. If a velocity distri-

bution is considered, the kernel has to be integrated over the whole range of possible Δv for each particle pair:

$$K(\Delta v_{\text{rms}}) = \sigma_{ij} \int_0^\infty \Delta v P_v(\Delta v | \Delta v_{\text{rms}}) P_{s/f}(\Delta v) d\Delta v, \quad (6.17)$$

where σ is the collisional cross section and Δv is the relative velocity. $P_v(\Delta v | \Delta v_{\text{rms}})$ is the velocity probability distribution (PDF), and $P_{s/f}(\Delta v)$ is the sticking/fragmentation probability as determined by the collision model discussed below.

Velocity distributions arise due to the stochastic nature of turbulence, and in this method, we assume all particles to interact with a Maxwellian velocity PDF, as believed to describe the behavior of large particles suspended in turbulence (see e.g. [Carballido et al. 2010](#)). An assumption is therefore that the turbulent velocities dominate over the deterministic drift velocities, which is true for particles of similar sizes or if the particles are sufficiently far away from $St \sim 1$ to not drift significantly. Because we are interested in the aspect of collision barrier breakthrough, where the interactions between relatively small, similar-sized particles are the most important, we consider this a valid approximation. A velocity PDF also has a very limited effect if the mean relative velocity is far above or below the fragmentation threshold velocity. For a more thorough approach that separates the stochastic and deterministic velocity effects, see [Garaud et al. \(2013\)](#).

For the collision models in this work, the possible outcome of a collision is either sticking or fragmentation, so that $p_s + p_f = 1$, where p is the probability of each collision type. In the model with pure coagulation, we always take $p_s = 1$. When fragmentation is included, we assume that destruction of both particles always occurs above a given collision velocity

$$p_f = \begin{cases} 0 & \text{if } v < v_f \\ 1 & \text{if } v > v_f, \end{cases} \quad (6.18)$$

where we take $v_f = 100$ cm/s as the fragmentation threshold velocity as found by [Blum & Münch \(1993\)](#). The fragments are put in a size distribution described by $n(m) \propto m^{-9/8}$. In this work, we are mostly concerned with the drift barrier, and consider a very idealized form of sweep-up and therefore neglect the effects of bouncing.

Mass transfer is a complicated process which is not yet fully understood or mapped out by laboratory experiments. Generally, mass transfer occurs when only the smaller of the particles fragments and the larger one is left intact, and parts of the fragmented particle sticks onto the surface of the target ([Wurm et al. 2005](#); [Teiser & Wurm 2009b](#); [Kothe et al. 2010](#)). This occurs when the particle mass ratio is so large that the collision energy is deposited only locally into the large one. To mimic this effect, we take mass transfer collisions to always occur for all fragmenting collisions above a critical mass ratio $m_1/m_2 > 1000$, and we assume that 50% of the mass of the fragmented particle is added to the larger. This is a major assumption,

as the collision outcome between two very large (> 10 cm) dust grains has never been investigated either in the laboratory or numerically.

6.4 RESULTS

We perform simulations with both the growth modes discussed in the previous sections. The simulations are done using the disk properties as in the toy-model, with an MMEN disk with an initial dust-to-gas ratio = 0.005 and $\alpha = 10^{-3}$, and for the relative velocities, we consider Brownian motion, turbulence, and radial and azimuthal drift.

We are here mostly concerned with the point of pile-up, and perform the simulations over a sufficiently wide range of radial distances to allow for the point of pile-up to be continuously supplied by drifting particles for the 10^5 yrs of simulation time. Although a part of the domain is outside the snowline, we only include the silicate collision properties discussed in the previous section. We represent the radial direction by 61 radial bins between 0.2 and 20 AU and use a resolution of 7 bins per mass decade² between $4 \cdot 10^{-6}$ and $4 \cdot 10^{18}$ g for a total of 168 mass bins. Particles that reach the largest mass bin are allowed to collide and fragment, but any coagulation is artificially turned off.

6.4.1 Pure coagulation

In Fig. 6.4, we show the evolution of the vertically integrated dust density distribution for the case of pure coagulation. As predicted from the toy-model approach, the growth across $St = 1$ in the inner disk is so fast that the drift barrier is overcome. Because of the higher dust densities, the growth proceeds the fastest at the inner radii. Even at 4 AU, however, the drift barrier is overcome after only 10^3 yrs. Later, particles at 9 AU grow through the $St = 1$ region. These particles however continue drifting for another few AU before they finally halt. At the end of the simulations, as significant fraction of 1-10 km-sized planetesimals have formed in the inner 4 AU.

After 10^4 yrs, the growth and drift has caused the smaller particle sizes to become so depleted that their growth rate slows down significantly. This causes a continuous inward shift of the point of drift breakthrough, and a clearing of particles in the $St = 1$ region. The low number densities are also the reason why a part of the population remains at smaller sizes even until the end of the simulation.

Because the outer particles at $r > 10$ AU are unable to growth past the drift barrier and decouple, they drift inwards into regions where they can either break through the barriers themselves or be accreted by the already existing planetesimal population. In either case, this causes a pile-up that increases as time progresses. In Fig. 6.5, we plot the radial depletion and

² This resolution is on the low end, but was a necessity due to the lack of time. High resolution simulations are in progress.

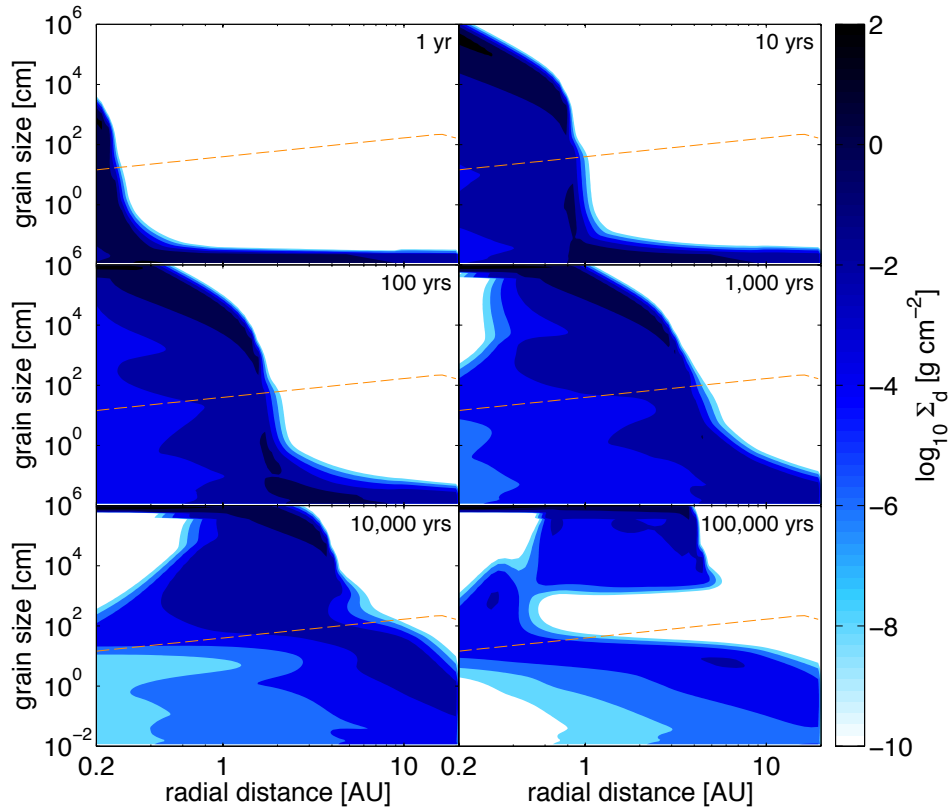


Figure 6.4: The dust density distribution for a pure coagulation scenario in an MMEN disk. The orange dashed line corresponds to $St = 1$ where the radial drift is the fastest.

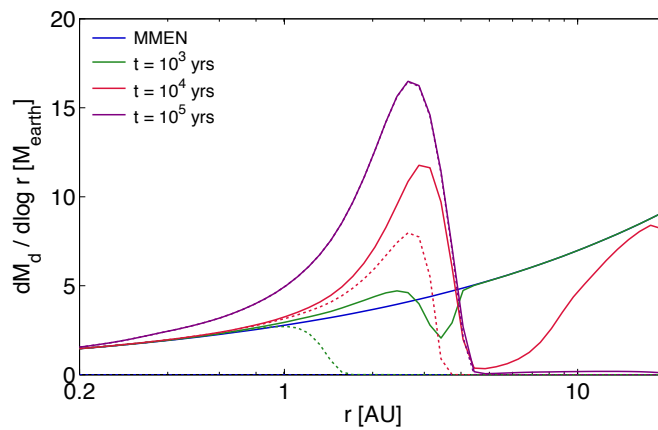


Figure 6.5: The total radial mass distribution for the case of pure coagulation in an MMEN disk, showing the evolution of the radial depletion and pile-up of the dust due to drift and breakthrough. The solid lines show the total dust mass, and the dotted lines show the mass of only the bodies of km-sizes or larger.

pileup of dust, and give both the total dust mass and the mass of only the km-sized planetesimals and larger. We can here see a significant enhancement of the dust population in the inner 4 AU. In terms of total dust mass, the simulation with this extremely massive disk was initiated with $126 M_{\oplus}$ of μm -sized dust within the inner 5 AU and ends with $232 M_{\oplus}$ of km-sized or larger planetesimals, which is an increase in dust mass corresponding to the entire dust population between 5 and 20 AU.

In this case, when the radial drift barrier can so easily be overcome, we find a mass loss of less than 1% of the total dust mass within the first 10^5 yrs. In the beginning, the smallest grains in the inner disk coagulate so quickly that the drift can be overcome, and even if the growth timescales are too long for breakthrough in the outer disk, the mass is simply collected farther in disk where the breakthrough can continue. Some of the mass is also swept up directly by the population of already formed planetesimals. These are so well decoupled from the gas that their drift velocities are less than 1 cm s^{-1} , corresponding to a drift timescale significantly longer than the disk lifetime.

6.4.2 Sweep-up growth

We now consider the sweep-up growth case, with the resulting size evolution given in Fig. 6.6. When fragmentation is a possibility, the dust population is at first halted below the barrier, which can be estimated by relating the turbulent relative velocity to the Stokes number (for details, see [Birnstiel et al. 2009](#)):

$$a_{\text{frag}} \approx \frac{\Sigma_{\text{g}}}{\pi \alpha \zeta} \left(\frac{v_{\text{f}}}{c_{\text{s}}} \right)^2 \quad (6.19)$$

Although the majority of the dust is halted by the fragmenting events between similar-sized particles, the impact velocity distribution and the mass transfer collisions both act to smear out the fragmentation barrier, by allowing a few lucky particles to avoid collisions and only be involved in either large mass-ratio mass transfer collisions or low-velocity sticking collisions, as we found in Chapter 3. After only a year, the first lucky particles manage to break through the fragmentation barrier in the innermost disk, and their number continue to increase both by newly formed lucky particles and by fragmenting events between themselves.

Even though the sweep-up growth rate is lower than the pure coagulation growth rate, it is still sufficient to also break through the radial drift barrier. Compared to the toy-model, the outermost point of breakthrough has increased from 0.8 AU to 2.5 AU. This discrepancy has several reasons. One is likely the artificial growth speed-up in this low-resolution simulation. With higher mass resolution, the point of breakthrough is likely to be moved inwards. But there are also physical reasons. In the outer disk, the particles are allowed to grow to 1 cm before they reach the fragmentation barrier, whereas we assumed a global 0.1 cm size for the small particles in the toy-model. This allows for the particles to settle towards the midplane,

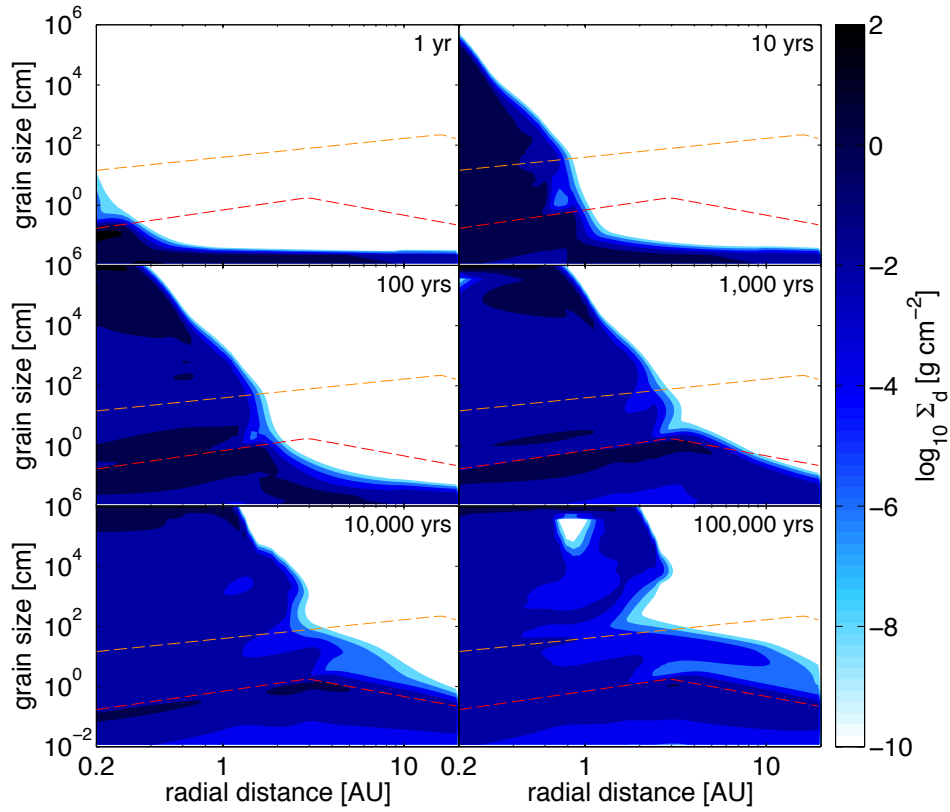


Figure 6.6: The dust density distribution for the full sweep-up collision model in an MMEN disk. The orange dashed line corresponds to $St = 1$, and the red dashed line corresponds to the fragmentation barrier.

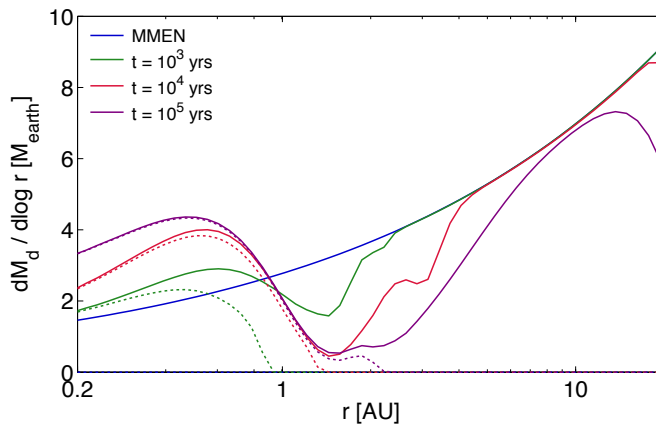


Figure 6.7: The total radial mass distribution for the case of sweep-up in an MMEN disk. The solid lines show the total dust mass, and the dotted lines show the mass of only the bodies of km-sizes or larger.

which increases the densities for the lucky grains to sweep up. The size-distribution is also so wide that assuming a single particle size becomes insufficient to accurately describe the collisional growth.

The growth of the newly formed planetesimals proceeds by the sweep up of the smaller grains, and the collisions between the planetesimals work to constantly replenish the smallest sizes. Compared to the case of pure coagulation, even at the end of the simulation, a significant fraction of dust still resides below the fragmentation barrier. Because the sweep-up is less efficient than coagulation, the total mass loss in this case corresponds to 7% of the total dust mass.

After only about 1,000 years, however, the larger particles start to dominate over the smaller ones in terms of mass in the innermost disk. However, the planetesimals are then so decoupled from the gas that their relative velocities are low (ignoring the possible mechanism of turbulent stirring quantified by [Okuzumi & Ormel 2013](#)), which limits the number of large particle fragmentation. The growth of the planetesimals is at this stage dominated by sweep-up of particles that are roughly 1 order of magnitude smaller in size. At yet larger sizes, the planetesimals are almost non-collisional between themselves, but retain high relative velocities to the smaller particles because these can still be excited by the turbulence. This limits the destructive fragmentation but still allows for further sweep-up growth.

In the outer disk, the particle growth is always limited by the fragmentation barrier. This limits their drift velocities, and slows down the depletion rate compared to the case of pure coagulation, as shown in [Fig. 6.7](#). We start with a total of $50 M_{\oplus}$ of dust in the form of μm -sized dust grains inside 1 AU. At the end of the simulation, this has increased to $90 M_{\oplus}$, predominantly in the form of planetesimals with sizes of > 1 km. As we can see in the figure, the overdensity is at most a factor of a few, and it is spread out between 0.1 – 0.9 AU, with the peak at 0.35 AU.

6.5 DISCUSSION AND CONCLUSIONS

We have studied the growth and drift of dust grains in the context of planetesimal formation in the inner part of the protoplanetary disk. This was done using both a toy-model approach and by the implementation of a collision model including mass transfer collisions and impact velocity distributions into a radial Smoluchowski code. We find that some grains are able to overcome both the collisional barriers and the drift barriers, and that planetesimals can form on timescales of only a few thousand years. Because the drift barrier can only be overcome locally in the inner region of the disk, this leads to a process where drifting particles pile up in a narrow annulus at distances depending on the collision model and the disk properties.

The effect of dust pile-up in the inner region of protoplanetary disks has been studied before. [Youdin & Shu \(2002\)](#) and [Youdin & Chiang \(2004\)](#) found that the surface density of dust in the form of mm-cm-sized chon-

drules can be sufficiently enhanced for gravitational instability to occur at roughly 1 AU. [Hughes & Armitage \(2012\)](#) studied a similar scenario but included an evolving protoplanetary disk. They did not find any significant pile-up of small particles, due to the inward motion of the gas, which is sufficiently fast to continuously remove the small particles. However, their dust growth mechanism is very simplified. For the large-particle growth and on the timescales that we study, gas accretion should only have a small impact.

[Laibe et al. \(2012\)](#) also argued that radial drift of large particles in the Stokes regime decreases with the radial distance, to the point where the radial drift would be completely halted, even for particles of constant size. Drift and pure coagulation was included by [Stepinski & Valageas \(1997\)](#) and [Laibe et al. \(2008\)](#), and they noticed dust pile-up as well as fast growth at ~ 20 AU. We find in this work that drift alone is not sufficient to cause any pile-up outside of the dust evaporation radius, and in order for all the growth barriers to be overcome, a more sophisticated collision scheme is required. The drift barrier can then be overcome thanks to the fact that the growth timescale decreases while the particles are drifting inwards.

Based on the observed exoplanets distribution, [Chiang & Laughlin \(2013\)](#) constructed a Minimum-Mass-Extrasolar-Nebula, which is more sloped and ~ 10 times more massive than the MMSN in the inner region. Though we use it as initial conditions, such a density distribution might also be a result of the pile-up mechanism. [Hansen & Murray \(2012\)](#) showed that when starting models with 50-100 M_{\oplus} in Earth-sized embryos inside 1 AU, it is possible to reproduce the observed distribution of hot-Neptunes and hot-super Earths. Utilizing the MMEN, we started with 50 M_{\oplus} of small dust and ended with 90 M_{\oplus} of planetesimals, with the bulk of the mass centered at 0.4 AU, which corresponds well to the required values. A recent study by [Ida et al. \(2013\)](#) also showed that newly formed gas giants in the inner disk are capable of scattering cores to the outer regions, where the gas accretion can proceed in-situ. This could be a way of forming the observed distant gas giants at ~ 30 AU with nearly circular orbits.

For the Solar System, [Hansen \(2009\)](#) showed that the distribution of the terrestrial planets can be reproduced when a total of 2 M_{\oplus} of mass is initially confined in planetary embryos of 0.005 M_{\oplus} within a narrow annulus between 0.7 and 1.0 AU. In the extremely heavy disk that we studied in this work, we end with a lot more mass but significantly further in. Conceptually, however, we find that pile-up would be capable of producing a local inner overdensity of planetesimals, but a disk parameter study will be required to determine whether an annulus of reasonable total mass can be produced at the necessary distance.

Future work will also require the transition regime from planetesimals to embryos to be studied further, which requires the inclusion of gravitational dynamics. The effect of turbulent stirring of planetesimals will also need to be considered ([Okuzumi & Ormel 2013](#); [Ormel & Okuzumi 2013](#)). Their prediction is that the excited relative velocity only starts for particle sizes > 100 m, which is already past the drift barrier, and the onset of

runaway growth can be initiated for bodies in the 10-100 km size range. A possible way around the destructive kilometer-size barrier might be that the first 10 km-sized bodies forms so fast, even before the planetesimal population is numerous enough for similar-sized collisions to be important. Because the pebble accretion mechanism studied by [Ormel \(2013\)](#) only becomes important for bodies of sizes >100 km, it is unlikely to be of help the sweep-up growth to circumvent the kilometer-sized barrier. Both of these points will be interesting aspects for future work.

The in-situ formation of the tightly-packed close-in exoplanets is in agreement with the fact that such systems observed by Kepler (although influenced by observational bias) are nearly co-planar ([Fang & Margot 2012](#)). It is possible that the idea of a local planetesimal formation region, be it in the innermost disk or centered on a long-lived pressure bump, needs to be considered as a means of forming the whole zoo of observed exoplanetary systems.

SUMMARY AND OUTLOOK

The aim of this thesis has been to improve the understanding of the physics and mechanisms involved in the growth barriers of the planetesimal formation process. By probing the robustness of the barriers to previously overlooked or too simplified physics, the goal was to investigate the possibility for dust to grow large.

The sweep-up growth mode discussed in Chapter 2 was a result of an extensive collaboration with the dust laboratory groups. By allowing dust grains to interact in ways that had not been accounted for in most previous dust evolution codes, we found growth to planetesimal sizes to be possible even at impact velocities well above the well-established fragmentation barrier. Although the principle idea of sweep-up has now been confirmed in several laboratory and dust evolution studies, the final outcome still depends on the exact calibration of the collision model.

Based on [Teiser & Wurm \(2009a\)](#), there are indications that high-velocity impacts with projectiles larger than ~ 1 mm are erosive regardless of the mass ratio between the projectile and target. This puts a limit to how large the average grain can be allowed to grow before the sweep-up process is inhibited. If mass transfer can instead occur as long as the mass ratio is large, the sweep-up scenario becomes a lot more flexible. Future collaboration between theory and laboratory is therefore crucial to verify (or modify) this formation channel. A major step also needs to be taken to consolidate the results from the laboratory and the numerical molecular dynamics simulations, and collision models with ices are just now starting to become possible from the laboratory. Meanwhile, the study of the collisional barriers will benefit from both advanced and idealized collision models.

There are now several suggestions for how the first seed particles can break through the fragmentation barrier to initiate sweep-up growth. In Chapter 2, we introduced the idea of "lucky" particle growth, by discussing the virtues of impact velocity distributions caused by the stochastic properties of turbulence. The stochasticity causes the collisional growth barriers to smear out, by allowing for a whole spectrum of collision outcomes even for a single pair of particles. If particles have a non-zero probability of sticking, even when the average collision is destructive, the sheer number of particles in the disk is likely to create a few lucky ones that can grow large enough to initiate sweep-up.

This is a promising scenario that could explain seed formation anywhere in the disk, but it is important to further understand the structure of the grains formed this way. If the lucky particles are formed by too low velocities, the outcome might be similar to hit-and-stick growth, where they will become almost fractal, and thus might not be strong enough to sur-

vive high-velocity collisions regardless of the mass ratio. Some laboratory experiments hint that these fractal-like structures are slightly stickier than usual, but that they are also easy to destroy once they have been formed (Kothe et al. 2013a). Another uncertainty lies in the shape of the velocity distribution. Due to the extreme spatial resolutions and high particle numbers required for direct numerical studies of the turbulent velocity distribution, extrapolation to the smallest scales is necessary. This makes the extracted distributions uncertain. If the velocity distribution is too wide, it might allow for too many large particles to form, and consequently too much large particle fragmentation to allow for sweep-up growth. If the velocity distributions are too narrow, on the other hand, no seeds might form at all.

Another scenario for seed formation might be due to the growth and radial mixing of "privileged" particles, discussed in Chapter 5. The dead zones that arise from a change in the gas ionization rate allows larger particles to form than in an active region, and if they are introduced to other parts of the disk by radial mixing, they can initiate sweep-up. The second effect of dead zones is the possible formation of pressure bumps at their edges. These regions halt the drift of the particles, and even if they are short-lived, it might be enough for some of the particles to grow sufficiently large to break through the drift barrier. The pressure bumps however need to be explored further, as their properties are still highly uncertain. In the case of the snowline dead zone and pressure bump that we utilized, the underlying assumption is that the total dust surface area is constant. Due to coagulation, we know that this will not be the case, and so the dead zone strength should decrease with time.

A third possibility of seed formation could be as a direct consequence of the porosity evolution. Because porous grains are stickier than compact grains, it is possible that the first generation of dust grains manage to grow larger before compaction and fragmentation sets in. If a few particles manage to avoid compaction, or compact without losing too much mass, they could become the first generation of seeds. We know from radioactive dating that cm-sized CAIs formed at the very first stages of the formation of the Sun, so at least some large grains must have been able to form early. It is therefore important to study the porosity evolution, something that has been largely neglected in this thesis. However, even if the capability is there to implement porosity also in Smoluchowski codes (Okuzumi et al. 2009), there is still too little laboratory data available to construct a complete model.

In Chapter 4, we expanded upon the work with velocity distributions, and also allowed for particles of similar aerodynamic properties to cluster together. This is a venue of grain growth that has never been probed before in a planet formation context, and with it follows several interesting aspects. Firstly, the particle clumping should result in higher collision rates, which could be important for the observable quantities in the outer disks. If the growth is fast enough, it might even lead to breakthrough of the radial drift barrier. Secondly, because clumping leads to primar-

ily low-velocity collisions, it will affect the balance between sticking and fragmenting collisions. If the sticking rate is boosted, the fragmentation barrier could occur at 1-2 orders of magnitude larger sizes than the nominal fragmentation barrier. This could be interesting for the initiation of the streaming instability in the outer regions of the disk.

In Chapter 6, we studied sweep-up growth in the innermost disk using a global disk code. The impact of the radial drift is highly dependent on the balance between the growth and drift. We discovered that for both growth by pure coagulation and for sweep-up, the growth can even be fast enough to overcome the drift in the inner few AU. This is both due to the inclusion of the Stokes drag regime as well as the rapidly increasing dust densities in the innermost disk. The result is a rapid formation and pileup of planetesimals within the first thousands of years. This could be a possible mechanism for the formation of the compact Kepler systems or the narrow planetesimal ring needed to explain the formation of the terrestrial planets in the Solar System.

An important next step will be to tie the planetesimal formation by sweep-up to the later evolutionary stages. The kilometer-size barrier introduced by Nelson (2005) and further discussed by Ormel & Okuzumi (2013), where the relative velocities are excited by the turbulent fluctuations, poses another difficulty for the further growth of the planetesimals. Sweep-up might once again be a solution to this problem, as the initially low number of growing planetesimals might result in low enough collision rates for the growth to go relatively unhindered even through the kilometer-size barrier.

The connection to the even later stages can be investigated by the use of planet population synthesis, where the coagulation models are just now starting to reach results that can be used as initial conditions (see Chapter 6 and Okuzumi et al. 2012). A great difficulty for growth via coagulation is to explain the presence of planets in the outer parts of the disk ($>10 - 20$ AU) due to the long growth timescales involved. However, a recent study by Ida et al. (2013) shows that newly formed gas giants in the inner disk are capable of scattering cores to the outer regions, where the gas accretion can proceed in-situ. This could be a way to form the observed distant gas giants at ~ 30 AU with nearly circular orbits. Maybe the idea of a local planetesimal formation region, be it in the innermost disk or centered on a long-lived pressure bump, needs to be considered as a means of forming the whole zoo of observed exoplanetary systems.

To conclude, the field of planetesimal formation has in recent years begun to spawn a number of interesting and viable mechanisms for the critical first growth stages. There are now a number of scenarios suggested that are capable of overcoming the growth barriers, both via coagulation and turbulent instabilities. The key to understanding the capabilities and limitations of the different scenarios will not only be to further develop the physics and numerics, but also to connect to the later formation stages by providing initial spatial and size distributions of the first generation of planetesimals.

BIBLIOGRAPHY

- Adachi, I., Hayashi, C., & Nakazawa, K. 1976, *Prog. Theor. Phys.*, 56, 1756
- Adams, F. C. 2010, *ARA&A*, 48, 47
- Alexander, R. D., Clarke, C. J., & Pringle, J. E. 2006, *MNRAS*, 369, 229
- Andre, P., Ward-Thompson, D., & Barsony, M. 1993, *ApJ*, 406, 122
- Andrews, S. M., Wilner, D. J., Hughes, A. M., Qi, C., & Dullemond, C. P. 2009, *ApJ*, 700, 1502
- Bai, X.-N. & Stone, J. M. 2010, *ApJ*, 722, 1437
- Balbus, S. A. & Hawley, J. F. 1998, *Reviews of Modern Physics*, 70, 1
- Barge, P. & Sommeria, J. 1995, *A&A*, 295, L1
- Beitz, E., Güttler, C., Blum, J., et al. 2011, *ApJ*, 736, 34
- Beitz, E., Güttler, C., Weidling, R., & Blum, J. 2012, *Icarus*, 218, 701
- Benz, W. & Asphaug, E. 1999, *Icarus*, 142, 5
- Birnstiel, T., Dullemond, C. P., & Brauer, F. 2009, *A&A*, 503, L5
- Birnstiel, T., Dullemond, C. P., & Brauer, F. 2010a, *A&A*, 513, 79
- Birnstiel, T., Ricci, L., Trotta, F., et al. 2010b, *A&A*, 516, L14
- Blum, J. & Münch, M. 1993, *Icarus*, 106, 151
- Blum, J. & Wurm, G. 2000, *Icarus*, 143, 138
- Blum, J. & Wurm, G. 2008, *ARA&A*, 46, 21
- Borucki, W. J., Koch, D., Basri, G., et al. 2010, *Science*, 327, 977
- Borucki, W. J., Koch, D. G., Basri, G., et al. 2011, *ApJ*, 728, 117
- Bottke, W., Durda, D. D., Nesvorný, D., et al. 2005, *Icarus*, 175, 111
- Bottke, W. F. J., Vokrouhlický, D., Rubincam, D. P., & Nesvorný, D. 2006, *Annual Review of Earth and Planetary Sciences*, 34, 157
- Brauer, F., Dullemond, C. P., & Henning, T. 2008, *A&A*, 480, 859
- Brauer, F., Dullemond, C. P., Johansen, A., et al. 2007, *A&A*, 469, 1169
- Carballido, A., Cuzzi, J. N., & Hogan, R. C. 2010, *MNRAS*, 405, 2339
- Chiang, E. & Laughlin, G. 2013, *MNRAS*, 431, 3444

- Ciesla, F. J. 2009, *Icarus*, 200, 655
- Connolly, H. C. J., Desch, S. J., Ash, R. D., & Jones, R. H. 2006, *Meteorites and the ...*, 383
- Cuzzi, J. N., Hogan, R. C., & Bottke, W. 2010, *Icarus*, 208, 518
- Cuzzi, J. N., Hogan, R. C., Paque, J. M., & Dobrovolskis, A. R. 2001, *ApJ*, 546, 496
- Cuzzi, J. N., Hogan, R. C., & Shariff, K. 2008, *ApJ*, 687, 1432
- Dauphas, N. & Pourmand, A. 2011, *Nature*, 473, 489
- Desch, S. J. 2007, *ApJ*, 671, 878
- Dittrich, K., Klahr, H., & Johansen, A. 2013, *ApJ*, 763, 117
- Dominik, C. & Tielens, A. G. G. M. 1997, *ApJ*, 480, 647
- Drazkowska, J., Windmark, F., & Dullemond, C. P. 2013, *A&A*, 556, 37
- Dullemond, C. P. & Dominik, C. 2005, *A&A*, 434, 971
- Dullemond, C. P., Dominik, C., & Natta, A. 2001, *ApJ*, 560, 957
- Dullemond, C. P., Hollenbach, D. J., Kamp, I., & D'Alessio, P. 2007, *Protostars and Planets V*, 555
- Dzyurkevich, N., Flock, M., Turner, N. J., Klahr, H., & Henning, T. 2010, *A&A*, 515, 70
- Dzyurkevich, N., Turner, N. J., Henning, T., & Kley, W. 2013, *ApJ*, 765, 114
- Fang, J. & Margot, J.-L. 2012, *ApJ*, 761, 92
- Fortier, A., Alibert, Y., Carron, F., Benz, W., & Dittkrist, K. M. 2013, *A&A*, 549, 44
- Garaud, P., Meru, F., Galvagni, M., & Olczak, C. 2013, *ApJ*, 764, 146
- Geretshauser, R. J., Meru, F., Speith, R., & Kley, W. 2011, *A&A*, 531, 166
- Geretshauser, R. J., Speith, R., Güttler, C., Krause, M., & Blum, J. 2010, *A&A*, 513, 58
- Gillespie, D. T. 1975, *Journal of Atmospheric Sciences*, 32, 1977
- Goldreich, P. & Ward, W. R. 1973, *ApJ*, 183, 1051
- Gustavsson, K. & Mehlig, B. 2011, *Physical Review E*, 84, 45304
- Gustavsson, K., Meneguz, E., Reeks, M., & Mehlig, B. 2012, *New J. Phys.*, 14, 5017
- Güttler, C., Blum, J., Ormel, C. W., & Dullemond, C. P. 2010, *A&A*, 513, 56

- Haisch, K. E. J., Lada, E. A., & Lada, C. J. 2001, *ApJ*, 553, L153
- Hansen, B. M. S. 2009, *ApJ*, 703, 1131
- Hansen, B. M. S. & Murray, N. 2012, *ApJ*, 751, 158
- Hartmann, L., Calvet, N., Gullbring, E., & D'Alessio, P. 1998, *Astrophysical Journal* v.495, 495, 385
- Hayashi, C. 1981, *Progress of Theoretical Physics Supplement*, 70, 35
- Hayashi, C., Nakazawa, K., & Nakagawa, Y. 1985, *Protostars and planets II*, 1100
- Heim, L.-O., Blum, J., Preuss, M., & Butt, H.-J. 1999, *Phys. Rev. Lett.*, 83, 3328
- Heißelmann, D., Blum, J., & Fraser, H. J. 2007, *Proc. 58th Int. Astronautical Congress 2007 (Paris: Int. Astronautical Federation)*, 2102
- Henke, S., Gail, H.-P., Trieloff, M., Schwarz, W. H., & Kleine, T. 2012, *A&A*, 537, 45
- Hubbard, A. 2012, *MNRAS*, 426, 784
- Hubbard, A. 2013, *MNRAS*, 1177
- Hughes, A. L. H. & Armitage, P. J. 2012, *MNRAS*, 423, 389
- Ida, S., Guillot, T., & Morbidelli, A. 2008, *ApJ*, 686, 1292
- Ida, S. & Lin, D. N. C. 2004, *ApJ*, 604, 388
- Ida, S., Lin, D. N. C., & Nagasawa, M. 2013, *arXiv*, 6450
- Ida, S. & Makino, J. 1993, *Icarus*, 106, 210
- Ilgner, M. & Nelson, R. P. 2006, *A&A*, 445, 205
- Johansen, A., Brauer, F., Dullemond, C. P., Klahr, H., & Henning, T. 2008, *A&A*, 486, 597
- Johansen, A., Klahr, H., & Henning, T. 2011, *A&A*, 529, 62
- Johansen, A., Oishi, J. S., Mac Low, M.-M., et al. 2007, *Nature*, 448, 1022
- Johansen, A., Youdin, A., & Klahr, H. 2009, *ApJ*, 697, 1269
- Kataoka, A., Tanaka, H., Okuzumi, S., & Wada, K. 2013, *arXiv*, 7984
- Kelling, T. & Wurm, G. 2009, *Phys. Rev. Lett.*, 103, 215502
- Kita, N. T., Huss, G. R., Tachibana, S., et al. 2005, *Chondrites and the Protoplanetary Disk*, 341, 558
- Kita, N. T., Nagahara, H., Togashi, S., & Morishita, Y. 2000, *Geochimica et Cosmochimica Acta*, 64, 3913

- Klahr, H. H. & Henning, T. 1997, *Icarus*, 128, 213
- Kley, W. & Nelson, R. P. 2012, *ARA&A*, 50, 211
- Kokubo, E. & Ida, S. 2000, *Icarus*, 143, 15
- Kokubo, E., Kominami, J., & Ida, S. 2006, *ApJ*, 642, 1131
- Kostinski, A. B. & Jameson, A. R. 2000, *Journal of Atmospheric Sciences*, 57, 901
- Kothe, S., Blum, J., Weidling, R., & Güttler, C. 2013a, *Icarus*, 225, 75
- Kothe, S., Blum, J., Weidling, R., & Güttler, C. 2013b, *arXiv*, 5532
- Kothe, S., Güttler, C., & Blum, J. 2010, *ApJ*, 725, 1242
- Kretke, K. A. & Lin, D. N. C. 2007, *ApJ*, 664, L55
- Kuroiwa, T. & Sirono, S.-i. 2011, *ApJ*, 739, 18
- Lada, C. J. 1987, in *IN: Star forming regions; Proceedings of the Symposium, Seward Observatory, Tucson, AZ*, 1–17
- Laibe, G., Gonzalez, J.-F., Fouchet, L., & Maddison, S. T. 2008, *A&A*, 487, 265
- Laibe, G., Gonzalez, J.-F., & Maddison, S. T. 2012, *A&A*, 537, 61
- Lambrechts, M. & Johansen, A. 2012, *A&A*, 544, 32
- Lammel, C. 2008, Bachelor's thesis, Technische Universität Carolo Wilhelmina Braunschweig
- Langkowski, D., Teiser, J., & Blum, J. 2008, *ApJ*, 675, 764
- Lee, M. H. 2000, *Icarus*, 143, 74
- Lee, M. H. 2001, *Journal of Physics A: Mathematical and General*, 34, 10219
- Leinhardt, Z. M. & Stewart, S. T. 2009, *Icarus*, 199, 542
- Leinhardt, Z. M. & Stewart, S. T. 2012, *ApJ*, 745, 79
- Lissauer, J. J., Fabrycky, D. C., Ford, E. B., et al. 2011, *Nature*, 470, 53
- Lissauer, J. J., Marcy, G. W., Rowe, J. F., et al. 2012, *ApJ*, 750, 112
- Lithwick, Y. 2013, *arXiv*, 3890
- Lynden-Bell, D. & Pringle, J. E. 1974, *MNRAS*, 168, 603
- Marchi, S., Bottke, W. F., O'Brien, D. P., et al. 2013, *arXiv*, 6679
- Markiewicz, W. J., Mizuno, H., & Voelk, H. J. 1991, *Astronomy and Astrophysics (ISSN 0004-6361)*, 242, 286

- Markowski, A., Quitté, G., Kleine, T., et al. 2007, *Earth and Planetary Science Letters*, 262, 214
- Martin, R. G. & Livio, M. 2013, *MNRAS*, 428, L11
- Mathis, J. S., Rumpl, W., & Nordsieck, K. H. 1977, *ApJ*, 217, 425
- Mayor, M. & Queloz, D. 1995, *Nature*, 378, 355
- Meru, F., Geretshauer, R. J., Schaefer, C., Speith, R., & Kley, W. 2013, arXiv, 825
- Mizuno, H. 1980, *Progress of Theoretical Physics*, 64, 544
- Morbidelli, A., Bottke, W., Nesvorný, D., & Levison, H. F. 2009, *Icarus*, 204, 558
- Mordasini, C., Alibert, Y., & Benz, W. 2009, *A&A*, 501, 1139
- Nagasawa, M. & Ida, S. 2011, *ApJ*, 742, 72
- Nakagawa, Y., Nakazawa, K., & Hayashi, C. 1981, *Icarus*, 45, 517
- Nakagawa, Y., Sekiya, M., & Hayashi, C. 1986, *Icarus*, 67, 375
- Nakamoto, T. & Nakagawa, Y. 1994, *ApJ*, 421, 640
- Nelson, R. P. 2005, *A&A*, 443, 1067
- Nelson, R. P. & Gressel, O. 2010, *MNRAS*, 409, 639
- Ohtsuki, K., Nakagawa, Y., & Nakazawa, K. 1990, *Icarus*, 83, 205
- Okuzumi, S. 2009, *ApJ*, 698, 1122
- Okuzumi, S. & Hirose, S. 2011, *ApJ*, 742, 65
- Okuzumi, S. & Ormel, C. W. 2013, arXiv, 1889
- Okuzumi, S., Tanaka, H., Kobayashi, H., & Wada, K. 2012, *ApJ*, 752, 106
- Okuzumi, S., Tanaka, H., & Sakagami, M.-a. 2009, *ApJ*, 707, 1247
- Okuzumi, S., Tanaka, H., Takeuchi, T., & Sakagami, M.-a. 2011a, *ApJ*, 731, 95
- Okuzumi, S., Tanaka, H., Takeuchi, T., & Sakagami, M.-a. 2011b, *ApJ*, 731, 96
- Ormel, C. & Okuzumi, S. 2013, arXiv, 1890
- Ormel, C. W. 2013, *MNRAS*, 428, 3526
- Ormel, C. W. & Cuzzi, J. N. 2007, *A&A*, 466, 413
- Ormel, C. W. & Spaans, M. 2008, *ApJ*, 684, 1291

- Pan, L. & Padoan, P. 2010, *Journal of Fluid Mechanics*, 661, 73
- Pan, L. & Padoan, P. 2013, arXiv, 307
- Pan, L., Padoan, P., Scalo, J., Kritsuk, A. G., & Norman, M. L. 2011, *ApJ*, 740, 6
- Papaloizou, J. C. B. & Lin, D. N. C. 1995, *ARA&A*, 33, 505
- Paraskov, G. B., Wurm, G., & Krauss, O. 2007, *Icarus*, 191, 779
- Paszun, D. & Dominik, C. 2009, *A&A*, 507, 1023
- Pérez, L. M., Carpenter, J. M., Chandler, C. J., et al. 2012, *ApJ*, 760, L17
- Pinilla, P., Benisty, M., & Birnstiel, T. 2012a, *A&A*, 545, 81
- Pinilla, P., Birnstiel, T., Ricci, L., et al. 2012b, *A&A*, 538, 114
- Pollack, J. B., Hubickyj, O., Bodenheimer, P., et al. 1996, *Icarus*, 124, 62
- Ricci, L., Testi, L., Natta, A., & Brooks, K. J. 2010a, *A&A*, 521, 66
- Ricci, L., Testi, L., Natta, A., et al. 2010b, *A&A*, 512, 15
- Rosotti, G. P., Ercolano, B., Owen, J. E., & Armitage, P. J. 2013, *MNRAS*, 430, 1392
- Russell, S. S., Hartmann, L., Cuzzi, J., & Krot, A. 2006, *Meteorites and the ...*
- Safronov, V. S. & Zvjagina, E. V. 1969, *Icarus*, 10, 109
- Sano, T., Miyama, S. M., Umebayashi, T., & Nakano, T. 2000, *ApJ*, 543, 486
- Schlaufman, K. C., Lin, D. N. C., & Ida, S. 2009, *ApJ*, 691, 1322
- Schräpler, R. & Blum, J. 2011, *ApJ*, 734, 108
- Schräpler, R., Blum, J., Seizinger, A., & Kley, W. 2012, *ApJ*, 758, 35
- Seizinger, A. & Kley, W. 2013a, *A&A*, 551, 65
- Seizinger, A. & Kley, W. 2013b, arXiv
- Sekiya, M. & Takeda, H. 2003, *Earth*, 55, 263
- Sekiya, M. & Takeda, H. 2005, *Icarus*, 176, 220
- Shakura, N. I. & Sunyaev, R. A. 1973, *A&A*, 24, 337
- Shaw, R. A. 2003, *Annual Review of Fluid Mechanics*, 35, 183
- Shaw, R. A., Kostinski, A. B., & Larsen, M. L. 2002, *Quarterly Journal of the Royal Meteorological Society*, 128, 1043
- Sirono, S.-i. 2011, *ApJ*, 733, L41

- Smoluchowski, M. V. 1916, *Physik. Zeit.*, 17, 557
- Stepinski, T. F. & Valageas, P. 1997, *A&A*, 319, 1007
- Stewart, S. T. & Leinhardt, Z. M. 2011, arXiv, 4588
- Stone, J. M., Gammie, C. F., Balbus, S. A., & Hawley, J. F. 2000, *Protostars and Planets IV* (Book - Tucson: University of Arizona Press; eds Mannings, 589
- Sundaram, S. & Collins, L. R. 1997, *Journal of Fluid Mechanics*, 335, 75
- Suyama, T., Wada, K., Tanaka, H., & Okuzumi, S. 2012, *ApJ*, 753, 115
- Tanaka, H., Himeno, Y., & Ida, S. 2005, *ApJ*, 625, 414
- Teiser, J., Küpper, M., & Wurm, G. 2011, arXiv, 785
- Teiser, J. & Wurm, G. 2009a, *A&A*, 505, 351
- Teiser, J. & Wurm, G. 2009b, *MNRAS*, 393, 1584
- Testi, L., Natta, A., Shepherd, D. S., & Wilner, D. J. 2003, *A&A*, 403, 323
- Thornton, C. & Ning, Z. 1998, *Powder Technology*, 99, 154
- Uribe, A. L., Klahr, H., Flock, M., & Henning, T. 2011, *ApJ*, 736, 85
- van Boekel, R., Waters, L. B. F. M., Dominik, C., et al. 2003, *A&A*, 400, L21
- van der Marel, N., van Dishoeck, E. F., Bruderer, S., et al. 2013, *Science*, 340, 1199
- Villeneuve, J., Chaussidon, M., & Libourel, G. 2009, *Science*, 325, 985
- Voelk, H. J., Jones, F. C., Morfill, G. E., & Roeser, S. 1980, *A&A*, 85, 316
- Wada, K., Tanaka, H., Suyama, T., Kimura, H., & Yamamoto, T. 2007, *ApJ*, 661, 320
- Wada, K., Tanaka, H., Suyama, T., Kimura, H., & Yamamoto, T. 2008, *ApJ*, 677, 1296
- Wada, K., Tanaka, H., Suyama, T., Kimura, H., & Yamamoto, T. 2009, *ApJ*, 702, 1490
- Wada, K., Tanaka, H., Suyama, T., Kimura, H., & Yamamoto, T. 2011, *ApJ*, 737, 36
- Walsh, K. J., Morbidelli, A., Raymond, S. N., O'Brien, D. P., & Mandell, A. M. 2011, *Nature*, 475, 206
- Wang, H.-H., Klessen, R. S., Dullemond, C. P., van den Bosch, F. C., & Fuchs, B. 2010, *MNRAS*, 407, 705
- Wang, L.-P., Wexler, A. S., & Zhou, Y. 2000, *Journal of Fluid Mechanics*, 415, 117

- Weidenschilling, S. J. 1977a, *MNRAS*, 180, 57
- Weidenschilling, S. J. 1977b, *Astrophys. & Space Sci.*, 51, 153
- Weidenschilling, S. J. 1980, *Icarus*, 44, 172
- Weidenschilling, S. J. 1997, *Icarus*, 127, 290
- Weidenschilling, S. J. 2011, *Icarus*, 214, 671
- Weidenschilling, S. J. & Cuzzi, J. N. 1993, In: *Protostars and planets III* (A93-42937 17-90), 1031
- Weidling, R., Güttler, C., & Blum, J. 2012, *Icarus*, 218, 688
- Weidling, R., Güttler, C., Blum, J., & Brauer, F. 2009, *ApJ*, 696, 2036
- Wetherill, G. W. 1990, *Icarus*, 88, 336
- Wetherill, G. W. & Stewart, G. R. 1989, *Icarus*, 77, 330
- Whipple, F. 1972a, in *From Plasma to Planet* (New York: Wiley Interscience Division)
- Whipple, F. L. 1972b, In: *Protostars and planets III* (A93-42937 17-90), 1
- Windmark, F., Birnstiel, T., Güttler, C., et al. 2012a, *A&A*, 540, 73
- Windmark, F., Birnstiel, T., Ormel, C. W., & Dullemond, C. P. 2012b, *A&A*, 544, L16
- Wurm, G., Paraskov, G. B., & Krauss, O. 2005, *Icarus*, 178, 253
- Wyatt, M. C. 2008, *ARA&A*, 46, 339
- Xie, J.-W., Payne, M. J., Thébault, P., Zhou, J.-L., & Ge, J. 2010, *ApJ*, 724, 1153
- Youdin, A. & Johansen, A. 2007, *ApJ*, 662, 613
- Youdin, A. N. & Chiang, E. I. 2004, *ApJ*, 601, 1109
- Youdin, A. N. & Goodman, J. 2005, *ApJ*, 620, 459
- Youdin, A. N. & Shu, F. H. 2002, *ApJ*, 580, 494
- Zsom, A. & Dullemond, C. P. 2008, *A&A*, 489, 931
- Zsom, A., Ormel, C. W., Dullemond, C. P., & Henning, T. 2011, *A&A*, 534, 73
- Zsom, A., Ormel, C. W., Güttler, C., Blum, J., & Dullemond, C. P. 2010, *A&A*, 513, 57

ACKNOWLEDGMENTS

I want to begin by thanking my advisor, Kees Dullemond, who has been a constant source of enthusiasm and energy. He encouraged me to follow my own ideas and plans, but was also there to provide insight and to give pointers when necessary. I was full of inspiration after every one of our meetings, and I think and hope that I have managed to absorb at least some of his way of thinking throughout the years. I am sure that this will come to use even after my brief career in astronomy.

I also want to thank Jürgen Blum, Til Birnstiel, Carsten Güttler, Karsten Dittrich, Joanna Drążkowska, Thomas Henning, Satoshi Okuzumi, Chris Ormel, Paola Pinilla, Andras Zsom, and Gerhard Wurm for their help and for the many great discussions throughout the years. I am also grateful for the nice and friendly office atmosphere provided by Christian Baczynski, Volker Gaibler, Helen Morrison, Jon Ramsey, Mei Sasaki, Elena Sellentin and Laszlo Szücs, that has even allowed for some occasional work.

It has been a great experience to have been a member of the Forschergruppe, and I especially want to mention the groups in Braunschweig and Duisburg, who gave me a great introduction to both the people and science of the field.

I am in debt to Stephan Henke and Karsten Dittrich for the help with the German Zusammenfassung, and to Laszlo Szücs for the great last-minute proof reading. I am also thankful to Kees Dullemond, Mario Tieloff, Thomas Henning and Matthias Bartelmann in my final thesis committee, and also to Ralf Klessen in the IMPRS committee, for taking their time with this thesis.

This section would also not be complete without a specific mention to everyone who walked with me *In the Shadow of Kings*, to everyone who attended the Happy Tuesdays and to the people of Henrik. Far too few get to experience the dangers and intrigues under a dark sun, build ancient wonders in less than half an hour, hurl fireballs towards pesky Slivers, or to direct Syphilis in his eternal struggle against death robots and orcs riding dinosaurs. Take all this on a weekly basis, and you have the best distraction there is from the hectic world of science.

Last of all, I want to thank my family for all their support and encouragement. But I owe most of all to Maria for being my best friend for ten whole years, and I hope at least another hundred years to come. With you, I can talk about everything scientific and non-scientific, and it is difficult to describe how happy I am for your ever-present support and patience with a boyfriend that so often trails off in his own dusty thoughts. It is because of you that these three years have been truly great!